

# PRECISION ENGINEERING CONSORTIUM

2017 ANNUAL REPORT  
VOLUME XXXI  
January 2018

---

**Sponsors:**

Los Alamos National Laboratory  
Oculus VR

**Faculty:**

Thomas Dow  
Ronald Scattergood  
David Muddiman  
Mark Pankow  
Victoria Miller  
Brendan O'Connor

**Graduate Students:**

Charan Bodlapti  
Noa McNutt

**Undergraduate Students:**

Alyssa Edwards

**Staff:**

Kenneth Garrard  
Anthony Wong  
Beth Deakle

**Consultants:**

Karl J. Falter  
Stephen Furst

# Table of Contents

<b>Summary</b>	<b>i</b>
1. Balloon Experimental Twin Telescopes for Infrared Interferometry <i>Ken Garrard, Stephen Furst and Thomas Dow</i>	1
2. The Role of Built Up Edge in Diamond Tool Wear When Machining Steel <i>Brandon Suit and Thomas Dow</i>	29
3. Machining Plastic Optics <i>Charan Bodlapati, Anthony Wong and Thomas Dow</i>	57
4. Selection of Surrogate Material to Study Dry Machining of Plutonium <i>Noa McNutt, Thomas Dow, Alyssa Edwards, Ken Garrard and Anthony Wong</i>	81
5. Finding Natural Frequency of a Piezoelectric Load Cell <i>Alyssa Edwards and Thomas Dow</i>	115
6. Microscale Lens Array: Focused Ion Beam Milling of Microscale Features <i>Anthony Wong</i>	125
7. Multi Lens Array – II: Indentation and Creation of the Mold <i>Gaurav Dave, Sriraghav Sridharan and Mark Pankow</i>	143
8. High Spatial Resolution Infrared Mass Spectrometry Imaging <i>Mark Bokhart, Milad Nazari, Måns Ekelöf, Ken Garrard, Jeffrey Manni and David Muddiman</i>	163
9. Mass Spectrometry Imaging Software <i>Ken Garrard, Mark Bokhart, Milad Nazari and David Muddiman</i>	183
10. Characterization of Single Abrasive Grit With Force and Visualization Techniques <i>David Gebb and Thomas Dow</i>	201
11. Design of a Microfluidic Device to Extract Dyes From Fibers for Forensic Analysis <i>Sean Gunning, Ken Garrard, Stephen Furst and Thomas Dow</i>	245
<b>Personnel</b>	<b>253</b>
<b>Graduates of the PEC</b>	<b>263</b>
<b>Academic Program</b>	<b>265</b>
<b>Fact Sheet</b>	<b>273</b>

# SUMMARY

The goals of the Precision Engineering Consortium (PEC) are: 1) to develop new technology in the areas of precision metrology, actuation, manufacturing and assembly; and 2) to train a new generation of engineers and scientists with the background and experience to transfer this technology to industry. Because the problems related to precision engineering originate from a variety of sources, significant progress can only be achieved by applying a multidisciplinary approach; one in which the faculty, students, staff and sponsors work together to identify important research issues and find the optimum solutions. Such an environment has been created and nurtured at the PEC for 34 years and the 100+ graduates attest to the quality of the results.

The 2017 Annual Report summarizes the progress over the past year by the faculty, students and staff in the Precision Engineering Consortium. During the past year, this group included 3 faculty, 2 graduate students, 1 undergraduate student, 2 full-time technical staff members and 1 administrative staff member. This diverse group of scientists and engineers provides a wealth of experience to address precision engineering problems. The format of this Annual Report separates the research effort into individual projects but there is significant interaction that occurs among the faculty, staff and students. Weekly seminars by the students and faculty provide information exchange and feedback as well as practice in technical presentations. Teamwork and group interactions are a hallmark of research at the PEC and this contributes to both the quality of the results as well as the education of the graduates.

A brief abstract follows for each of the projects and the details of the progress in each is described in the remainder of the report.

## **1. Balloon Experimental Twin Telescopes for Infrared Interferometry (BETTII)**

The NASA BETTII is designed to study the infrared emissions from star formation and active galactic nuclei through a double-Fourier Michelson interferometer located on a balloon at an altitude of 37 km. The BETTII external optics include a pair of identical beam-reducing, four-mirror telescopes, each with a 522 mm aperture off-axis segment of a parabolic surface. These telescopes were designed, built and assembled at the NC State University Precision Engineering Consortium and are composed entirely of thin-walled aluminum components. The mounting structure is designed to be lightweight and stiff to reduce thermal equilibration time in the rarified air at the edge of space and to maintain robust alignment of the optical elements. The mounts also prevent deformation of the large optical elements via custom-build kinematic Kelvin couplings and fixed-load clamps; the maximum form error of the optical surfaces are 300 nm RMS.

## **2. The Role of Built-Up Edge (BUE) in Diamond Tool Wear When Machining Steel**

Despite its potential in many applications, diamond turned steel has long been considered improbable due to the inability to attain acceptable surface roughness and form. These difficulties lie in the rapid changes of the tool geometry due to wear and workpiece adherence. Experiments were conducted to investigate the effect of tool wear and workpiece adherence on the tool geometry and the subsequent bulk temperatures of the diamond tool, machining forces and chips produced. The results conclude that workpiece pickup dominates changes in effective tool geometry by nearly two magnitudes in size compared with tool wear. Finite element simulations were performed of the chip formation process with and without the dominating workpiece adherence. Comparatively, the geometry of workpiece adherence produces a more efficient cutting process despite the expected negative effects on the generated surface. Force results with the addition of the BUE geometry closely aligned with those of the experimental results, while simulations with the theoretical tool geometry produced forces much higher than the experimental results. Experimental chip thicknesses also matched closely with the workpiece adherence addition to the tool. This adherence acts as a protecting layer on the tool due to its low thermal conductivity in comparison to diamond. More heat flows through the workpiece and chip because the effective tool is no longer a heat sink. Workpiece adherence has a significant effect on the chip formation process when diamond turning steel in comparison to tool wear effects.

## **3. Machining Plastic Optics**

Polymers play a vital role in the optical industry. They have low specific mass, excellent optical properties when compared to mineral glasses and are commonly used for manufacturing lenses. Single point diamond turning is widely used to machine plastic lenses. However, information on the parameters that can optimize the surface finish and minimize diamond tool wear during machining of plastics is lacking. The goal of this research is to address these two problems: surface finish and tool wear for several plastic materials. Three polymers are being used in this research: Poly (methyl Methacrylate) (PMMA), Polycarbonate (PC) and Zeonex®. This report covers the initial results of the project and the challenges faced during diamond turning of these three materials.

## **4. Selection of Surrogate Material to Study Dry Machining of Plutonium**

The goal of this project is to study the onset of built-up edge on a carbide tool during dry machining of plutonium ( $\delta$  - phase Ga Alloy [3]). This phenomenon degrades the surface finish as well as the figure error of the surface. Material properties were surveyed and experiments conducted to find a surrogate material that would behave in a manner similar to plutonium but without the health issues related to that radioactive material. Several materials



including Oxygen Free High Conductivity (OFHC) annealed copper, 1100 aluminum and 1199 aluminum were machined with different Kennametal Carbide Tools on a precision lathe. A series of experiments involving non-overlapping cuts were made with each of these materials and the surface geometry, cutting forces and tool pickup were measured. The results indicated that 1199 (pure) aluminum exhibits the pickup problem observed with plutonium. After choosing the 1100 aluminum, it was used in experiments involving overlapping cuts. The 1199 aluminum develops the most pickup at high cutting speed and low depth of cut. Now that a surrogate material has been identified, the next step will be to verify that changes in these parameters will influence the pickup in the same way as plutonium.

#### **5. Finding Natural Frequency of a Piezoelectric Load Cell**

This report discusses a method of determining the natural frequency of a piezoelectric load cell used in dynamic force measurement. The experiment showed that the natural frequency of the tool holder and load cell ranges between 11-12 kHz. To create this impulse, 4 lb. fishing line was secured around the tool holder/load cell system. The applied impulse is created by loading the fishing line slowly until it snaps suddenly. This procedure disconnects the load cell from the loading system so that the load cell is not subjected to a continuous or repeated excitation. Previous tests at the PEC were conducted and the resonant frequency was measured to be approximately 11 kHz. In those experiments, the impulse was applied by tapping the load cell. However, it is difficult to contact the load cell only once when manually tapping it. Once excited, the trigger feature on the oscilloscope is used to measure the oscillation and the natural frequency. This report finds that applying the impulse to the load cell using the fishing line is an effective way to create the impulse to measure the resonant frequency of the system.

#### **6. Microscale Lens Array: Focused Ion Beam Milling of Microscale Features**

This research investigates the fabrication of microscale features in glassy carbon that will be used as a die to stamp features into a mold for injection molding of plastic lenses. The concept is to FIB mill a die with multiple features (4-9) and then stamp those features at a high repetition rate (>100/second) to create a mold for a large lens array. The features are nominally spherical with radii on the order of 20  $\mu\text{m}$  that would, with the parameters given above, create a mold with  $3 \times 10^6$  lenses in an hour. The material removal rate of the FIB has been quantified and it was estimated that a single lens feature could be milled in a matter of minutes. A simulation tool was developed to assist in planning the FIB milling process that is similar to CAM for conventional milling. Finally, the inputs for the simulation, such as beam shape, were quantified.

## **7. Multi Lens Array – II: Indentation and Creation of the Mold**

This report is focused on understanding the indentation process for forming micro lens arrays. A finite element model has been developed to understand the plastic flow of this indentation process. It will be used to optimize this process to produce the best possible optical arrays. Preliminary results show promise for understanding how the deformation process works and offer insights on where to minimize the error to the surrounding lenses in a continuous high-speed indentation process.

## **8. High Spatial Resolution Infrared Mass Spectrometry Imaging**

High spatial resolution in mass spectrometry imaging (MSI) is crucial to understanding the biology dictated by molecular distributions in complex tissue systems. Here, we present MSI using infrared matrix-assisted laser desorption electrospray ionization (IR-MALDESI) at 50  $\mu\text{m}$  resolution. An adjustable iris, beam expander, and aspherical focusing lens were used to reduce tissue ablation diameters for MSI at high resolution. The laser beam caustic was modeled using laser ablation paper to calculate relevant laser beam characteristics. The minimum laser spot diameter on the tissue was determined using tissue staining and microscopy. Finally, the newly constructed optical system was used to image hen ovarian tissue with and without oversampling, detailing tissue features at 50  $\mu\text{m}$  resolution.

## **9. Mass Spectrometry Imaging Software**

A major update to the mass spectrometry imaging (MSI) software MSiReader is presented, offering a multitude of newly added features critical to MSI analyses. MSiReader is a free, open-source, and vendor-neutral software written in MATLAB and is capable of analyzing most common MSI data formats. A standalone version of the software which does not require a MATLAB license is also distributed. Newly incorporated data analysis features expand the utility of MSiReader beyond simple visualization of molecular distributions. A quantification tool allows researchers to calculate absolute concentrations exclusively through MSiReader software, significantly reducing analysis time. An image overlay feature for visualizing complementary imaging modalities, an ionization polarity filter, and a quality assurance feature to calculate and display mass measurement accuracy (MMA) have also been added. Most importantly, as new features have been added performance has not degraded, in fact it has been dramatically improved. These new tools and performance improvements enable the MSI community to evaluate their data in greater depth and in less time.

## **10. Characterization of Single Abrasive Grit with Force and Visualization Techniques**

The goal of this project was to study the tool wear, geometry and forces based on operating parameters in a grinding process experienced by a single abrasive grits. Individual abrasive grits on a coated abrasive are generally within a given size range but can have a range of

cutting geometries. Grit geometries can also change as grits wear and fracture. Experiments were performed to determine an effective experimental procedure for testing and visualizing a single triangular shaped alumina grinding grit remove material. Two different geometries of the individual grits were tested in the two different orientations. Cutting forces were measured using a three axis load cell and simultaneous high speed video was recorded at 6006 frames per second. The experimental depth of cut varied from 5 – 60  $\mu\text{m}$  and the surface cutting speed from 1 – 8 m/s. High speed videos were used to measure chip shear angles by measuring chip speeds. Shear angle measurements were limited to a maximum of 1 m/s cutting speed by the video quality at high speed. Material build up at the cutting interface was sometimes observed when tool forces rose to the point of grit fracture. Abrasive grit geometry was measured through workpiece surface profiling techniques and optical microscopy. Machining experiments were completed on 304 stainless steel, 4330V steel, 1215 steel and 52100 steel.

#### **11. Design of a Microfluidic Device to Extract Dyes from Fibers for Forensic Analysis**

Analysis of fiber evidence from a crime scene is an important aspect of criminal investigation. Fibers are identified and compared by morphology and the molecular makeup of the coloring dyes. Separation of dye from fiber is a tedious process involving aggressive and hazardous solvents that can take a skilled lab technician up to 30 minutes per sample. It is also destructive. The objective of this research was to design and build a microfluidic system to automate the extraction process using a minimal amount of a sample.

# 1 BALLOON EXPERIMENTAL TWIN TELESCOPES FOR INFRARED INTERFEROMETRY

**Kenneth P Garrard**

Senior Research Scholar, PEC

**Stephen Furst**

Smart Material Solutions, Inc.

**Thomas Dow**

Professor, Mechanical and Aerospace Engineering

*The NASA BETTII – Balloon Experimental Twin Telescope for Infrared Interferometry – is designed to study the infrared emissions from star formation and active galactic nuclei through a double-Fourier Michelson interferometer located on a balloon at an altitude of 37 km. The BETTII external optics include a pair of identical beam-reducing, four-mirror telescopes, each with a 522 mm aperture off-axis segment of a parabolic surface. These telescopes were designed, built and assembled at the NC State University Precision Engineering Consortium and are composed entirely of thin-walled aluminum components. The mounting structure is designed to be light weight and stiff to reduce thermal equilibration time in the rarified air at the edge of space and to maintain robust alignment of the optical elements. The mounts also prevent deformation of the large optical elements via custom-built kinematic Kelvin couplings and fixed-load clamps; the maximum form error of the optical surfaces are 300 nm RMS.*



## 1.1 INTRODUCTION

The NASA Balloon Experimental Twin Telescope for Infrared Interferometer (BETTII) is a balloon-based observatory designed to study the infrared emissions from star-forming regions, the center of active galactic nuclei, galaxy evolution, and the formation of planetary systems around other stars [1, 2, 3]. The optical design allows unmatched,  $\sim 0.5$  arcsec angular resolution so that individual stars within a nebula or cluster can be isolated [1]. BETTII will capture the interference fringes corresponding to source spectra in infrared wavelengths between 30-90  $\mu\text{m}$ . The entire balloon-borne system shown in **Figure 1** includes two identical sets of external optics comprised of a flat turning mirror (siderostat) and a four-mirror beam compressor. These optics are mounted on an 8 m carbon fiber space frame and carried to an altitude of 37 km by a helium-filled balloon. At this altitude the air pressure is only 0.2% of that at sea level and atmospheric absorption and disturbances are greatly reduced, providing similar observing conditions to those enjoyed by much more expensive orbiting telescopes. The project is headed by the Goddard Space Flight Center (GSFC) and BETTII was launched in June of 2017.

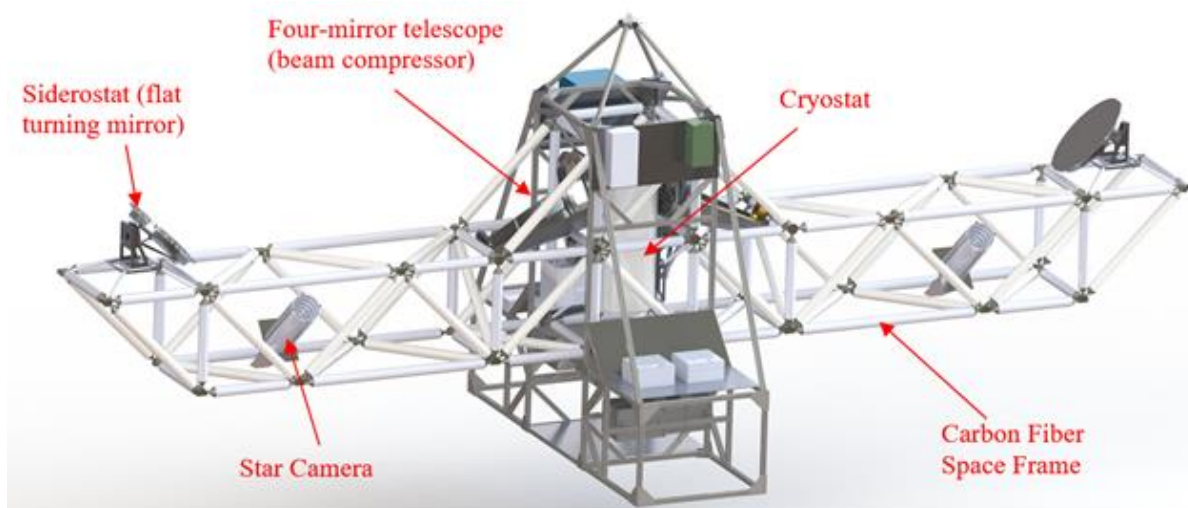


**Figure 1.** NASA's 8 meter long, 1000 kg BETTII gondola.

### 1.1.1 Optical System

The optical system is a double-Fourier Michelson interferometer [4]. It takes light from two identical sets of external optics and compares them in a cryogenic chamber. Each set of external optics has a turning mirror on the periphery of the space frame called a siderostat and a four-mirror telescope that acts as a beam compressor, as shown in **Figure 1**. The pair of back-to-back four-mirror telescopes near the center of the space frame provide the magnifying power.

The mechanical design and building of the mirrors and mounting structure of the external beam compressor telescopes is the subject of this work. The all-aluminum telescopes are off-axis and tilted  $13.3^\circ$  with respect to the parent optical axis, eliminating any obscuration of the aperture. The telescopes are essentially off-axis concentrators, delivering collimated light to the instrument package as shown in **Figure 2**. In each telescope, the primary mirror is a segment of a 2.758 m radius of curvature parabola that is 651 mm off-axis with an aperture of 522 mm, as shown in **Figure 3**. These mirrors were machined at the NC State University Precision Engineering Consortium using a diamond turning lathe with a custom fast-tool servo – a high bandwidth linear machine tool axis that is capable of cutting features that are not symmetric about the spindle centerline [5, 6]. The flat mirror has a 220 mm diameter, and the secondary and tertiary are both small (<40 mm aperture) and have complex non-rotationally symmetric designs.

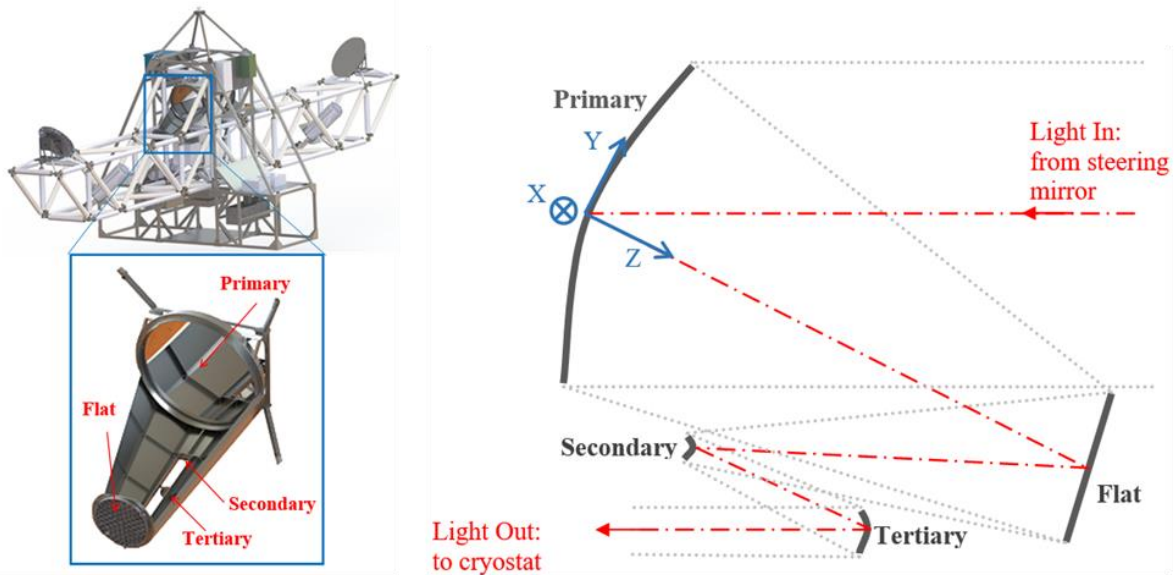


**Figure 2.** Four mirror beam compressor telescope with 3 non-rotationally mirrors and one flat mirror.

**Table 1.** Optical surface and alignment tolerances.

Mirror	Form error (nm RMS)	Surface finish (nm RMS)	Alignment		
			X, Y (mm)	Z (mm)	Rx, Ry (arcmin)
Primary	300	100			1
Flat	300	100	2 (excess aperture)	0.03	0.4
Secondary	300	100	0.1	0.05	1
Tertiary	300	100	0.2	0.1	1

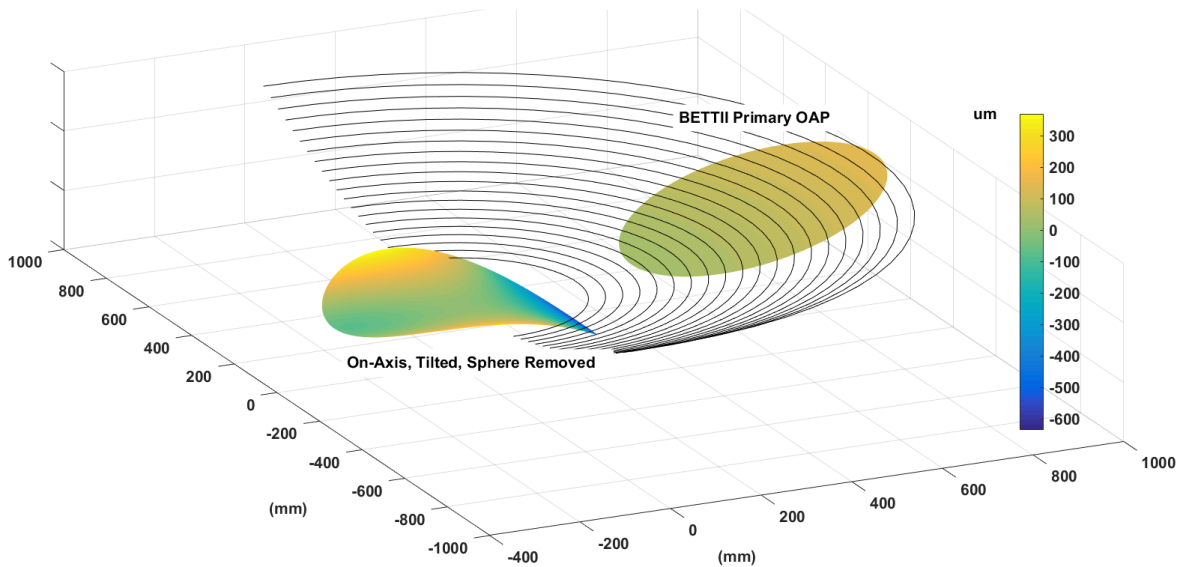


**Figure 3.** Primary mirror showing parent parabola (wire mesh), off-axis 522 mm aperture section that defines the BETTII Primary, and the non-symmetric residual when the optic is rotated to be cut on axis.

The form error and alignment tolerances for the telescope optics are critical for their design and are derived from the wavelengths being studied that range from 30-90  $\mu\text{m}$  for the science objectives and 1.0-2.5  $\mu\text{m}$  for tracking. The optical objective is to have form errors less than 1/10<sup>th</sup> the minimum science wavelength of 30  $\mu\text{m}$ , or 3  $\mu\text{m}$ . However, this objective includes added errors of multiple optics in both telescopes plus alignment errors and contraction effects (i.e. inhomogeneity in coefficient of thermal expansion), so the form error tolerance for each individual optic is 300 nm RMS. Form requirements and alignment tolerances are shown in **Table 1**.

### 1.1.2 Design Challenges

The balloon-based mission brings with it many unique challenges for designing and fabricating an optical system. For example,

1. During the ascent into the high atmosphere, the telescope will experience temperature changes of 150 °K and the temperature at 37 km is ~220 °K. This is an issue because of both thermal contraction/expansion and thermal equilibration time.
2. Convective heating/cooling is extremely slow at high altitude where air pressure is 0.2% sea-level. Radiation dominates in determining temperature.

3. The telescopes are tilted  $13.3^\circ$  with respect to the horizontal, making the mirrors more susceptible to gravitational distortion.
4. The telescopes need to be light weight because of balloon payload restrictions and to minimize thermal mass.
5. Alignment of the optics must be done on the ground in conditions significantly different from operating conditions at high altitude.
6. The system must withstand a 5 g load upon parachute deployment during the descent after each one-night mission.

Designing diamond turned metal optics and optical mounts for aerospace applications is not new [7]; however, as performance requirements continue to increase for ever more sensitive instruments and the associated costs must be controlled, new techniques must be developed. Previous missions including the Japanese Advanced Meteorological Imager (JAMI) [8] and the Thermal Emissions Imaging System (THEMIS) [9] have overcome their challenges by carefully balancing system performance requirements with time to flight and cost by adjusting materials, mechanical design and assembly methods. One of the challenges of designing light-weighted metal optical systems for flight systems has consistently been the isolation of bolting stresses from the optical surface. Particularly in aluminum, threaded fasteners can induce local stresses near the yield point of the material. The impact of these stresses can be significant even over large distances since even highly localized stresses usually induce significant moments. This problem is often exacerbated by low aspect ratios and skin thicknesses of light-weighted mirrors usually dictated by low mass requirements. Established mounting techniques [10, 11, 12] have focused on integrating flexures into the substrates of metal mirrors to reduce the influence of bolt stresses. This technique can be effective to a point but is usually costly and must be carefully considered since the large accelerations experienced by flight systems preclude the use of very compliant flexures. Additionally, compliant flexures that are very effective at isolating mounting stresses generally perform poorly at locating components accurately. The challenge, then, becomes mounting components precisely to withstand high acceleration but without distorting the optical surfaces. This paper illustrates how, using innovative structural design and fabrication techniques, two lightweight four-mirror off-axis telescope assemblies were produced at the NC State University Precision Engineering Consortium.

The non-rotationally symmetric primary mirrors of the BETTII optical system are diamond-turned using a fast tool servo and the flat mirrors are diamond-turned as well. To overcome the thermal and weight challenges, the entire system must be thin-walled. This gives the telescope a large



surface area to volume ratio to reduce the thermal time constant. Unfortunately, thin structures complicate fabrication because they deflect under the cutting forces and during removal from holding fixtures, leading to print-through and form errors. Thin optics are also more likely to deflect when mounted on a tilted telescope assembly. So in addition to being thin the structure must be very stiff to prevent print through, misalignment, and deflection due to gravity sag and mounting. The entire structure is machined from AL6061-T6 to avoid stresses due to mismatched thermal expansion/contraction. All parts are heat treated after rough machining to relieve stress left over from the stock and machining process.

## 1.2 MIRROR DESIGN

There were four main goals for the mirror design.

1. Limit the thickness to ~2 mm to reduce weight and thermal time constant.
2. Prevent gravity sag when the mirrors are mounted 13.3° from vertical.
3. Prevent deflection due to print-through and mounting to a holding chuck.
4. Decouple deflections in the mounting structure from the optical surfaces via kinematic couplings.

### 1.2.1 Off-Axis Parabolic Primary

**Figure 4** shows the design of the primary mirror. Raised bosses on the back of the mirror are lapped flat and bolted to a diamond-turned mounting chuck with carefully controlled bolting forces. The light-weighting pattern on the back has thicker ribs with a wide spacing to combat gravity sag and thin ribs spaced 30 mm apart to reduce the amplitude of print-through during diamond turning. The front of the mirror has 3 toroidal features that form half of a kinematic Kelvin coupling. The optical surface is 2.5 mm thick, outer rim is 5.0 mm thick, major spars are 4.0 mm, minor ribs are 2.0 mm, and mass is 5.73 kg. Analysis shows that gravity will cause this design to sag by 426 nm PP when tilted 13.3°, as shown in **Figure 5**. This telescope is designed to study long wave-length (> 30 μm) light, so peak-to-valley form errors due to gravity sag on the order of 400 nm are acceptable.

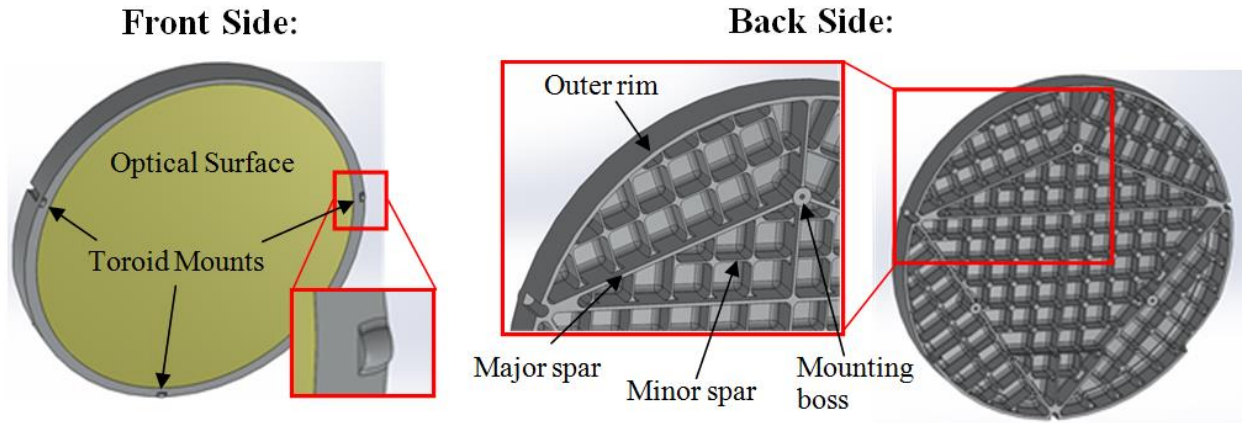


**Figure 4.** Primary mirror front (left) with kinematic coupling and back (right) with light-weighting ribs and mounting bosses.

Since the surface of the mirror is only 2.5 mm thick, print-through due to tool thrust force is a concern. Analysis was done by applying 1 N force at many locations on the front of the mirror and examining predicted deflections. The sum profile – approximated by placing an equivalent pressure load on the front face – is shown in **Figure 5**. **Table 2** shows that print-through is expected to produce features less than 141 nm PV at the locations furthest from the mounting bosses.

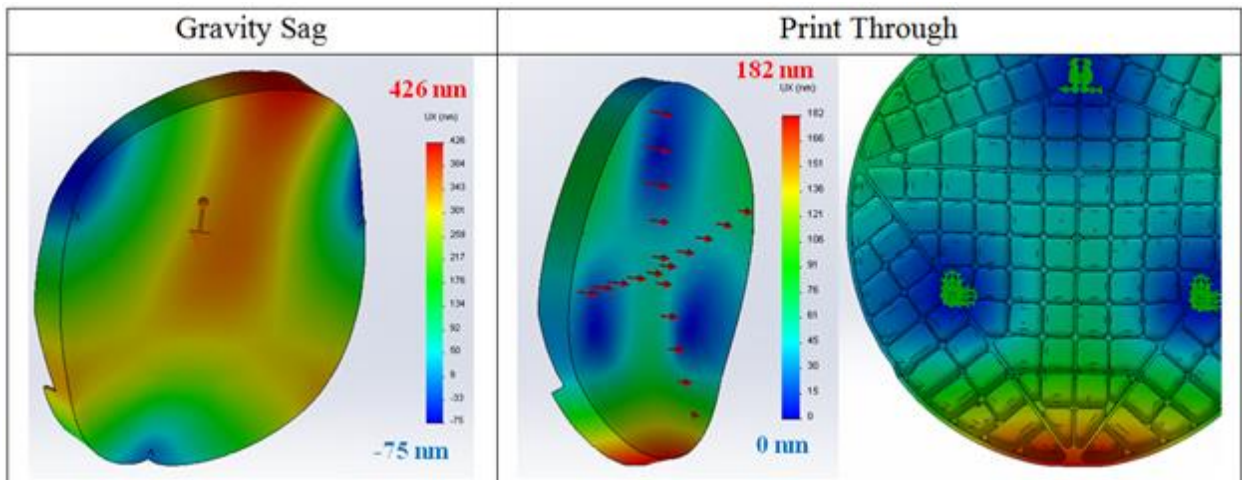


**Figure 5.** Deflection of primary mirror due to gravity (left) and print-through (right).

**Table 2.** Predicted deflection due to 1 N tool thrust force at different locations.

Location	Deflection (nm)	Resulting Error (nm)
Main Mounting Boss	32	0
Major Spar (near boss)	39	7
Outer Rim	173	141
Minor Spar	85	53
Between Minor Spars	118	86

### 1.2.2 Flat Turning Mirror

The flat mirror posed the same challenges as the primary but with a smaller diameter. The flat mirror uses the same toroid-shaped feature for its kinematic mount as the primary. The back of the flat mirror is light-weighted, but because it is half the size of the primary, the simple pattern shown in **Figure 6** is sufficient to combat gravity sag as well as print-through. Also, the features on the back side of the flat mirror can be cut out with a square end mill, eliminating the need for weight-adding fillets at the bottom of the pockets. The outside of the flat mirror is 254 mm in diameter and 12.7 mm deep. The face is 2 mm thick, the outer rim is 4 mm wide, and the rest of the ribs on the back are 2 mm wide, giving a total mass of 0.64 kg. As with the primary, raised bosses on the back are lapped flat and used for mounting during diamond turning.

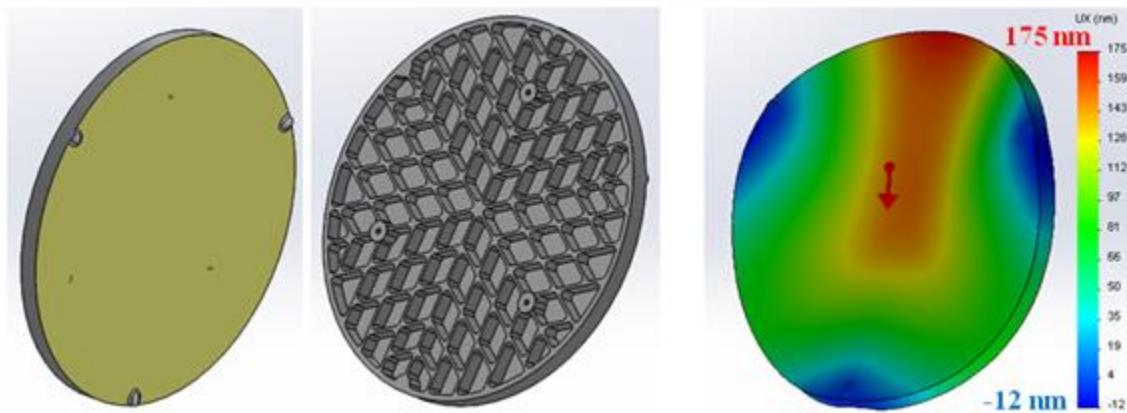


**Figure 6.** Front (left) and back (middle) of flat turning mirror. Deflection due to gravity (right).

### 1.3 MOUNTING STRUCTURE DESIGN

For the mounting structure, the design challenge was to adequately support and accurately align the four optics without inducing bending in the large, thin optics. This is accomplished by the combination of mounting rings that are bolted to each end of the trough and kinematically supporting the two mirrors via a novel set of diamond-machined Kelvin couplings [11]. Due to constraints in the BETTII space frame, the entire telescope assembly has to be mounted from behind the primary, resulting in a significant overhanging load. The flat mirror is 0.64 kg and suspended 811 mm from the primary. Both telescope assemblies are mounted to the titanium and carbon fiber space frame by struts attached to the primary mounting ring. The struts have flexures that allow the aluminum mirrors and trough to contract at a different rate than the space frame without imparting significant moments into the optical structure.

The components in the mounting structure are shown in **Figure 7** and listed in **Table 3**. Each part is machined from a single piece of aluminum 6061-T6 and heat-treated to relieve internal stresses. The two sides of the trough are first joined in the middle to produce a one-piece base. Then the rings can be attached and shimmed as needed to align the primary and flat mirrors, as described below. The trough is simultaneously light and stiff to reduce the distortion from the overhanging flat mirror. The large surface area to volume ratio, shown in **Table 3**, also makes this structure an excellent heat sink and reduces the thermal time constant of the entire assembly – accomplishing a critical design goal. The faceted design facilitates machining of the 1.5 mm thick trough by providing 3 flat outer surfaces that can be held on a flat vacuum chuck while the pockets on the inside of the trough are milled out with a square end mill.

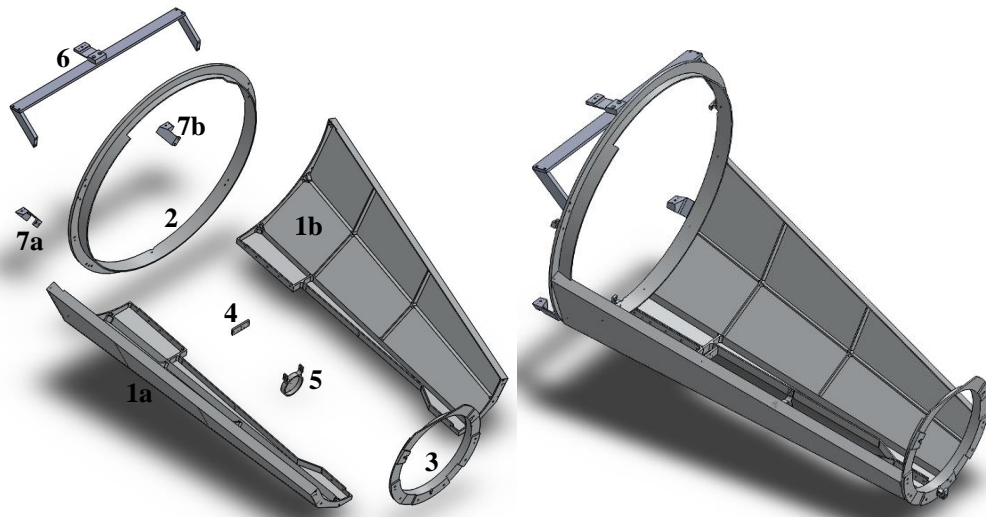


**Figure 7.** Mounting structure with thin-walled trough and coupling rings.

FEM simulations were used to determine the stiffness, with particular emphasis on stiffness in the vertical, Y direction. This stiffness was modeled at 0.054 N/ $\mu\text{m}$ , as indicated by **Figure 8**, which shows a 184  $\mu\text{m}$  deflection in response to a 10 N overhanging load. A frequency analysis was also performed indicating a first natural frequency at 32 Hz. This natural frequency is high enough to limit transient vibrations persisting in the telescopes after disturbances due to atmospheric instability or telescope pointing motions.

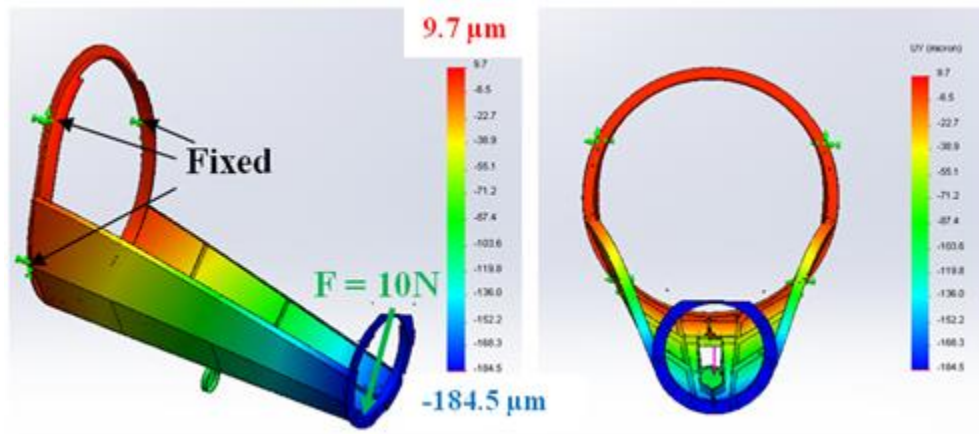


**Figure 8.** Deflection of mounting structure in the Y direction due to a 10 N overhanging load.

**Table 3.** Component size and weight summary.

	Component	Surf/Vol ( $\text{mm}^2/\text{mm}^3$ ) $\times 10^6 =$ ratio ( $\text{mm}^{-1}$ )	Mass (kg)
1	Trough (assembled)	$1.223/1.238 = \mathbf{0.99}$	3.356
2	Primary Mirror Ring	$0.191/0.330 = \mathbf{0.58}$	0.891
3	Flat Mirror Ring	$0.082/0.152 = \mathbf{0.54}$	0.411
4	Secondary Mirror Ring	$0.003/0.004 = \mathbf{0.66}$	0.012
5	Tertiary Mirror Ring	$0.012/0.013 = \mathbf{0.93}$	0.034
6	Flexure Brackets (top)	$0.069/0.182 = \mathbf{0.38}$	0.292
7	Flexure Brackets (bottom)	$0.017/0.054 = \mathbf{0.31}$	$0.055 \times 2$
	Primary Mirror	$1.295/2.122 = \mathbf{0.61}$	5.729
	Flat Mirror	$0.189/0.236 = \mathbf{0.80}$	0.638
	Total	$3.121/4.466 = \mathbf{0.70}$	11.473

**Table 3** shows the surface area, volume, and mass of each component within the structure. It is important to try to keep the surface area to volume ratio – and thus thermal time constant – similar



between the components. Note that the mounting rings have a lower ratio due to thick bosses, but they also have a large contact area with the trough structure that has the highest surface to volume ratio. The flexure brackets also have a lower ratio, but they are designed specifically to accommodate such stress gradients. After assembly, thermally conductive paste and tape will be applied to speed conductive heat transfer between the thin-walled trough and the thicker components.

The mirrors are attached to the rings using a kinematic Kelvin coupling that enables repeatable mounting and decouples deformations in the mounting structure from the optical surface. The Kelvin coupling consists of a toroidal feature that is on the front of each mirror and a triangular groove in the mounting rings, as shown in **Figure 9**. Since these mounting features are on the front of the mirror, they can be cut using the same fast-tool servo that is used to make the non-rotationally symmetric optical surfaces. Alignment between the mirrors and the toroidal mounting features is thus greatly improved.

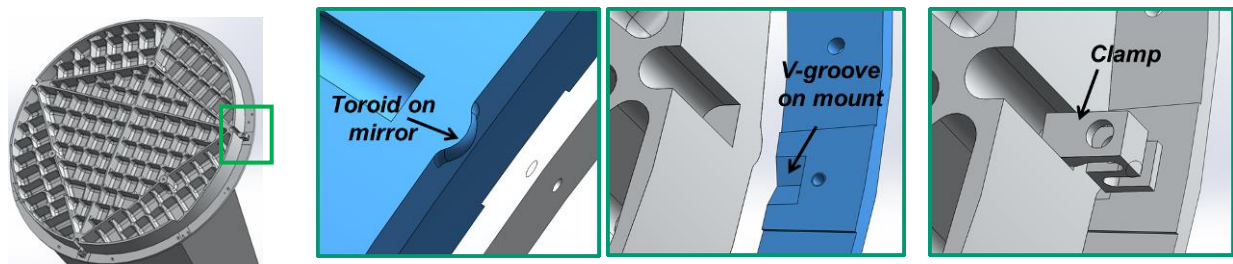


**Figure 9.** Kinematic coupling mounts.

The mirrors are held in place by clamps that provide a constant, pre-determined load through the center of the toroid features thus minimizing moments that would induce distortion to the mirror. Each clamp is designed to provide a fixed, 85 N load directly through the center of the toroidal mounting feature. The clamp profile keeps peak stress at the contacts below yield. Hertzian stress analysis [13] resulted in a 30 mm design radius for the spherical contacting surface. The clamp has a stiffness of 170 N/mm and has 0.5 mm of interference so that when the bolt is tightened it provides a fixed load of 85 N, as shown in **Figure 10**. The design is also relatively insensitive to small variations in flexure deflection, producing less than a 5 N change in load for a 25  $\mu\text{m}$  variation. Each mirror has 3 clamps for a total mounting load of 255 N for both the 5.73 kg (56.2 N) primary and the 0.64 kg (6.3 N) flat mirrors.

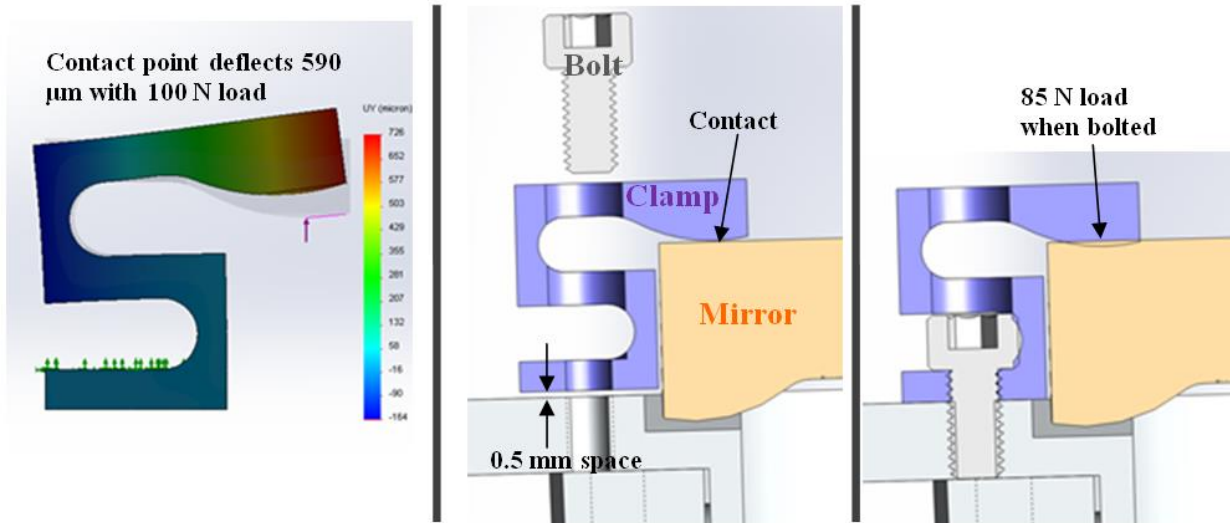


**Figure 10.** Clamps used to secure mirrors in Kelvin coupling. FEM model (left), clamp before is bolted (middle) and clamp with 0.5 mm interference after bolt is tightened (right).

Another challenge with the mounting structure is interfacing the all-aluminum telescope with the carbon fiber space frame truss structure of BETTII. Carbon fiber has very low thermal expansion coefficient compared to aluminum (**Table 4**[Error! Reference source not found.](#)), so when the balloon rises into the cooler temperatures on its way to 37 km altitude, the space frame will contract less than the telescope. The resulting thermal stress will deform the mounting structure and lead to deformation of the optical surfaces or misalignment between the four mirrors in the telescope or of the telescope with the cryostat optics. **Figure 11** shows that three flexures are used to join the primary ring and trough mount to BETTII's space frame via an X mount structure. The flexures are oriented such that they are centered about the middle of the primary, allowing them to easily expand and contract in the radial direction from the center of the telescope. The lower two flexures are at 45° from the bottom, giving them a wide profile in both the vertical and horizontal directions to reduce bending due to gravity and disturbance due to horizontal rotations of BETTII during pointing.

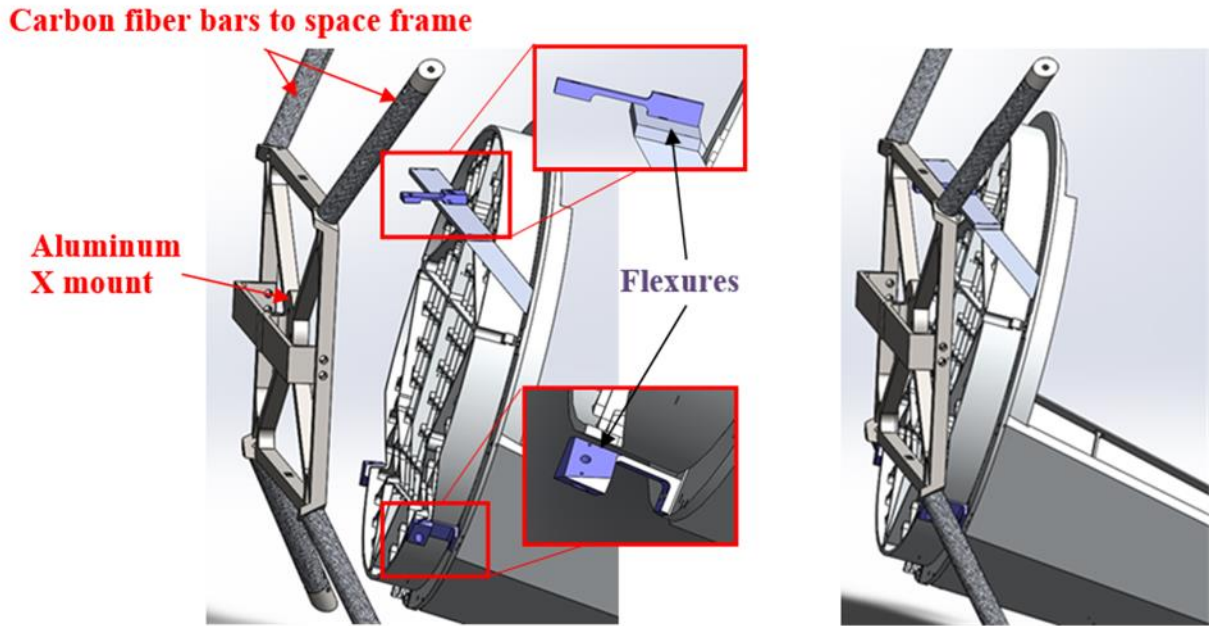


**Figure 11.** Flexures that connect aluminum telescope to the carbon fiber bars and space frame.

All of the elements in the telescope will contract due to the 150 °K temperature cycle that the telescope experiences during ascent. Once at science altitude, temperature will be around 220 K, about 73 K lower than fabrication temperature. **Table 4** shows peak thermal contraction, calculated with Equation (1).

$$\delta_T = \alpha_T L \Delta T \quad (1)$$

Where  $\delta_T$  is the contraction in  $\mu\text{m}$ ,  $\alpha_T$  is thermal expansion coefficient, in  $\mu\text{m}/\text{m}/^\circ\text{K}$ ,  $L$  is the span length in m, and  $\Delta T$  is temperature change in Kelvin. The optics in the telescope are all aluminum and designed to expand and contract together without imparting a stress or misaligning the optics. The flexures in **Figure 11** absorb the difference in contraction between the carbon fiber space frame and the aluminum telescope. The maximum deflection of the flexures is 1.1 mm in the vertical direction and 1.4 mm in the horizontal.

The 10-32 bolts that hold the mount together are 316 stainless steel because stainless has a relatively high thermal expansion coefficient, like aluminum. The aluminum spars on the mount between each nut and bolt are 8 mm thick and contract by 28  $\mu\text{m}$ , and the bolt itself contracts only 20  $\mu\text{m}$  potentially producing 8  $\mu\text{m}$  of slack in the bolts. However, when torqued to 45 Nm, the bolts become pre-stretched by 12.5  $\mu\text{m}$ , so even during peak contraction the bolts will be in enough tension to prevent the components from becoming misaligned.



**Table 4.** Thermal contraction of different components due to 150 °K temperature cycle.

Element	$\alpha_T$ [ $\mu\text{m}/\text{m}/\text{K}$ ]	$L$ [m]	$\delta_T$ [ $\mu\text{m}$ ]
Trough mount between primary and flat mirrors	23.1	0.811	2,810
Primary Mirror (optical aperture)	23.1	0.538	1,864
Flat Mirror (optical aperture)	23.1	0.224	776
Mounting structure bolt holes	23.1	0.008	28
Mounting structure bolts (316 Stainless)	16.5	0.008	20
Carbon fiber space frame at X mount (horizontal)	~3	0.460	207
Carbon fiber space frame at X mount (vertical)	~3	0.376	169
Telescope at Flexure Mounts (horizontal)	23.1	0.460	1,594
Telescope at Flexure Mounts (vertical)	23.1	0.376	1,303

## 1.4 STRUCTURE FABRICATION AND VALIDATION

Each component in **Figure 7** was machined from solid stock of aluminum 6061-T6. The large pieces that are assembled to make the trough each start out as a 200 kg block before being milled to the final mass of 1.68 kg. The mounting structure was machined by Weststar Precision (Apex, NC) and the mirror blanks by JMD Manufacturing (Wilmar, MN). After machining, all components underwent a heat treat process [8] to relieve residual stress from both the machining process and the quenching, drawing and tempering processes.

The mount was designed with ease of assembly and alignment of the optics in mind. The first step in assembly is to connect the two sides of the trough structure via a series of 7 bolts along the bottom of the trough. The procedure is described below and depicted in **Figure 12**.

1. Stand both sides of the trough on the primary mirror end upright on a ground flat and then bolt the sides together with a series of 7 bolts with nuts.
2. Attach the primary ring to the trough structure. Two 1/8" pins that go through reamed holes in the primary ring and the end of the assembled trough are used to locate the ring. Then a set of 4 bolts secure the ring via threaded holes in the end of the trough.
3. Next the flat ring is attached with two pins and 4 bolts, as above. The surface between the assembled trough and the flat ring can be shimmed to change the distance between the primary and the flat mirrors during optical alignment.

4. The secondary mirror mount is fixed to the bottom of the trough via two 1/16" pins and a bolt on one side, and 1 pin and 1 bolt on the other. The surface between the secondary mirror and the secondary mirror mount can easily be lapped or shimmed for alignment. Also, a pin can be removed to allow the mirror to rotate up and down.
5. The tertiary mirror mount is attached to the bottom of the trough with 3 pins and 2 bolts, as above.
6. The entire telescope is aligned with respect to the cryostat optics by placing shims between the two lower flexure mounts and the X mount structure. The interferometer hangs from the back of the X mount and is aligned to the telescopes in the vertical direction by placing spacers between the cryostat and the X mount.
7. After the telescope mount is assembled to the X mount, the flat mirror is mounted to the flat ring via the Kelvin coupling and clamps in **Figure 10**. This causes the rest of the mounting structure to deflect due to the overhanging load.
8. Finally, the primary mirror is mounted to the primary ring via the Kelvin coupling. This is done as the last step to prevent deflections from the overhanging load of the flat from being transferred into the large mirror through friction in the Kelvin coupling.

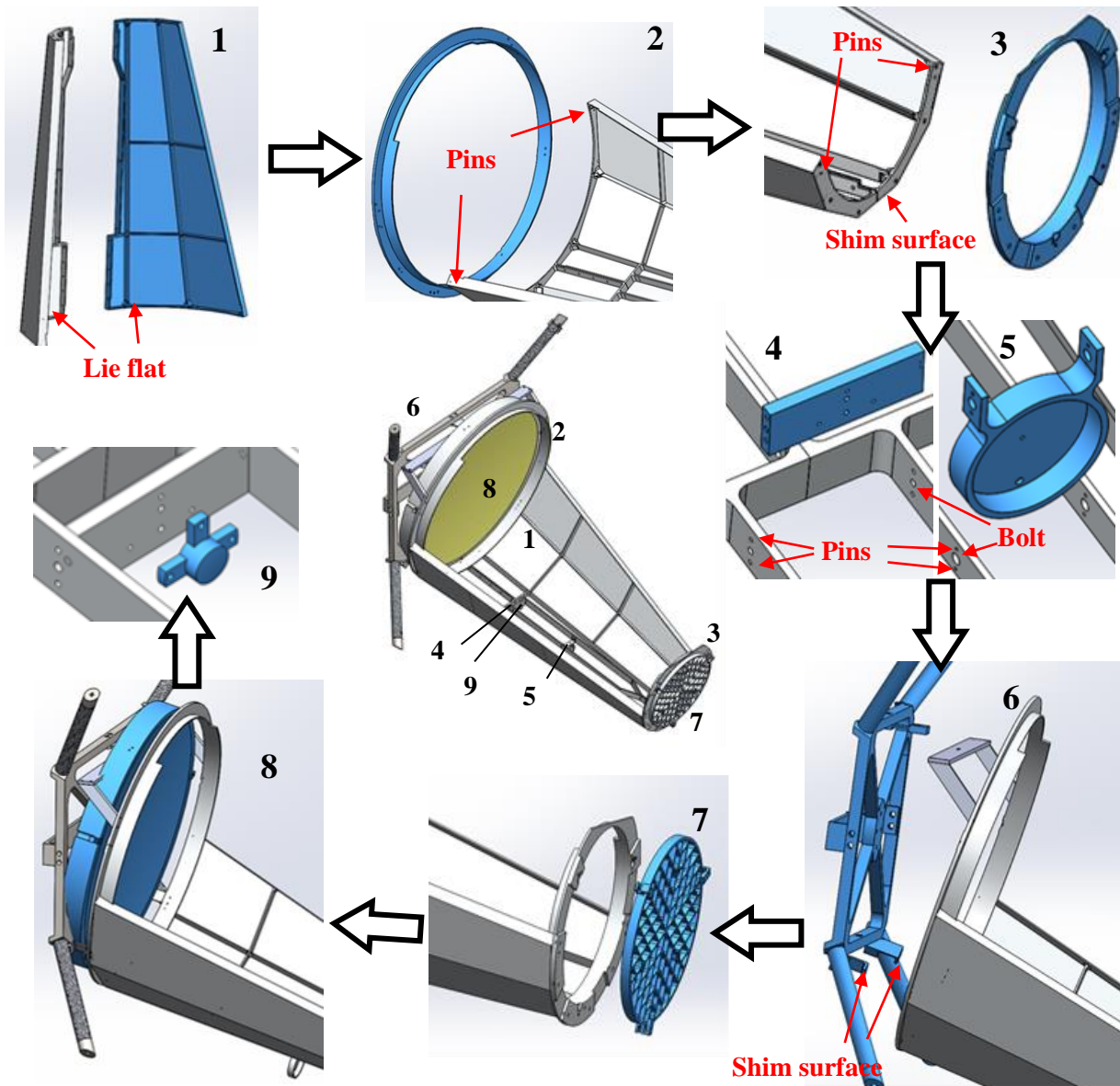


**Figure 12.** BETTII external optic assembly procedure.

All of the designed parts were machined and assembly was conducted according to the plan above. After step 1, the difference in length of the two sides of the 811 mm long trough was found to be 0.09 mm by measuring the step height on the flat end. All bolts in the structure were 10-32 316 stainless steel socket cap screws with 316 stainless nuts. They were tightened to 45 Nm of torque. The assembled mounting structure is shown in **Figure 13**.



**Figure 13.** BETTII telescope mounting structure.

The stiffness of the trough structure was measured in the same way as the clamps – by bolting the primary ring to an optical table and measuring deflections with a Federal gage while pushing on the structure with a force gage, as shown in **Figure 8**. The stiffness in the vertical direction is most critical at  $0.063 \text{ N}/\mu\text{m}$ , compared to the simulated value of  $0.054 \text{ N}/\mu\text{m}$ . The resonant frequency was measured by replacing the Federal gage with a capacitance gage and tapping the structure, as shown in **Figure 14**. The displacement response and FFT of the cap gage measurement after an impulse test is also shown in **Figure 14**, indicating a natural frequency at 36 Hz. This compares favorably to the lowest natural frequency of 32 Hz from the frequency analysis performed in FEM. It is not surprising that the measured natural frequency is higher than simulation, since the fabricated mount structure also had a higher measured stiffness. The 36 Hz frequency is also higher than the 24 Hz natural frequency of the space frame structure that serves as a benchmark.

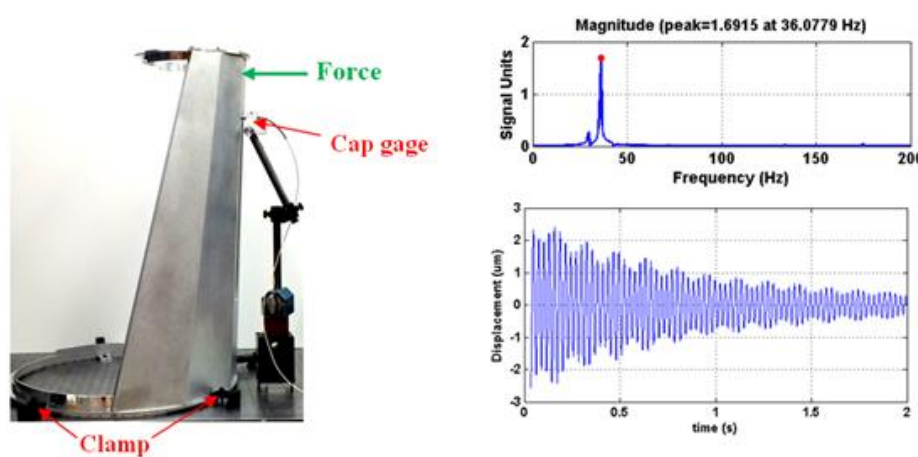


**Figure 14.** Measuring the mount stiffness and natural frequency (left) and FFT of an impulse test (right).

The dimensions and stiffness of the custom built clamps and mirror structure were measured to obtain an estimate of the clamping load applied. **Figure 15** shows the clamp. The total height of the clamp,  $h$ , and the thickness of the contacting pad,  $t$ , were measured with micrometers and the undeflected clamp height,  $h_0$ , was calculated as the difference. All 12 clamps had undeflected heights between 13.24 and 13.29 mm (design was 13.26 mm). The distance between the contact surface on the back of the mirror and the mounting ring to which the clamps were bolted,  $h_1$ , was measured using a coordinate measuring machine (CMM). These heights ranged between 13.70 and 13.73 mm, making for possible clamp deflections ranging between 0.41 and 0.49mm (design was 0.45 mm).

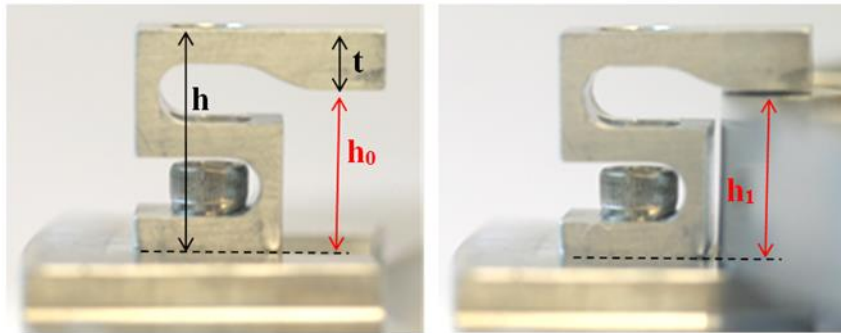


**Figure 15.** Custom fixed-load clamps for kinematic Kelvin coupling, undeflected (left) and holding the flat mirror (right).

The stiffness of the clamps was measured by bolting the clamp to an optical table then measuring deflection using a Federal gage while pushing on the clamp with a force gage. The stiffness was constant at 0.176 N/ $\mu$ m for multiple applied loads up to 83 N. Therefore the clamp loads are expected to range between 72.2 and 86.2 N, compared to the designed load of 85 N. In practice, the clamps displayed the ease of use and good repeatability that was anticipated in the design.

The primary role of the Kelvin coupling is to mount the thin, flexible optics to the mounting structure without imparting a moment into the optical surface. To test this, the flat mirrors were measured on a Zygo GPI (Zygo Corp., Middlefield, CT) laser interferometer while sitting on top of 3 pegs on the back-side of the mirror, opposite the toroid mounting features, as shown in **Figure 16**. Then the stiff, L-shaped flat ring was attached to the flat using the Kelvin coupling and custom clamps, and the flat was measured again. A comparison between the measurements is shown in **Figure 16** and demonstrates that no significant change occurred in the surface shape, despite the three ~85 N clamp loads. Both interferometer measurements show three high spots at the location of the mounting supports and low spots in between where the thin mirror has sagged due to gravity. The RMS surface error on the flat sitting on 3 support posts (left in **Figure 16**) is 181 nm and the RMS error of the flat bolted to the mounting ring (right) is 163 nm.

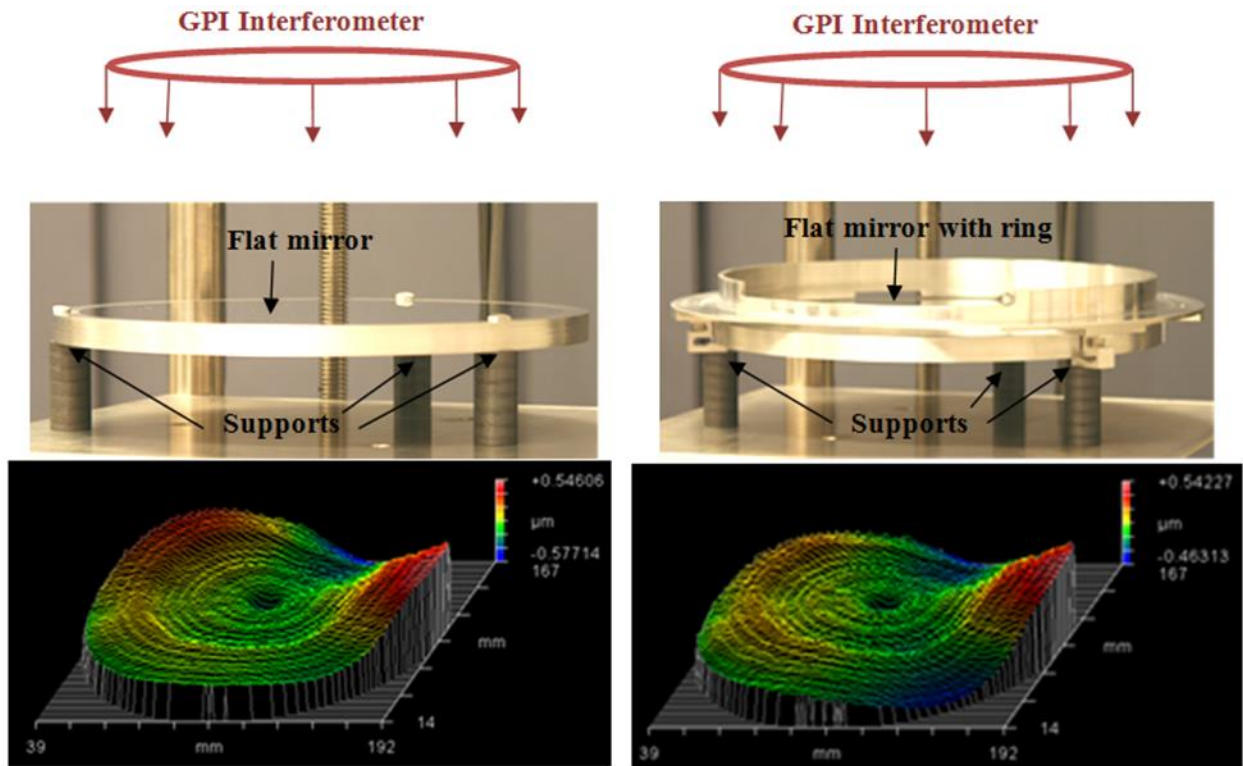


**Figure 16.** Surface form error of flat mirror unmounted (left) and clamped in kinematic mount (right).

## 1.5 MACHINING THE OPTICAL SURFACES

### 1.5.1 Flat Mirror

The flat mirror was bolted to the spindle of a NanoForm 600 DTM through three, flat bosses on the back of the mirror. These bosses were threaded for a  $\frac{1}{4}$ -20 stud to connect them to the diamond turned face of the chuck. The stiffness of the mirror was measured with a cap gage and load cell and ranged between 0.7 – 1.5 N/ $\mu$ m depending on proximity to the mounting boss. The flat mirror was machined at 200 rpm with a crossfeed of 25  $\mu$ m/rev, and the final form error was 0.175  $\mu$ m rms with a surface finish of 30 nm rms. There was no indication of print-through of the light-weighting features on the face of the 2.5 mm thick face of the mirrors from the interferometer measurements. The residual form error for the flat is shown in **Figure 16**.

### 1.5.2 Machining the Primary with FLORA II

Because of the size and the lack of rotational symmetry, the mirror must be machined on a DTM using a fast tool servo (FTS). In this case, a Nanoform 600 DTM was coupled with the FLORA II



fast tool servo built at the PEC [5, 6]. The spindle speed is 60 rpm to avoid significant centrifugal distortion. The final finishing pass requires 3 hours, during which time the oil flow and chip vacuum are continuously managed to prevent loose chips from degrading surface finish. The tool path for machining the off-axis parabolic section on axis is created by translating the off-axis aperture to the center of rotation, tilting it and subtracting the best fit rotationally symmetric surface. For an off-axis parabola the best fit on-axis surface is another parabola. The resulting sag is 13 mm and this is the path that the DTM axes follows from the OD to center. The 1 mm correction for the non-rotationally symmetric surface, shown in **Figure 17** is simultaneously added by the FTS.

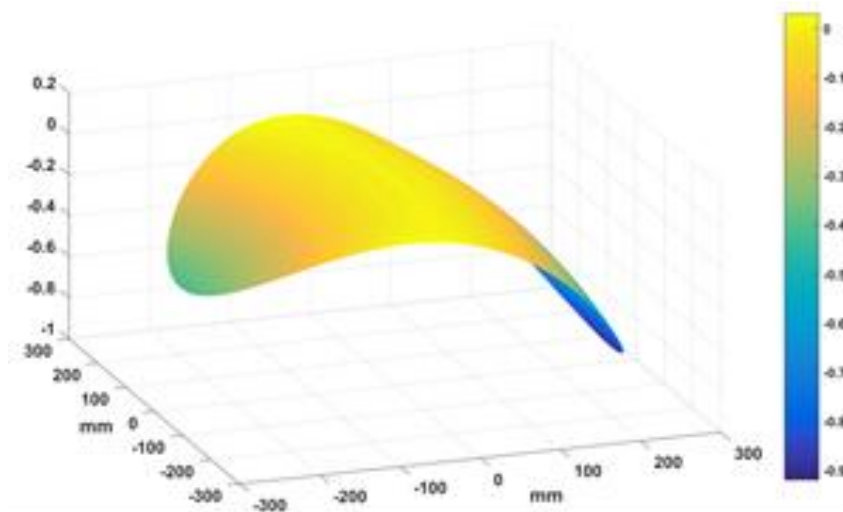


**Figure 17.** Non-rotationally symmetric component of the primary mirror.

FLORA II is a voice-coil-driven, air-bearing FTS with a range of 8 mm that can move the required 1 mm excursion for the primary mirror at 60 rpm with a following error of  $\pm 22$  nm. However that performance is predicated on a complex control system that includes position feedback and velocity and acceleration feed-forward. The controller update rate is 20 kHz, so every 50  $\mu$ sec new position, velocity and acceleration set points are calculated. The control system uses an Analog Devices SHARC 21061 32-bit floating point DSP.

Following a technique developed at the PEC, an analytic solution to the decomposition of the off-axis paraboloid into an on-axis rotationally symmetric shape and a non-rotationally symmetric residual was found [14] and the solution implemented using VisualDSP++ on the FLORA controller. On each update cycle the controller uses these coefficients to estimate the required feed forward set points. The primary mirror shortly after rough machining is shown in **Figure 19** mounted on the Nanoform 600 spindle with FLORA in the foreground.

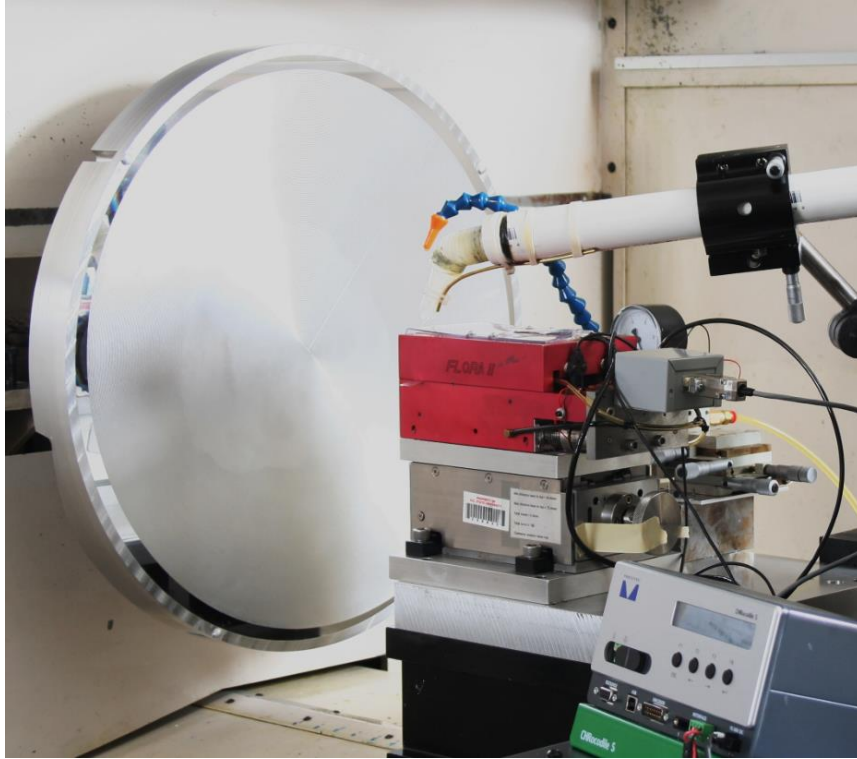


**Figure 18.** Rough machining the primary mirror with FLORA II on the Nanoform 600.

### 1.5.3 In-process Tool Replacement

When cutting the large primary mirror, each roughing pass will involve 2 km of cutting distance and the finishing pass 9 km. Since 8-10 roughing passes may be needed to clean up the part, it is desirable to replace the tool between roughing and finishing processes. Previous measurements with this round-nose tool indicated that the tool edge is expected to recede by 700 nm in Z and edge radius increase to 750 over the first 12 km of cutting, as shown in **Figure 19**. The SEM EBID technique for measuring tool wear was developed by Arcona and Dow at the PEC, and used extensively by Lane [15] and Hessler [16]. In **Figure 19**, the flank face is on the right, rake face is on the left, and worn edge is oriented vertically. The red dots are placed on the deposited EBID contamination line and compared to the profile of the sharp tool, with the area shaded in green representing the worn area of  $2.16 \mu\text{m}^2$ .



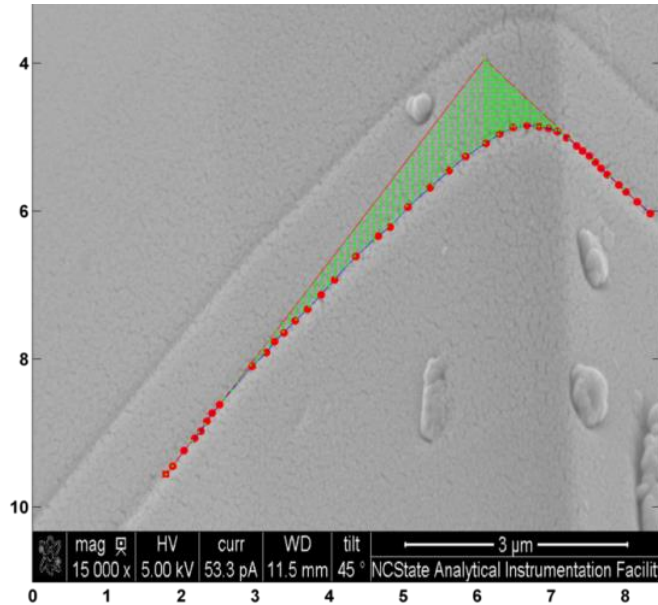


**Figure 19.** SEM image showing the edge of a diamond tool worn by cutting 12 km of AL 6061.

The large, non-axially symmetric part cannot be removed and precisely replaced while the tool is changed, so the new tool must be located at the spindle centerline without using the common method of cutting a spherical test plug. To accomplish this task, a new method was developed to locate the nose of the tool with a confocal chromatic aberration (CA) probe. The CA probe used, Precitec CHRocidile S, RB200 031, has a 5 μm diameter spot and 10 nm vertical resolution. The probe is mounted to the x-axis as shown in **Figure 20** and is used to scan the top of the diamond.

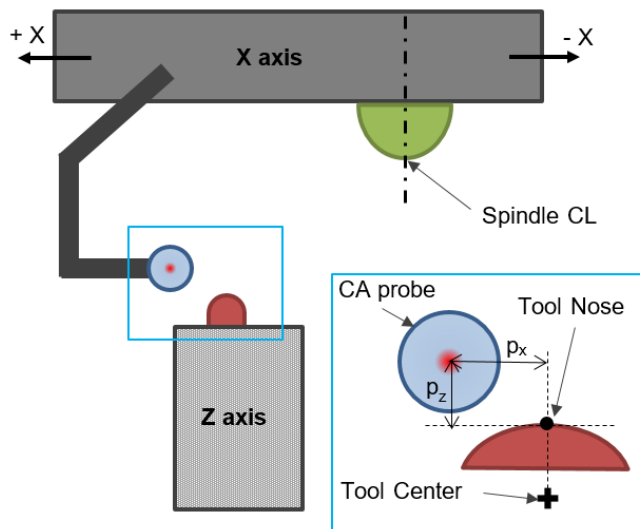


**Figure 20.** Schematic showing the spindle and probe mounted on the X axis and the tool on the Z axis.

The user jogs the axes to a position just off the nose of the tool, indicated by the G55 CS in **Figure 21**. Then the scan makes 9 traces across the tool in Z and the data is filtered to eliminate points that are not on the top of the diamond. A circle is fit to the edge points of the diamond and the center points and radius of this circle locates the nose of the tool. In the scan in **Figure 21**, the fit circle has a radius of 1.010105 mm, center of  $\langle -0.01404, -1.09305 \rangle$ , and the average edge height of 0.03929 mm.

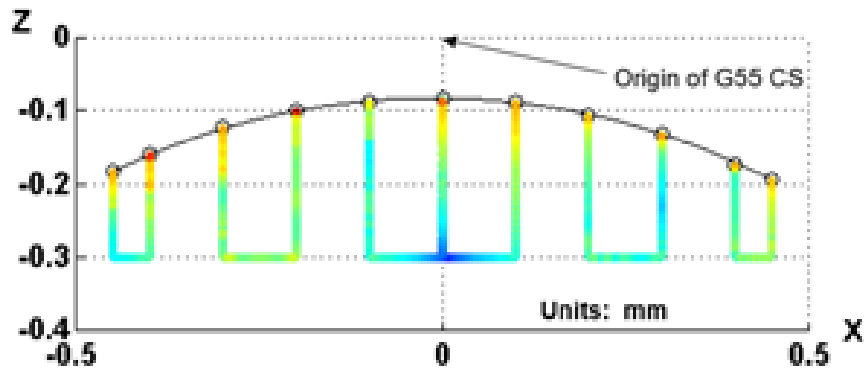


**Figure 21.** CA probe measurement of a tool.

When the new tool is mounted, the scan in **Figure 21** is repeated using the same fixed probe and deviations in the tool location are calculated. Deviations are corrected by first raising FLORA on the micro-height adjuster, then re-scanning to find the X and Z positions again. Finally, the X and Z offsets on the machine are adjusted so that the new tool will be aligned with the spindle centerline. The process was successfully verified by cutting test plugs before and after the tool replacement. The repeatability of the tool location measurement was validated by taking 8 measurements on the same tool. Given the same scan starting position, the standard deviation of the X, Z and height measurements were 58 nm, 71 nm, and 15 nm respectively. When varying the starting position of the scan within a 35  $\mu\text{m}$  range, the deviations increased to 538 nm, 200 nm, and 37 nm.

## 1.6 CONCLUSIONS

A novel method of supporting and mounting light-weighted metal optics for a demanding aerospace application has been demonstrated. The validation experiments showed that the design of the mounting structure was a success. The mount has a stiffness of 63 N/mm with a first natural frequency of 36 Hz, despite being an overhanging span nearly 1 m long and weighing ~5 kg. Diamond turning and subsequent measurement of the flat mirrors showed that the light-weighting ribs did not print through to the optical surface. The kinematic Kelvin coupling and custom clamps that join the mirrors to the mounting structure were also validated by measuring

the flat before and after mounting, with little observable difference down to the 10 nm scale. This demonstrates the effectiveness of a repeatable and easy-to-use mounting concept for light-weight mirrors.

### 1.6.1 First Mission

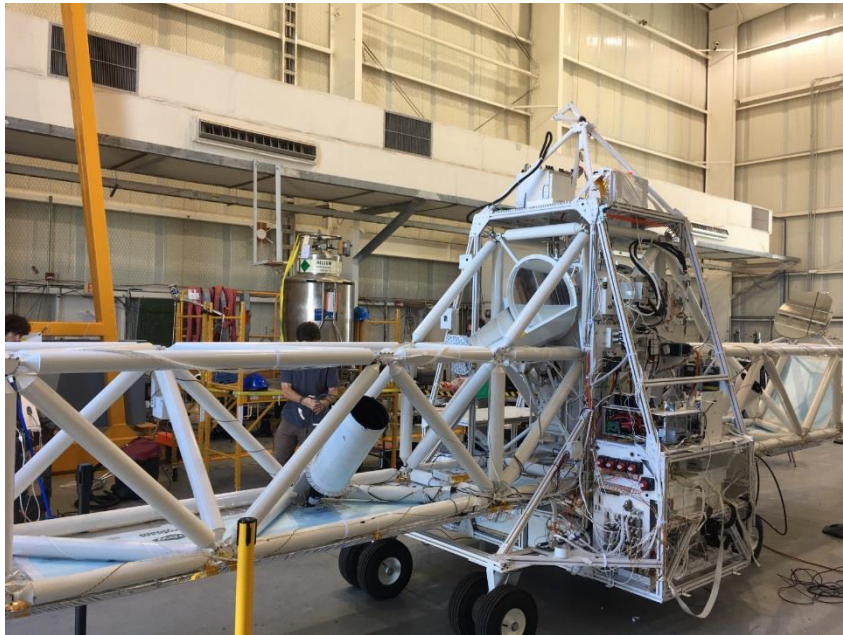


**Figure 22.** BETTII being assembled (top) and BETTII ready for launch (bottom).

In September of 2016 BETTII was assembled at Goddard Spaceflight center and transported to the balloon launch site in Palestine, Texas. **Figure 22** shows the nearly completed gondola in the assembly bay and ready for launch. However surface winds remained too high for several days and the launch was eventually rescheduled for 2017.



**Figure 23.** The first launch of BETTII.

Finally on June 10<sup>th</sup>, 2017 BETTII was launched and the event was recorded by a videographer from the North Carolina Museum of Natural Sciences. A still image from his video is shown in **Figure 23**. The overnight mission was successful and 10 SSD's of data were collected. However the dual release mechanism malfunctioned and released the Helium balloon and the unfurled parachute at 37 km altitude. The gondola was returned to the earth's surface without the benefit of a parachute to slow its descent. Most of BETTII was destroyed; however the SSD's containing data survived. The data has yet to be analyzed.

## 1.6.2 Acknowledgements

The authors would like to acknowledge funding from NASA Goddard Spaceflight Center.

## REFERENCES

1. Rinehart, S. A. "The balloon experimental twin telescope for infrared interferometry (BETTII). *Proceeding of the SPIE 7734*, 77340K (2010).
2. Rinehart, S. A., Rizzo, M., Benford, D. J., Fixsen, D. J., Veach, T. J., Dhabal, A., Leisawitz, D. T., G. Mundy, L., Silverberg, R. F., Barry, R. K., Staguhn, J. G., Barclay, R., Mentzell, J. E., Griffin, M., Ade, P. A. R., Pascale, E., Klemencic, G., Savini, G., and JuanolaParramon, R. "The Balloon Experimental Twin Telescope for Infrared Interferometry (BETTII): An Experiment for High Angular Resolution in the Far-Infrared." *Publications of the Astronomical Society of the Pacific*, Vol. 126, No. 941 (July 2014), pp. 660-673.
3. Rinehart, S.A., Barclay, R.B., Barry, R.K., Benford, D.J., Calhoun, P.C., Fixsen, D.J., Gorman, E.T., Jackson, M.L., Jhabvala, C.A., Leisawitz, D.T., Maher, S.F., Mentzell, J.E., Mundy, L.G., Rizzo, M.J., Silverberg, R.F., Staguhn, J.G. "Design and status of the balloon experimental twin telescope for infrared interferometry (BETTII): an interferometer at the edge of space." *Proceedings of the SPIE – The International Society for Optical Engineering*, 8445, p 844508. 2012.
4. Mariotti, J. M. and Ridgeway, S. T. "Double Fourier spatio-spectral interferometry: combining high spectral and high spatial resolution in the near infrared." *Astron. Astrophys.* 195, pp 350-363. 1988.
5. Chen, Qunyi, "Design and Control of a Fast Long Range Actuator for Single Point Diamond Turning." *PhD Dissertation*. NC State University, Raleigh, NC 2009.
6. Zdanowicz, E. M. "Design of a Fast Long Range Actuator – FLORA II." *Masters Dissertation*. NC State University, Raleigh, NC. 2009.
7. Mimovich, M. E., Griffee, J. C., and Gooding, J. C. "Optical mounts for harsh environments." *Proceedings of SPIE 7424*, 74240B (2009).
8. Toland, R. W., Ohl, R. G., Barthelmy, M. P., Zewari, S. W., Greenhouse. M. A., and MacKenty, J. W. "Effects of forged stock on cryogenic performance of heat treated aluminum mirrors." *Proceedings of SPIE 5172, Cryogenic Optical Systems and Instruments*, 21-24 (2003).
9. Schaefer, J. "Single Point Diamond Turning: Progress in Precision," *International Optical Design, Technical Digest (CD) (Optical Society of America, 2006)*, paper ThB1.

10. Bell, J. L.; Pavlov, M. M. "Design and analysis of a beryllium three-mirror anastigmat telescope for the Japanese Advanced Meteorological Imager (JAMI)." *Proc. SPIE 5658, Applications with Weather Satellites II*, 91-102 (2005).
11. Sweeney, M. N. "Advanced manufacturing technologies for light-weight post-polished snap-together reflective optical system designs." *Proc. SPIE 4771, Optomechanical Design and Engineering 2002*, 144-154 (September 9, 2002); doi:10.1117/12.482154.
12. Yoder, P. R., *Mounting Optics in Optical Instruments*, SPIE Press, 2008.
13. Young, C. Y. and Budynas, R. G. "Roark's Formulas of Stress and Strain." Seventh edition, Section 14.3, p 703. *McCraw Hill*, 2002.
14. K. Garrard, T. Bruegge, J. Hoffman, T. Dow and A. Sohn. Design tools for freeform optics. *Proc. SPIE*, 5874, 95-105, 2005.
15. BM Lane, *Material Effects and Tool Wear in Vibration Assisted Machining*. PhD Thesis North Carolina State University 2012.
16. GS Hesler. *Investigating the Mechanisms of Diamond Tool Wear Cutting Ferrous Materials Using a Quantitative Study of Machining Parameters*. MS Thesis, North Carolina State University.



## 2 THE ROLE OF BUILT-UP EDGE (BUE) IN DIAMOND TOOL WEAR WHEN MACHINING STEEL

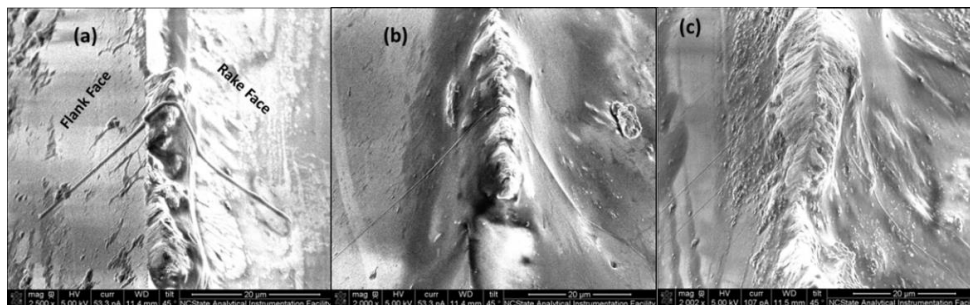
**Brandon Suit**

Manufacturing Engineer  
OCC, Lockheed Martin  
Orlando, FL

**Thomas A. Dow**

Dean F Duncan Distinguished University Professor in Mechanical Engineering  
Director, Precision Engineering Consortium  
North Carolina State University

*Despite its potential in many applications, diamond turned steel has long been considered improbable due to the inability to attain acceptable surface roughness and form. These difficulties lie in the rapid changes of the tool geometry due to wear and workpiece adherence. Experiments were conducted to investigate the effect of tool wear and workpiece adherence on the tool geometry and the subsequent bulk temperatures of the diamond tool, machining forces and chips produced. The results conclude that workpiece pickup dominates changes in effective tool geometry by nearly two magnitudes in size compared with tool wear. Finite element simulations were performed of the chip formation process with and without the dominating workpiece adherence. Comparatively, the geometry of workpiece adherence produces a more efficient cutting process despite the expected negative effects on the generated surface. Force results with the addition of the BUE geometry closely aligned with those of the experimental results, while simulations with the theoretical tool geometry produced forces much higher than the experimental results. Experimental chip thicknesses also matched closely with the workpiece adherence addition to the tool. This adherence acts as a protecting layer on the tool due to its low thermal conductivity in comparison to diamond. More heat flows through the workpiece and chip because the effective tool is no longer a heat sink. Workpiece adherence has a significant effect on the chip formation process when diamond turning steel in comparison to tool wear effects.*





## 2.1 INTRODUCTION

Usage of diamond as a cutting tool began as early as the 18<sup>th</sup> century [1]. In the 19<sup>th</sup> century, precision lathe work was combined with diamond tools to attain mirror-like finishes on softer materials, such as copper or gold. As applications expand, the demand for specific materials, such as steel, has increased. Steel is an ideal material for precision molds due to its wear resistance. However, diamond turning of steel is hindered by two complexities: tool wear and workpiece material adhering to the tool. Because of the change in tool geometry due to these factors, a specific surface finish and form cannot be economically attained. Usage of steel in precision applications requires post-process polishing to reduce the surface roughness down to the required level. This extra step increases fabrication time and costs.

### 2.1.1 Tool Wear

Diamond tool wear is defined as loss of the diamond material during machining. Even commonly diamond turned materials, such as aluminum, copper, and electroless nickel wear the tool during machining. However, because of the high hardness of diamond, tool wear rates when machining these materials are low and allow for an economical diamond turning process [2]. In comparison, carbide formers like iron wear the diamond tool at a much higher rate. Lane et al. [3] showed AISI 1215 wore a diamond tool at a 1000 times higher rate than Al-6061-T6.

Many investigations [3-13] have attributed the accelerated tool wear to a thermochemical wearing mechanism, such as oxidation, graphitization or diffusion, rather than the more common abrasive wear seen when machining materials with no chemical affinity for carbon. Thermochemical mechanisms are dependent upon the reactivity of the elements and the available energy to initiate a reaction. This would mean there are two controlling factors for tool wear: temperature and the reactivity of the elements. Lane [9] and Hesler [14] both advanced a temperature dependent model for tool wear when machining low carbon steel. Results showed a minimum wear rate at 1 m/s that was believed to be due to the amount of energy present and reaction time. Suppression methods, such as cryogenic turning [13], atmospheric modifications [6,12], workpiece modifications [11], and vibration-assisted machining [15] have all been attempted, but hold limited success. The effect of all of these modifications is to either eliminate the available energy to initiate a reaction or to reduce the reactivity of the workpiece's iron for the tool's carbon.

Change in the tool geometry due to wear when machining is most often characterized as an extension of the wear on the clearance face and an enlargement of the cutting edge radius. Past investigations [7,8,12] use basic microscopes to observe the change in tool geometry. Measurements of the wear lands were done by characterizing the length of worn region on the clearance face of the tool, however an exact profile of the worn tool was not possible. An SEM

Electron Beam Induced Deposition (EBID) was developed at the Precision Engineering Center (PEC) to provide a profile of a worn tool [16]. Since its inception, investigations at the PEC have been able to analyze the exact profile of a worn tool and relate them to other measurements such as forces and surface roughness [3,9,14,15,17,18]. The enlargement of the cutting edge radius and wear of the clearance face affects the chip formation process and the subsequent required forces to create a surface. Drescher [17] measured the relationships between tool wear, forces and surface roughness when diamond turning 6061 aluminum. He determined the surface roughness deteriorated after a certain amount of wear accumulated. This was also evident in the force measurements during machining. Lane et al. [3] and Hesler [14] then measured a similar increase in cutting and thrust force due to tool wear when diamond turning 1215 steel. Pavel et al. [19] discussed the effect of tool wear on surface finish when using PCBN tools on hardened steels for continuous and interrupted cutting.

### **2.1.2 Built Up Edge**

Workpiece adherence to the tool, or a Built-Up Edge (BUE), occurs when machining ductile materials, such as steel [20]. The material is often referred to a cap of work-hardened material covering the rake face and cutting edge of the tool [21-23]. The size of the BUE depends upon the original tool geometry, workpiece material, and machining parameters. Chao et al. [24] discussed the effects of cutting speed and feedrate on the chip-tool temperature and the subsequent ability for a BUE to form. The ability of the BUE to form was found to be proportional with feedrate, but only occurred in a specific cutting speed range. The importance of temperature has also been thoroughly analyzed by Bandyopadhyay [21], who proved the effect of temperature on the ability of the BUE to form by preheating the tool to specified temperatures. By measuring forces and the created surface roughness, the BUE was determined to be eliminated once tool was heated above the recrystallization temperature of steel. Iwata et al. [25] concluded the BUE formed once cracking began within the chip. These cracks were believed to be caused by the extensive shearing in the chip formation zone. Tomac et al. [26] provided a study of these factors and others affecting the BUE formation. This summary included temperature, cutting speed, strain hardening of the workpiece, adhesion properties between the workpiece and tool, and the micro-crack formation of workpiece material.

Past investigations have also attempted to model and predict the formation of the BUE. Childs [20,27,28] introduced damage models to the finite element simulations to predict the formation of the BUE with specific machining parameters. Fang et al. [29] proposed a modified slip-line model to predict the BUE size and proposed the BUE is simple just a matter of metal flow rather than specific properties. Uhlmann et al. [23] compared experimental in-situ stress measurements with the prediction of finite element models that incorporated the BUE geometry. They showed the influence of the BUE on the chip formation and stress state in the chip formation zone.

The change in the effective tool geometry due to the formation of a BUE has been well documented in previous investigations. Heginbotham et al. [22] used a quick stop technique to observe the direct change in tool geometry due to the BUE. They defined four types of BUE which were dependent on the machining parameters. Iwata et al. [25] also used SEM observations for their analysis on BUE. Uhlmann et al. [23] provided images of the BUE in their stress measurements, while Jacobson et al. [30] provided images when defining a new classification system that was similar to the one produced by Heginbotham et al. [22]. The basic profile of the BUE is defined as adhered to the rake face and cutting edge of the tool. The adhered material extends away from the cutting edge and potentially significantly downward if large enough. The effective rake angle of the tool increases and the cutting edge radius is enlarged. Potential form errors occur if the BUE extends the intended depth of cut. Surface roughness errors occur due to the enlarged cutting edge radius and rough surface of the “new” tool. This effect was noticeable in Bandyopadhyay’s [21] experiments as he measured the surface roughness of the machined components. Oishi [31] investigated the elimination of the BUE and the subsequent ability to turn a specular surface on steel if the steel is above a critical hardness value.

Although the surface roughness is considered poor when machining with a BUE, the cutting process can actually become more efficient due to the change in tool geometry. Often the BUE increases the effective rake angle of the tool; this reduces the cutting force required for machining as defined by Merchant’s famous model [32]. Korkut et al. [33] analyzed face milling 1040 steel and confirmed the BUE actually created a more efficient cutting process by changing the effective rake angle of the tool. Stress measurements by Uhlmann et al. [23] produced similar conclusions. The BUE can act as a separating layer between the workpiece flow and diamond tool. Conducting experiments with high speed steel tools and mild steel workpieces, Ramaswami theorized BUE affected tool wear by increasing abrasive and adhesive wear but provided an absence of diffusive type wear [34]. Work hardened particles from the formation of BUE were more abrasive on the tool and caused fracture, but diffusive wear was eliminated due to the protection the BUE provided the tool from the reactive material flow. Bowden et al. conducted frictional sliding tests with steel on diamond and showed the potential for BUE formation at the interface to protect the diamond from wear [35]. In DT steel materials, wear is believed to be largely due to thermochemical mechanisms, such as diffusion, so BUE potentially reduces wear of the diamond when machining steel.

### **2.1.3 Goals of this Project**

The purpose of this project is to investigate the presence of tool wear and BUE affecting the chip formation process when diamond turning steel. Both factors have been cited in countless previous investigations as difficulties in machining operation. The first step was to conduct experiments to attain a basis for understanding the effect of tool wear and BUE on the tool geometry. This change

in tool geometry will then affect the cutting process and subsequent surface generation. Measurements of these changes provide a comparison on which one may be dominating the cutting process when diamond turning steel. Finite element simulations were then used to provide insight into how the tool geometry change affects the chip formation process. Initial simulations were conducted with the ideal clean and sharp tool geometry, while further simulations incorporated the combined effect of BUE and tool wear. Forces, stresses, temperatures, shear angle and chip thicknesses were all examined and compared with experimental results when possible.

## 2.2 EXPERIMENTAL SETUP

### 2.2.1 General

Experiments were conducted on a Pneumo ASG 2500 DTM as shown in Figure 1. The two axes are supported by hydrostatic oil bearings, while the spindle is supported by an air bearing. Workpieces are mounted to the spindle on the z-axis using a vacuum chuck. The tool, mounted on the x-axis in Figure 1, is positioned to machine the outer diameter of the workpiece. The DTM uses laser interferometry to measure the position of each axis with 2.5 nm resolution. MobilMet Omicron cutting oil was sprayed onto the tool in all of the experiments.

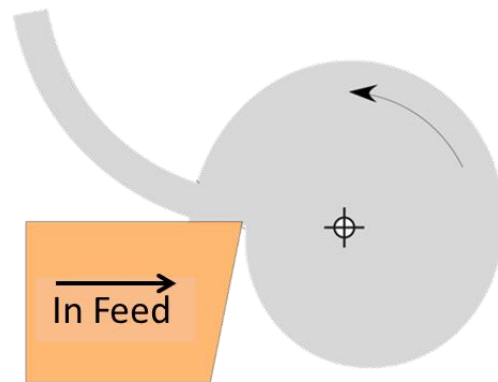
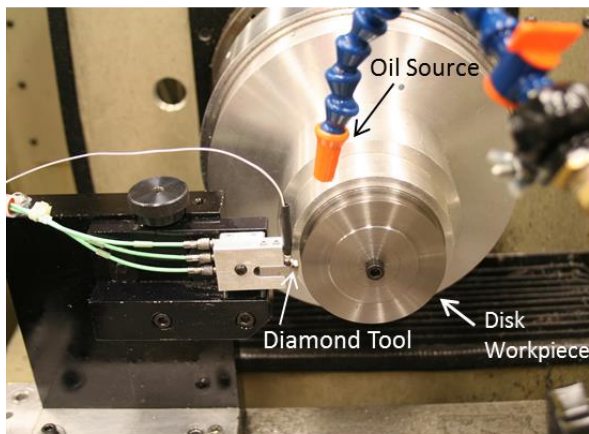


**Figure 1.** Setup for experiments.

An orthogonal setup was devised using a narrow disk shaped workpiece and a straight nose diamond tool. This simplifies cutting to a two dimensional process as the chip thickness is constant across the contact width. The tool is fed from the outside diameter of the workpiece at specific feedrate to set the depth of cut. Cutting speed is determined from the spindle speed and exact diameter of the workpiece. Cutting distance is set by how many revolutions the tool is fed into the workpiece. The cross sectional area of the uncut chip was defined as rectangular with the DoC

and disk width as the dimensions. Figure 2 shows the disk-shaped workpiece and diamond tool used during experiments. The cutting edge of the diamond tool is 3.5 mm wide, while the disk shaped workpiece was approximately 1 mm wide. This provided three locations for experiments on the diamond tool before needing to relapped.

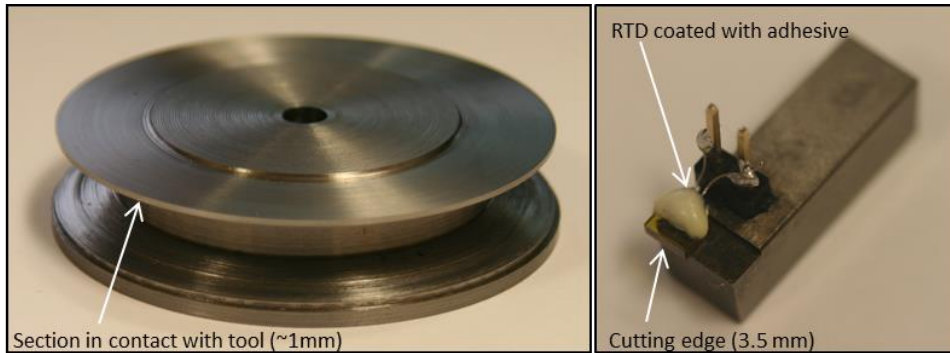


**Figure 2.** Workpiece and tool used during experiments.

### 2.2.2 Force Measurements

Analysis of the forces during machining can provide evidence of changes in tool geometry. To investigate the forces during these experiments a Kistler 9251A three-axis load cell was attached to the tool holder as shown in Figure 3. The cutting force,  $F_C$ , is defined as parallel to the direction of cutting, while the thrust force,  $F_T$ , is defined as perpendicular to the direction of cutting. The signal was directed into a Kistler 5004 amplifier where the signal was then processed by a National Instrument cRIO. Usage of LabVIEW software allowed for recording and real time observation of the measurements. The natural frequency of the system with the diamond tool and shank in place was 11.6 KHz.

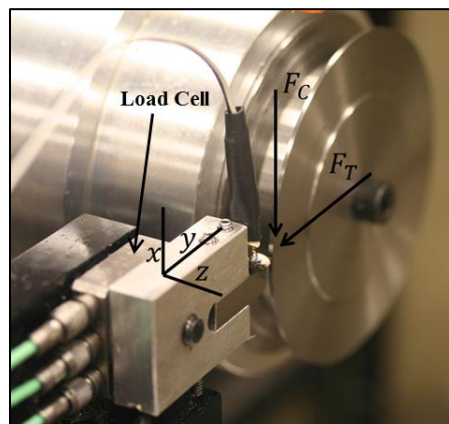


**Figure 3.** Loadcell used for force measurements.

### 2.2.3 Temperature Measurements

Bulk temperature of the diamond was measured using a Resistance Thermometer Device (RTD). Temperatures can be measured due to the RTDs linear change in resistance with temperature. These also have a high sensitivity and stability in comparison to other temperature measuring devices [14]. Combined with the high diffusivity of the diamond ( $80,000 \text{ mm}^2/\text{s}$ ) allows for fast response time capable of measuring steady state forces after only a few seconds. A  $1000 \Omega$  RTD was used with 3M's TC-2810 thermally conductive adhesive on the top of the diamond as shown in Figure 2.

### 2.2.4 Tool Wear and BUE Measurements

The difficulty in measuring the wear of a diamond tool is the complex geometry and the small changes that take place during machining. Drescher [17] reviewed the many techniques developed to quantify the wear region of diamond tool and initially developed the SEM-EBID technique, which was then enhanced by Lane [3]. Electron Beam Induced Deposition (EBID) naturally occurs in a Scanning Electron Microscope (SEM) due to the contamination of hydrocarbons within the vacuum chamber. By changing the scanning pattern to line geometry, a line can be drawn across the cutting edge of the tool. This line defines the profile of the worn tool and the image can be used to measure the worn cross sectional area. This method is nondestructive to the fragile diamond tool and the line is easily removed. Figure 4 provides an example of the method. Matlab is used to trace out the profile and rotate to provide a comparison with the profile before the experiment. This method is extended to profile the BUE on the tool.

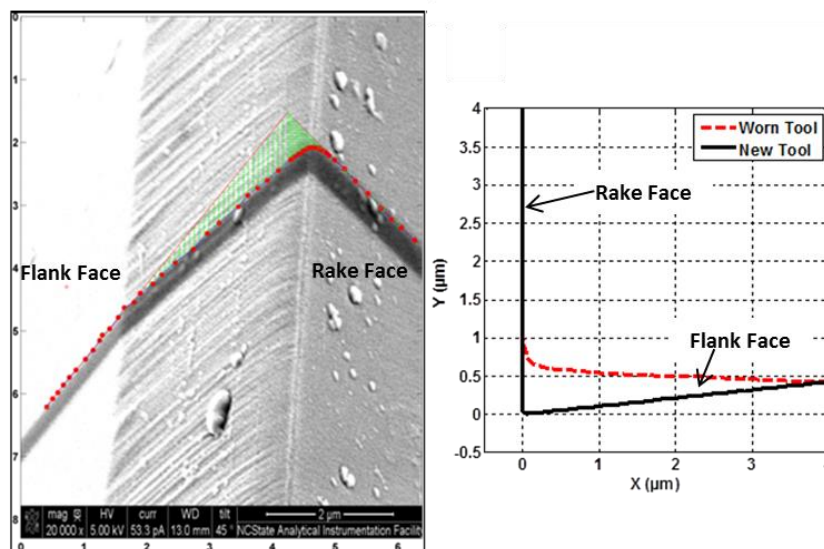


Figure 4. EBID technique used to profile a worn tool and BUE.

## 2.3 EXPERIMENTAL RESULTS

A total of eighteen experiments were conducted at a constant speed of 2 m/s. Six experiments were conducted at a depth of cut of 2, 5 and 10  $\mu\text{m}$  each. Cutting speed was kept at a constant average of 2 m/s, while cutting distance varied between 10, 20 and 30 m. Disk width (and subsequent contact width) was set at 0.94 and 1.2 mm each.

Table 1 provides the parameters of the six experiments conducted at each depth of cut.

**Table 1.** Machining parameters for the six experiments conducted at each DoC.

Experiment	Cutting Distance (m)	Disk Width (mm)	Comments
1	10	0.94	
2	20	0.94	2 <sup>nd</sup> cut - no relapping
3	30	0.94	3 <sup>rd</sup> cut - no relapping
4	10	0.94	
5	20	1.20	
6	20	1.20	

### 2.3.1 Forces

Force measurements were taken during all experiments. As an example, Figure 5 shows the force measurements for each DoC on a 1.2 mm wide disk for 20 m of cutting. Forces were constant after the initial plunge into the workpiece. The initial surge in forces at the contact point is likely due to compliance in the axes.

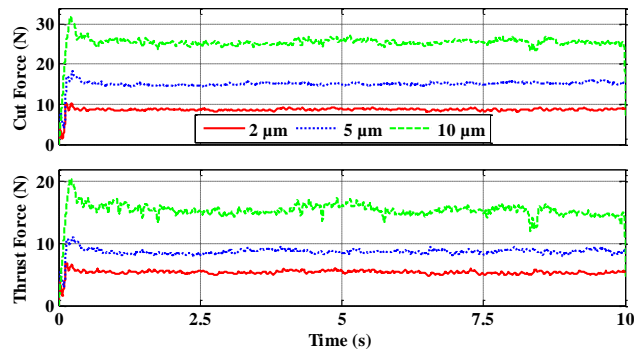


**Figure 5.** Example of cutting and thrust force measurements at each DoC.



The middle 50% of the data was used to calculate the average cutting and thrust force for each experiment. In the case of Figure 5 this would be from 2.5 to 7.5 seconds. Normalizing forces with respect to the chip width shows a dependency only on DoC. Figure 6 shows the average normalized forces as well as the standard deviation as a function of DoC. Average cutting forces were 8.1, 13.6 and 22.9 N as the DoC increased. Normalized thrust forces produced a standard deviation of 1.14, 0.58 and 0.79 N, respectively.

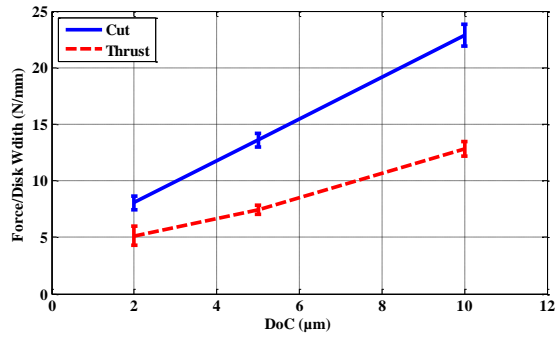


**Figure 6.** Normalized forces with respect to the chip/disk width.

Normalization of forces with respect to the uncut chip size gives insight into the efficiency of the cutting process. Factors such as temperature, strain hardening or strain rate sensitivity can affect the required force to form a chip depending upon the set machining parameters. Figure 7 shows the average forces normalized with respect to the uncut chip area. The normalized cutting and thrust forces decreased as the actual uncut chip area increased. This means the cutting process became more efficient with the larger chip, even though the overall magnitude of the forces were larger. Potentially reasoning may be due to thermally weakening of the material or the effective change in tool geometry from the formation of a BUE. Previous investigations [23,33,36,37] hypothesized the BUE increases the effective rake angle of the tool and reduces the forces required for machining.

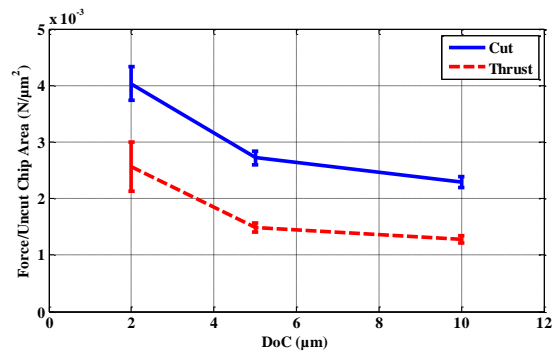


**Figure 7.** Normalized forces with respect to the uncut chip area.

### 2.3.2 Temperatures

Temperature measurements were taken during all 18 experiments. Figure 8 (a) provides an example of cutting on the 0.94 mm disk for 30 m while Figure 8 (b) provides an example of cutting on the 1.2 mm disk for 20 m. Bulk temperature of the diamond rises quickly after contacting the workpiece. Temperatures become relatively steady after approximately 5 seconds of contact. Small variations are due to the effectiveness of the cutting oil or presence of chips on the diamond.

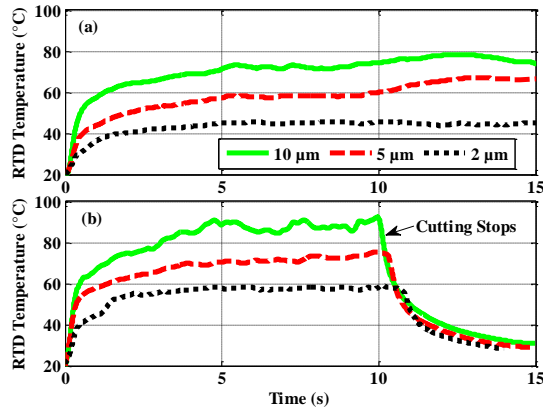


**Figure 8.** Example of temperatures measurements at each depth of cut on the 0.94 mm (a) and 1.2 mm (b) disks.

Using the steady state temperatures of the longest experiments for each disk width, a relationship between the theoretical uncut chip area and change in RTD temperature measurements is shown in Figure 9. Temperature of the diamond is determined by the amount of heat generated and percentage that flows into the tool. Heat generation can be estimated as the product of the cutting force and cutting speed. Subsequently, cutting force has a relationship with chip size as shown in Section 2.3.1. This makes the bulk temperature have a high correlation with the machining parameters, such as chip size.

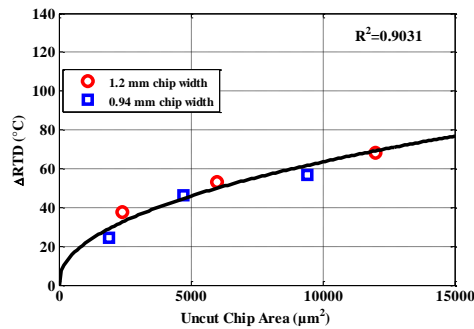


**Figure 9.** Relationship of temperature measurements with respect to the uncut chip area.

### 2.3.3 Built Up Edge

SEM images of BUE on the diamond tool were taken after each machining test to measure the “new” tool geometry. The tool was soaked in acetone to remove the cutting oil to reduce charging issues in the SEM but not remove the BUE. Figure 10 shows the tool after 10 m of cutting at (a) 2, (b) 5 and (c) 10  $\mu\text{m}$  DoC. Substantial changes in the tool geometry are noticeable due to the adherence of the workpiece material. All images were taken at the same magnification and the BUE is much more noticeable with the increasing DoC. The 2  $\mu\text{m}$  DoC experiment produced a small BUE for only short segments. The 5  $\mu\text{m}$  DoC experiment had larger and longer segments of a BUE, while the 10  $\mu\text{m}$  had the largest and most continuous BUE.

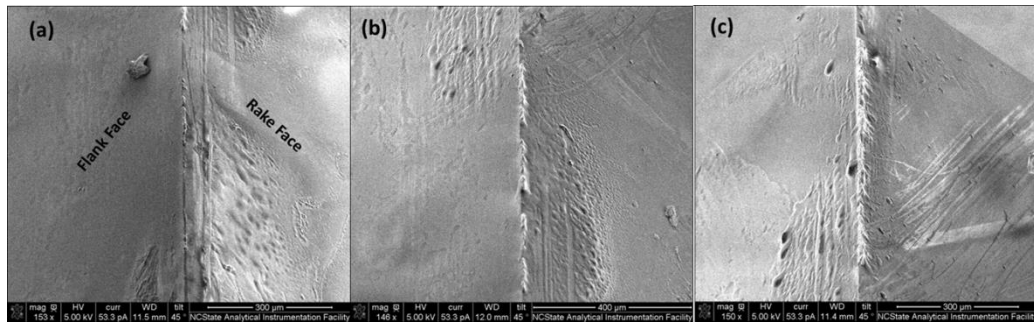


**Figure 10.** BUE observations after experiments at (a) 2 (b) 5 and (c) 10  $\mu\text{m}$  DoC.

Figure 11 shows magnified images of the BUE on the tool for the same experiments as shown in Figure 10. The EBID technique developed for tool wear was implemented to examine the profiles of the BUE. The beauty of this technique is that it allows for measurement of the extension of the BUE away from the rake face as well as an estimation of the effective cutting edge radius.

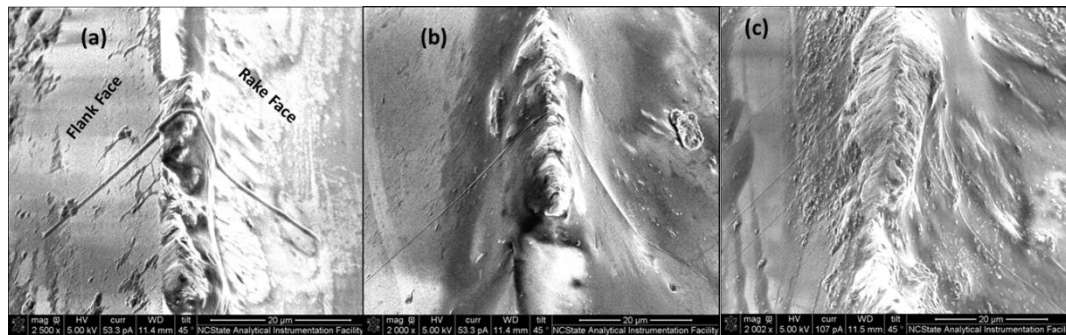


**Figure 11.** EBID technique on BUE after experiments at (a) 2 (b) 5 and (c) 10  $\mu\text{m}$  DoC.

Figure 12 is the profile of each BUE shown in Figure 11. The extension of the BUE as well as the effective cutting edge radii are provided in each image. Observations show the 10  $\mu\text{m}$  DoC

produces a much larger BUE in comparison to the smaller DoC experiments. This correlates with previous investigations, such as Chao [24], about the effect of feedrate (or chip size) on the BUE. These profiles will be used to investigate the effect of the BUE on the chip formation process with the finite element simulations in Section 2.3.6.

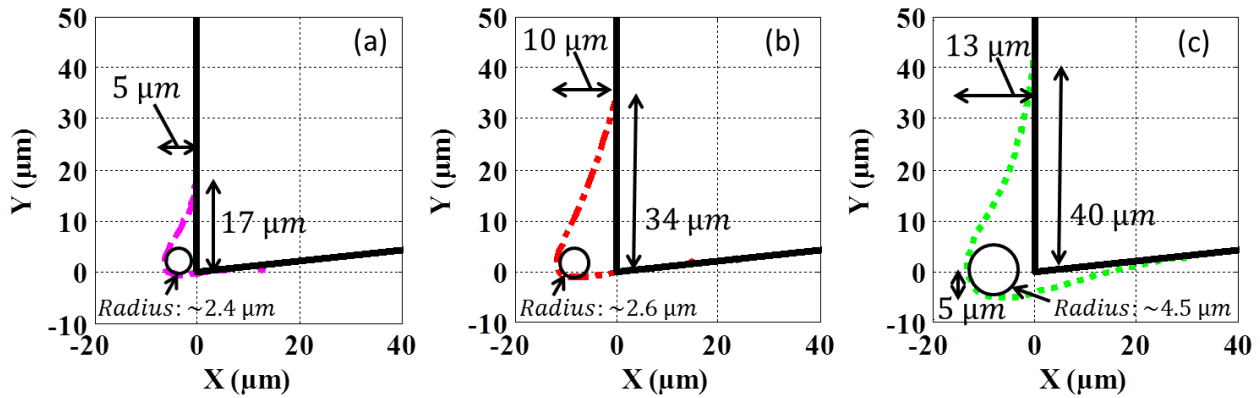


**Figure 12.** Geometry of the BUE measured through the EBID technique after a (a) 2 (b) 5 and (c) 10  $\mu\text{m}$  DoC.

### 2.3.4 Tool Wear

Once the BUE was imaged, it was removed with a strong acid mixture (Keller’s solution). This has been the standard procedure at the PEC in the past before a worn diamond tool was measured. The same EBID technique used to measure the BUE was used to image the tool edge after each experiment. Figure 13 shows the wear lands after specific machining parameters. The rake face and flank face orientation of the images are shown on Figure 13(a). The EBID process requires the image to be stretched in the vertical direction to produce the “real” tool x-section. The diamond tools were orientated consistently in the SEM for all measurements. Figure 13 shows the wear lands after machining 1215 steel for a total cutting distance of 60 m at 2 m/s with a chip width of 0.94 mm. Figure 13(a) and Figure 13(b) were taken at 35 kX, while Figure 13 (c) was taken at 50 kX. The change in magnification was needed because of the smaller wear land for the largest DoC (10  $\mu\text{m}$ ).

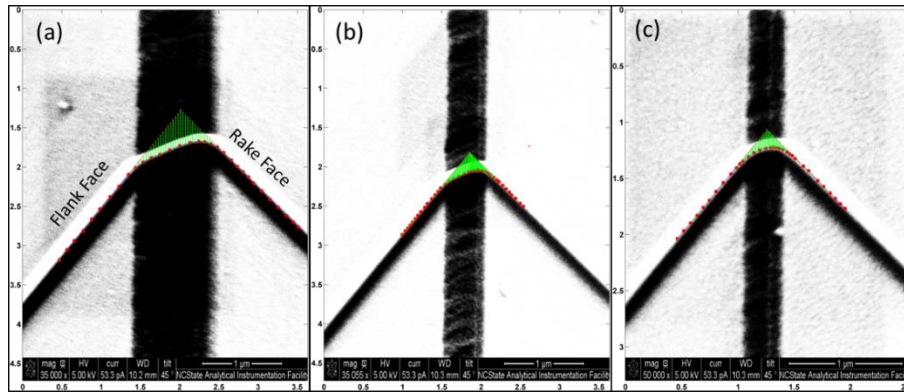


**Figure 13.** Geometry of the BUE measured through the EBID technique after a (a) 2 (b) 5 and (c) 10  $\mu\text{m}$  DoC.

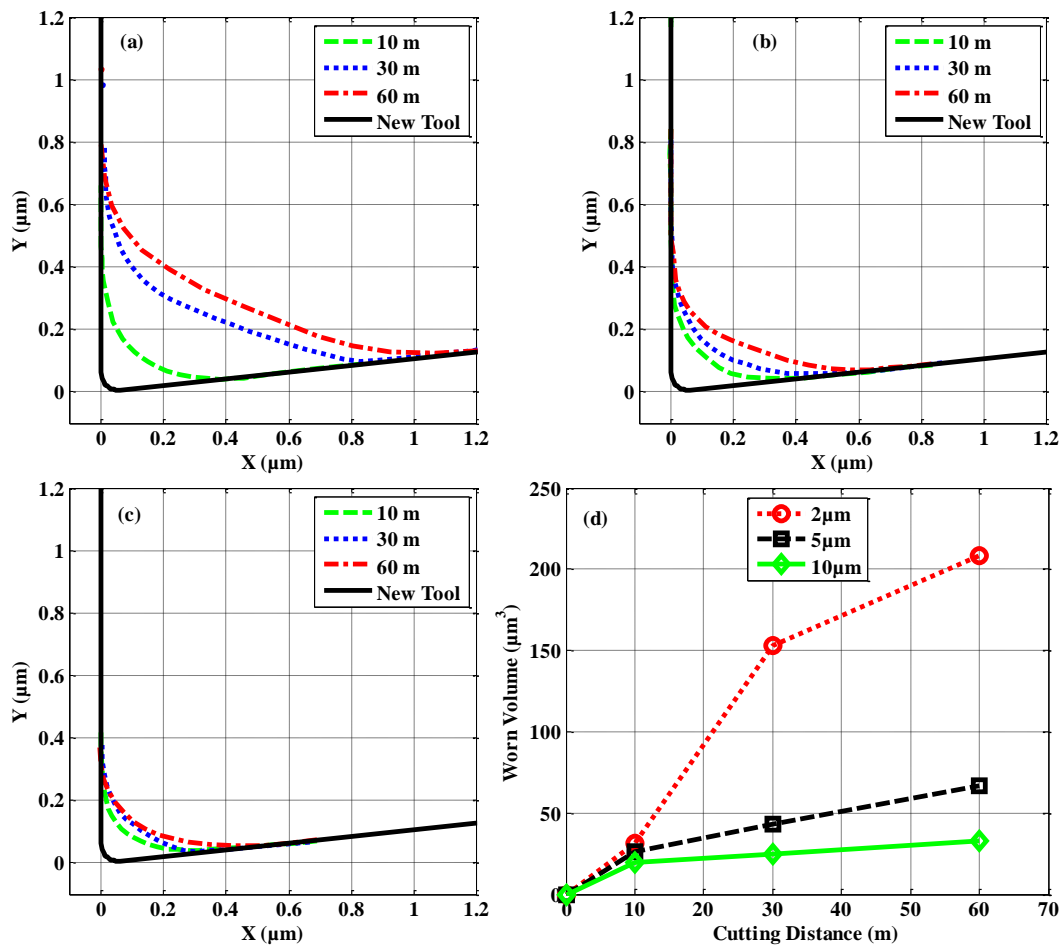


**Figure 14.** Progression of the wear land after machining at a (a) 2 (b) 5 and (c) 10  $\mu\text{m}$  DoC. Wear volumes are provided in (d).

Figure 14 provides the progression of the wear lands after machining each DoC for 10 m, 30 m, and 60 m. Figure 14(d) provides the progression of the measured worn volume of the tool for each DoC. The worn volume is defined as the change in tool profile from before and after the conducted machining. The volume was estimated by multiplying the measured worn cross sectional area by the length of contact between the tool and workpiece. Each DoC was machined at separate locations on the diamond without intermittent lapping between experiments. Clearly, the largest wear lands were produced by the smallest DoC (and smallest chip size) despite increased heat generation and subsequent tool temperatures as the DoC increases. These results were contrary to previous investigations [9,14,15] which showed a relationship between the tool wear and the subsequent tool temperature from varying the cutting speed. This means there may be another factor at play affecting the wear rate of the diamond tool as the chip size increases.

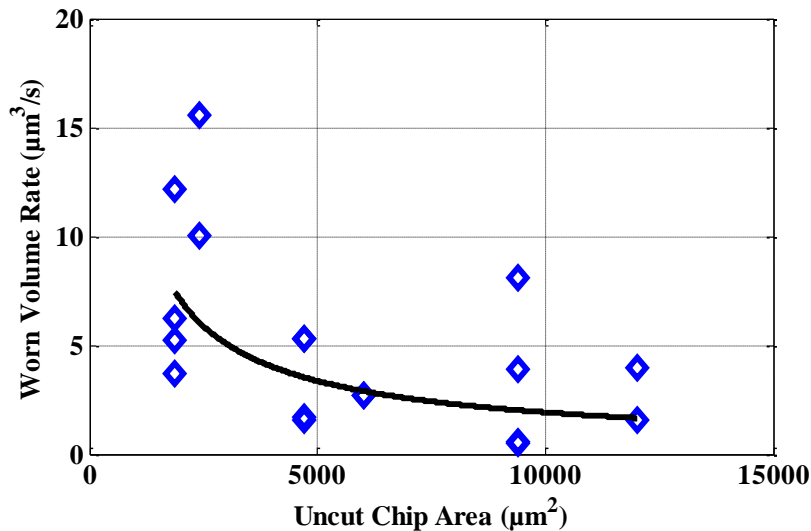


**Figure 15.** Wear volume rate for all 18 experiments with respect to the uncut chip area.

Figure 15 provides the wear rates measured for all 18 experiments with respect to the uncut chip area. Wear rate is defined as the change in the tool profile from before and after the conducted machining. The combined 18 experiments again show the wear rate is not clearly related to the uncut chip area and expected temperature relationship. The BUE is believed to potentially be acting as a protective layer on the diamond against thermochemical wear as discussed in previous literature. This concept was discussed in the overview of previous literature. Section 2.3.3 showed the enlargement of the BUE with the chip size. If this adhered material covers the cutting edge and separates the diamond tip from the flow of the workpiece material, then the direct relationship (that was found in previous investigations by varying cutting speed) with the wear rate and temperature may be obstructed. The effect increases with the larger chip size (due to larger BUE forming) and would explain why wear rate has no substantial relationship with the chip size.

### 2.3.5 Net Tool Geometry Change

Although tool wear and BUE both change the tool geometry, the BUE was much larger and actually covered the worn cutting edge. Figure 16 shows a comparison of the largest worn profiles for each DoC (after 60 m of total cutting) and the BUE that was profiled. Size of the tool wear was approximately 1% of the size of the BUE for all three DoCs, making it relatively insignificant due to the issue of a BUE formation. This indicates the BUE is the dominating effect on the cutting process in comparison to the tool wear, when diamond turning steel. Because of this, the chip formation process is likely affected by the rapid adherence of workpiece material rather than any wearing of the tool.

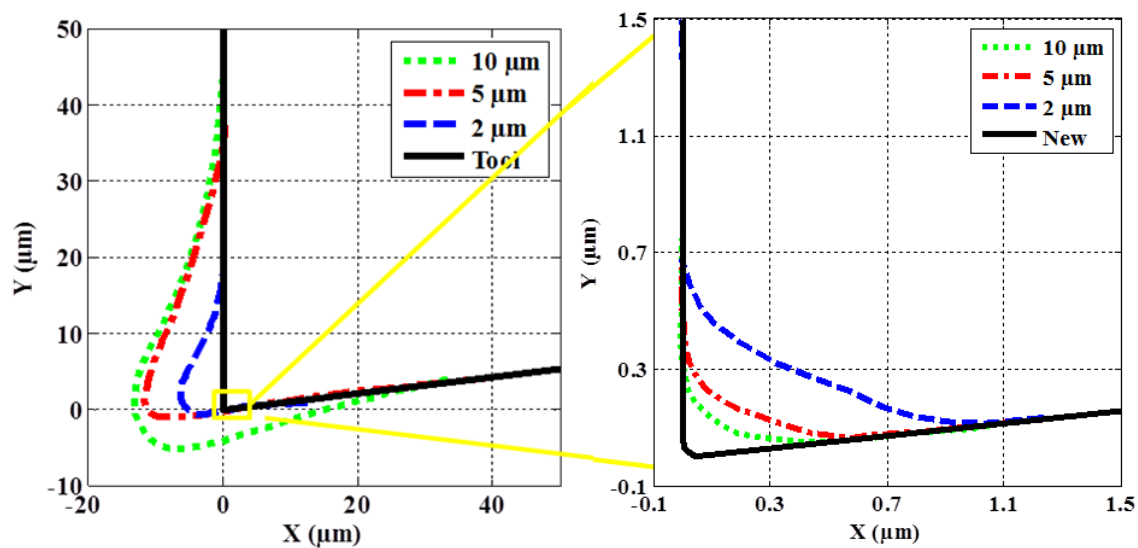
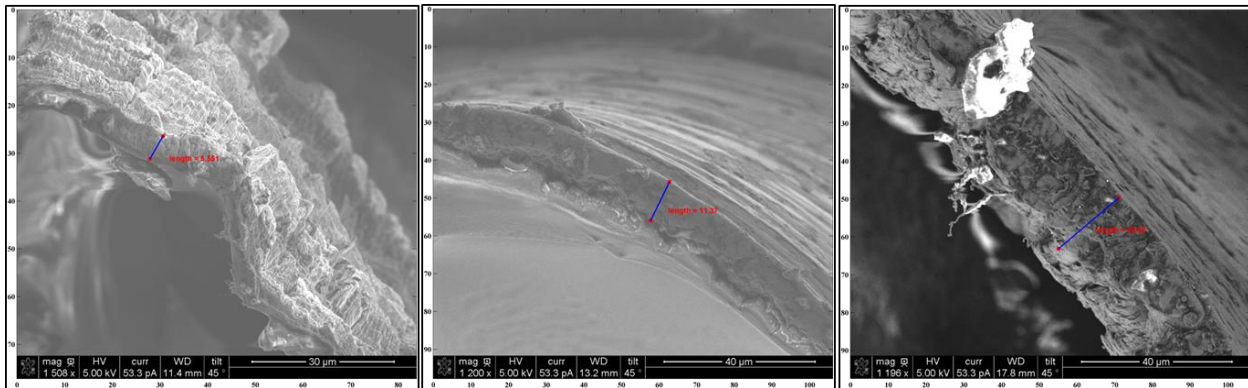


Figure 16. Size differential of worn cross sectional areas and the observed BUE.

### 2.3.6 Chip Size

After a set of experiments, chips were examined for comparison with the finite element simulations. For all experiments continuous chips formed with minimal intermittent breakage. Information about the chips can provide important information with respect to the shear angle of the cutting process. The chip thicknesses were measured using an SEM as shown in Figure 17. They were measured to be 5.55, 11.37, and 20.05 μm from the 2, 5 and 10 μm DoC experiments, respectively.





**Figure 17.** SEM observations of the chip gave the ability to measure the thickness.

## 2.4 FINITE ELEMENT SIMULATIONS

ThirdWave's AdvantEdge was used to investigate the effect of changes in tool geometry due to the BUE and tool wear on the predicted forces, chip thicknesses, stress and temperatures. Due to the large ratio of contact width to the depth of cut, the process can be considered a two-dimensional plane strain case. This allows for the running of two-dimensional simulations, rather than three-dimensional simulations; which reduces computation time substantially. AdvantEdge incorporates a power law to determine changes in yield strength of the workpiece material. The model includes the effects of thermal softening, strain hardening and strain rate sensitivity. A variety of parameters can be set to effect the accuracy of results and computation time including, but not limited to meshing parameters, boundary conditions, friction coefficient, workpiece and tool size.

Six simulations were conducted with two separate sets consisting of the previously specified DoC (2, 5 and 10  $\mu\text{m}$ ). The 1<sup>st</sup> set of simulations included a theoretical tool with no effects of BUE or tool wear. The 2<sup>nd</sup> set of simulations included the effects of the BUE. Tool wear was not incorporated due to the massive size differential compared to the BUE that consistently occurred on all experiments. Each simulation was conducted at the 2 m/s cutting speed. Cutting distance was specified at 400  $\mu\text{m}$ . This length of cut produced a fully formed chip while not requiring a long computational time. Workpiece width was set at 0.94 mm and thus will only be compared to experimental results with the same width. Meshing parameters were kept constant for all simulations. Figure 18 shows the general AdvantEdge setup and an expanded view.

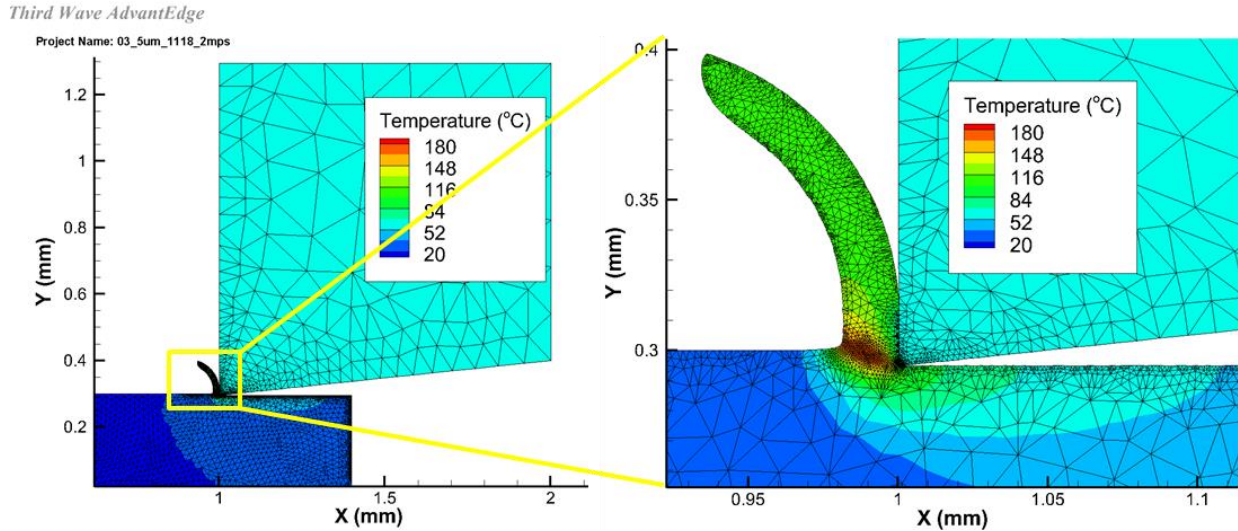


**Figure 18.** Imagining of the chip formation process from a 5  $\mu\text{m}$  DoC.

Due to the absence of 1215 steel in the AdvantEdge library, 1118 steel was used as a substitute. Table 2 provides a comparison of the similar properties each steel alloy has. The yield and ultimate strength are different; however this property will dynamically change during the simulation due to the power law incorporating thermal softening, strain hardening and strain rate sensitivity. Hardness of the workpiece piece was set at 180 Brinell Hardness after measurements of the experimental piece were done using a Zwick 3212 Hardness Tester. Workpiece size was set at 0.3 mm in height and 1 mm in length.

**Table 2.** Material property comparison of experimental and theoretical workpiece materials [38].

Material	1215	1118
Thermal Conductivity ( $\frac{W}{m \cdot K}$ )	51.9	51.9
Specific Heat ( $\frac{kJ}{g \cdot ^\circ C}$ )	472	472
Modulus of Elasticity ( <b>GPa</b> )	200	200
Yield Strength ( <b>GPa</b> )	415	315
Ultimate Tensile Strength ( <b>MPa</b> )	540	525

## 2.4.1 Tool Setup

**Table 3.** Material property comparison of diamond tool and BUE material [38].

Material	Diamond	BUE (1215/1118 Steel)
Thermal Conductivity $W/(m * K)$	2000	51.9
Specific Heat $kJ/(kg * K)$	520	472
Density $kg/m^3$	3200	7870
Modulus of Elasticity (GPa)	1200	200
Poisson Ratio	0.2	0.3

### First Set of Simulations

The first set of simulations consisted of a 0.5  $\mu\text{m}$  cutting edge radius with a 0° rake angle and 6° clearance angle. The face angles were consistent with the experimental tools, but the cutting edge radius was enlarged to a 0.5  $\mu\text{m}$  cutting edge radius. This was required so that computation time did not expand past 2 days for each simulation. Properties of a single crystal diamond were used and are found in Table 3. The back and top of the tool had isothermal boundary conditions matching the RTD measurements shown in Section 2.3.2. Isothermal boundaries remove heat from the tool and thus can potentially produce erroneously low temperatures in the chip formation area if they are placed too close to the area of interest. To ensure the set temperatures did not have an overbearing influence, the tool was sized at 1 mm by 1 mm and thus the isothermal boundary conditions were placed in the approximate location of the actual RTD in the experiments. Figure 19 shows the 5  $\mu\text{m}$  DoC simulation and the isothermal boundary conditions.

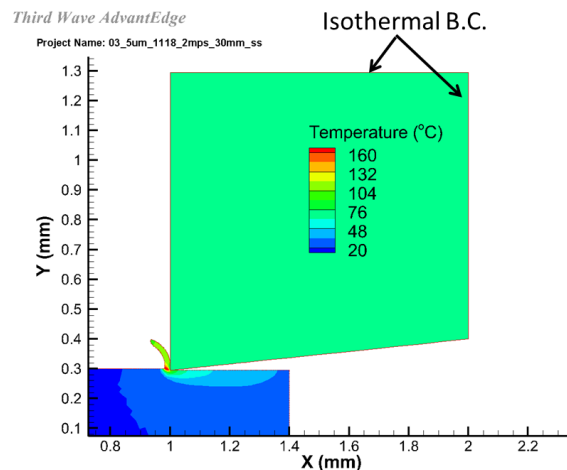


**Figure 19.** Isothermal boundary condition of diamond tool.

## Second Set of Simulations

The second set of simulations consisted of extracting the BUE profile measured using the SEM-EBID technique as shown in Section 2.3.3. Due to AdvantEdge's inability to design a composite tool (part steel for the BUE and the actual diamond), two options were available for these simulations: combine the steel BUE profile and diamond tool profile and use only a single set of material properties or use just the BUE profile and with the accurate material properties. Although the former option allows the placement of the specified boundary conditions much further away from the chip formation zone (and hence having less potential effect), the inability to accurately model the material properties of the entire tool will reduce the accuracy of the results. The latter was chosen in an attempt to accurately model the steel properties (as provided in Table 3) for only the BUE portion. This option then requires the setting of an isothermal or adiabatic boundary condition at the back of the BUE. Since the back of the BUE is in contact with the highly conductive diamond an adiabatic boundary condition will produce erroneously high results due to the absence of any heat conduction away from the BUE. As the best option, isothermal boundary conditions were chosen to allow for this conduction of heat. The isothermal boundary condition was set at the expected peak temperature of the diamond tool found from using SolidWork's Finite Element Thermal Study process in Suit's thesis [39]. This model provides an estimation of the steady state temperatures and temperature gradients based on the material properties and known temperatures of a 3D CAD model. After accurately setting up a correctly dimensioned model, the process involved using varying amounts of heat to match the experimental RTD measurement with the model's predicted temperature at the back of the tool. The peak temperature of the heat input area at the tip of the tool was then recorded and was used as the isothermal boundary condition for the AdvantEdge setup. The heat input area for this model was roughly estimated by using a worn tool profile. Temperatures of 65, 105 and 126 °C were used for the 2, 5 and 10  $\mu\text{m}$  DoC simulations, respectively. Figure 20 shows the BUE simulation for the 5  $\mu\text{m}$  DoC profile and isothermal boundary conditions. Notice the difference in size compared to Figure 19.

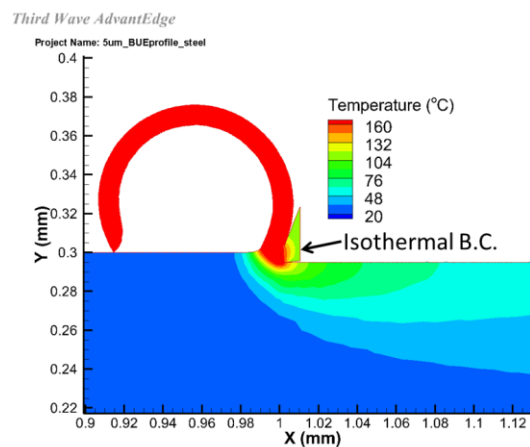


**Figure 20.** Isothermal boundary condition of the BUE during simulations.

## 2.4.2 Force Results

Average forces of each simulation were calculated based on the middle 50% of the simulation. Each simulation attained steady state cutting and thrust forces well before this point; consistently within the first 10%. Figure 21 shows the average cutting and thrust force for the simulations and experimental results discussed in Section 2.3.1. Although both simulations are similar to the experimental results for the 2  $\mu\text{m}$  DoC, the difference increases with the DoC. The 5  $\mu\text{m}$  DoC simulations with the theoretical tool geometry produce 43% and 36% error for the cutting and thrust force, respectively. Comparatively, the BUE simulation produced more accurate results with only 4% and 20% error for the cutting and thrust force, respectively. The 10  $\mu\text{m}$  DoC simulations with the theoretical tool geometry produce 70% and 51% error results in comparison to the experimental cutting and thrust forces. The BUE simulation produced closer results with only 11% error for the cutting force and 12% error for the thrust forces. This shows that including the BUE in the tool geometry much more closely matches the simulation results to the experimental results across all DoCs.

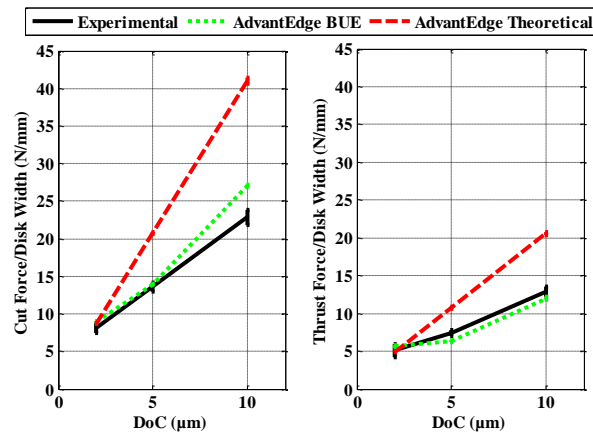


**Figure 21.** Comparison of experimental and AdvantEdge force results.

The lack of incorporating the BUE most likely causes an over prediction of the forces due to the absence of the rake angle change. An increase in the rake angle lowers the required forces to form the chip and has been discussed in previous investigation [23,33]. Thermal softening of the material may also cause a reduction in forces with the presence of the low conductive BUE layer. Since the BUE has a thermal conductivity of 40x less than the diamond, the heat is removed less efficiently from the chip formation zone. This causes the chip formation zone to reach higher temperatures with the addition of the BUE layer separating the heat generating area from highly thermally conductive diamond. Regardless of the exact reasoning, the addition of the BUE is observed to create a more efficient chip formation process in comparison to having only the theoretical tool geometry present. This is most noticeable for the 5 and 10  $\mu\text{m}$  DoC values in

Figure 22 as the BUE simulations required less force per unit of uncut chip area. The lack of reduction in the 2  $\mu\text{m}$  DoC simulation is likely due to such a small BUE layer measured and applied within the simulation. The BUE simulations also more closely match the experimental results in comparison to the theoretical tool geometry simulations and provide further evidence that the BUE is dominant factor when diamond turning steel.

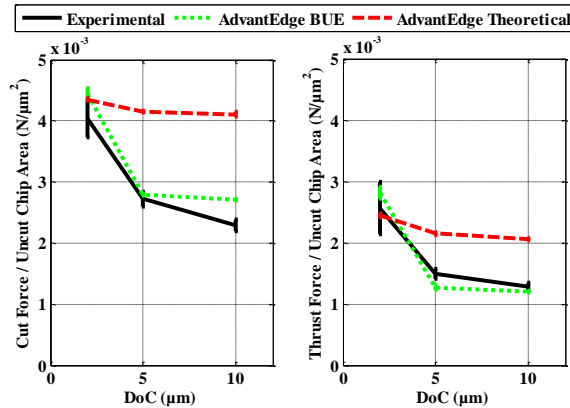


Figure 22. Comparison of experimental and AdvantEdge normalized force results.

### 2.4.3 Chip Size

Chips were measured to compare with the experimental results of Section 2.3.6. Figure 23 shows the chip thickness of the 10  $\mu\text{m}$  DoC simulations for a theoretical tool and BUE tool. Measurements were done after the point of separation between the chip and the tool. This means the theoretical 0° rake angle allows for a horizontal measurement as shown, while the BUE rake angle requires measurements taken at an angle.

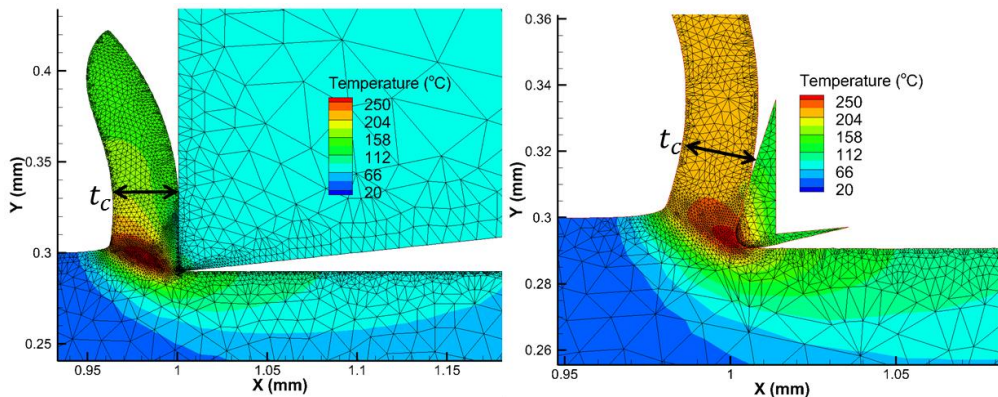
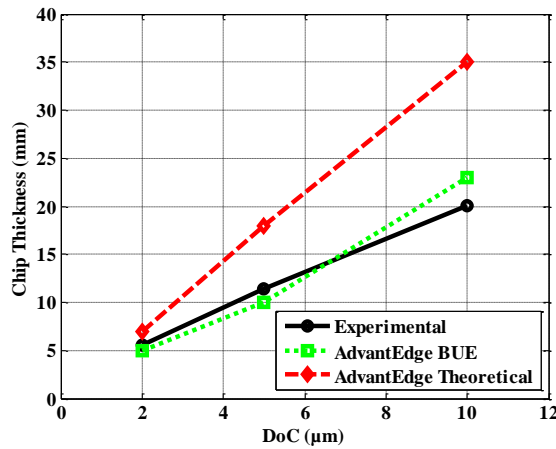


Figure 23. Location of chip thickness measurements for the theoretical tool (left) and BUE simulations (right).



Figure 24 shows the measured chip thicknesses of the experimental and simulations. Simulations with the BUE change to the tool geometry produced much closer results to the experimental results. Percent error with reference to the experimental results was 10, 12 and 15% for the BUE simulations. Comparatively, the theoretical simulations produced much larger percent errors at 26, 58 and 75%, respectively.



**Figure 24.** Comparison of simulation results with the experimental results for measured chip thickness.

### 2.4.4 Heat Flow

Due to addition of the low thermally conductive BUE layer, the heat flow through each of the three major components (tool, chip and workpiece) changes dramatically. To investigate this, analysis of the heat partition was performed by outlining a control volume around the major heat generation area as show in Figure 25.

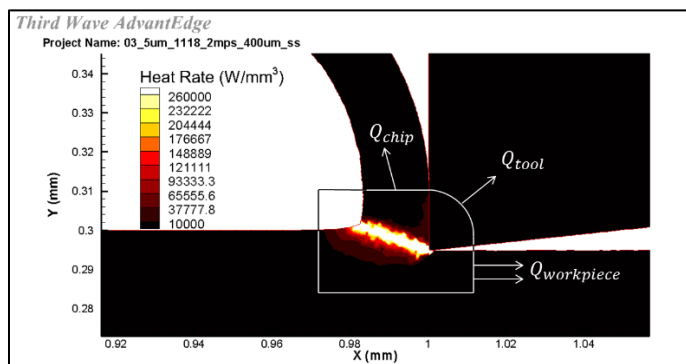


**Figure 25.** Control volume around the source of heat generation.



Equation (1) shows that power generation ( $P_{total}$ ) is the summation of heat flow in the tool ( $\dot{Q}_{tool}$ ), chip ( $\dot{Q}_{chip}$ ) and workpiece ( $\dot{Q}_{workpiece}$ ). Power generation was equivalent to the product of the cutting speed and cutting force that was shown in Equation (1).

$$P_{total} = \dot{Q}_{tool} + \dot{Q}_{chip} + \dot{Q}_{workpiece} \quad (1)$$

Heat flow through the workpiece and chip were measured using Equation (2) where the density ( $\rho$ ), cross-sectional area ( $A$ ), cutting speed ( $v_c$ ), specific heat ( $c_p$ ) and average temperatures ( $T$ ) are all known quantities by extracting data lines from the simulation results. The tool heat input was then measured by the difference between these two components and the total power generated. The tool heat input was then measured by calculating the difference between these two components and the total power generated.

$$\dot{Q} = \rho A v_c c_p (T_{final} - T_{initial}) \quad (2)$$

Figure 26 shows the results for the BUE and theoretical tool simulations. Total power generation was noticeably lower for the BUE simulations compared to the theoretical tool simulations as the DoC increased. This was due to the lower cutting forces that were also more closely aligned with the experimental results. For the theoretical simulations, the majority of the heat flowed through the tool due to the diamond's high thermal conductivity. However, with the addition of the BUE all three components hold the same thermal conductivity and thus the tool no longer dominates the heat partitions. This is shown in Figure 27 as percentages of the total heat generated into each component are described.

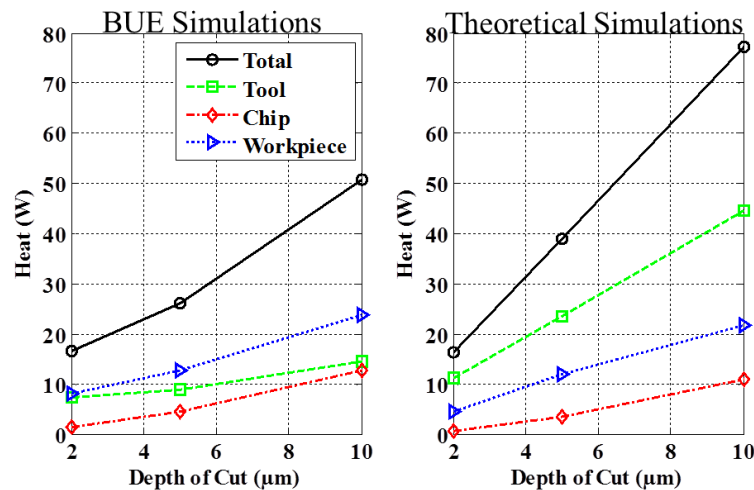


**Figure 26.** Comparison of heat partitions for BUE and theoretical tool simulations.

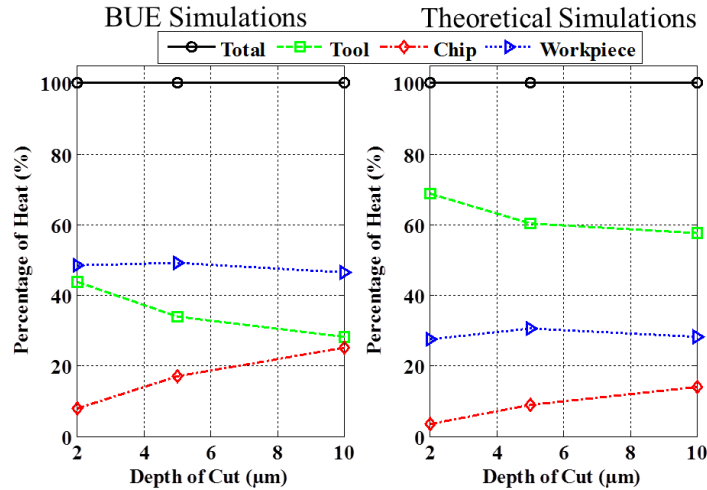


**Figure 27.** Comparison of heat partition percentages for BUE and theoretical tool simulations.

For each set of simulations, heat flowed through the workpiece at a relatively consistent percentage. BUE simulations showed near 50% of the heat flowing through the workpiece in comparison to approximately only 30% with the theoretical tool. Heat flow into the chip also increased for the BUE simulations in comparison to the theoretical simulations. The BUE simulations predicted between 8-25% of the heat flowing through the chip, while the theoretical simulations predicted between 3-14%. As the DoC increased, each set of simulations also showed a percentage increase in the heat flow through the chip to offset the decrease in heat flow through the tool. Both the chip and workpiece components received higher amounts of heat in the BUE simulations due to the BUE acting as an insulator for the tool.

Despite the BUE simulations producing less heat, the higher percentage of heat flow provided a net increase in the total amount of heat going into the chips. The BUE simulations had approximately 1.3, 4.5 and 12.8 W flowing into the chip as the DoC increased while the theoretical tool simulations had approximately 0.6, 3.5 and 10.9 W. Combined with the smaller sized chips that were produced (as discussed in Section 2.4.3, this resulted in much hotter chips being produced as a way to remove heat from the shear zone. This is noticeable in Figure 23 where the 5 μm DoC simulations are shown and the chip from the BUE geometry is approximately 170°C while the chip from the theoretical tool geometry is approximately 105°C. Figure 28 shows the average chip temperature of each simulation. BUE simulations produced a general 60°C hotter chip due to the additional heat input into the smaller sized chip.

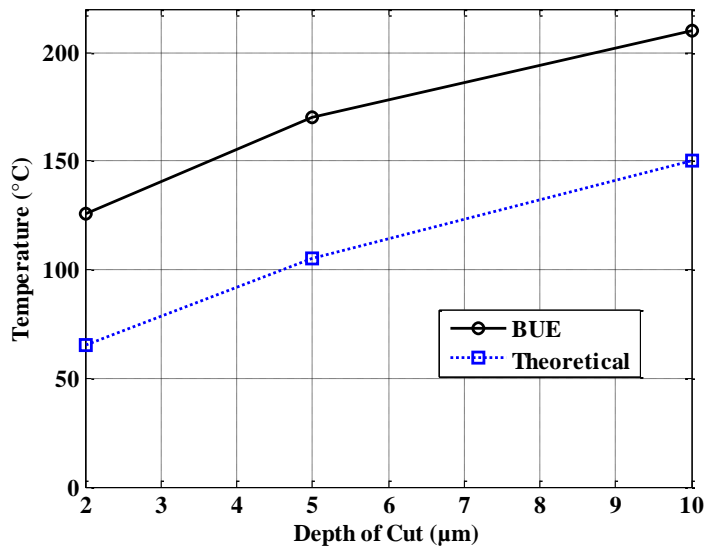


**Figure 28.** Comparison of chip temperatures for BUE and theoretical simulations.

## 2.5 CONCLUSIONS

A substantial amount of built up edge occurs when diamond turning steel. This results in a change in the tool geometry by creating an enlarged cutting edge radius and increasing the rake angle. The BUE was present at all depths of cut and occurred whether cutting fluid was used or not. The magnitude of the BUE was approximately twice that of the tool wear.

A comparison of simulation results with experiments supports the hypothesis of consistent effect of BUE on the cutting and chip formation process. BUE simulations matched experimental results for force measurements and chip thickness. The presence of a BUE results in a more efficient cutting process which produces lower forces and increases heat flow into the chip and the workpiece while reducing heat flow into the tool. The BUE insulates the tool.

## REFERENCES

1. Evans, Chris. "Precision Engineering: An Evolutionary View." *Bedford: Cranfield Press*, 1989 1 (1989).
2. Oomen, J. M., and J. Eisses. "Wear of Monocrystalline Diamond Tools during Ultraprecision Machining of Nonferrous Metals." *Precision Engineering* 14.4 (1992): 206-18.
3. Lane, B. M., et al. "Diamond Tool Wear when Machining Al6061 and 1215 Steel." *Wear* 268.11–12 (2010): 1434-41.
4. Shimada, S., et al. "Suppression of Tool Wear in Diamond Turning of Copper Under Reduced Oxygen Atmosphere." *CIRP Annals - Manufacturing Technology* 49.1 (2000): 21-4.
5. Paul, Ed, et al. "Chemical Aspects of Tool Wear in Single Point Diamond Turning." *Precision Engineering* 18.1 (1996): 4-19.
6. Hitchiner, M. P., and J. Wilks. "Factors Affecting Chemical Wear during Machining." *Wear* 93.1 (1984): 63-80.
7. Thornton, A. G., and J. Wilks. "Tool Wear and Solid State Reactions during Machining." *Wear* 53.1 (1979): 165-87.
8. Thornton, A. G., and J. Wilks. "The Wear of Diamond Tools Turning Mild Steel." *Wear* 65.1 (1980): 67-74.
9. Lane, B. M., T. A. Dow, and R. Scattergood. "Thermo-Chemical Wear Model and Worn Tool Shapes for Single-Crystal Diamond Tools Cutting Steel." *Wear* 300.1–2 (2013): 216-24.
10. Brinksmeier, E., and R. Gläbe. "Advances in Precision Machining of Steel." *CIRP Annals - Manufacturing Technology* 50.1 (2001): 385-8.
11. Brinksmeier, E., R. Gläbe, and J. Osmer. "Ultra-Precision Diamond Cutting of Steel Molds." *CIRP Annals - Manufacturing Technology* 55.1 (2006): 551-4.
12. Casstevens, J. M. "Diamond Turning of Steel in Carbon-Saturated Atmospheres." *Precision Engineering* 5.1 (1983): 9-15.
13. Evans, C., and J. B. Bryan. "Cryogenic Diamond Turning of Stainless Steel." *CIRP Annals - Manufacturing Technology* 40.1 (1991): 571-5.
14. Hesler, G. "Investigating the Mechanisms of Diamond Tool Wear Cutting Ferrous Materials using a Quantitative Study of Machining Parameters." Master of Science Mechanical Engineering North Carolina State University, 2014.
15. Lane, B. M. "Material Effects and Tool Wear in Vibration Assisted Machining." PhD North Carolina State University, 2012.
16. Drescher, J. "Scanning Electron Microscopic Technique for Imaging a Diamond Tool Edge." *Precision Engineering* 15.2 (1993): 112-4.

17. Drescher, J. D. "Tool Force, Tool Edge, and Surface Finish Relationships in Diamond Turning." PhD North Carolina State University, 1992.
18. Shi, Meirong. "Thermo-Chemical Tool Wear in Orthogonal Diamond Cutting Steel and Stainless Steel." North Carolina State University, 2010.
19. Pavel, Radu, et al. "Effect of Tool Wear on Surface Finish for a Case of Continuous and Interrupted Hard Turning." *Journal of Materials Processing Technology* 170.1–2 (2005): 341-9.
20. Childs, T. H. C. "Ductile Shear Failure Damage Modelling and Predicting Built-Up Edge in Steel Machining." *Journal of Materials Processing Technology* 213.11 (2013): 1954-69.
21. Bandyopadhyay, B. P. "Mechanism of Formation of Built-Up Edge." *Precision Engineering* 6.3 (1984): 148-51.
22. Heginbotham, WB, and SL Gogia. "Metal Cutting and the Built-Up Nose." *Proceedings of the Institution of Mechanical Engineers* 175.1 (1961): 892-917.
23. Uhlmann, Eckart, Steffen Henze, and Katrin Brömmelhoff. "Influence of the Built-Up Edge on the Stress State in the Chip Formation Zone during Orthogonal Cutting of AISI1045." *Procedia CIRP* 31 (2015): 310-5.
24. Chao, BT, and GH Bisacre. "The Effect of Speed and Feed on the Mechanics of Metal Cutting." *Proceedings of the Institution of Mechanical Engineers* 165.1 (1951): 1-13.
25. Iwata, Kazuaki, and Kanji Ueda. "Fundamental Analysis of the Mechanism of Built-Up Edge Formation Based on Direct Scanning Electron Microscope Observation." *Wear* 60.2 (1980): 329-37.
26. Tomac, Nikola, et al. *A Study of Factors that Affect the Build-Up Material Formation*. Springer, 2005.
27. Wegener, Konrad, and Thomas HC Childs. "Fifth CIRP Conference on High Performance Cutting 2012 Developments in Simulating Built Up Edge Formation in Steel Machining." *Procedia CIRP* 1 (2012): 78-83.
28. Childs, T. H. C. "Towards Simulating Built-Up-Edge Formation in the Machining of Steel." *CIRP Journal of Manufacturing Science and Technology* 4.1 (2011): 57-70.
29. Fang, N., and P. Dewhurst. "Slip-Line Modeling of Built-Up Edge Formation in Machining." *International Journal of Mechanical Sciences* 47.7 (2005): 1079-98.
30. Jacobson, Staffan, and Per Wallén. "A New Classification System for Dead Zones in Metal Cutting." *International Journal of Machine Tools and Manufacture* 28.4 (1988): 529-38.
31. Oishi, K. "Built-Up Edge Elimination in Mirror Cutting of Hardened Steel." *Journal of engineering for industry* 117.1 (1995): 62-6.
32. Merchant, M. Eugene. "Mechanics of the Metal Cutting Process. I. Orthogonal Cutting and a Type 2 Chip." *Journal of Applied Physics* 16.5 (1945): 267-75.

33. Korkut, I., and M. A. Donertas. "The Influence of Feed Rate and Cutting Speed on the Cutting Forces, Surface Roughness and Tool–chip Contact Length during Face Milling." *Materials & Design* 28.1 (2007): 308-12.
34. Ramaswami, R. "The Effect of the Built-Up-Edge (BUE) on the Wear of Cutting Tools." *Wear* 18.1 (1971): 1-10.
35. Bowden, F. P., and E. H. Freitag. "The Friction of Solids at very High Speeds. I. Metal on Metal; II. Metal on Diamond." *Proceedings of the Royal Society of London. Series A, Mathematical and Physical Sciences* 248.1254 (1958): 350-67. JSTOR.
36. Shaw, M. C. *Metal Cutting Principles*. Eds. J. R. Crookall, M. C. Shaw, and N. P. Suh. New York, New York: Oxford University Press, 2005.
37. Schey, J. A. *Introduction to Manufacturing Processes*. 2nd Ed. New York: McGraw-Hill, 1983.
38. "MatWeb Online Materials Information." Web. <<http://www.matweb.com/>>.
39. Suit, Brandon Michael. "Analysis of Accelerated Tool Wear and Built Up Edge when Diamond Turning Ferrous Materials," MS Thesis, 2016.

### 3 MACHINING PLASTIC OPTICS

**Charan Bodlapati**

Graduate Student

**Anthony Wong**

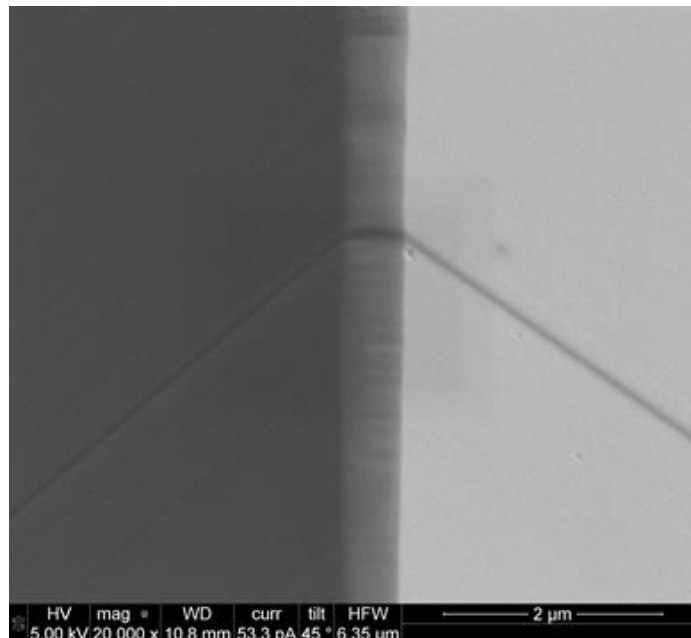
Research Associate

**Thomas Dow**

Professor

Mechanical and Aerospace Engineering

*Polymers play a vital role in the optical industry. They have low specific mass, excellent optical properties when compared to mineral glasses and are commonly used for manufacturing lenses. Single point diamond turning is widely used to machine plastic lenses. However, information on the parameters that can optimize the surface finish and minimize diamond tool wear during machining of plastics is lacking. The goal of this research is to address these two problems: surface finish and tool wear for several plastic materials. Three polymers are being used in this research: Poly (methyl methacrylate) (PMMA), Polycarbonate (PC) and Zeonex®. This report covers the initial results of the project and the challenges faced during diamond turning of these three materials.*





### 3.1 INTRODUCTION

Optical devices are extremely important since they play a critical role in optical recording and display. Diamond turning (DT) of plastics is influenced by a wide variety of factors such as glass transition temperature of the polymer, material properties and operator controlled cutting conditions. Single point diamond turning (SPDT) is one of the common methods to create plastic optics. Diamond being one of the hardest materials in the nature, and polymers are relatively soft; little tool wear is expected. But the optical industry claims that tool wear is a major problem. This research aims a) to investigate the best possible conditions for machining plastic optics in order to produce a surface with optical surface quality ( $R_a < 5 \text{ nm}$ ) b) to study the wear process and Built up Edge (BUE) that occurs on the tool and c) to study how the material properties act as a limiting factor in determining the quality of surface finish achieved.

DT is a precision lathe operation where workpiece material is removed by a single crystal diamond tool. The DT process is typically performed on a machine with precise hydrostatic air or oil bearings with axis displacement controlled with interferometric measurements. DT allows for the creation of optical surfaces. The current production of lenses starts with rough cutting the so called "blank". The process creates the rough form of the lens, but not the correct optical quality. If the surface roughness of the rough cut blank is too high for intermediate polishing, the blank is first transported to a grinding machine. After grinding the blank is transported to the polishing machine for polishing to optical quality. The transporting and fixing the blank on other machines introduces form inaccuracies in the final product [1, 2]. The DT process enables a high flexibility in the production process and an increased production rate of asymmetric products [3, 4].

### 3.2 DETAILS OF THE PROJECT

The three polymers used in this research are Polymethyl methacrylate (PMMA), Polycarbonate (PC), Polystyrene (PS) and Zeonex®. PMMA is a transparent thermoplastic with refractive index of 1.49 and capable of light transmission up to 92% within a wavelength of 300 nm to 900 nm making it one of the most important materials in the optical industry. Polycarbonate is a thermoplastic with refractive index of 1.60 and capable of light transmission up to 89% within a wavelength of 300 nm to 900 nm. PC is high yield strength material and is used by 35% of lens industry in USA. Zeonex® is a cyclo-olefin polymer which is used as a general transparent engineering plastic. Its low birefringence and high light transmission made it a very common material in optical components. Detailed list of properties of the three plastics are shown in Table 1.

**Table 1. Material properties**

<b>Material</b> <b>Property</b>	<b>PMMA</b>	<b>PC</b>	<b>Zeonex®</b>
<b>Refractive index</b>	1.49	1.6	1.53
<b>Abbe Number *</b>	58	27.86	56
<b>Light transmission (%)</b>	92	89	91.7
<b>Density (g/cm<sup>3</sup>)</b>	1.18	1.20	1.01
<b>Glass transition temperature (°C)</b>	105	147	139
<b>Critical entanglement molecular wt. (g/mole)</b>	29,500	6,000	P
<b>Coefficient of linear expansion (10<sup>-5</sup> °C)</b>	5.9	7.0	6.0
<b>Specific heat (Cal/g-°C)</b>	0.35	0.36	Proprietary
<b>Dielectric breakdown strength (KV/mm)</b>	15.8-19.7	15-67	40
<b>Youngs modulus (MPa)</b>	1800-3100	2100-2900	2500
<b>Thermal conductivity at 23°C (W/m-K)</b>	0.167	0.19-0.22	Proprietary
<b>Thermal diffusivity (mm<sup>2</sup>/s)</b>	0.121	0.147	50
<b>Yield Strength (MPa)</b>	55.5	89.6	62
<b>Hardness ASTM D785 (metric)</b>	94	108-120	50

The controllable parameters that effects machining of plastics are as follows:

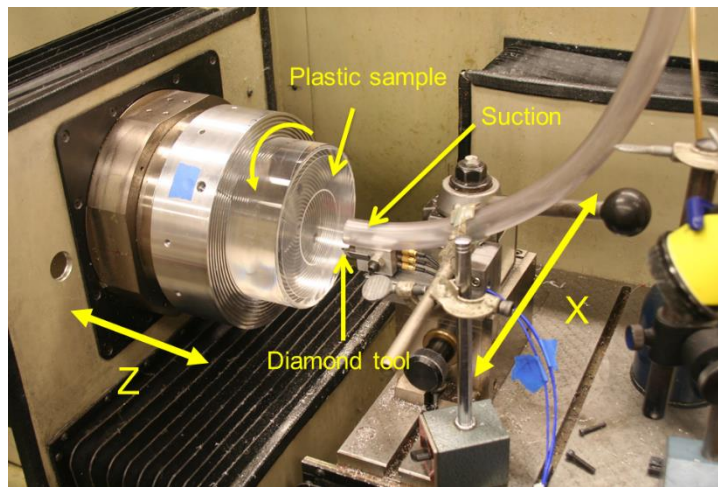
- |                  |             |
|------------------|-------------|
| Crossfeed        | Tool Wear   |
| Depth of cut     | Lubrication |
| Cutting speed    | Tool radius |
| Tool orientation |             |

### **3.3 SURFACE FINISH STUDY**

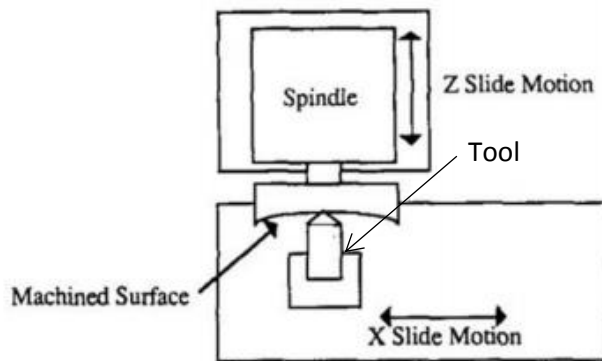
The first step in this project was to compare the surface finish created on the three materials. The surfaces generated were measured using Zygo NewView 100 white light interferometer and

Taylor Hobson Talysurf profilometer. After cutting, images of tool edges were captured in the Scanning Electron Microscope (SEM) and the tool wear was characterized using Electron Beam Induced Deposition (EBID) technique [5] and analyzed using a MatLab program (digitize18.m). The goal of this project is to determine the optimal conditions for machining each polymer which generates optical quality finish minimizing tool wear.

The overview of the experimental apparatus is shown in Figure 1. The experiments utilized the Pneumo ASG 2500 Diamond Turning Machine (DTM). A DTM is a precision computer numerically controlled (CNC) lathe with a single point diamond tool. The ASG has two orthogonal slideways and the workpiece is mounted to the spindle (Z axis) using a vacuum chuck. The tool is mounted on the X-axis. The ASG utilizes a laser interferometers with 2.5 nm resolution to measure the x and z slide positions. The tool was attached to the tool post with a three axes, piezoelectric KISTLER load cell. The tool starts in the positive X direction of the part and moves inward as the part rotates in counter clockwise direction. A separate suction system shown in Figure 1 was used to remove chips through the 1 inch diameter plastic tube..



(a) Overview of DTM used for the initial facing experiments



(b) Top down view of setup [6]

**Figure 1.** Experimental Instrumentation

### 3.3.1 PMMA Experiments

It was found from the literature [2] that PMMA is easily machinable and for that reason it was selected as the first material to study. A series of experiments were performed to determine the influence of cross-feed on the achievable surface finish using a 0.5 mm radius monocrystalline diamond tool. The crossfeed was varied from 3.2  $\mu\text{m}/\text{rev}$  to 98.52  $\mu\text{m}/\text{rev}$  at 3 m/s cutting speed. The variation of RMS roughness with crossfeed is shown in Figure 2. Theoretical surface roughness was calculated using Equation 1.

$$\text{Theoretical RMS roughness} = \frac{f^2}{26.6R} \quad (1)$$

where  $f$  is cross feed and  $R$  is radius of the diamond tool. The curve was expanded in the cross feed direction from 3  $\mu\text{m}/\text{rev}$  to 20  $\mu\text{m}/\text{rev}$  is shown in Figure 3.

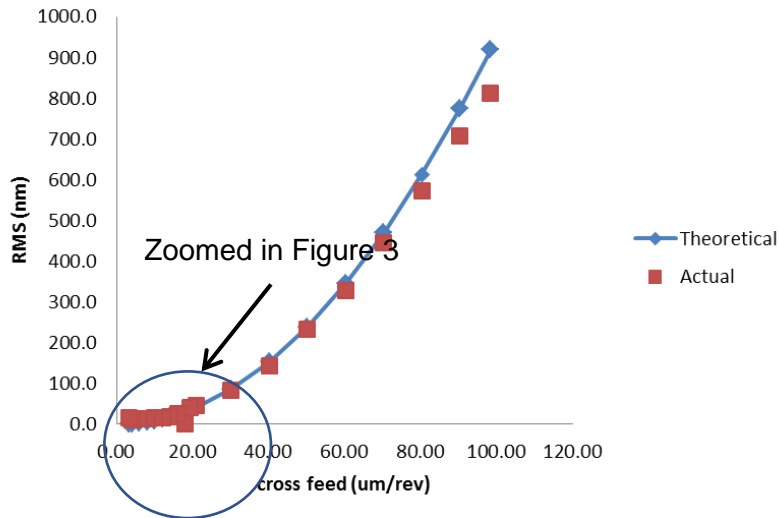


**Figure 2.** Crossfeed vs RMS roughness in PMMA using a 0.5 mm radius tool

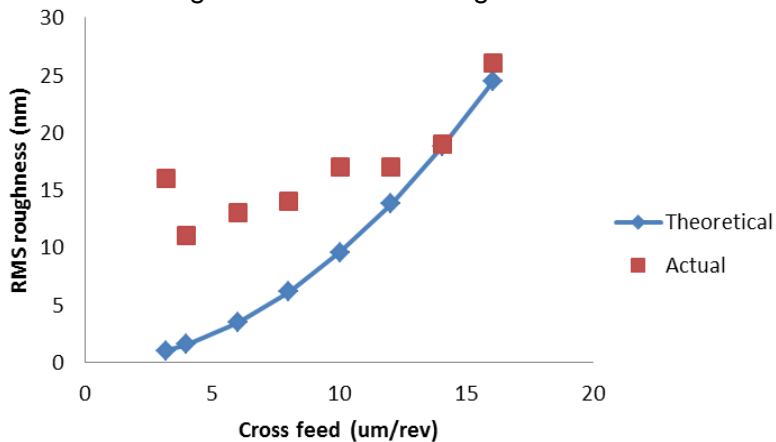


**Figure 3.** Crossfeed from 3  $\mu\text{m}/\text{rev}$  to 20  $\mu\text{m}/\text{rev}$  zoomed from Figure 2

Figure 3 shows that at smaller feed rates, the surface finish does not approach zero as the model would predict but approaches an asymptote at about 10 nm rms.

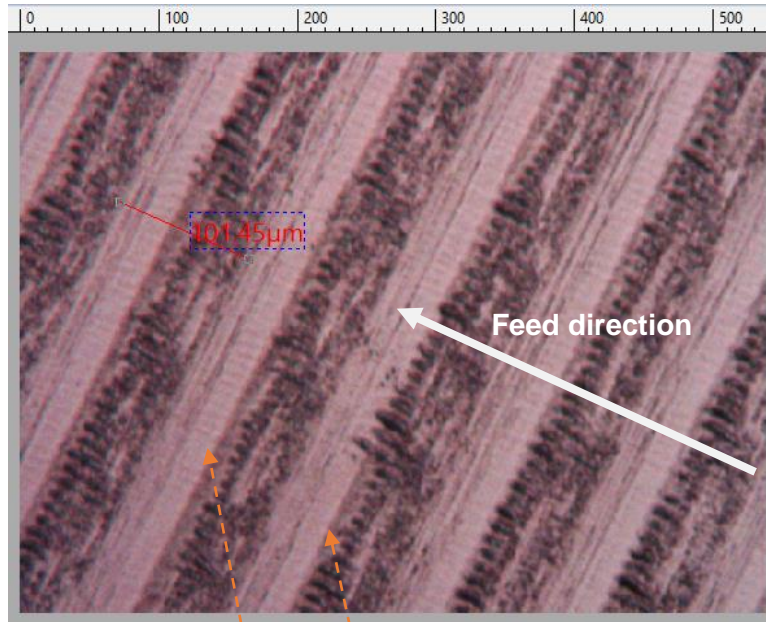


**Figure 4.** Surface finish of PMMA cut at 100 µm/rev (OD is to the right)

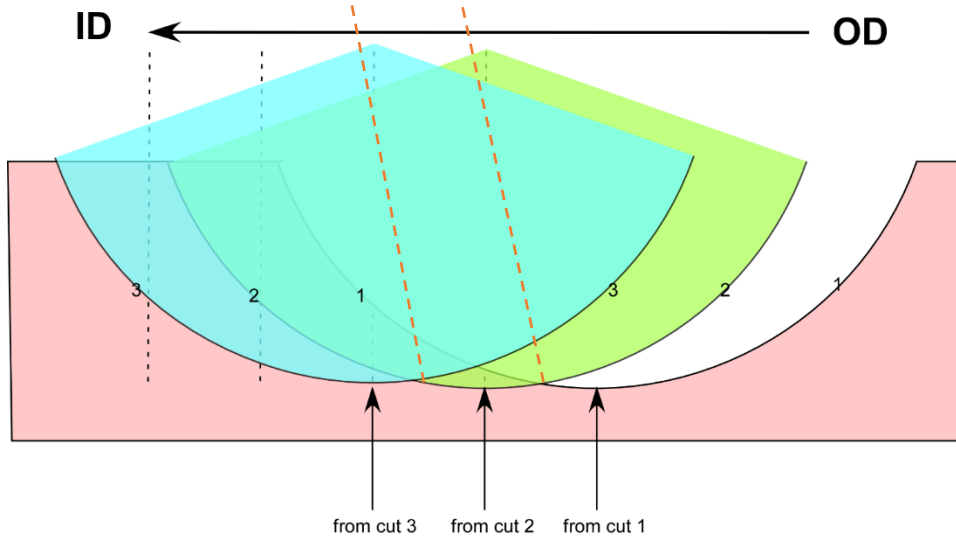


**Figure 5.** Cross-section details of the chip creation

Figure 5 shows the details of the material removal process while machining the PMMA surface in Figure 4. It shows 3 passes of the tool beginning at the right hand side where the tool pushes through the material and removes a crescent shaped cross-section. The tool makes a spiral path around the workpiece and arrives at the cross-section in Figure 5 one federate to the left and removes the next cross-section - cut 2. Note that the thickness of the chip from cut 2 is large at

the top right of the cut but goes to “zero” at the LHS for all subsequent cuts. This surface (marked “from cut 2”) is now the finished surface and will not be touched by the tool again. To achieve the theoretical finish value from Eq. 1, the tool must cut the surface “from cut 2” to zero thickness on the LHS; which, of course, is impossible. So the surface finish can approach the theoretical finish, but never achieve it. So, by extension there is some chip thickness that is too small to be removed by the tool edge but rather would pass under the tool and pop up on the other side. Therefore, one explanation for actual roughness not following a parabolic relationship with crossfeed could be that the tool is plowing rather than removing the material or it could be vibration as in Figure 4 or it could be tool wear changing the edge sharpness of the tool.

The microscope image in Figure 4 shows the surface features of this cut. The surface roughness and the high-frequency features across the cut are clear in this particular example. More details of the chip are in Figure 6 which again shows 3 passes of the tool but the feed is in the opposite direction from Figure 5. One observation is that the geometry of the chip is very dependent on the radius of the tool. For the same feed rate, a smaller tool radius makes a shorter, thicker chip. Because the surface finish is dependent on the chip approaching zero thickness, the angle of the chip as it approaches the edge of the cut may be important. This chip angle is defined below.

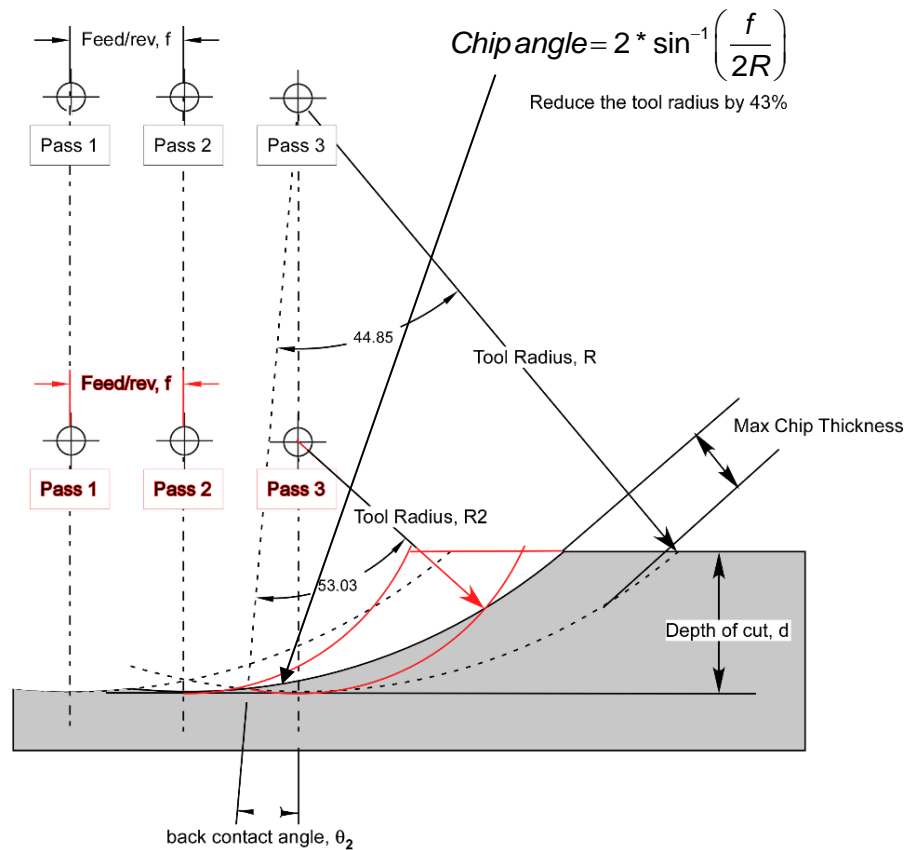


**Figure 6.** Geometry of the chip. Changing the tool radius (but keeping the rest the same) makes the included angle of the chip larger and may be the reason for better surface finish.

**Effect of Depth of Cut** To show the influence of depth of cut on the surface finish, the three materials were machined at 20  $\mu\text{m}$ , 40  $\mu\text{m}$ , 60  $\mu\text{m}$  and 80  $\mu\text{m}$  depth of cut. A 0.5 mm radius diamond tool was used to cut all three materials in this experiment. PMMA was the first material to be machined followed by PC and Zeonex respectively. The relative comparison of RMS roughness with depth of cut is shown in Figure 7.

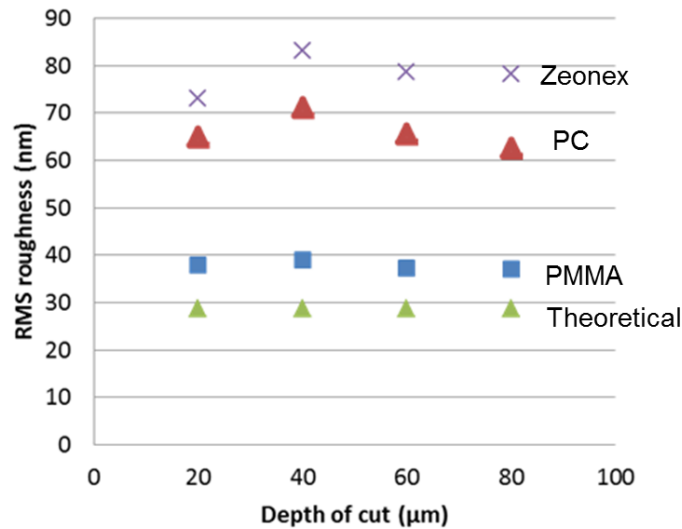


**Figure 7.** RMS roughness vs depth of cut

Based on Figure 7, the surface of PMMA is closest to the theoretical finish followed by Polycarbonate and Zeonex®. Figure 8 shows the NewView surface profiles of Polycarbonate and Zeonex. The RMS surface finish of both materials was large compared to PMMA and the theoretical value. Based on the images in Figure 8, there are a large numbers of peaks in both the materials but more in the Zeonex. Based on literature [7], Polycarbonate chips can become statically charged and, as a result, tend to stick on machined surface and create peaks on the profile. Based on this experiment, chip control was deemed an important parameter when machining PC and Zeonex.

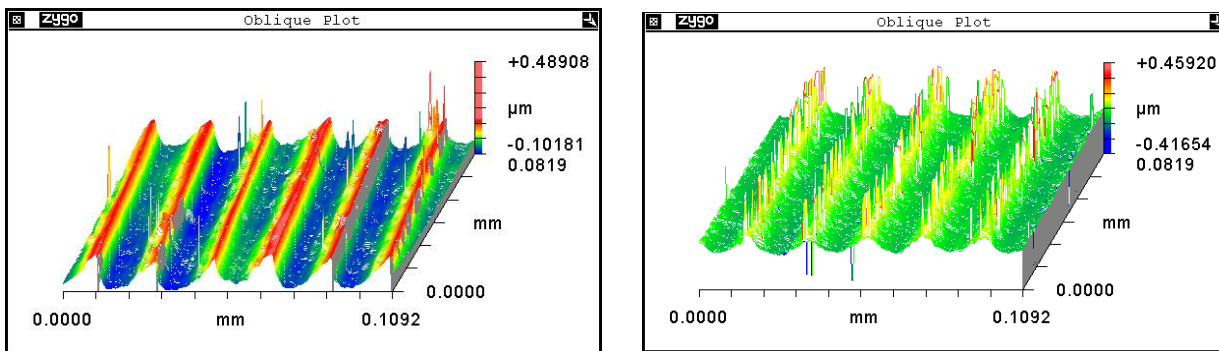


**Figure 8.** Surface profiles of PC (left) and Zeonex (right)



**Adding an air nozzle and ionizer** Plastic cutting experiments on PMMA at the PEC in 1997 were performed on 25 mm square specimens that were located on the face of the spindle about 100 mm from the center of rotation. Cutting was intermittent and short chips on the order of 25 mm long were generated. To blow these chips away from the cutting interface, a stream of air was used. The primary problem was that the statically charged acrylic chips were attaching themselves to the surface of the part. The tool would then intersect with the chips on the surface and drag them across the freshly machined surface, causing degradation of the finish. In addition to being a source of chip management problems, static discharge damage to tools was quoted by tool manufacturers as a concern when diamond machining insulators such as PMMA.

To address the chip/tool damage when machining PC and Zeonex in the current experiments, an ionizer was added to the machine mounted just below the tool shown in Figure 9. The tool and workpiece are the same as in Figure 1 except that the ionizer was added. An ionizer is a device that uses high-voltage to electrically charge air molecules that simultaneously neutralize and clean the plastic surfaces. The air ionizer consists of an air nozzle and a power supply, connected via a shielded high-voltage cable. The electrode at a potential of 5000 V inside the air nozzle forms a corona with the grounded housing of the air nozzle. The ionizer neutralizes the charge on the plastic chips so that they do not stick to the workpiece and makes it easier to entrain the chip in the vacuum chip extractor. The specifications of ionizer are given in Table 2.

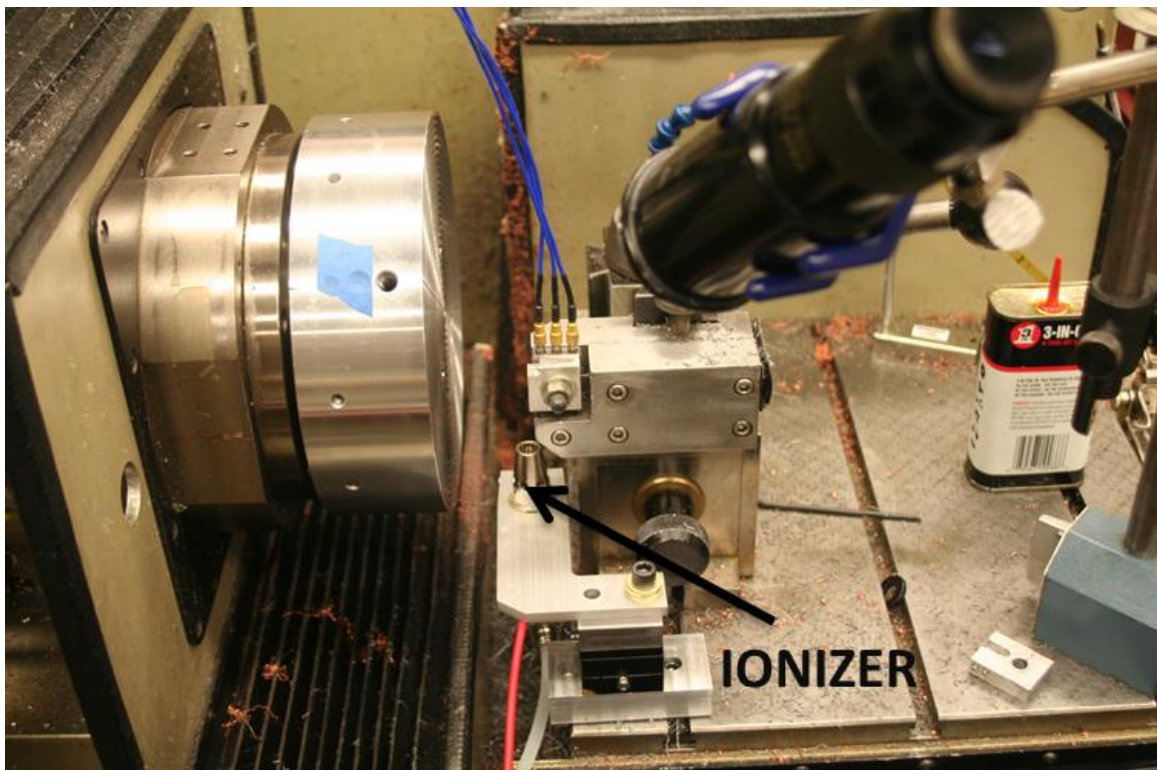


**Figure 9.** Experimental setup with air ionizer

**Table 2.** Ionizer Specifications

Ionizer	Electrostatics, Inc HPN (AC)
Power Unit	Herbert Static Control, 50 Hz
Max. air pressure (psi)	15-30 psi
Input Voltage (v)	120
Output Voltage (KV)	4
Current Limited (mA)	5

### 3.3.2 Experiments on PC

Polycarbonate samples were cut at 20  $\mu\text{m}$  depth of cut and 20  $\mu\text{m}/\text{rev}$  feed with a 0.5 mm radius diamond tool. The theoretical RMS is 28.3 nm. A similar experiment without ionizer was already performed and results were presented in Figure 7. This experiment was performed while blowing ionized air and the chips were sucked using a suction system. When both ionizer and suction were used the surface roughness of PC dropped from 65 nm to 48 nm for a theoretical RMS finish of 28.3 nm. The difference in surface profile with and without using ionized air is shown in Figure 10. The peaks in Figure 10(a) due to chips were eliminated and smooth grooves in Figure 10(b) were produced when ionizer was used.

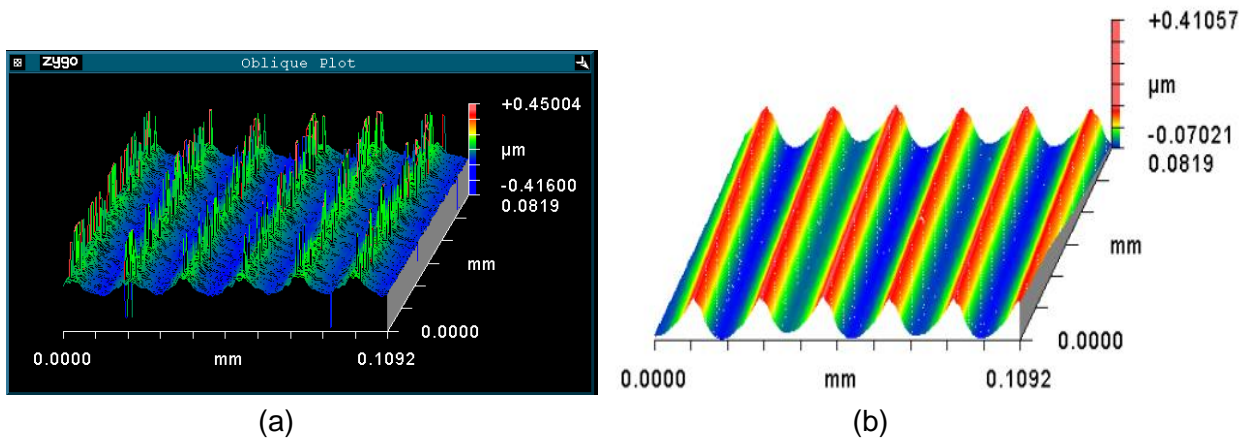
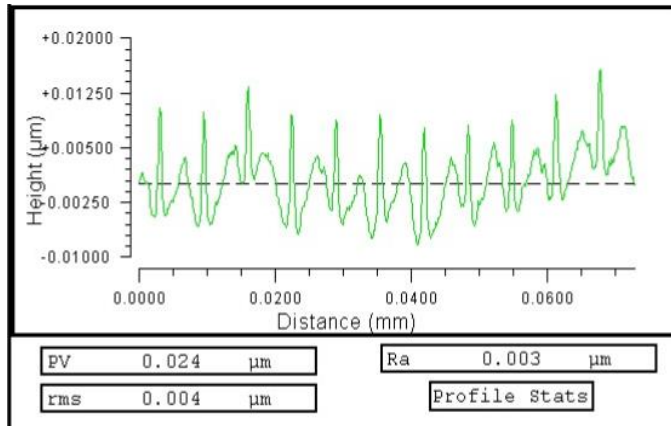
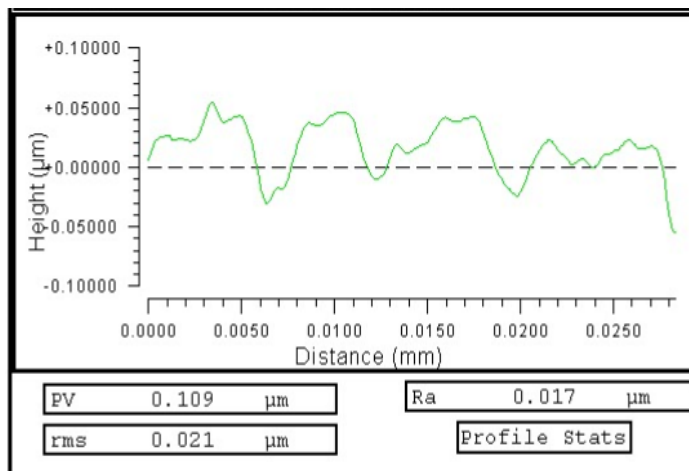


**Figure 10.** Surface profiles of PC with (a) only suction (b) with ionizer and suction

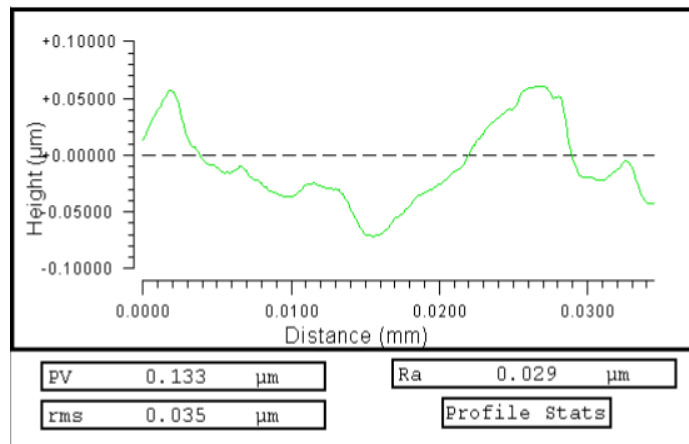
**Optical Finish Experiments #1** Using the experimental setup in Figure 9, all three materials were cut using a re-lapped 0.5 mm radius diamond tool. The theoretical RMS finish for these experiments was 3 nm RMS using a crossfeed of 6.5  $\mu\text{m}/\text{rev}$  with a depth of cut of 10  $\mu\text{m}$ . PMMA was the first material to be cut followed by PC and Zeonex. The surface roughness measurements were shown in Figure 11(a) to (c). The cutting distance for all three materials was 5 km. After cutting all three materials PMMA was once again machined at same cutting conditions with the same tool. The surface was then measured in NewView and is shown in Figure 11(d)



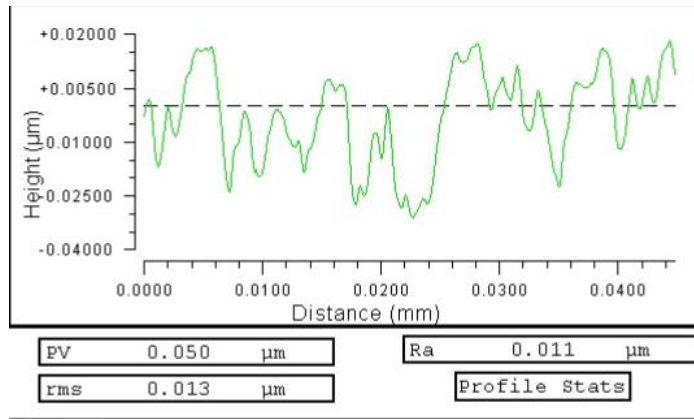
(a) PMMA



(b) PC



(c) Zeonex®



(d) PMMA

**Figure 11.** Surface profiles measured on NewView white light interferometer after machining 5 Km of the plastic surface

Figure 11(b) and (c) indicate higher RMS surface roughness than the theoretical RMS of 3 nm. Figure 11(a) shows that surface finish obtained in PMMA is close to theoretical finish. On the other hand, Figure 11(d) shows that the surface roughness of PMMA increased from 4 nm to 13 nm after 5 km of cutting, which may be attributed to tool wear after cutting Polycarbonate and Zeonex®. It was also found that some plastic material was left on the tool after every cut but it was quite easy to remove it with acetone on a Q-tip and minimal force. The image of the tool after cutting is shown in Figure 12. From this point on, the tool was cleaned after every cut. For future experiments and tool will be inspected under 500 X magnification microscope to make sure that it is clean.

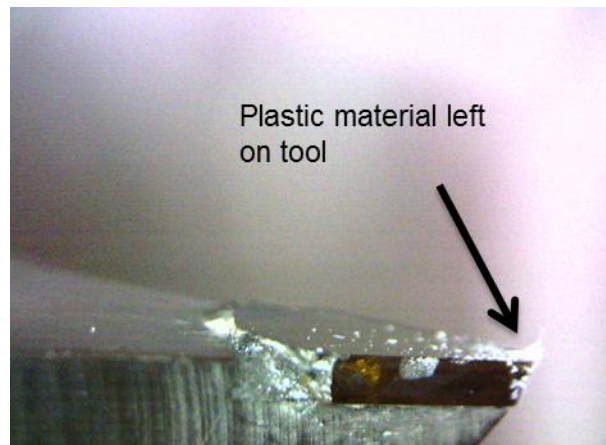
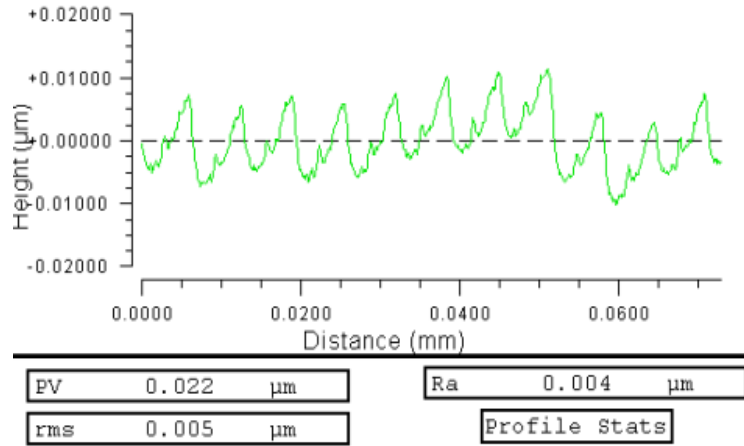


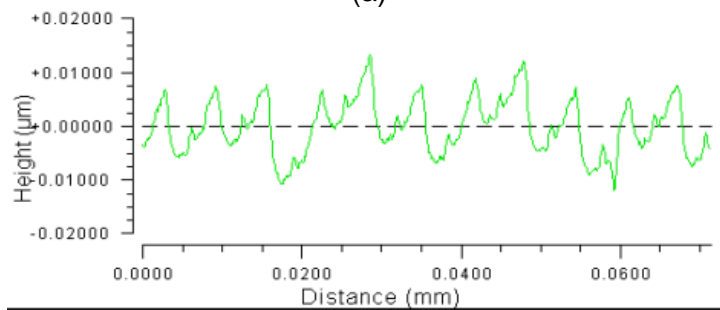
**Figure 12.** Workpiece material left on tool after cutting

**Optical Finish Experiments #2** To check the reproducibility of the PMMA experiments, the sample was cut using a re-lapped 0.5 mm tool with a crossfeed is 6.5 µm/rev and a depth of cut of 10 µm. The theoretical RMS finish was 3 nm. Ionized air was blown on to the tool from bottom and chips were simultaneously collected using suction. This experiment was repeated three times

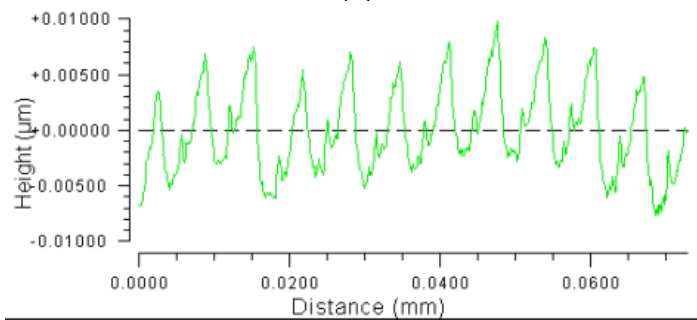
on the same sample and conditions with the same tool but the tool was cleaned after every cut using q-tip dipped in acetone. The surface roughness measurements are shown in Figure 13 (a-c).



(a)



(b)



(c)

**Figure 13.** Surface profiles of PMMA using the same tool used to cut the PMMA, PC and Zeonix (a) first cut (b) second cut (c) third cut

In Figure 13 (a-c), and 13 (c), the surface roughness values for PMMA are close to 5 nm. This can be attributed to tool cleaning after every cut and cutting distance for each cut was 1 km so the tool was not worn after cutting PMMA for 8 km shown in Figure 14. From the initial surface finish studies performed on PC, chip management was identified to be an important parameter to achieve high-quality surface finish for Polycarbonate and Zeonex®. PMMA achieved better surface finish than other two materials in the experimental conditions used. Effect of other machining parameters will be addressed in future experiments.

**EBID Technique for Tool Geometry** Diamond tool wear has been studied at the PEC for over 25 years. It began with models of the cutting process by Drescher [9] and Arcona [10]. During these research projects, new techniques for measuring the tool geometry were developed and used to quantify changes in the nose radius as well as wear on the clearance surface that occurs due to sliding of the workpiece. Figure 14 shows an example of tool wear after machining PMMA for a distance of 8 Km. The technique (Electron Beam Induced Deposition) utilizes a contamination line drawn by an SEM beam that is scanned back-and-forth over the surface and leaves a line of hydrocarbon contamination due to impurities in the vacuum system.

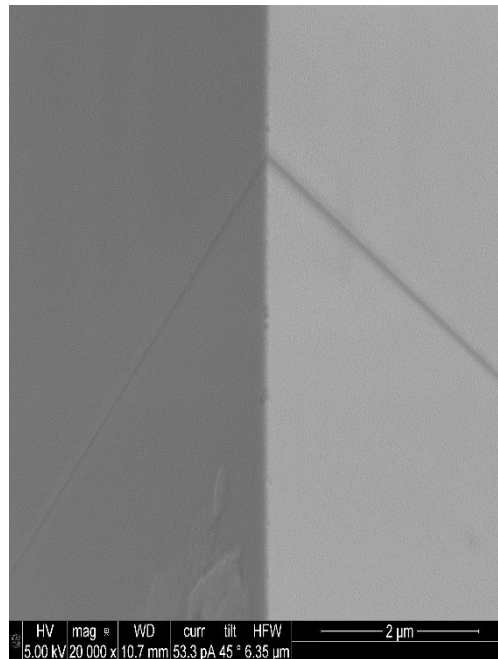


**Figure 14.** Tool was still sharp after cutting PMMA for 8 km (20,000 x)

### 3.4 Experimental Setup for Wear Experiments

The experimental apparatus is the same as Figure 1. The workpiece is mounted to the spindle (Z axis) using a vacuum chuck. The tool is mounted on the DTM X-axis. The tool was attached to the tool post with three axes, piezoelectric KISTLER load cell. The tool starts in the positive X



direction of the part and moves inward all while the part rotates in counter clockwise direction. A separate suction system shown in Figure 1 was used to remove chips at the time of machining.

This experiment was to study the wear of diamond tools wear machining PMMA and polycarbonate. Experiments were performed with a zero rake angle monocrystalline 0.537 mm nose radius re-lapped diamond tool. After machining, the diamond tool wear was analyzed using EBID technique in SEM images [5]. In addition, a non - overlapping spiral was cut on the sample. In a non-overlapping cut, the feed per revolution of tool is high enough (250 mm/min) that the grooves do not overlap and a series of complete grooves can be created as shown in Figure 15. The result shows the geometry of the tool after that cutting distance and whether the tool was worn or if it picked up plastic from the workpiece. After the non-overlapping spiral the sample was faced with a feed of 5  $\mu\text{m}/\text{rev}$  and 5  $\mu\text{m}$  depth of cut. The total cutting distance was 66 km. After facing for 66 km, non-overlapping cut was repeated.

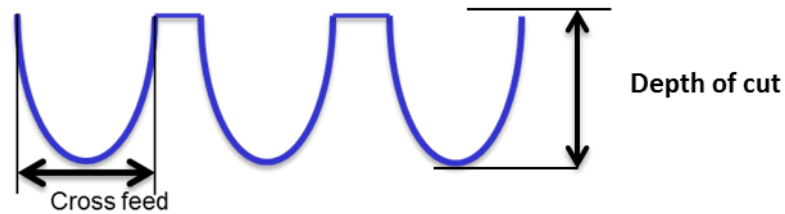


**Figure 15.** Cross sectional view of non-overlapping spiral.

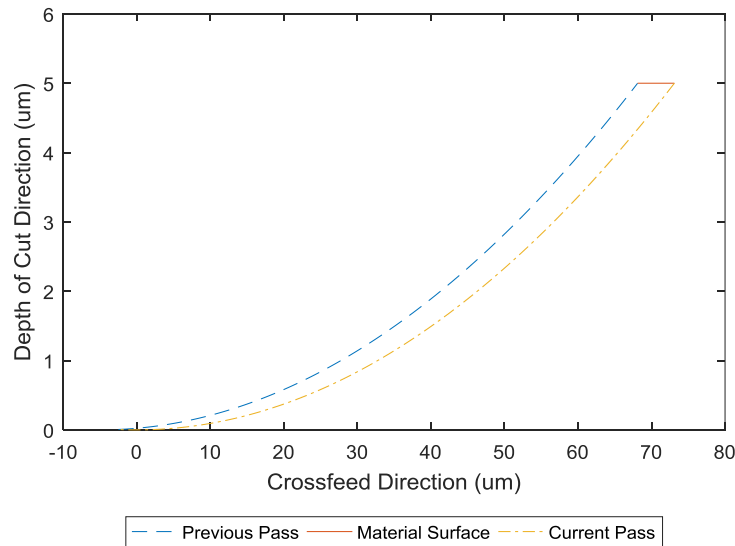


**Figure 16.** Chip geometry for nose radius of 0.537 mm, feed of 5  $\mu\text{m}/\text{rev}$  and 5 $\mu\text{m}$  depth of cut



Non-overlapping grooves were measured using a Talysurf profilometer. The tool was cleaned before observing in the SEM. To clean the tool, it was determined that Chloroform will dissolve polycarbonate. The tool was ultrasonicated in Chloroform for 10 minutes. A 3D printed plastic fixture was used to suspend the tool in the solvent and was reused for this cleaning operation. The plastic fixture was dissolved in chloroform and chloroform fumes caused it to drip down the tool. The tool was then soaked in Chloroform for 10 minutes to remove the material from the fixture. Next the tool was soaked in Acetone for 5 minutes. Finally, the diamond was rinsed in Isopropanol. Figure 16 shows the theoretical chip created by the facing operation. The front contact angle is  $7.8^\circ$ , and the back contact angle is  $0.3^\circ$  shown in Figure 16. This chip is  $75.8 \mu\text{m}$  wide and has a maximum thickness of  $660 \text{ nm}$ .

To compare wear in case of PMMA and PC, both the materials were machined with a  $0.5 \text{ mm}$  radius diamond tool. The experimental setup was similar to the previous experiment except for the use of ionized air and suction system to collect chips during machining. Both PMMA and PC were machined at a crossfeed of  $6.5 \mu\text{m}/\text{rev}$  but with a cutting distance  $8 \text{ Km}$  for PMMA and  $3 \text{ Km}$  for the PC. The tool was then cleaned using acetone and imaged under the SEM. The SEM images of the tool are shown in Figure 17.

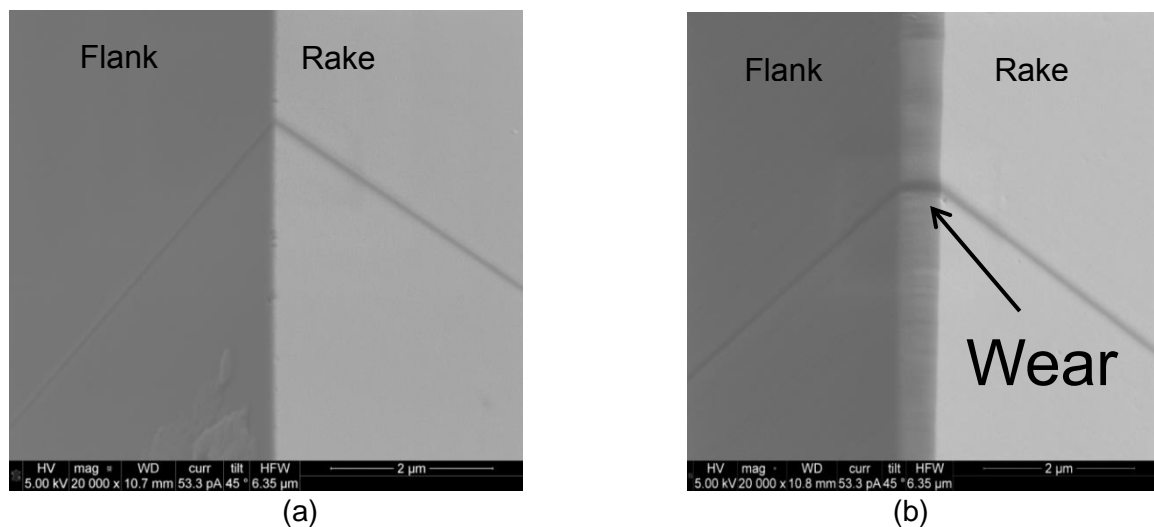


**Figure 17.** SEM images with EBID line (a) PMMA after 8 km of cutting (b) PC after 3 km of cutting (20,000 x)

Figure 17 (a) shows the tool used to cut PMMA and 17 (b) used for PC at a cutting distance about 40% less. The wear flat on the tool is clear in the PC experiment and is also shown in Figure 18 based on using the EBID line and orientating the image to show the cross-section. The sharp blue image is the cross-section of the new tool and the red line show how the edge of the tool has been worn due to sliding of the machined material on the flank face of the tool.

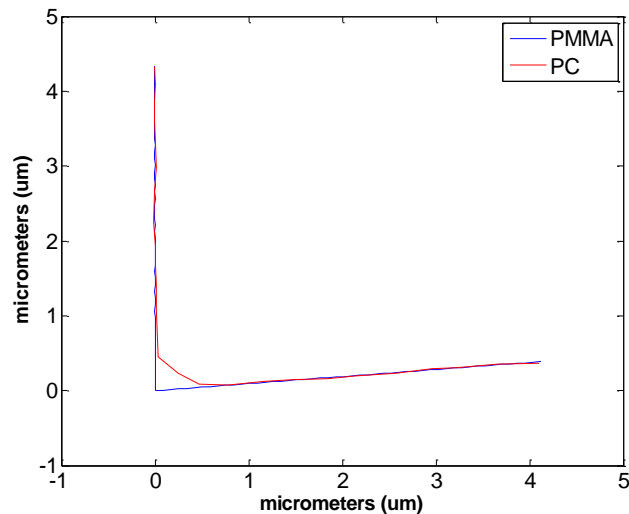


**Figure 18.** Worn tool profile after cutting PMMA for 8 km and PC for 3 km

### 3.5 Plunging Experiment To Measure Tool Wear

This experiment was conducted on the Nanoform DTM. The goal was to create a geometry with a uniform depth of cut across the width of the part and not like the chip from a facing cut shown in Figure 16 where the chip thickness varies from 0 to some portion of the feed rate. This variation in chip thickness and the lack of precise positioning of the tool inside the SEM, makes it difficult to know what the expected chip thickness and wear geometry will be. Having a consistent chip geometry was thought to be an advantage.

In this experiment, the tool was plunged in from the outer diameter of the cylindrical sample as shown in Figure 19. The setup of the experiment is displayed in Figure 20. The tool started in the positive X direction of the part and moved inward (to the right), while the part rotated counter clockwise with respect to the view shown in Figure 19. A plastic disk was bolted to a smaller aluminum fixture, shown in Figure 21. The bolted disk was then mounted on the vacuum chuck of the Nanoform. The disks were centered with a dial indicator. The load cell measured cutting force (Y); thrust force (X) and side force (Z). The temperatures were collected using an RTD attached on the top face of the shank; the temperatures at the shear zone and where the chip slides the rake face will be higher. Therefore, the temperatures measured will be lower than the actual tool-workpiece interface temperatures.

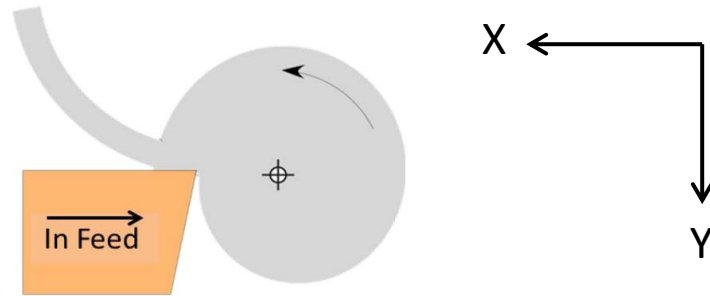


**Figure 19.** Plunging experiment

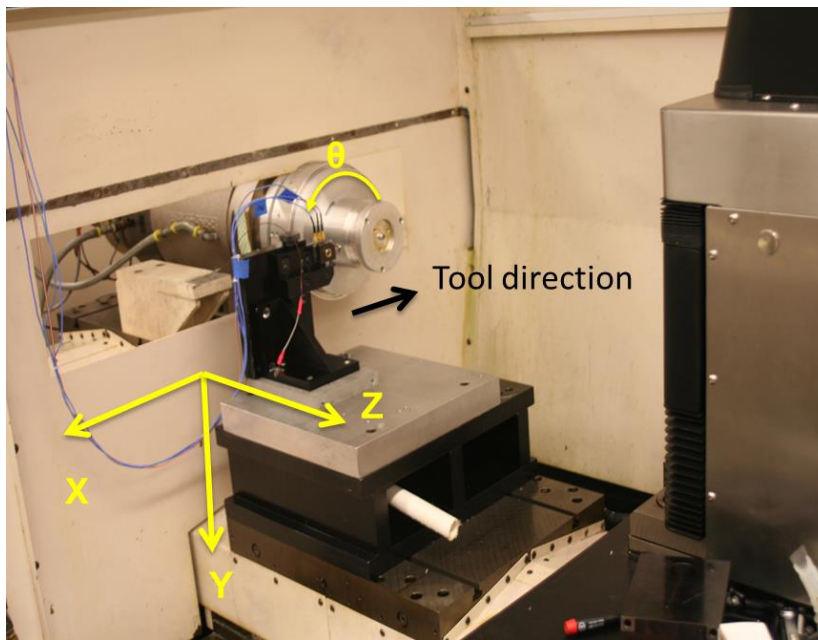


**Figure 20.** Nanoform setup for the experiments

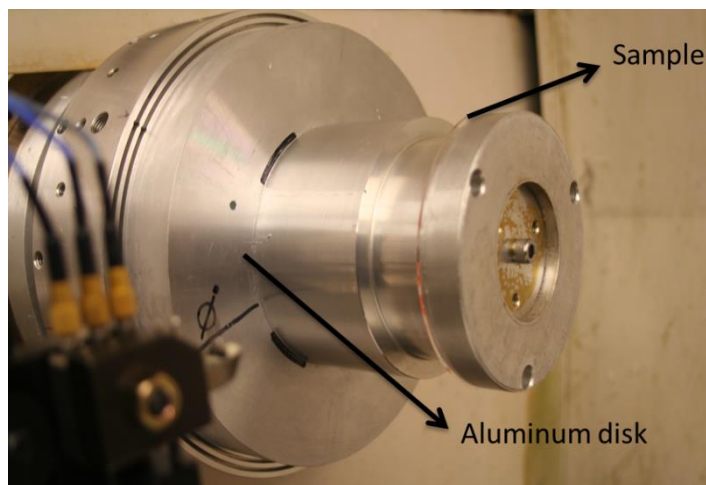


**Figure 21.** Fixture to hold workpiece

**Plunging Experiments** This experiment was performed to study tool wear using a straight edge diamond tool when machining the edge of a 5" diameter by 1 mm thick plastic disk. The tool was 3.5 mm wide and was plunged into the OD of the sample with a feed rate of 5  $\mu\text{m}/\text{rev}$  as shown in Figure 19. Two experimental locations on the tool were used as shown in Figure 22. The left location 1 in Figure 22 of square tool was used to machine PC whereas location 2 used to machine PMMA. This experiment was performed to observe a uniform depth of cut for the same cutting conditions for these two materials.

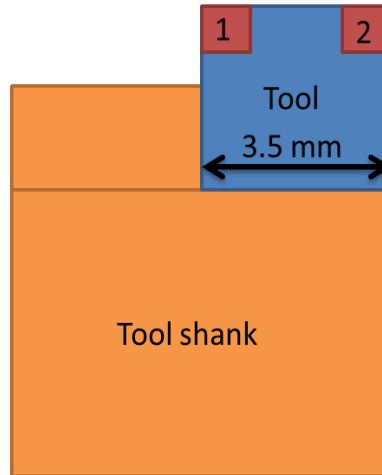


**Figure 22.** Cutting locations on diamond tool

5 disks of PC were machined using location 1 on the diamond and 5 disks of PMMA were machined using location 2 on the diamond. Force and temperature data was captured during cutting. Representative cutting force plots for the two materials are shown in Figure 23 and temperature plots are shown in Figure 24. From Figure 23, it can be seen that for similar cutting conditions, PMMA required more cutting force than did PC.

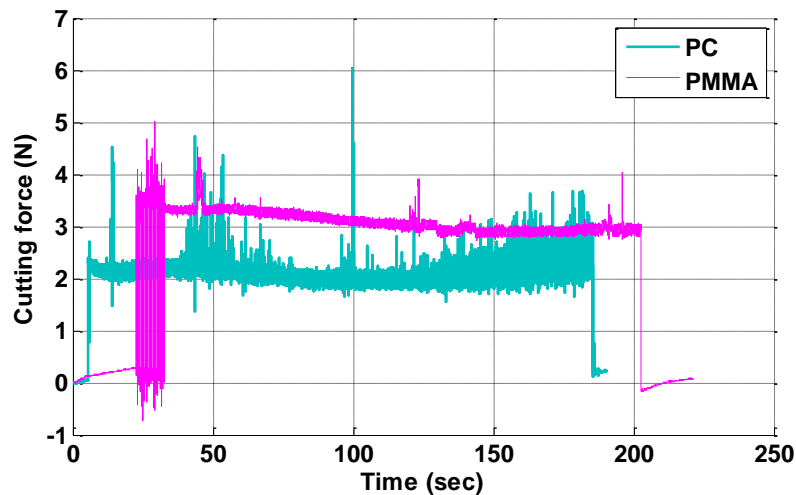


**Figure 23.** Force plots of PMMA and PC

From Figure 24, it can be seen that PMMA experienced higher temperature (~10° C) than that of PC. This can be attributed to the fact that the thermal diffusivity of PC is 20% more than that of PMMA, which indicates that heat diffuses faster in case of PC.

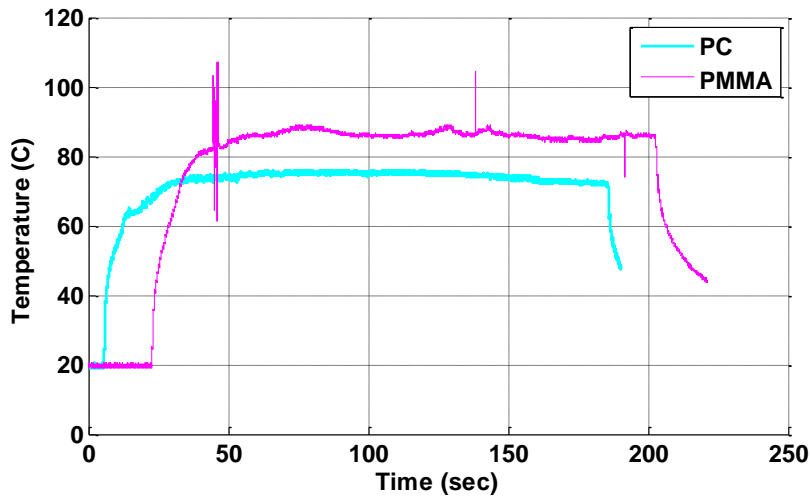


**Figure 24.** Temperature of PMMA and PC

The total heat flowing into diamond is 4.5 W from cutting zone for PC and 5 W for PMMA. The temperature data presented above is measured on the diamond tool and was not the exact tool-workpiece interface temperature. In contrast to arguments of Gubbels [2], the actual temperature at the interface can be much higher, which indicates that there can be a fair chance for PMMA to reach its glass transition temperature (105° C). The diamond tool was observed in SEM, after cutting 4.315 km on each material. Overview of diamond tool is shown in Figure 25.

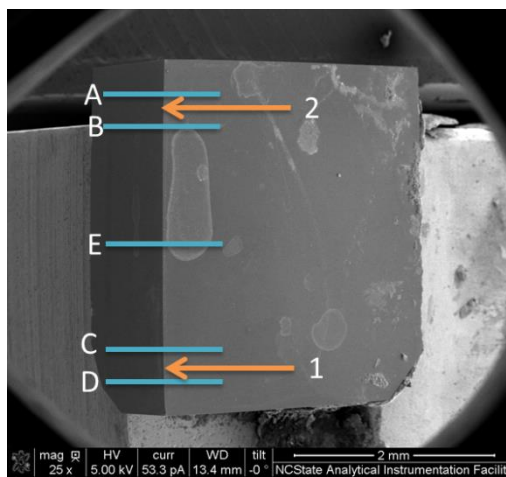


**Figure 25.** SEM image of square diamond tool

Locations A and B represent the cutting zone which was used to cut PMMA whereas locations C and D represent the cutting zone which was used to cut PC. Location E is at the center of tool which was not used. Tool wear was observed to be greater on the cutting edge that was used to machine PC. However, “Lichtenberg Figures” which was believed to be due to tribo-electric wear by Gubbels [1], was observed near C and D (edge where PC was machined). This is shown in Figure 26. However, this “Lichtenberg figure” was not observed in the locations where PMMA was cut.

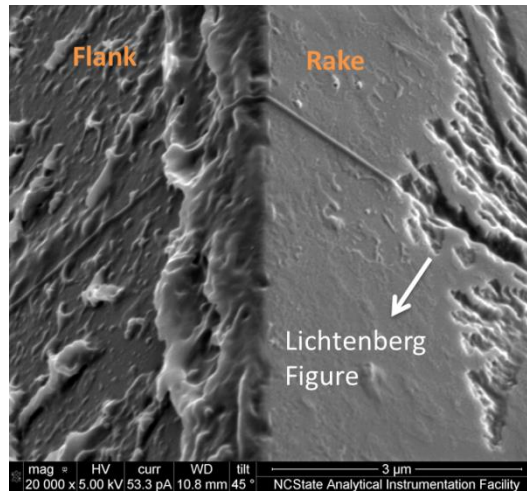


**Figure 26.** “Lichtenberg Figure” at Location D in Figure 26

Plunging experiments were performed under similar cutting conditions with ionized air blowing from bottom of tool and chips were collected using suction during machining. After cutting, tool was cleaned using chloroform and ultrasonicated. Sonication is the act of applying sound energy to agitate particles in a sample, for various purposes. Ultrasonic frequencies (>20 kHz) are usually used, leading to the process also being known as ultrasonication. The tool was observed under the Scanning electron microscope (SEM) and was analyzed. The total cutting distance was 4.5 km on PMMA and 4.5 km on PC.

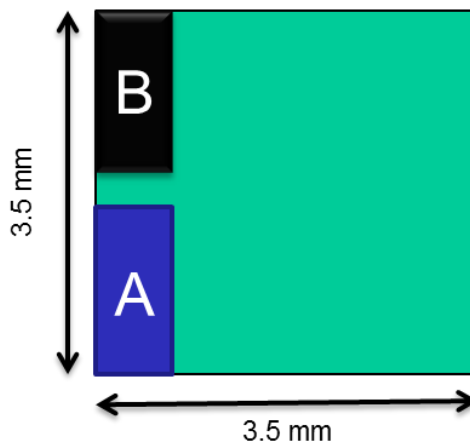


**Figure 27.** Square cutting tool with cutting zones

Overview of diamond tool and cutting zones are shown in Figure 27. In Figure 27, Location A was used to machine PC and Location B was used to machine PMMA.

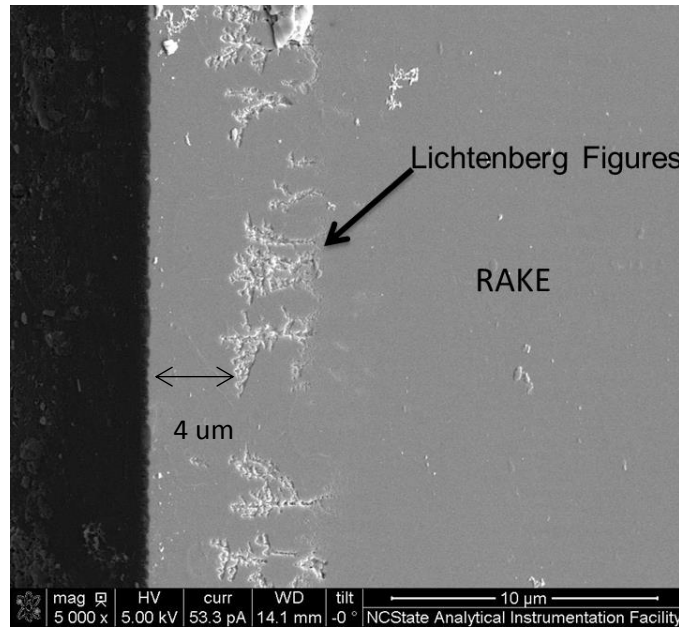


**Figure 28.** Lichtenberg Figures found across cutting edge in location A in Figure 30

From Figures 28, high density “Lichtenberg Figures” were observed on the tool. The density of these Lichtenberg figures on diamond was much higher than the previous experiment where PC was machined under same conditions without ionizer. Moreover, no Lichtenberg Figures were observed in Location B. These Lichtenberg figures were found to be located away from the cutting edge.



**Tool Wear/Surface Finish Study** Figure 29 shows the arrangement to do long tool wear tests while managing the chips so they will not interact with the finished surface and degrade the surface finish. The workpiece is a 50 mm diameter rod which are readily available in PMMA and PC but not for Zeonex. The rod is 80 mm long and coupled with the standard feed rate used in this report, each pass will be 1 Km cutting distance. The spindle rotates CCW and the tool is on the left side, so the chip will exit to the left. It is small and light enough so it is immediately pulled up into the vacuum. In a demonstration of the robustness of the system, the vacuum box is removed and the 2" dia vacuum inlet is on the ceiling about 5 feet above the workpiece. The cutting is started with the ionizer blowing from below and the ceiling vacuum pulling from the top and within a few seconds the chip finds the ceiling vacuum and stays connected through out one pass of the tool.

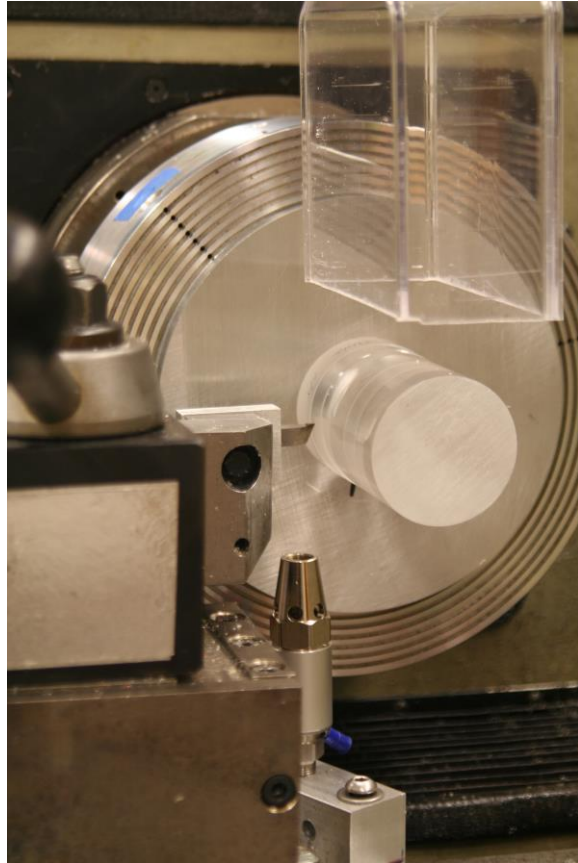


**Figure 29.** DTM setup to measure tool wear and chip management.

The plastic is mounted to an aluminum plate that is vacuumed to the DTM spindle. The diamond tool is shown and the ionizer is just below it. The box at the top is the chip vacuum which is powered with a large industrial vacuum cleaner. It does a great job capturing the chip from the cutting process.

### 3.6 CONCLUSIONS

For all the machining parameters used, PMMA was found to be having better surface finish at zero rake angle than other two materials. Tool wear in case of PC was observed to be higher than PMMA both in case of plunging and facing cuts. Chip collection and chip dimensions were found to affect surface finish of PC. A standard chip setup will be developed to address the issue of static chips sticking to the surface of PC and Zeonex and to compare all three materials.

In future experiments, the effect of cutting speed, tool radius and rake angle on the surface finish will be investigated in case of all three materials. Variation of tool wear with cutting distance will be investigated by performing long distance cuts on three materials under same cutting conditions. Optimum conditions for three materials that provides optical surface finishes minimizing tool wear will be determined.

## REFERENCES

1. A. Hof and K. Mehlkopp. *Process for manufacturing optical surfaces and shaping machine for carrying out this process*, Patent WO9713603, 1997.
2. G. P. H. Gubbels, *Diamond Turning of Glassy Polymers*, PhD thesis, Enscheda, 2006.
3. M.J.M. Renkens. *Design of an axially controlled spindle unit for high precision diamond turning*, PhD thesis, Technische Universiteit Eindhoven, Eindhoven, 1997.
4. Falter, P.J. and T.A. Dow. *A Diamond Turning Apparatus for Fabrication on Non Rotationally Symmetric Surfaces*, pages 187–201. Springer-Verlag, Berlin, 1988.
5. Shi, M., T.A.Dow., *Diamond Tool Wear Measurement by Electron-Beam-Induced Deposition*, Precision Engineering, p. 718-721, 2010.
6. Allen, William, *A High Performance Embedded Machine Tool Controller*.
7. D.A. Kobayashi, *Machining of Plastics*, Robert E.Krieger Publishing Company, Pages 50-120, 1981.
8. Shaul M. Aharoni & N. Sanjeeva Murthy, *Effects of Solvent-induced Crystallization on the Amorphous Phase of Polycarbonate of Bisphenol*, International Journal of Polymeric Materials and Polymeric Bio-Materials, Vol 42, Pages 275-283, 1998.
9. Drescher, Joseph, *Tool Force, Tool Edge, and Surface Finish Relationships in Diamond Turning*, PhD thesis, NC State University, 1991.
10. Arcona, Christopher, *Tool Force, Chip Formation and Surface Finish in Diamond Turning*, PhD thesis, NC State University, 1996.

## 4 SELECTION OF SURROGATE MATERIAL TO STUDY DRY MACHINING OF PLUTONIUM

**Noa McNutt**

Undergraduate Researcher

**Thomas Dow**

Professor

Mechanical and Aerospace Engineering

**Alyssa Edwards**

Undergraduate Researcher

**Ken Garrard**

Senior Research Scholar

Precision Engineering Center

**Anthony Wong**

Research Associate

Precision Engineering Center

*The goal of this project is to study the onset of built-up edge on a carbide tool during dry machining of plutonium ( $\delta$  - phase Ga Alloy [3]). This phenomenon degrades the surface finish as well as the figure error of the surface. Material properties were surveyed and experiments conducted to find a surrogate material that would behave in a manner similar to plutonium but without the health issues related to that radioactive material. Several materials including Oxygen Free High Conductivity (OFHC) annealed copper, 1100 aluminum and 1199 aluminum were machined with different Kennametal Carbide Tools on a high-precision lathe.*

*A series of experiments involving non-overlapping cuts were made with each of these materials and the surface geometry, cutting forces and tool pickup were measured. The results indicated that 1199 (pure) aluminum exhibits the pickup problem observed with plutonium. After choosing the 1199 aluminum, it was used in experiments involving overlapping cuts. The 1199 aluminum develops the most pickup at high cutting speed and low depth of cut. Now that a surrogate material has been identified, the next step will be to verify that changes in these parameters will influence the pickup in the same way as plutonium.*



## 4.1 INTRODUCTION

This project investigates possible techniques to machine plutonium without the use of a cutting fluid. Dry machining presents Los Alamos (LANL) with an opportunity to reduce time and costs associated with separating and disposing of radioactive cutting lubricant that is a byproduct of machining plutonium. Unfortunately, dry machining also presents a challenge: how to prevent soft materials such as plutonium from “sticking” to the tip of the tool. This sticking behavior ultimately leads to a formation on the edge of the tool called a “built-up-edge” or BUE. This BUE results in poor surface finish and figure error on the final plutonium part.

The project is to reproduce this BUE using a non-radioactive surrogate material for plutonium, while using similar tooling, feeds and speeds to those used at Los Alamos. An ideal surrogate should have similar density, hardness and “stickiness” as plutonium. Once this material is found, a series of turning experiments will investigate how to maximize tool life and surface finish while minimizing the presence of built-up-edge, all without the use of a cutting fluid.

## 4.2 DETAILS OF THE EXPERIMENTS

### 4.2.1 Sample Geometry

To investigate how different tools and materials produce a new surface, a high-precision ASG-2500 Diamond Turning Machine (DTM) was used. Each material sample was a 100 millimeter diameter disc. Once turned flat, a countersunk hole was drilled in the center of the disc. The disc was bolted to a larger aluminum disc and mounted to the ASG-2500's vacuum chuck as shown in Figure 1. The disc was centered on the vacuum chuck and the front face of each disc was turned flat again.

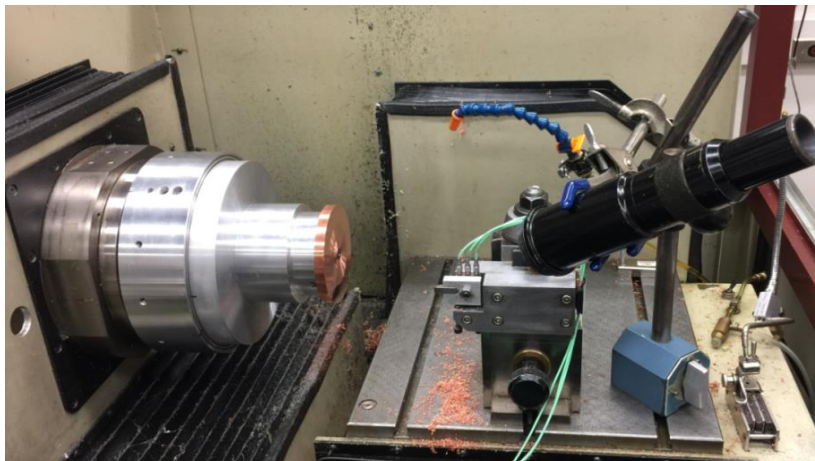


**Figure 1.** The ASG-2500 DTM Set up with a Copper Sample Disc

The tool of interest was installed onto the tool post supported by a three axis, piezoelectric KISTLER load cell to measure the cutting forces on the tool. The front face of the sample was turned from the outer diameter of 100 millimeters to an inner diameter of 40 millimeters. This means that surface speed started at 2.8 m/s at the onset of the cut at 50 millimeters radius, and finished at 1.1 m/s at the inner radius of 20 millimeters at 550 rpm. Two types of face turning operations were conducted; overlapping feedrate and non-overlapping feed rate. The overlapping feedrate (length/time) creates a smooth surface and requires a cross-feed (length/revolution) that is less than or equal to the width of one groove left by the tool. The width of a groove is dependent on tool geometry, depth of cut and spindle speed. The non-overlapping feedrate creates a surface with a spiral shaped groove. This requires a cross-feed that is greater than or equal to the width of one groove. Throughout the cutting process, the Kistler piezoelectric load cell recorded tool cutting forces.

#### 4.2.2 Tools

Two different tools were evaluated during the study. Both were Kennametal V-Series carbide inserts, similar to those used for turning plutonium at LANL. A detailed description of each tool is in Table 1. Throughout the remainder of the report, tools will be referenced by their tool number defined below in Table 1. Rake angle is described in Figure 3 and the tool shown has a positive rake angle.

**Table 1.** Geometry of Carbide Tools Used in the Study

Tool Number	Manufacturer	Model No.	Nose Radius (mm)	Rake Angle (°)	Chip Breaker (yes or no)
1	Kennametal	VBGT331HP	0.4	35	no
2	Kennametal	VBGT331LF	0.4	5	yes

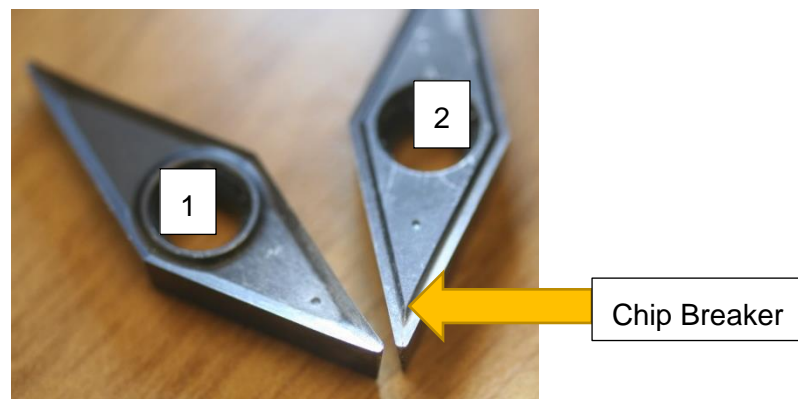


**Figure 2.** Photographs of the Two Kennametal tools. Tool 1(Left) and Tool 2 (Right). Notice the Raised Region Offset From the Tip of Tool 2. This is the Chip Breaker.

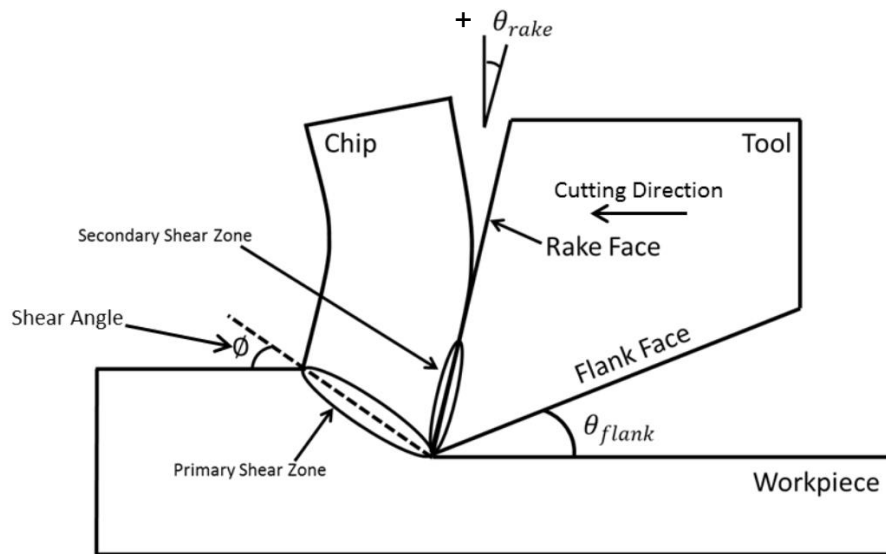


**Figure 3.** Schematic of Orthogonal Cutting, Tool with Positive Rake Angle

### 4.2.3 Speed, Feed and Depth of Cut

Table 2 describes feeds and speeds used for both overlapping and non-overlapping operations.

**Table 2.** Feeds and Speeds Used in Turning Operations in the Study

	<b>Non- Overlapping Feedrate</b>	<b>Overlapping Feedrate</b>
<b>Feedrate (mm/min)</b>	300	22
<b>Depth of Cut (μm)</b>	25	60, 80, 100
<b>Spindle Speed (rev/min)</b>	550	550

Speeds and feeds used for overlapping cuts were similar to those used at LANL. Speeds and feeds used for non-overlapping cuts were designed to have a similar uncut chip area to the overlapping cuts. Note that the tool starts at the outer radius of the disc and feeds inward. This means that the cutting speed is highest at the onset of the cut 2.8 m/s, and will decrease as the tool feeds inward, to 1.1 m/s.

### 4.2.4 Workpiece Materials

A number of different materials were considered with the goal of finding a material that displayed built-up-edge characteristics similar to  $\delta$ -phase Ga alloyed plutonium. To determine an appropriate surrogate, a series of material properties were selected as criteria. These properties should influence both mechanical and thermal performance of each potential surrogate.

**Mechanical Properties** Mechanical properties of interest were Density, Hardness, Ultimate Tensile Strength (UTS), Yield Tensile Strength (YTS) and Modulus of Elasticity. An ideal surrogate should have similar mechanical properties, ie, stress-strain curve, to those of the  $\delta$ -phase Ga alloyed plutonium. This means that it will show similar deformation to plutonium under similar loading conditions. This deformation under stress is ultimately responsible for the formation of the chip. UTS, YTS and Elastic Modulus are all material properties that describe the shape and magnitude of the stress-strain curve. The density of the material will pertain to the dynamics of the chip upon its removal from the workpiece. The hardness is an easily measurable quantity that relates to the strength of the material. All mechanical properties of potential surrogates are listed in Table 3 and each has Face Centered Cubic lattice structure. This means that they are susceptible to galling when they come into sliding contact with other metals. This could potentially cause a BUE and alter the surface finish of a surrogate sample.

**Table 3.** Mechanical Properties for Potential Surrogate Metals, Numbers adjacent to Material Names Refer to References

<b>Property</b>	<b>Plutonium (<math>\delta</math>) [1]</b>	<b>Aluminum 1100 [2]</b>	<b>Aluminum 1199 [2]</b>	<b>OFHC Copper (Full Anneal) [2]</b>	<b>Babbitt (Pb 75%) [2]</b>
<b>Density (g/cm<sup>3</sup>)</b>	19.8	2.71	2.70	8.93	10.2
<b>Hardness (HV)</b>	45	34	31	30	22
<b>UTS (MPa)</b>	130	110	115	210	72
<b>YTS (MPa)</b>	100	103	110	35	42
<b>Elastic Mod (GPa)</b>	43	68.9	62	110	24.5

As shown in Table 3, plutonium has a density approximately 2x that of Copper and Babbitt and 5x higher than Aluminum. Aluminum is similar to plutonium metal in hardness, UTS, YTS and Modulus of Elasticity. The stress/strain curve in Figure 4 compares the response of the metals and indicates the similarity between Pu and Al.



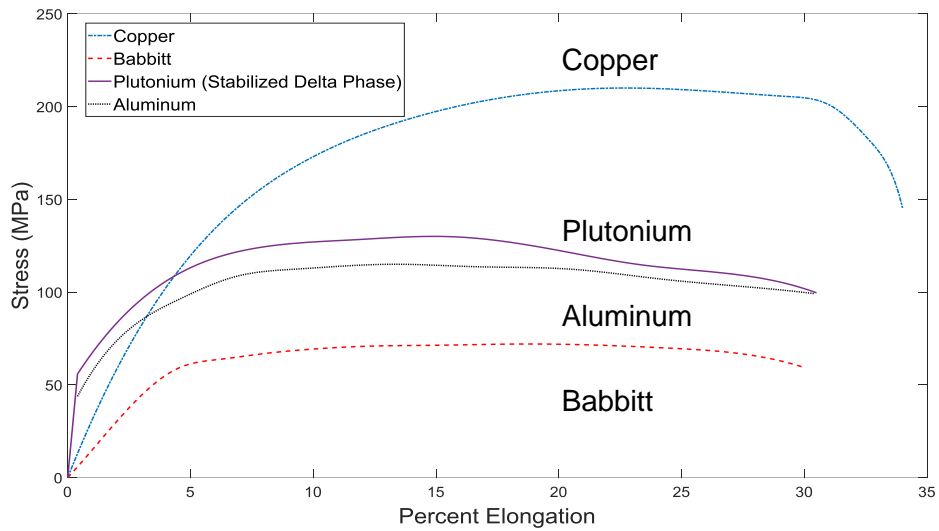


**Figure 4.** Stress-Strain Diagrams of Potential Surrogate Metals [1, 2, 3]

**Thermal Properties** An important material property related to BUE is Thermal Diffusivity which is thermal conductivity/(density x specific heat). Thermal diffusivity describes how quickly a material can move heat from a warmer point to a cooler point. Low thermal diffusivity would result in higher local tool temperature during cutting. This is desirable since the thermal diffusivity of the plutonium metal ( $4 * 10^{-6} \text{ m}^2/\text{s}$ ) is very low. Thermal properties of each material are displayed in Table 4. Al is most similar to Pu with regards to Thermal Diffusivity.

**Table 4.** Thermal Properties of Potential Surrogate Metals, Numbers adjacent to Material Names Refer to References

Property	Plutonium ( $\delta$ ) [1]	Aluminum 1100 [2]	Aluminum 1199 [2]	OFHC Copper (Full Anneal) [2]	Babbitt (Pb 75%) [2]
Thermal Conductivity (KW/mK), K	0.0084	0.22	0.24	0.398	0.024
Specific Heat (Kj/Kgk), c	0.13	0.904	0.9	0.385	0.163
Thermal Diffusivity ( $\text{m}^2/\text{s}$ ), $\alpha$	4e-6	8.98E-05	9.9e-5	1.1e-4	1.4e-4

All properties relating to plutonium were obtained from OJ Wick's Plutonium handbook [1]. Properties for all other materials were obtained from the metals handbook via <http://matweb.com> [2]. To determine which of the four potential surrogates will perform closest to plutonium metal in a machining environment, a scoring system was utilized. The Machining Surrogate Score (MSS) is a combination of four material properties: Density, Thermal Conductivity, Specific Heat and Yield Tensile Strength (YTS). This means that the score will account for density of the chip, heat generated, heat transfer during cutting and the shape of the stress strain curve of each material.

The MSS is calculated by multiplying the normalized differences in the values of YTS and Thermal diffusivity between a potential surrogate and the plutonium. The MSS is defined in Equation 1. Note that density, specific heat and thermal conductivity are included within thermal diffusivity.

$$MSS_X = \left( \frac{YTS_{PU} - YTS_X}{YTS_{PU}} \right) \times \left( \frac{TD_{PU} - TD_X}{TD_{PU}} \right) \quad (1)$$

The subscript in Equation 1 indicates the material; Pu is plutonium and X is the material of interest. Figure 5 shows the results of the MSS calculations for all four materials of interest. A perfect score for a surrogate is zero because it would exactly match the properties of Pu. The lower score, the better a surrogate material matches the properties of the  $\delta$ -phase Ga alloyed Pu.

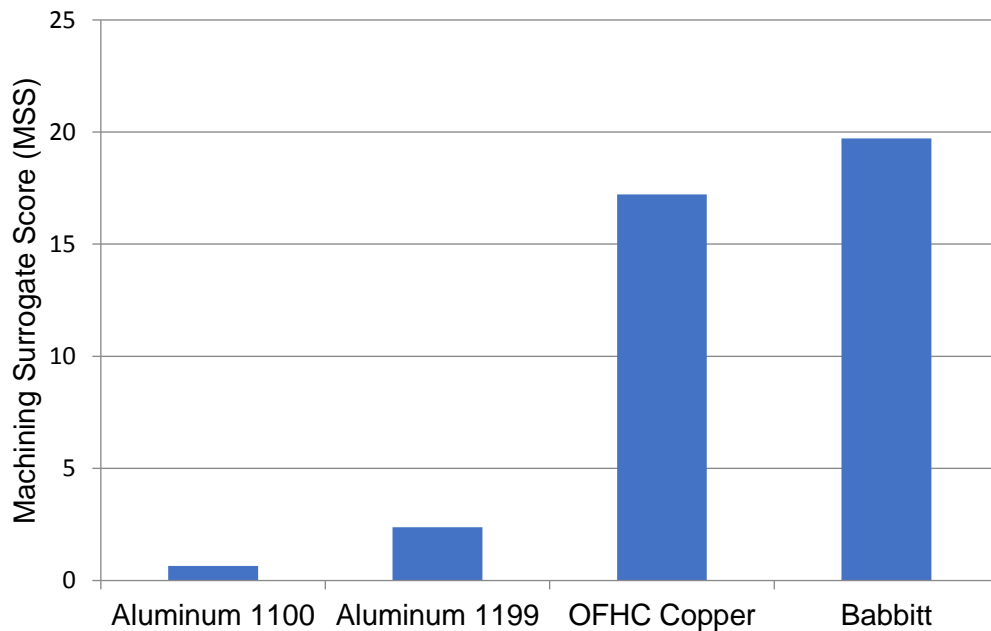


**Figure 5.** MSS of All Four Potential Surrogate Metals. A Smaller Value Suggests the Material is a Better Surrogate for Pu which has a Value of Zero.

As shown in Figure 5, aluminum 1199 and aluminum 1100 have much lower MSS scores than Babbitt or copper. This would indicate that the two aluminum alloys would be better surrogates

than Babbitt or copper. Due to the potential for harm from the handling of lead, Babbitt was only machined briefly. It did produce a continuous chip and good surface finish. OFHC copper, aluminum 1199 and aluminum 1100 were chosen to study on the DTM.

### 4.2.5 Machining Experiments

**Cutting Force Measurements** A three-axis Kistler piezoelectric load cell was used to capture machining forces. As the part was cut, the load cell sent a voltage signal to a data acquisition system, where it was multiplied by a predetermined gain. This gain is calibrated by hanging a known weight from the tip of the tool, and dividing that known weight by the voltage sent by the piezo. Cutting forces push down on the cutting edge of the tool. Increases in cutting forces can indicate the presence of a built up edge on the cutting edge of the tool. An example of a cutting force plot can be seen in Figure 6. Cutting forces were only recorded for non-overlapping experiments.

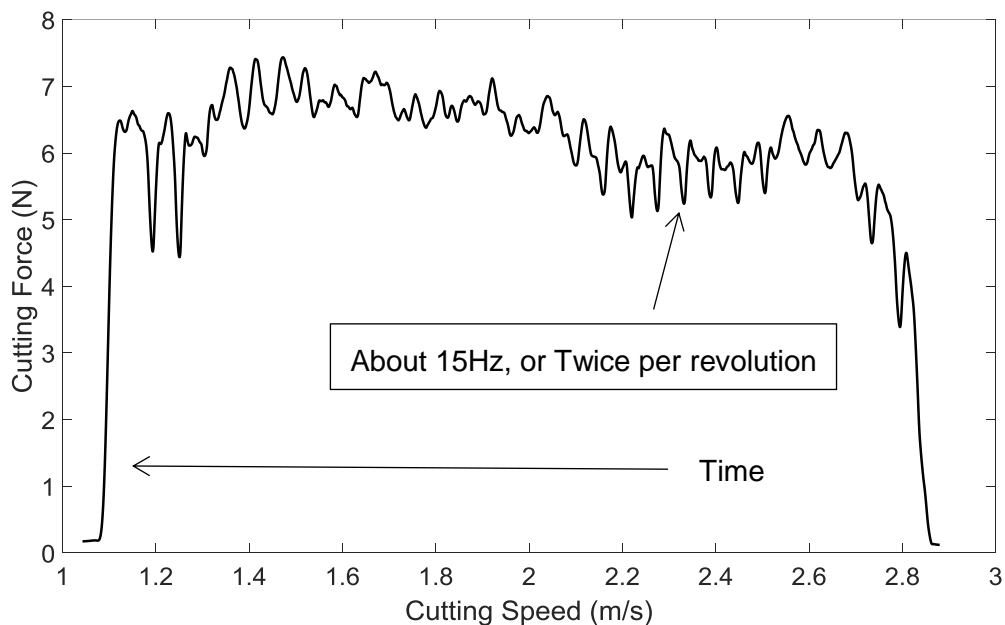


**Figure 6.** Cutting Forces Measured during a Non-Overlapping Pass on 1199 Alum using Tool 1. Conditions: Crossfeed = 545  $\mu\text{m}/\text{revolution}$ , Spindle RPM = 550, Depth = 25  $\mu\text{m}$ .

**Talysurf Profilometer Measurements** After turning with an overlapping feedrate, a Talysurf stylus profilometer was used to measure surface roughness. The profilometer has a 10 nanometer vertical resolution. As shown in Figure 7, a stylus profilometer can make a 2 dimensional trace of

the surface of a machined part cut with an overlapping feed rate, which can be compared to a theoretical surface.

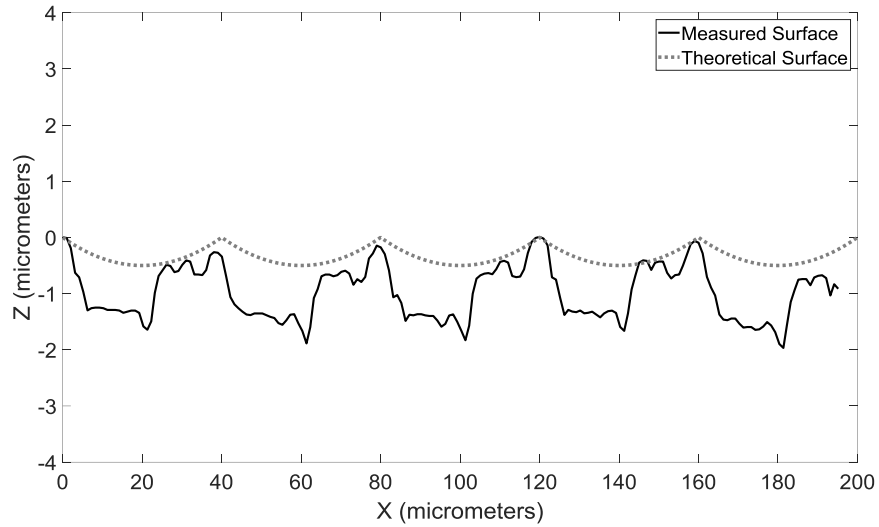


**Figure 7.** A Surface Profile Created with an Overlapping Feed Rate of  $40\ \mu\text{m}/\text{rev}$ , spindle rpm = 550, Depth =  $80\ \mu\text{m}$ .

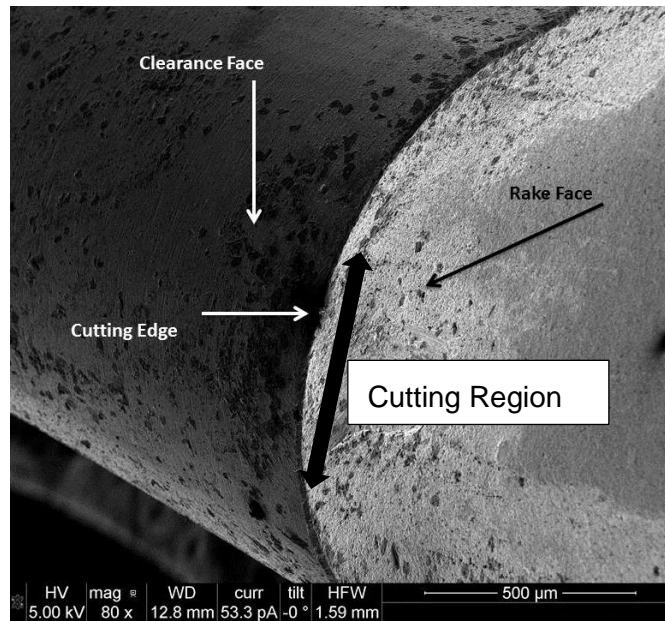


**Figure 8.** SEM at Low-Magnification (80x) Showing the Imperfections in the Cutting Edge of the Tool.

The overlay of theoretical and measured surface features in Figure 7 shows that the tool is not a perfect circle on a  $\mu\text{m}$  scale. There are features on the cutting edge that are machined into the

workpiece and are very repeatable for each pass of the tool. Figure 8 shows the edge of the tool as measured in an SEM at a low magnification of 80x in order to see a large portion of the edge. The width of the chip for these cutting conditions would be 450  $\mu\text{m}$ .

**Built-Up-Edge Measurement** After performing a turning operation using a non-overlapping feedrate, the Talysurf stylus profilometer was used to measure the groove geometry and compare that groove to the shape of a theoretical groove from the published tool radius. An increase in groove area could be observed if a strain hardened built up edge is generated during the cut. Figures 9 and 10 show this for a different tool and workpiece. The parabolic lines signify the published shape of the tool. The shaded area signifies area that is present in the groove that is not the shape of the tool. This means that a strain hardened built up edge is likely present on the edge of the tool, since strain hardened BUE can become the effective cutting edge [6]. Figure 9 below shows an example where no significant built up edge is present, notice the small size of the shaded area. Figure 10 shows an example where strain hardened built up edge was present. Notice the large difference between the theoretical tool shape and the shape that the tool produced.

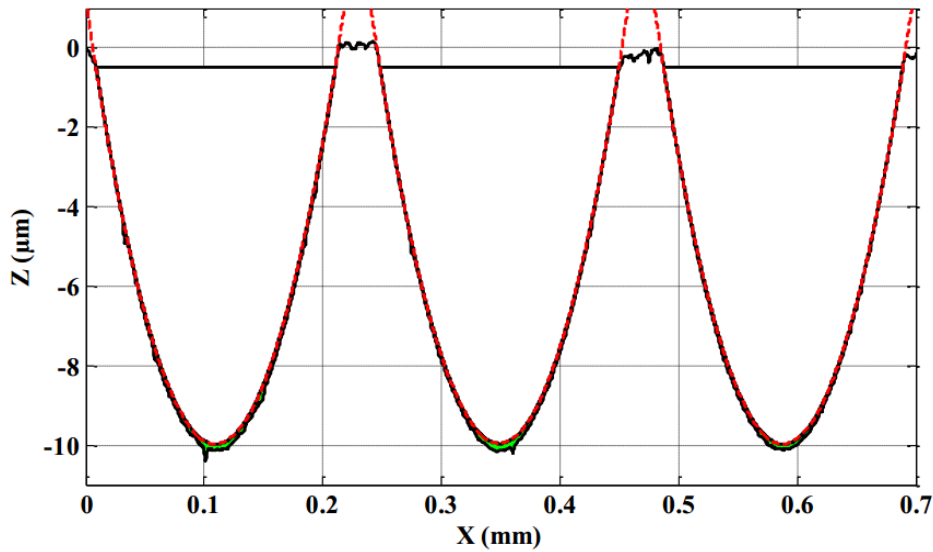


**Figure 9.** An Example of Three Grooves Not Displaying Evidence of Strain Hardened Built Up Edge, 6061 Aluminum Cut with A Diamond (0.5 mm edge radius) [5].

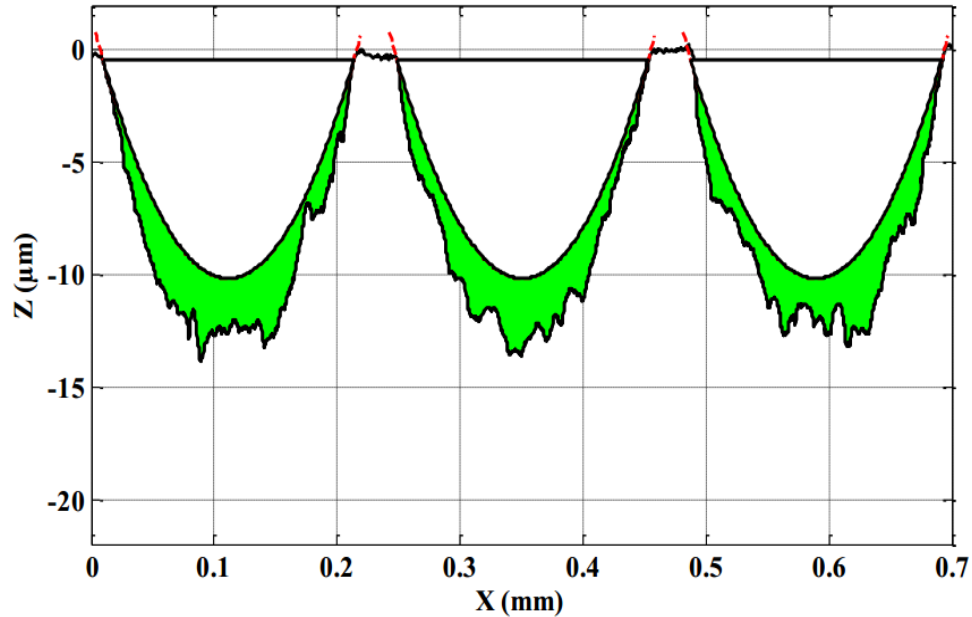


**Figure 10.** An Example of Three Grooves Displaying Evidence of A Strain Hardened Built Up Edge, 1045 Steel Cut with a Diamond (0.5 mm edge radius) [5].

It is important to remember that Figure 10 is a product of diamond turning of steel in previous experiments at the PEC. Due to the relatively pure nature of the metals in this study, strain hardening might not occur. Figures 9 and 10 are included purely to introduce the method of detecting built up edge.

**Galling** requires two properties common to most metals - cohesion through metallic-bonding attractions and plasticity (the ability to deform without breaking). The tendency of a material to gall is affected by the ductility of the material. Typically, hardened materials are more resistant to galling whereas softer materials of the same type will gall more readily. The propensity of a material to gall is also affected by the specific arrangement of the atoms, because crystals arranged in a face-centered cubic (FCC) lattice will usually allow material-transfer to a greater degree than a body-centered cubic (BCC). This is because a face-centered cubic has a greater tendency to produce dislocations in the crystal lattice, which are defects that allow the lattice to shift, or "cross-slip," making the metal more prone to galling. However, if the metal has a high number of stacking faults (a difference in stacking sequence between atomic planes) it will be less apt to cross-slip at the dislocations. Therefore, a material's resistance to galling is usually determined by its stacking-fault energy. A material with high stacking-fault energy, such as aluminum or titanium, will be far more susceptible to galling than materials with low stacking-fault energy, like copper, bronze, or gold. Conversely, materials with a hexagonal close packed (HCP) structure, such as cobalt-based alloys, are extremely resistant to galling.

Galling occurs initially with material transfer from individual microscopic grains, on a microscopic scale, which become stuck or even diffusion welded to the adjacent surface. This transfer can be enhanced if one or both metals form a thin layer of hard oxides with high coefficients of friction, such as those found on aluminum or stainless-steel. As the lump grows it pushes against the adjacent material and begins forcing them apart, concentrating a majority of the friction heat-energy into a very small area. This in turn causes more adhesion and material build-up. The localized heat increases the plasticity of the galled surface, deforming the metal, until the lump breaks through the surface and begins plowing up large amounts of material from the galled surface. Methods of preventing galling include the use of lubricants like grease and oil, low-friction coatings and thin-film deposits like molybdenum disulfide or titanium nitride, and increasing the surface hardness of the metals using processes such as case hardening and induction hardening [7].

Galling between a surrogate material and the carbide tools could be a potential cause for BUE in these experiments. OFHC copper, 1100 aluminum, 1199 aluminum and plutonium are all ductile, FCC materials, susceptible to galling issues.

**Scanning Electron Microscope Imaging** While profilometer measurements and force measurements can correlate with the presence of a built up edge, the only way to definitively determine the presence of a built up edge is to visually observe it. To achieve high magnification and clarity in images of the tools, an FEI Quanta Dual Beam electron microscope was used to image each tool directly after turning a part. Figure 8 displays an example of an image of a tool captured with the Quanta electron microscope. Layers of the surrogate metal will be present on the rake face of the tool if BUE is present.

**High Magnification Imaging** While a part was being turned, a high magnification (100x) video camera was used to record the interaction between the tool and the part. This provides real time evidence of the presence of BUE on the tool. Figures 11 and 12 are schematics of the tool removing a chip from the workpiece. Figures 13 and 14 are screenshots from a video of the same process. Figure 13 shows a snap shot of the tool removing a chip from the part without BUE, with continuous chip formation on the left, and cyclic chip formation on the right. Figure 14 shows a snap shot of a tool removing a chip from the part with BUE, without any smooth chip formation.



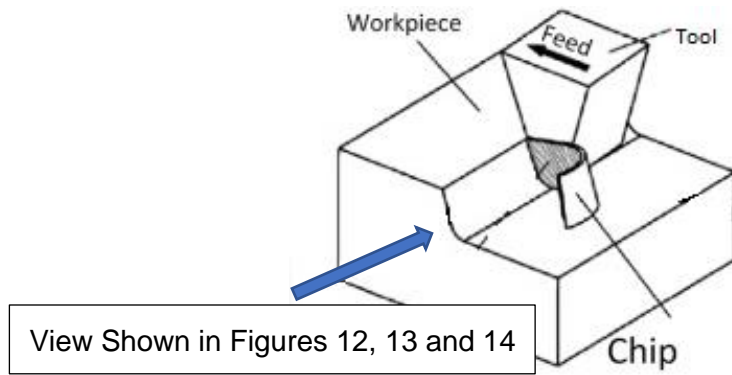


**Figure 11.** Schematic of Tool Removing a Chip from the Workpiece [4]

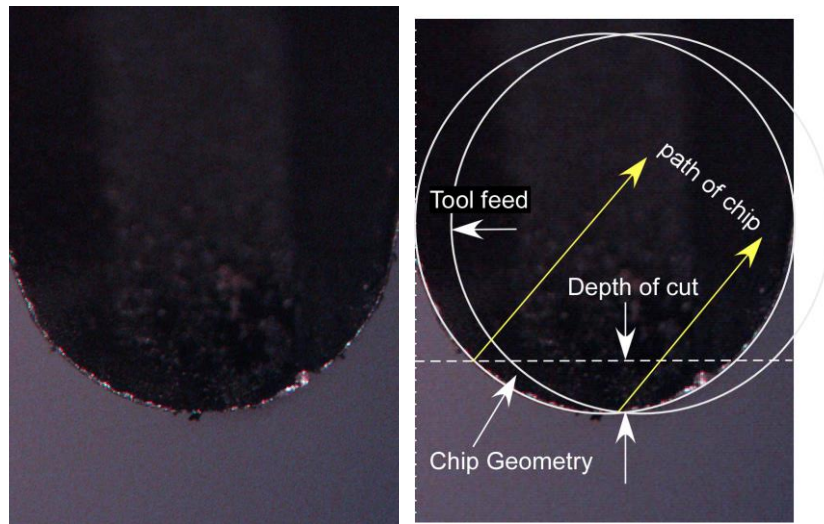


**Figure 12:** Image of the Kennametal tool (Left) with sketch of chip motion (Right)

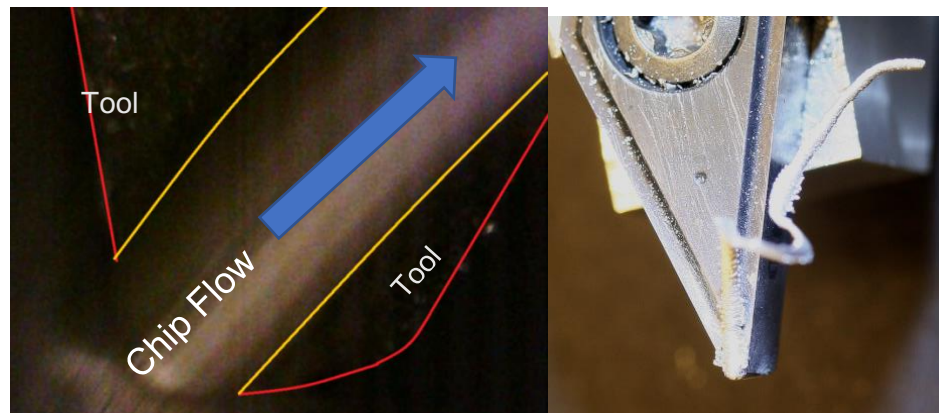


**Figure 13.** Tip of the Tool Removing a Long, Continuous Chip from the Part, with no BUE (Left), a Long Chip Stuck to the Tip of the Tool (Right), This shows the Cyclic Occurrence of the BUE

Notice the straight, smooth region streaking across the center of Figure 13 (left). This is a smooth, continuous chip. This type of chip is indicative that no built up edge is present, and the tool is functioning as desired. While, the image on the right is not the same phenomenon that is shown on the left, it is a good representation of what it might look like if the tool could be removed in the middle of the cut and photographed. Figure 13 (Right), shows an example of cyclic chip formation, Figure 13 (Left) shows an example of continuous chip formation.

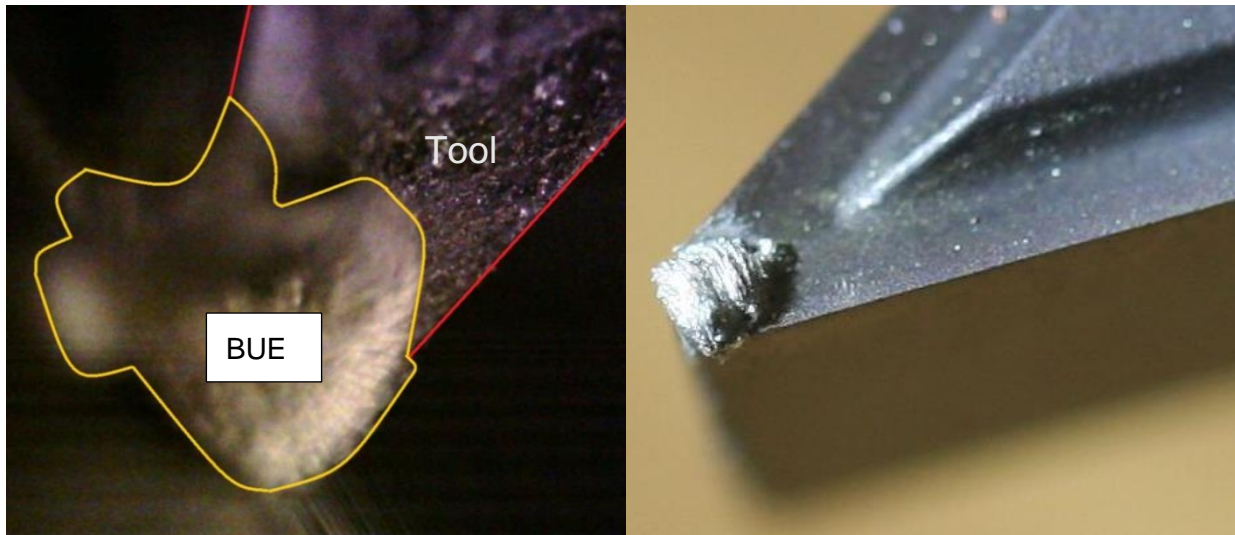


**Figure 14.** BUE at the Tip of the Tool, the Mass on the Tool Edge is BUE (Left), Low Magnification Photograph of the Same Phenomenon Taken After Turning (Right).

The mass on the tip of the tool displayed in Figure 14 is a built up edge. This indicates that the workpiece material is sticking to the tool due to galling and could potentially harm the surface finish of the final part. Figure 14 is an example of no chip formation occurring.

#### 4.2.6 Results

OFHC copper, 1100 aluminum and 1199 aluminum were tested using a non-overlapping feed rate. This allows any strain hardened BUE to be detected using a stylus profilometer as described in Figures 9 and 10.

## OFHC Copper, Non-Overlapping Feedrate

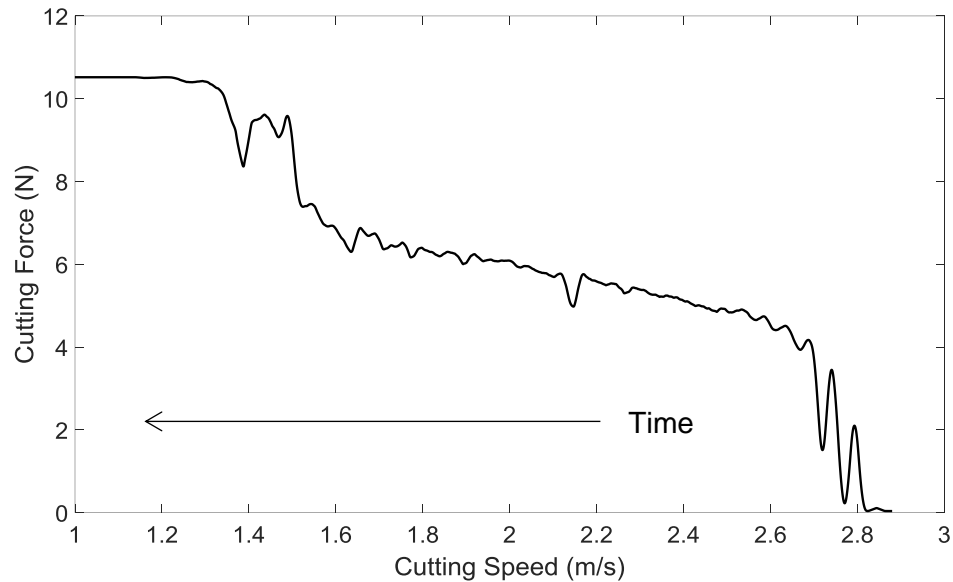


**Figure 15.** Cutting Forces Measured during a Non-Overlapping Pass on OFHC Copper using Tool 1. Using a Feedrate of 300 mm/min Turned at 550 rpm at a Depth of Cut of 25  $\mu\text{m}$ .

Figure 15 shows that cutting force was lower at higher cutting speeds on OFHC copper. This is likely due to the change of material properties as the cutting temperature increased with the cutting speed. Note that the variation in speed is due to the decreasing radius as the tool feeds from the outside of the part to the inside. At low speeds, the load cell saturated at about 10.5 N, causing the forces to appear constant.

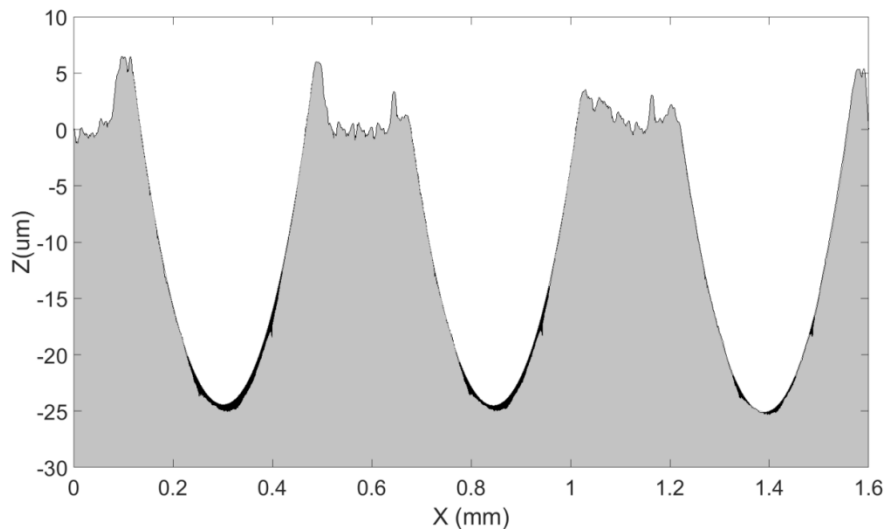


**Figure 16.** Three Grooves in OFHC Copper Turned with Tool 1. Feedrate of 300 mm/min Turned at 550 rpm at a Depth of Cut of 25  $\mu\text{m}$

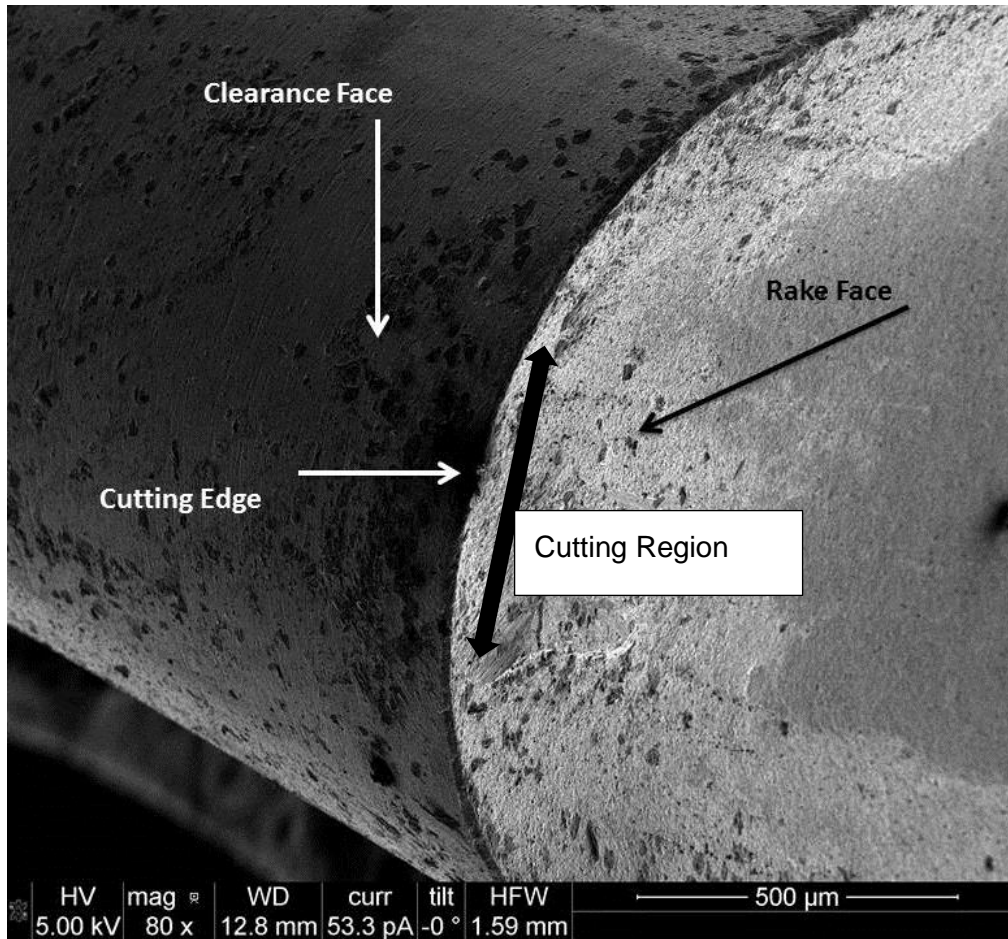


**Figure 17.** SEM Image of Tool 1 After Turning a Non-Overlapping Groove on OFHC Copper. Using a Feedrate of 300 mm/min Turned at 550 rpm at a Depth of Cut of 25  $\mu\text{m}$ .

Figure 16 shows the same method of measuring BUE as shown in Figures 9 and 10. The light shaded region represents the copper work piece. The dark shaded region is the area that cannot be accounted for by the theoretical shape of the round tool. The depth of cut can be seen as the depth of the three grooves, about 25  $\mu\text{m}$ . Some features are present above the 0 on the z axis. These could be a result of plastic deformation called plowing. This is when material is pushed out and up from the groove to the surface, rather than removed entirely. Similar to Figure 9, the small magnitude of the dark shaded region signifies that little strain hardened BUE is present. Due to the repeatability of the shape of the shaded area, it is likely that small tool defects are the cause rather than BUE. Figure 17 shows little evidence of significant BUE on the cutting edge of the tool. If BUE was present, layers of copper would be apparent on the rake face adjacent to the cutting edge.

## 1100 Aluminum, Non-Overlapping Feedrate

Using a feedrate of 300 mm/min, an 1100 aluminum disc was turned at 550 rpm at a depth of cut of 25  $\mu\text{m}$ .

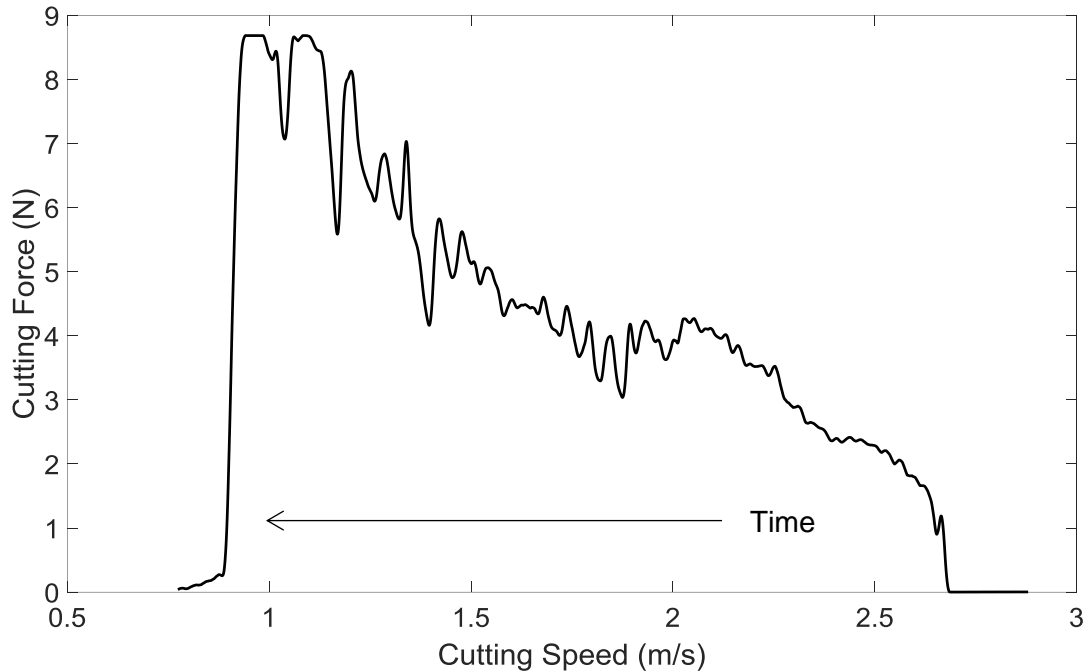


**Figure 18.** Cutting Forces Measured during a Non-Overlapping Pass on 1100 Aluminum using Tool 1, Using a Feedrate of 300 mm/min Turned at 550 rpm at a Depth of Cut of 25  $\mu\text{m}$ .

Similar to OFHC copper, the forces in Figure 18 measured when cutting 1100 aluminum increase as the cutting velocity slows. This is likely a result of changing material properties due to high temperatures at the tool-workpiece interface. The magnitude of the force is lower than that of copper; this is expected since 1100 aluminum has lower yield strength. Note that the variation in speed is due to the decreasing radius as the tool feeds from the outside of the part to the inside; therefore, cutting speed is highest at the onset of the cut.

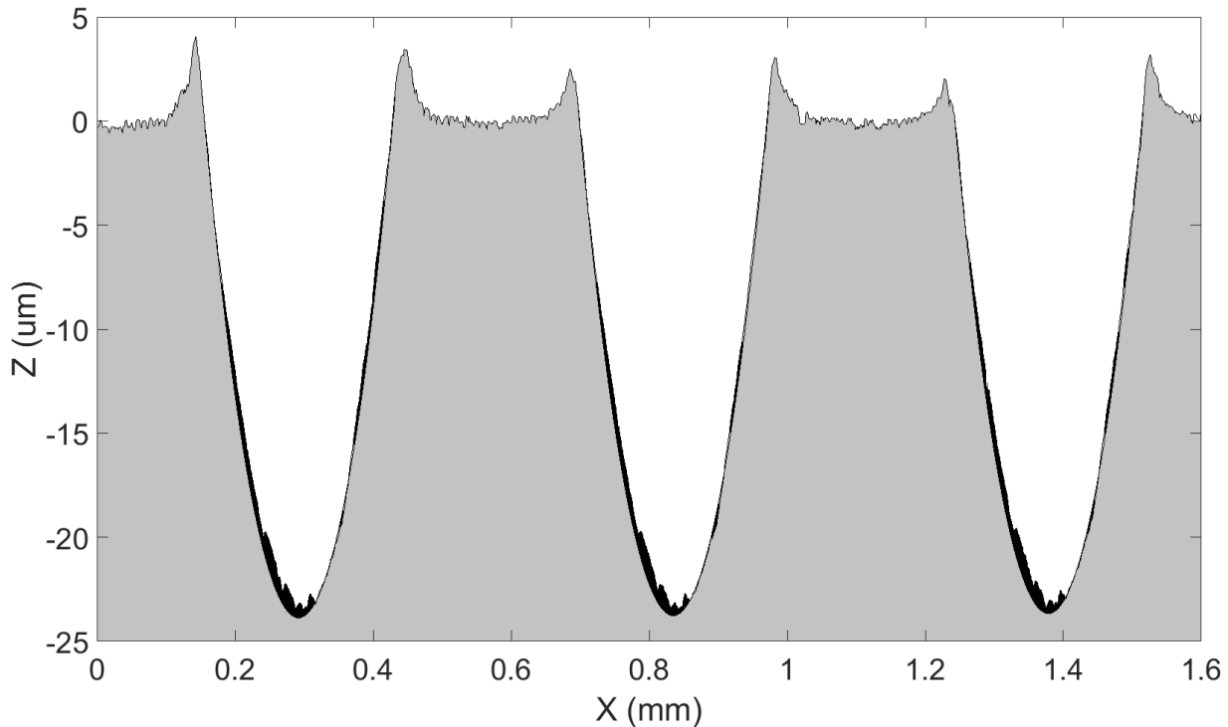


**Figure 19.** Three Grooves in 1100 Aluminum Turned with Tool 1, Using a Feedrate of 300 mm/min Turned at 550 rpm at a Depth of Cut of 25  $\mu\text{m}$

Figure 19 shows the same method of measuring BUE as shown in Figures 9 and 10. The light shaded region represents the 1100 aluminum work piece. The dark shaded region is area that differs between the shape of the theoretically round tool, and the measured grooves. The depth of cut can be seen as the depth of the three grooves, about 25  $\mu\text{m}$ . Some features are present above the 0 on the z axis. These could be a result of plastic deformation called plowing. Similar to Figures 9 and 16, the small magnitude of the dark shaded region signifies that no strain hardened BUE is present.

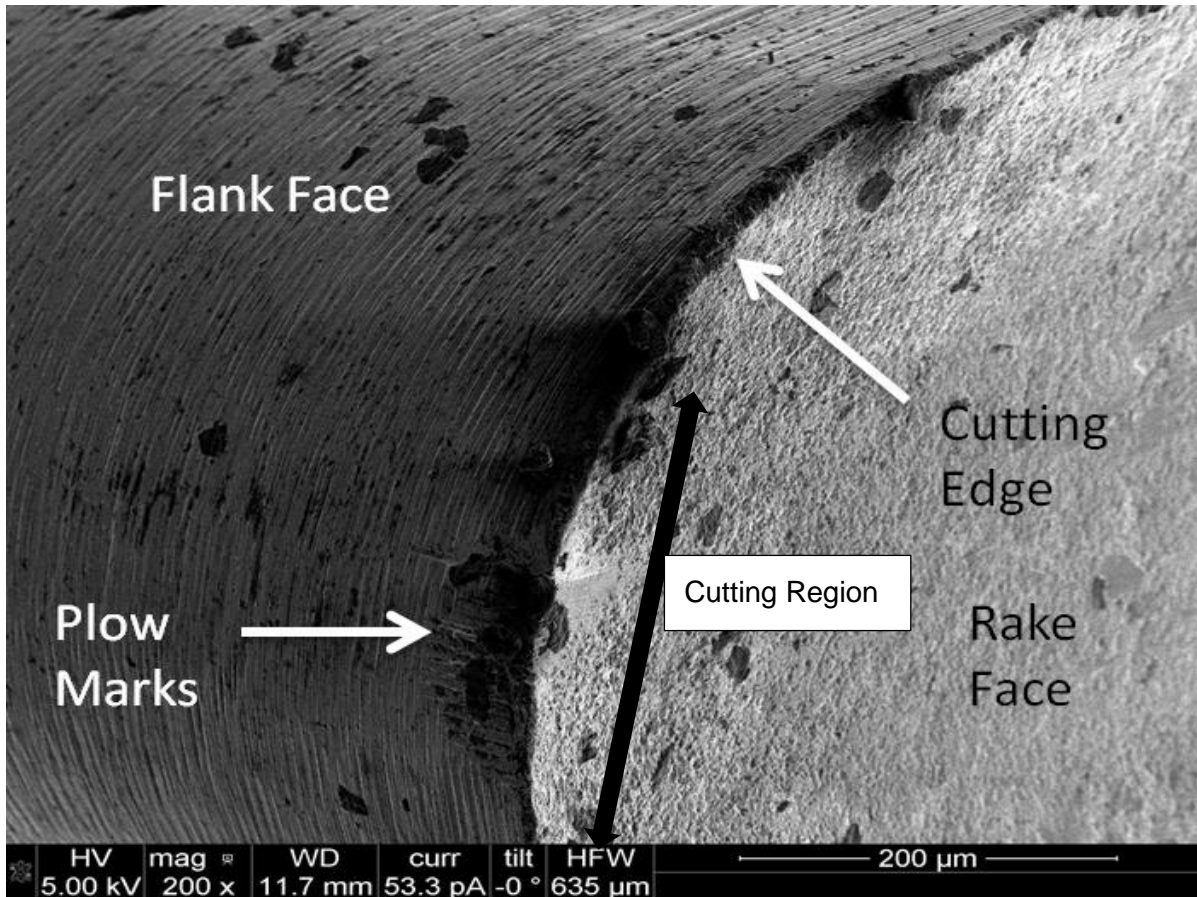


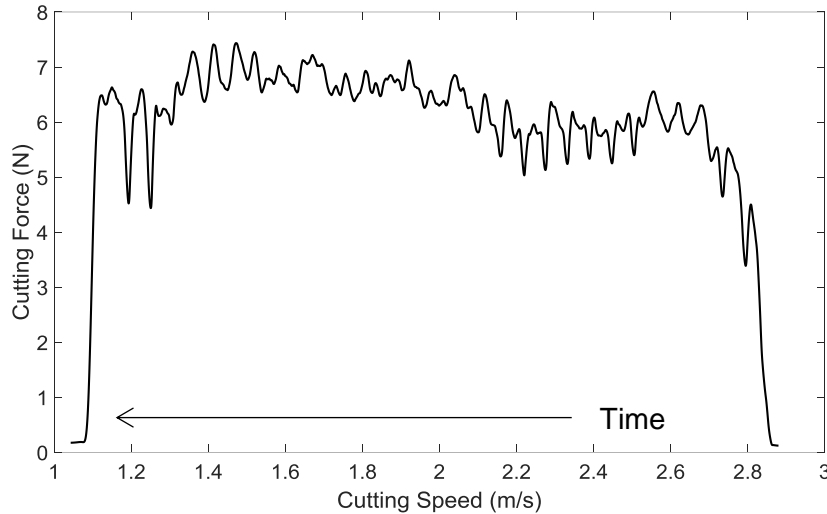
**Figure 20.** SEM Image of Tool 1 After Turning a Non-Overlapping Groove on 1100 Aluminum, Using a Feedrate of 300 mm/min Turned at 550 rpm at a Depth of Cut of 25 μm

Small plow marks are present on the SEM image of the tool. The small plow marks on the cutting edge can be seen on the Talysurf trace at the bottom of each groove. Due to lack of large features on the rake face of the tool and large dark area on Figure 19, it can be concluded that little to no BUE occurred during the cutting of 1100 aluminum.



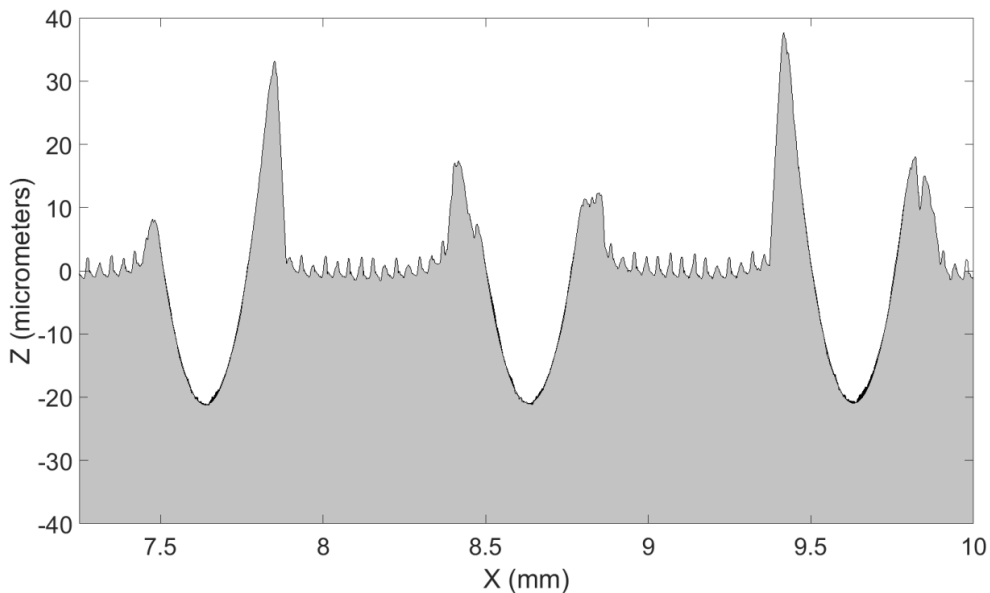
## 1199 Aluminum, Non-Overlapping Feedrate

Using a feedrate of 300 mm/min, an 1199 aluminum disc was turned at 550 rpm at a depth of cut of 25  $\mu\text{m}$ .



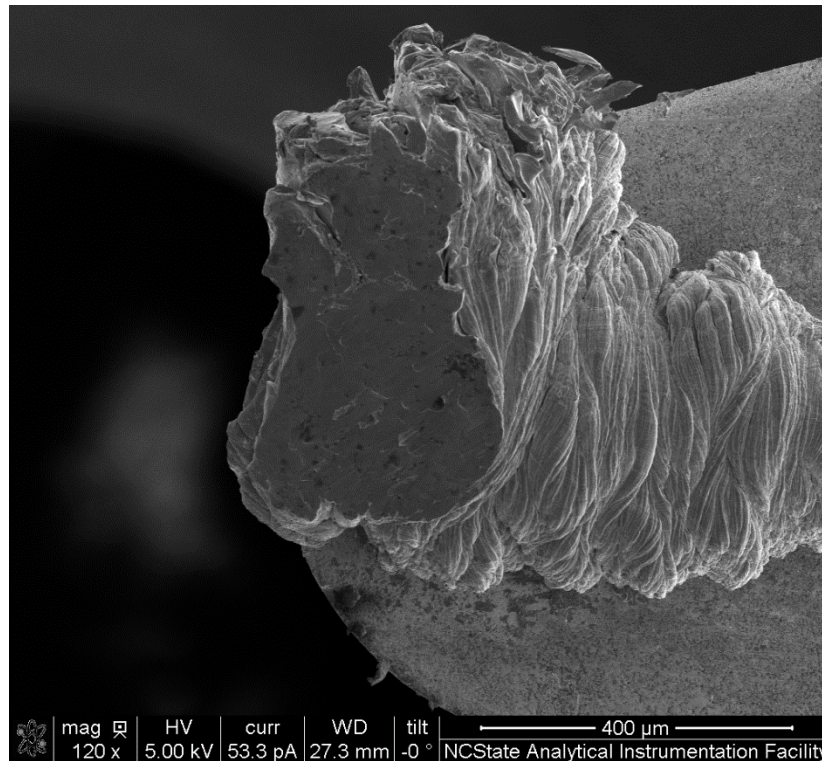
**Figure 21.** Cutting Forces Measured during a Non-Overlapping Pass on 1199 Aluminum using Tool 1, Using a Feedrate of 300 mm/min Turned at 550 rpm at a Depth of Cut of 25  $\mu\text{m}$

Figure 21 shows that unlike OFHC copper or 1100 aluminum, cutting force does not seem to be a strong function of cutting speed. Forces of about 6 to 7 Newtons were recorded. It is possible that the presence of a built up edge is the cause for the lack of a downward on the force graph.



**Figure 22.** Three Grooves in 1199 Aluminum Turned with Tool 1, Using a Feedrate of 300 mm/min Turned at 550 rpm at a Depth of Cut of 25  $\mu\text{m}$

Figure 22 shows the same method of measuring BUE as shown in Figures 9 and 10. The light shaded region represents the 1199 aluminum work piece. The dark shaded region is area that differs between the shape of the theoretically round tool, and the measured grooves. The depth of cut can be seen as the depth of the three grooves, about 25  $\mu\text{m}$ . Some features are present above the 0 on the z axis. These could be a result of either plastic deformation called plowing. Similar to Figure 9, the small magnitude of the dark shaded region signifies that little strain hardened BUE is present.



**Figure 23.** SEM Image of Tool 1 After Turning a Non-Overlapping Groove on 1199 Aluminum, Using a Feedrate of 300 mm/min Turned at 550 rpm at a Depth of Cut of 25  $\mu\text{m}$

Figure 23 shows a low magnification (120x) SEM image of tool 1 after turning 1199 aluminum. A large non strain hardened built up edge is present on top of the rake face of the tool. On the left side of the BUE, a large flat plane is present. This plane and the others below it are parallel to the rake face of the tool. This is in contrast with the planes of the ripples in Figure 14, where the planes are parallel with the flank face of the tool. This could be due to fact that no continuous chip formation occurred on Figure 14, and cyclic continuous chip formation occurred in Figure 23.

## 1199 Aluminum, Overlapping Feedrate

After strong evidence of a large built up edge was detected in the scanning electron microscope image above in Figure 23, it was determined that further experiments should be conducted with 1199 aluminum. To determine if the presence of non-strain hardened built up edge affects surface finish and if it can be prevented, a series of turning operations with overlapping feed rates were conducted.

### Effects of Tool Geometry

First, two samples of 1199 aluminum were cut at 80  $\mu\text{m}$  depth, 22 mm/min feed rate. The first cut used tool 1, which has a +35 degree rake angle and no chip breaker. The second cut used tool 2, which has a +5 degree rake angle and chip breaker. Both are KC5010 grade tools with a 0.4mm nose radius. This means that in theory, both should produce the same surface finish.

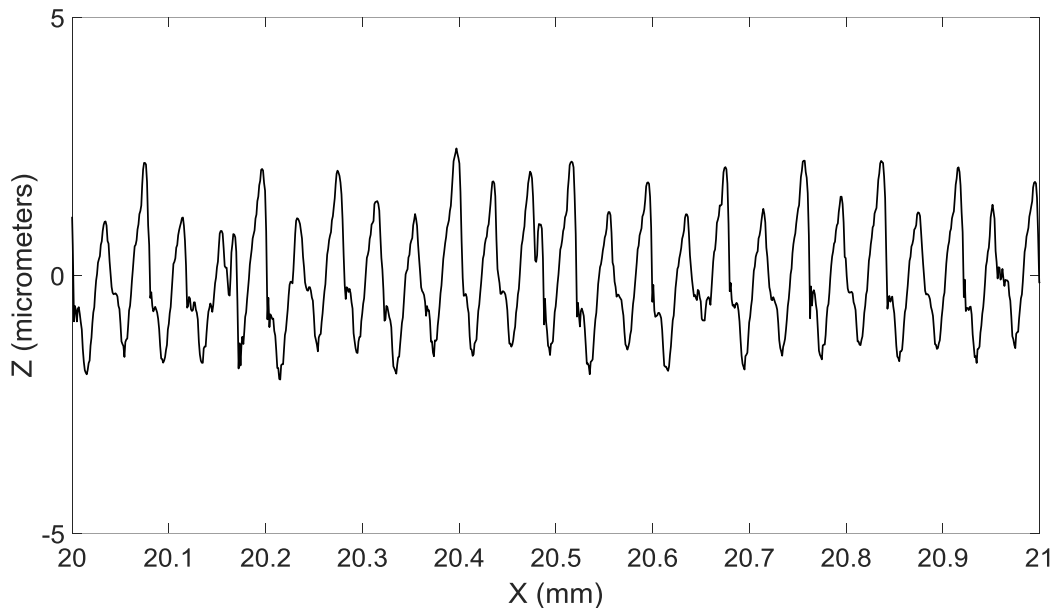


**Figure 24.** Surface Profile of an Overlapping Pass in 1199 Aluminum Turned by Tool 1, Using a Feedrate of 22 mm/min Turned at 550 rpm at a Depth of Cut of 80  $\mu\text{m}$

Notice that the features on the surface in Figure 24 are sharp, consistent and about 4  $\mu\text{m}$  in peak to valley distance. The frequency of the features occurs at 40  $\mu\text{m}$ , which is the same as the cross feed of the tool. The theoretical surface finish of this cut is 0.26  $\mu\text{m}$  RMS. The RMS surface finish of this cut was measured to be 1.14  $\mu\text{m}$ , about 4x rougher than theoretical. While the finish is not close to theoretical, it is likely that this discrepancy is due to imperfect tooling rather than BUE. Features caused by BUE would lack uniformity and regularity, and would likely not occur at the predicted frequency of 40  $\mu\text{m}$ . No BUE was observed visually on the tool.

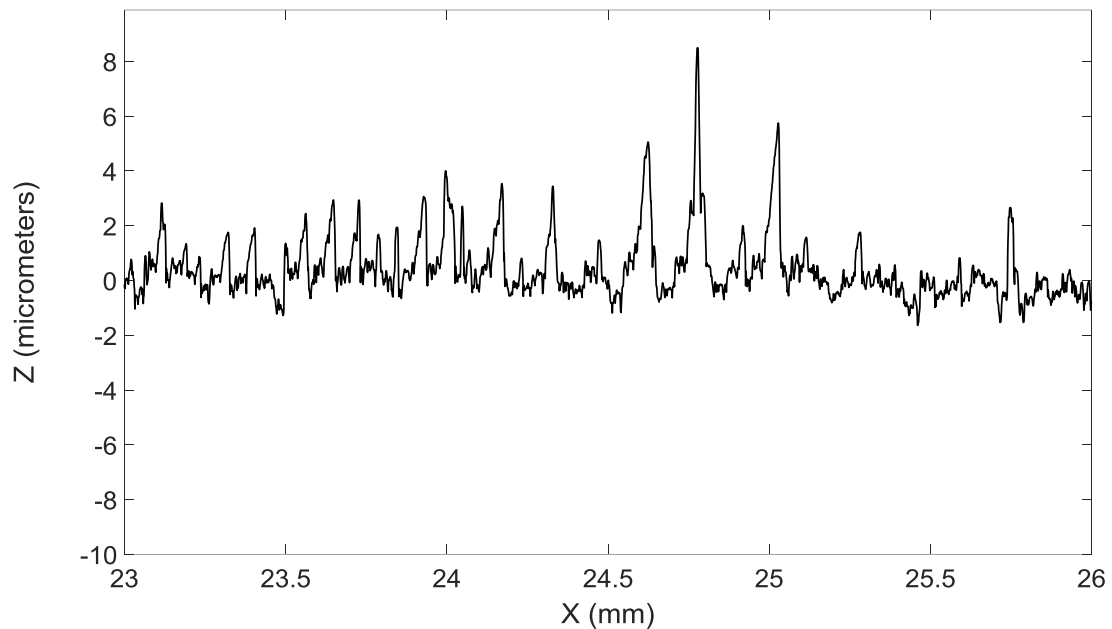


**Figure 25.** Surface Profile of an Overlapping Pass in 1199 Aluminum Turned by Tool 2, Using a Feedrate of 22 mm/min Turned at 550 rpm at a Depth of Cut of 80  $\mu\text{m}$

This surface in Figure 25 has features that are irregular, and reach up to 8  $\mu\text{m}$  above the surface. No consistent wavelength can be observed in these larger features. This is potentially evident of non-strain hardened built up edge on the tool.



**Figure 26.** Photograph of Tool 2 after Turning an Overlapping Cut on 1199 Aluminum, Using a Feedrate of 22 mm/min Turned at 550 rpm at a Depth of Cut of 80  $\mu\text{m}$

Figure 26 above is a photo of the tip of the tool after an overlapping pass on 1199 aluminum. A ball of aluminum on the tip of the tool is the prominent feature. It was measured to be about 300  $\mu\text{m}$  above the surface of the carbide tool. This BUE is likely the cause for the irregular features present on Figure 25.

Despite the evident presence of BUE on Tool 2 during the overlapping pass, it did not perform significantly worse than Tool 1 by RMS surface roughness metrics.

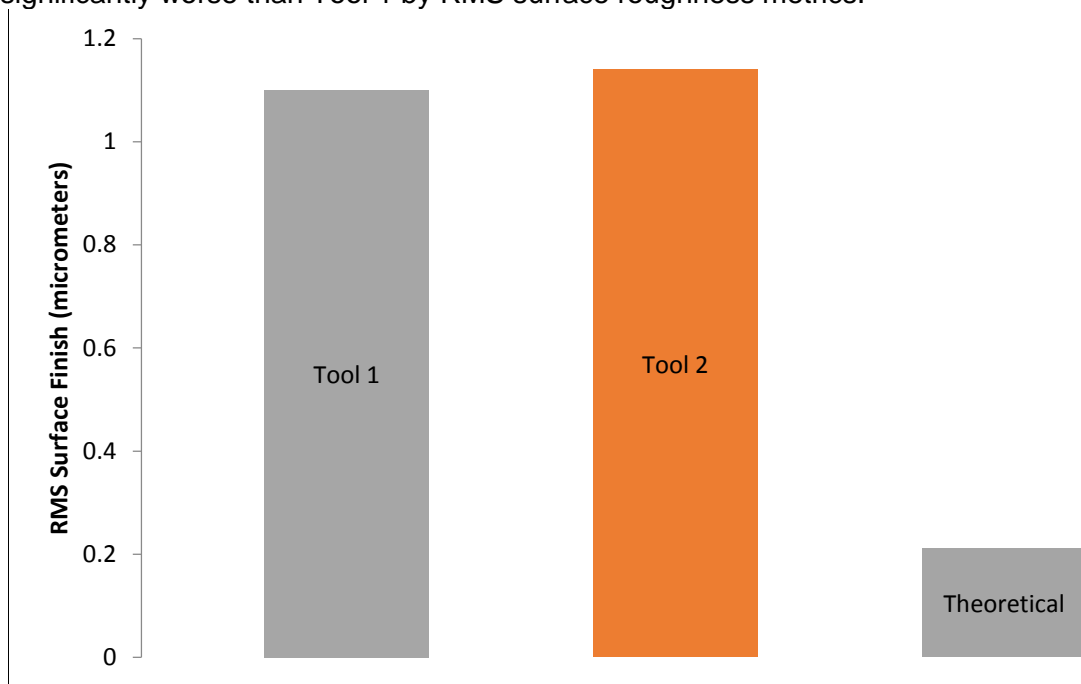
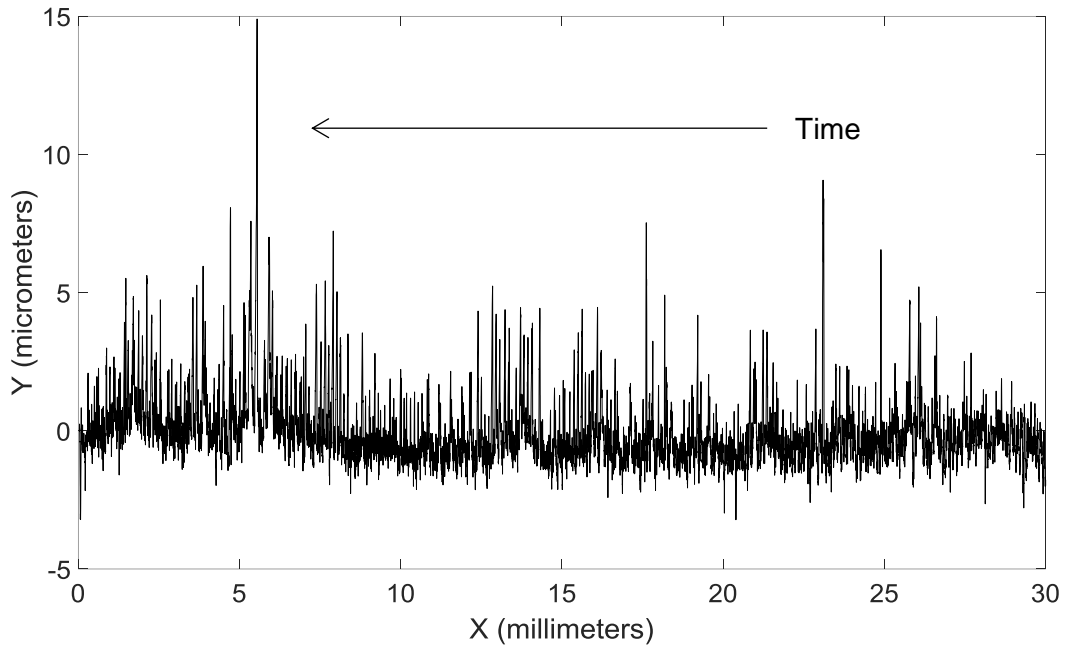


**Figure 27.** Graph of RMS Finish Created by Both Tools on 1199 Aluminum at 80  $\mu\text{m}$  Depth of Cut, Overlapping Cut, Using a Feedrate of 22 mm/min turned at 550 rpm

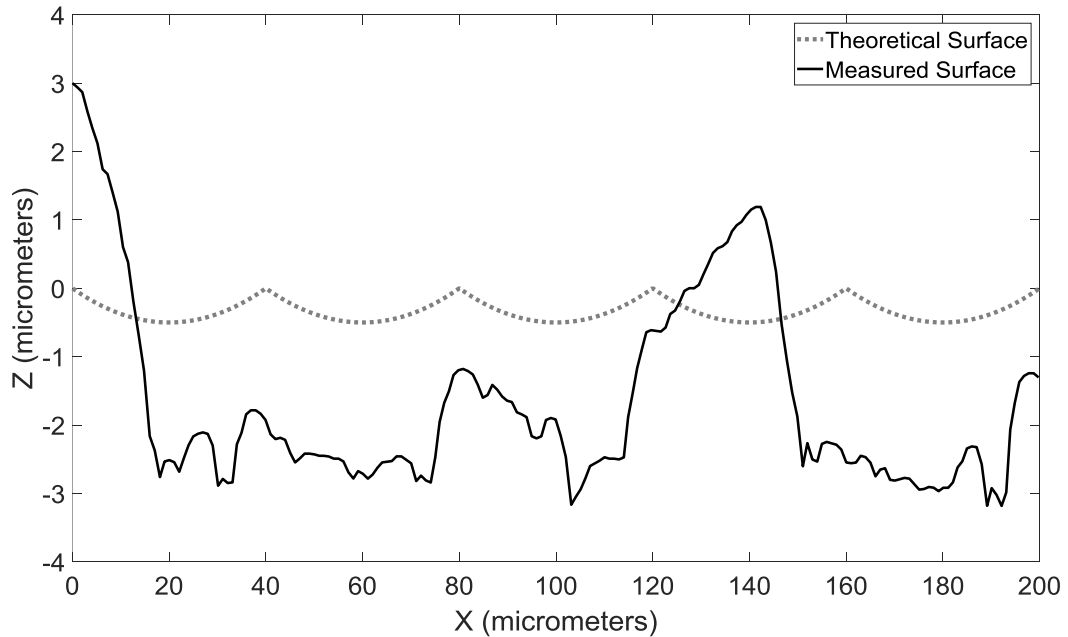
Figure 27 summarizes the surface finish results from the different tools. Both tools performed much worse than the theoretical values. On peak to valley surface finish measurements, Tool 1 performed much better than Tool 2, but since peak to valley is not a good metric of surface finish, it was not considered. Neither Tool 1 nor Tool 2 performed better than the other in RMS surface finish metrics, despite the presence of non-strain hardened BUE on Tool 2.

### Effects of Depth of Cut

To investigate the effects of depth of cut on BUE and surface finish and determine if it can be controlled, Tool 2 was used at three different depths of cut, 60, 80 and 100  $\mu\text{m}$ . Feedrate and spindle speed were held constant at 22 mm/min and 550rpm, respectively.



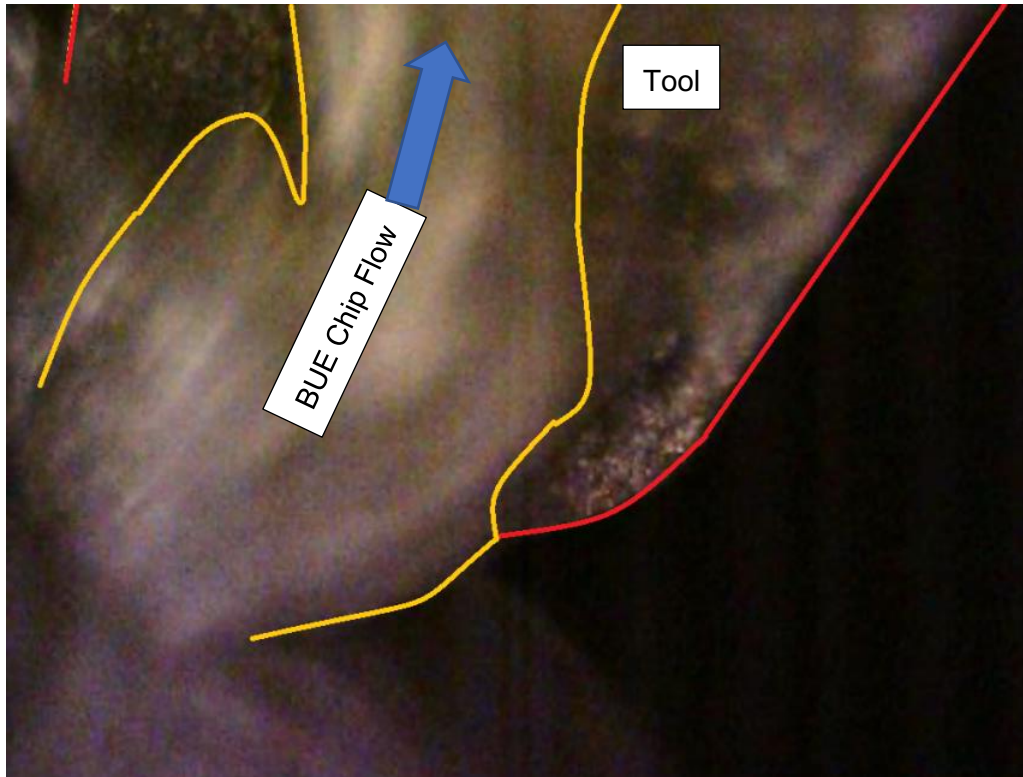
**Figure 28.** Surface Profile of 1199 Aluminum Turned with Tool 2 at 60  $\mu\text{m}$  Depth of Cut, Turned at 550 RPM at a Feed Rate of 22 mm/min



**Figure 29:** Comparison of Surface Created at 60  $\mu\text{m}$  Depth of Cut to Theoretical Surface, Tool 2, Turned at 550 RPM at a cross feedrate of 40  $\mu\text{m}$  per Revolution

Figures 28 and 29 show a surface that is irregular, and has many peaks above the surface. The tallest of which is 15  $\mu\text{m}$ . These features are likely a result of BUE. Theoretically, this surface has an RMS roughness value of 0.26  $\mu\text{m}$ . The measured RMS roughness of this surface is 1.33  $\mu\text{m}$ .

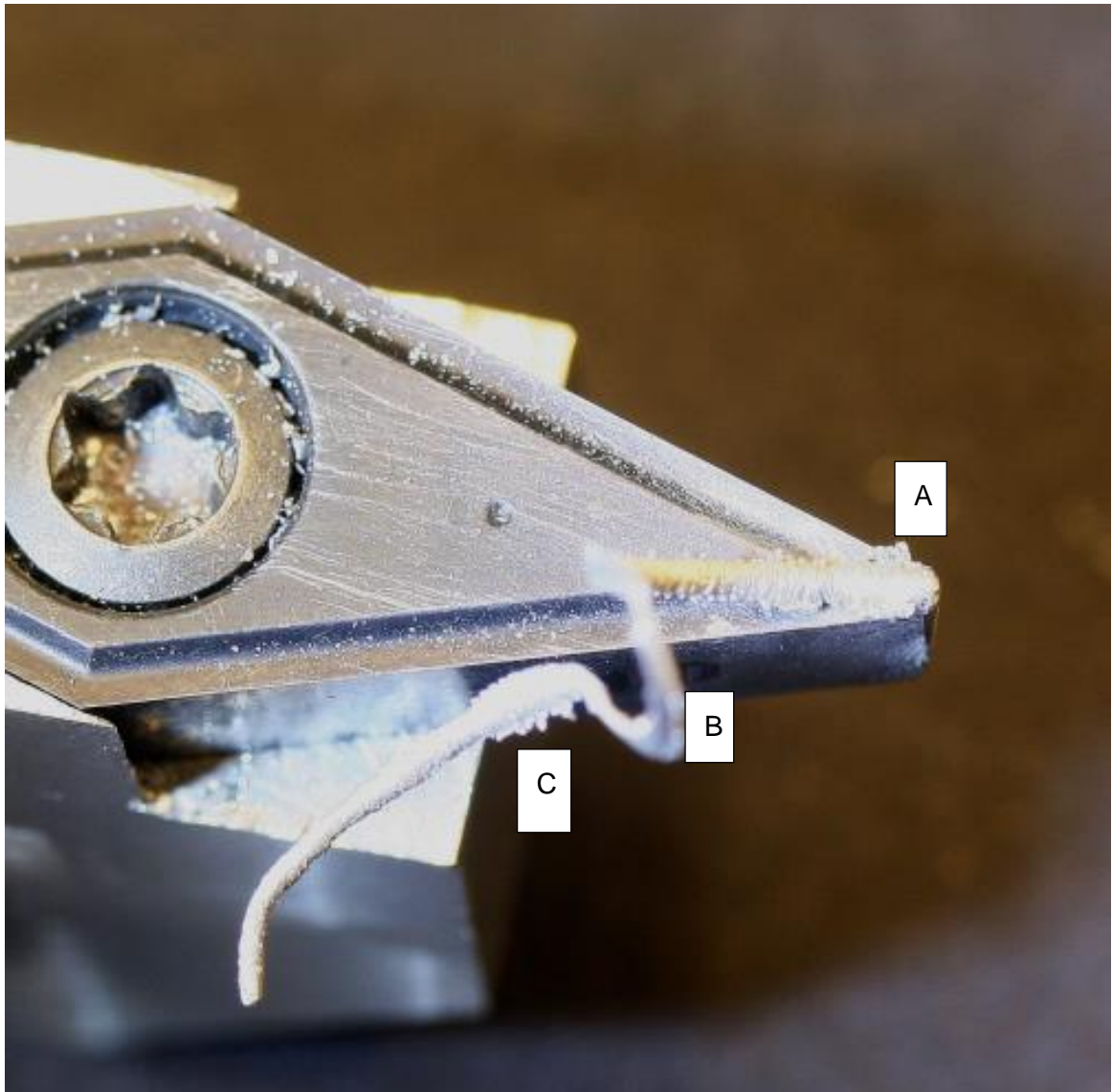
About 5x rougher than theoretical. Figure 29 shows a comparison of 5 cross feeds of the theoretical surface versus the measured surface. Notice the lack of repeating features on the 60  $\mu\text{m}$  depth of cut surface.



**Figure 30.** Chip Formation at 60  $\mu\text{m}$  Depth of Cut, Tool 2, Turned at 550 RPM at a Feed Rate of 22 mm/min

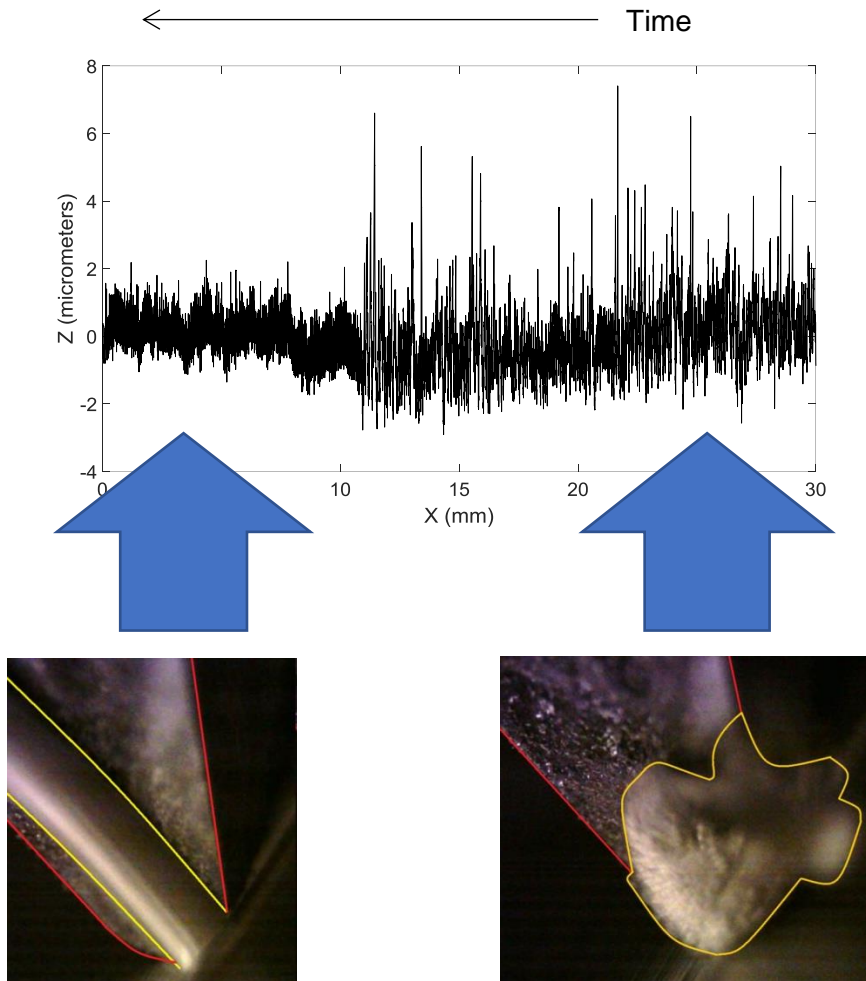
Using a high magnification camera during the turning operation, photographs of the chip formation were captured. Figure 31 shows chip formation at 60  $\mu\text{m}$  depth of cut. Notice the irregular shape of the chip. This is due to galling between the chip and the tool. An ideal chip will be smooth, straight and ribbon-like. This style of irregular chip formation persisted throughout the duration of the turning operation. While there was no long term built up edge present, the chips adhesion to the tool still presented issues with galling. This phenomenon is similar to that described by Figure 14.





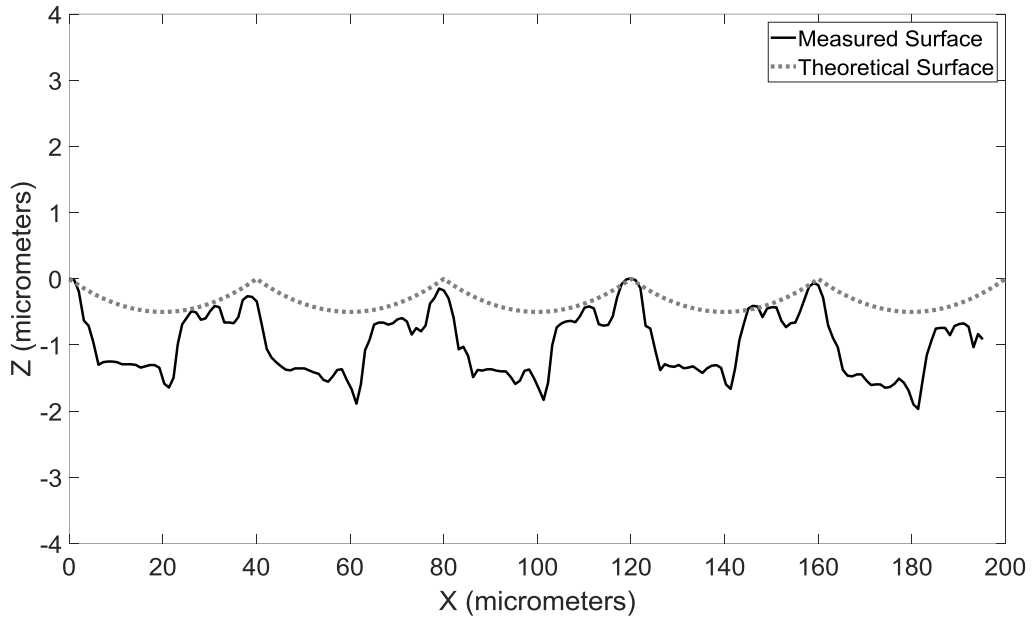
**Figure 31.** A photograph of Tool 1 After Turning an Overlapping Groove in 1199 Aluminum, Using a Feedrate of 22 mm/min, Turned at 550 rpm at a Depth of Cut of 60  $\mu\text{m}$

Figure 31 shows a photograph of the same tool and BUE that is imaged in Figure 30. Notice the ripple patterns on the chip at the tip of the tool (labeled "A"). Eventually, region A will break off of the tip of the tool and flow as a chip. As the chip travels off of the tip of the tool, normal cutting operation resumes, and the chip forms a curl (Labeled "B"). On the side of the curl furthest from the tool tip, another region of ripple patterns is present (Labeled "C"). This region was once attached to the tip of the tool in the same manner as A is in this picture. This indicates that periods of sticking, like region A and C, are broken up with normal chip flow, like region B.



**Figure 32.** Surface Profile of 1199 Aluminum Turned with Tool 2 at 80  $\mu\text{m}$  Depth of Cut, Turned at 550 RPM at a Feed Rate of 22 mm/min

Figure 32 shows an interesting phenomenon on the surface of the part. This cut could be divided into two clear regimes. To the left of 11 mm, the surface is consistent, smooth, and contains less tall features. This correlates with the formation of a smooth, continuous chip. To the right of the 11 mm line, the surface contains many tall, irregular features. This correlates with BUE on the tool. This change across the range of the cut is due to changing cutting speed as the radius decreases as the tool feeds toward the middle of the part.



**Figure 33.** Comparison of Surface Created at 80  $\mu\text{m}$  Depth of Cut to Theoretical Surface, Tool 2, Turned at 550 RPM at a Feed Rate of 40  $\mu\text{m}$  per Revolution, Below 1.77 m/s Cutting Speed. This is a zoomed in version of the same data displayed on the left side of Figure 32.

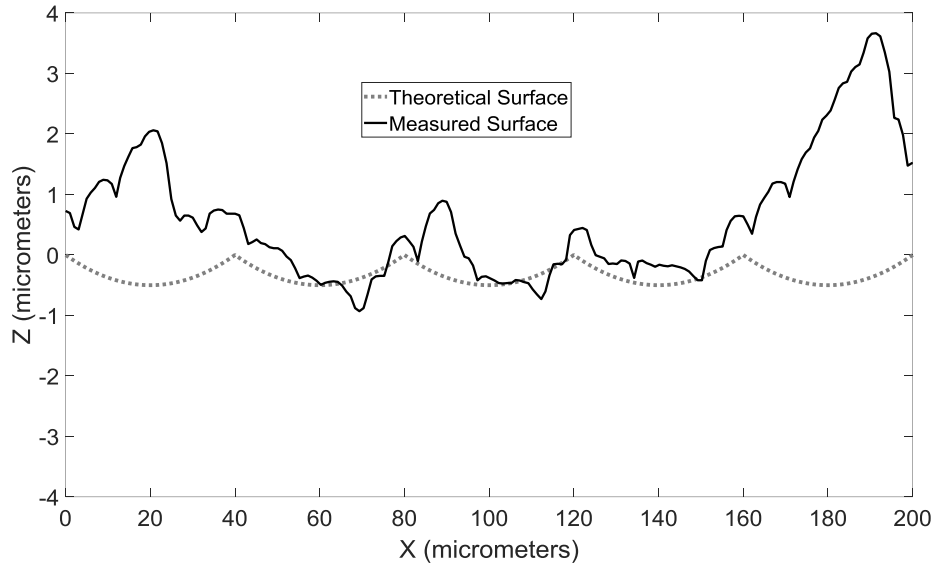


**Figure 34.** Comparison of Surface Created at 80  $\mu\text{m}$  Depth of Cut to Theoretical Surface, Tool 2, Turned at 550 RPM at a Feed Rate of 40  $\mu\text{m}$  per Revolution, Above 1.77 m/s cutting speed. This is a zoomed in version of the same data displayed on the right side of Figure 32.

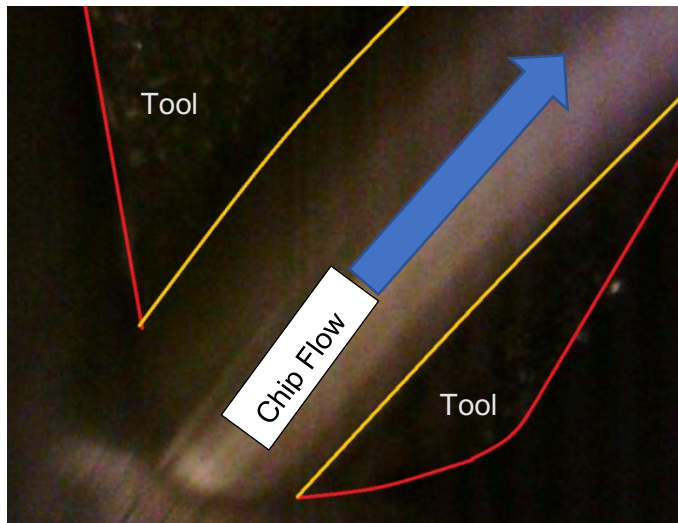
Figures 33 and 34 show the difference between the surface finish on the aluminum 1199 part at different surface speeds. Figure 33 pertains to the left side of Figure 32, where chip formation is

continuous. Figure 34 pertains to the right side of Figure 32, where BUE occurs intermittently, and no smooth, continuous chip is generated.

**Table 5.** Surface Finish Above and Below 1.77m/s. Tool 2. Aluminum 1199

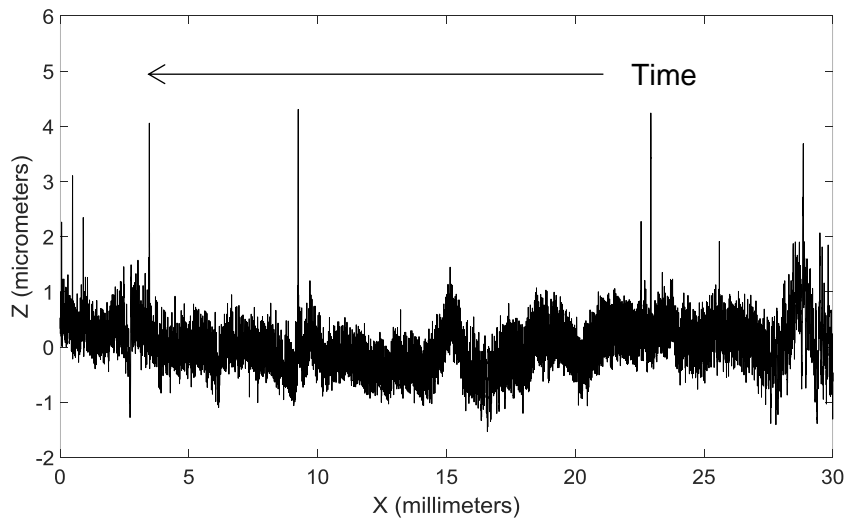
	Tool 2 (<1.77m/s)	Tool 2 (>1.77 m/s)
Theoretical RMS Surface Finish (µm)	0.26	0.26
RMS Surface Finish (µm)	0.62	1.16

Table 5 quantifies this surface speed phenomenon witnessed at 80 µm depth of cut. The line at 11 mm on the x axis on Figure 32 equates to 1.77 m/s surface speed at 550 rev/min. RMS surface finish is significantly improved when cutting speed is below 1.77 m/s.



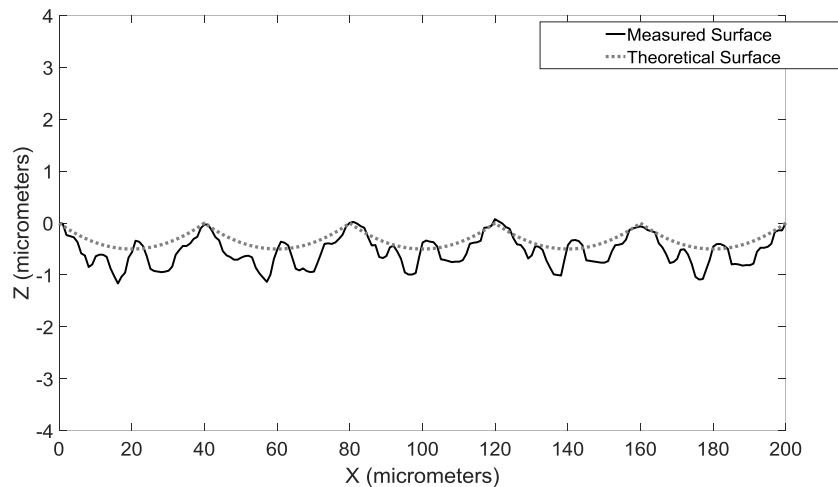
**Figure 35.** Chip Formation at 100 µm Depth of Cut, Tool 2, Turned at 550 RPM at a Feed Rate of 22 mm/min.

Figure 35 is a photograph of the chip formation at 100 µm depth of cut. The photograph shows a smooth, ribbon-like, "laminar" chip flowing across the center of the photo, over the surface of the tool. This style of chip formation was present throughout the duration of the turning operation. No evidence of BUE was evident.



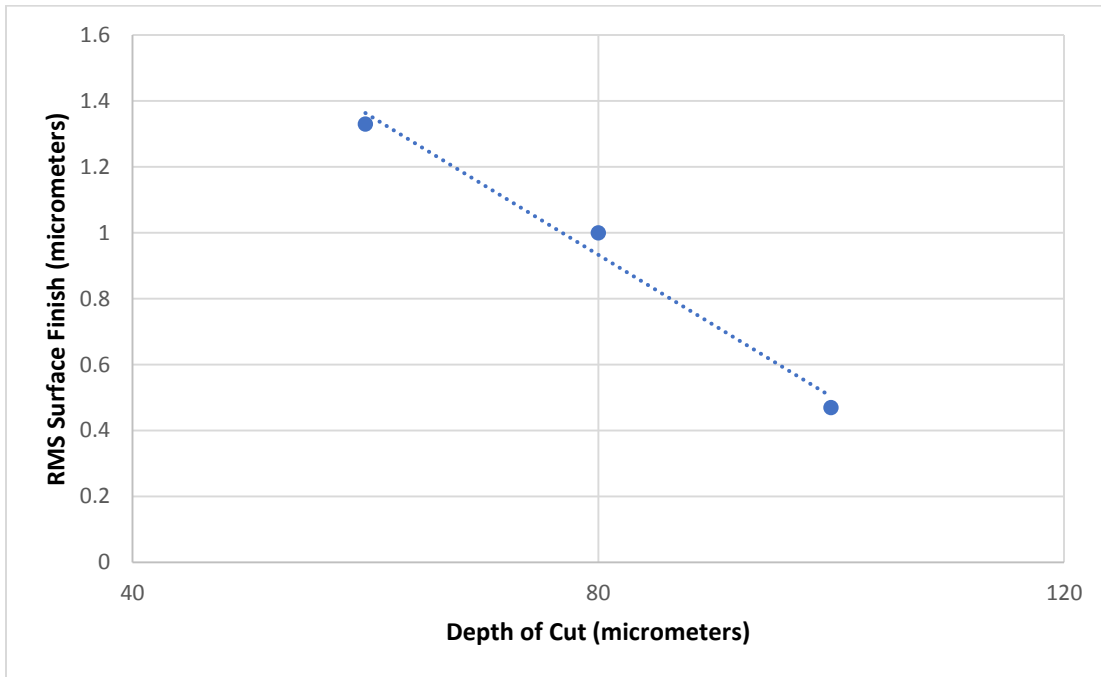
**Figure 36.** Surface Profile of 1199 Aluminum Turned with Tool 2 at 100  $\mu\text{m}$  Depth of Cut, Turned at 550 RPM at a Feed Rate of 22 mm/min

Figure 36 shows a surface that has only 5 peaks of greater than 3  $\mu\text{m}$ . RMS surface finish is about 0.45  $\mu\text{m}$ , about 2x as large as the theoretical 0.26  $\mu\text{m}$ .



**Figure 37.** Comparison of Surface Created at 100  $\mu\text{m}$  Depth of Cut to Theoretical Surface, Tool 2, Turned at 550 RPM at a Feed Rate of 40  $\mu\text{m}$  per Revolution. This is a zoomed in version of the same data displayed in Figure 36.

Figure 37 shows 5 cross feeds of the surface cut at 100  $\mu\text{m}$  depth compared to the 5 theoretical feeds. 5 distinct, repeatable grooves can be seen. The theoretical RMS surface roughness 0.26  $\mu\text{m}$  is about 2x smaller than the measured roughness of 0.47  $\mu\text{m}$  observed at 100  $\mu\text{m}$  depth of cut.



**Figure 38.** Graph of RMS Surface Finish Created by Tool 2 on 1199 Aluminum at 60, 80 and 100  $\mu\text{m}$  Depth of Cut

Figure 38 shows the RMS finish values compared to theoretical values. RMS values improve as the depth of cut increases. The theoretical surface finish of  $0.26 \mu\text{m}$  was not attained under any conditions.

## 4.3 CONCLUSIONS

### 4.3.1 Best Surrogate Material

Due largely in part to photographic and SEM evidence, it was determined that 1199 aluminum displayed the greatest ability to form a built up edge on the tool. 1199 aluminum was also found to have the most similar stress-strain curve and thermal diffusivity to  $\delta$ -phase Ga alloyed plutonium metal. Due to these observations, 1199 aluminum is the most fitting surrogate to plutonium metal out of the group including 1100 aluminum and OFHC anneal copper.



**Figure 39.** Side by Side Comparison of Built Up Edge Formed by Aluminum 1199 (L) and Plutonium Metal (R)

Figure 39 shows similar built up edge formations on the tip of carbide tool. The Image on the left is 1199 aluminum, the image on the right is plutonium. Both images show the side of the tool with a built up edge present on the rake face of the tool. The aluminum BUE is about 3x larger than the plutonium BUE.

### **4.3.2 Best Cutting Conditions**

Using 1199 aluminum and constant feeds and speeds, it was determined that cuts with higher depth of cut and lower surface speeds produced the best surfaces without the use of cutting fluid. Both 60 and 80  $\mu\text{m}$  depths of cut displayed tendencies to form a BUE when at higher cutting speeds. 100  $\mu\text{m}$  depth of cut showed no evidence of BUE at any speed tested in the study, and resulted in the best surface finish.

### **4.3.3 Future Considerations**

#### **Investigation into Two Regime Dry Turning**

As witnessed when 1199 aluminum was turned at 80  $\mu\text{m}$  depth of cut, two distinct regimes of cutting were witnessed: above 1.77 m/s surface speed and below 1.77 m/s surface speed. The regime below 1.77 m/s could be described as "laminar" chip formation. This regime resulted in better surface finish, and no presence of built up edge. The regime above 1.77 m/s can be described as "turbulent". This regime is marked by the presence of intermittent formation of built up edge and poor surface finish. Further defining these regimes at different depths could result in better surface finish with more predictable results.



### **Similar Results in 1199 Aluminum and Plutonium Metal**

While a built up edge has now been observed while dry turning both 1199 aluminum and plutonium metal, further research is required to determine if methods of built up edge prevention developed on 1199 aluminum have any parallel effects when turning plutonium metal.

### **Further Force Recording**

Cutting and thrust forces need to be recorded in overlapping cuts with 1199 aluminum. This will produce an overall resultant force on the tool that can be correlated with tool life, surface finish and presence of BUE.

## **REFERENCES**

1. Wick, OJ, *Plutonium Handbook A guide to the Technology- Volumes I and II*. Page 82, Figure 4-42, 1980.
2. *Metals Handbook, Vol.2 - Properties and Selection: Nonferrous Alloys and Special-Purpose Materials*, ASM International 10th Ed, 1990.
3. Hecker, S, Stevens, M *Los Alamos Science Number 26: Mechanical Behavior of Plutonium and Its Alloys*, 339, Figure 2, 2000.
4. "Effect of cutting edge radius on surface roughness in diamond turning of transparent MgAl<sub>2</sub>O<sub>4</sub> spinel ceramic." *Optical Materials*. Figure 2, 2016.
5. Suit, Brandon, *Analysis of Accelerated Tool Wear and Built Up Edge When Diamond Turning Ferrous Materials. Masters Thesis, Precision Engineering Center, North Carolina State University*. 2016.
6. Heginbotham, WB, and SL Gogia. "Metal Cutting and the Built-Up Nose." *Proceedings of the Institution of Mechanical Engineers 175.1 (1961): 892-917*. Web.
7. *Wikipedia Contributors, "Galling"*. 2017. Web.

## 5 FINDING NATURAL FREQUENCY OF A PIEZOELECTRIC LOAD CELL

**Alyssa Edwards**

Undergraduate Student

**Thomas Dow**

Professor

Mechanical and Aerospace Engineering

*This report discusses a method of determining the natural frequency of a piezoelectric load cell used in dynamic force measurement. The experiment showed that the natural frequency of the tool holder and load cell ranges between 11-12 kHz. To create the impulse, 4 lb. fishing line was secured around the tool holder/load cell system. The applied impulse is created by loading the fishing line slowly until it snaps suddenly. This procedure disconnects the load cell from the loading system so that the load cell is not subjected to a continuous or repeated excitation. Previous tests at the PEC were conducted and the resonant frequency was measured to be approximately 11 kHz. In those experiments, the impulse was applied by tapping the load cell. However, it is difficult to contact the load cell only once when manually tapping it. Once excited, the trigger feature on the oscilloscope is used to measure the oscillation and the natural frequency.. This report finds that applying the impulse to the load cell using the fishing line is an effective way to create the impulse to measure the resonant frequency of the system.*



## 5.1 INTRODUCTION

Natural or resonant frequency of an object is the oscillation at which it vibrates when not exposed to a continuous or repeated external load. This report examines a method of measuring the natural frequency of the Kistler 9251A model piezoelectric load cell used during precision turning experiments. The report aims to develop a standard Test for measuring natural frequency that can be referenced when calibrating the piezoelectric load cell. The natural frequency measurements are taken by instantaneously removing a static force to initialize an oscillation. The vibration is then recorded by an oscilloscope and analyzed to determine the natural frequency.

Finding the natural frequency of a load cell is important to turning experiments, because it can affect the interpretation of the acquired data. As the tool is subjected to forces during turning experiments, the load cell measures the deflection and sends that information to the data acquisition system to be converted and recorded as force measurements. When analyzing the recorded data, it is important to consider the load cell's natural vibration and what role it plays in the force measurements.

## BACKGROUND

The Kistler 9251A piezoelectric load cell measures forces in the x, y and z directions. Forces in the x and y directions are measured by two quartz pairs sensitive to shear. Forces in the z direction are measured by a single quartz pair that is sensitive to pressure. Electrical signals are sent to the connectors which are converted to forces and recorded by the data acquisition system. According to Kistler's technical data, this load cell has a stiffness of about 1000 N/micrometer in the x and y directions and 2600 N/micrometer in the z direction and weighs 32 grams. Figure 1 maps the x, y and z directions and gives dimensions of the load cell defined by Kistler Models 3 Component Force Sensor manual.

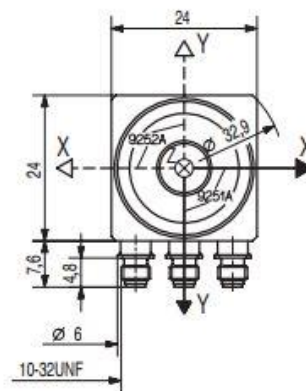


**Figure 1:** Kistler 9251A Load Cell Sketch

Technical data concerning the Kistler load cell that was used to measure forces in the machining operations discussed in other sections of this report is found in Table 1. Table 1 shows a comprehensive list of the Kistler 9251A load cell's technical data.

**Table 1:** Technical data for load cell from Manufacturer

Characteristic	Kistler 9251A		
	X, Y directions	Z direction	Units
Range	-2.5...2.5	-5...5	kN
Threshold	<0.1	<0.1	N
Sensitivity	-8	-4	pC/N
Temperature Coefficient of Sensitivity	-.02	-.02	%/° C
Stiffness	1000	2600	N/μm
Natural Frequency	--	--	--
Linearity	<±1	<±1	%FSO
Cross Talk	<±3	<±3	%
Insulation Resistance	>10	>10	TΩ
Capacitance	30	30	pF
Operating Temperature Range	--	--	-60..150 ° C
Mass	--	--	32 g

Theoretical natural frequency is dependent on the stiffness  $k$  and the moving mass  $m$  of the object. Eq.1 is the natural frequency for a single degree of freedom spring/mass system where  $\omega_n$  is the natural frequency in Hertz.

$$\omega_n = \frac{1}{2\pi} \sqrt{\frac{k}{m}} \quad (1)$$

Note that Table 1 does not include a value for the load cell's natural frequency because the moving mass is not known by the manufacturer. Drescher [1] found it to be around 8 kHz. Based on these results, he found the moving mass that would produce a natural frequency of 8 kHz to be 400 grams. Using Equation 1 with  $m$  equal to 400 grams and  $k$  equal to the 1000 N/μm (as in Table 1) Drescher recorded as the stiffness shown in Table 1, the calculation made is as follows:

$$\omega_n = \frac{1}{2\pi} \sqrt{\frac{1000 \times 10^6}{0.4}} = 8000 \text{ Hz}$$

It is unclear what was the source of the 400 gram mass used in Drescher’s calculation. As previously stated, the mass used to calculate natural frequency is the mass of the object. If the load cell’s mass is only 32 grams as given in Table 1, then the load is not just the mass of the load cell.

In his MS thesis [2], David Gebb found the resonant frequency in the cutting force direction (vertical) to be 11.6 kHz. To measure this value, he tapped the load cell with a small hammer and recorded the oscillation with an oscilloscope. Using the Fast Fourier Transform (FFT), the data was converted to singular frequencies. The most common frequency was the 11.616 kHz. This is the value used as a reference for the measurements in this paper. Using this frequency, the moving mass needs to be:

$$m = \frac{K}{(2\pi\omega_n)^2} = 190 \text{ grams}$$

If this mass was in the form of a cube of aluminum, the size would be 1.6 inch (40 mm) on a side. That seems way too big. So there must be other factors that determine the natural frequency and how to measure it directly is the focus of this research.

## 5.2 DETAILS OF THE PROJECT

### Load Cell

The same ASG diamond turning machine setup was used for all natural-frequency testing. The equipment and setup are explained later in this report. The mass of the tool holder and load cell used are summarized in Table 2. Load cell specifications are in Table 1.

**Table 2.** Mass of objects used during Testing

Object	Mass (g)
Load Cell	32
Tool Holder	13.7

The moving mass of the load cell is all of the mass supported by the load cell. In the case reported here, it includes the diamond tool, the tool holder, half of the bolt that passes through the hole in the load cell, the nut, on the load side of the load cell. See the discussion above related to the source of the natural frequency.

### 5.2.1 Experimental Setup

The ASG set-up was a typical turning experiment conducted at PEC. Figure 2 depicts how the tool holder and load cell are attached to the ASG diamond turning machine. The load cell sits behind the tool holder and is attached with a bolt. The connectors are labeled according to which

axis they measure deflection. Note this set up is an example used for developing a method to Test natural frequency. There are other load cell positions and tool holder combinations that may affect the resonant frequency differently than in this experiment.

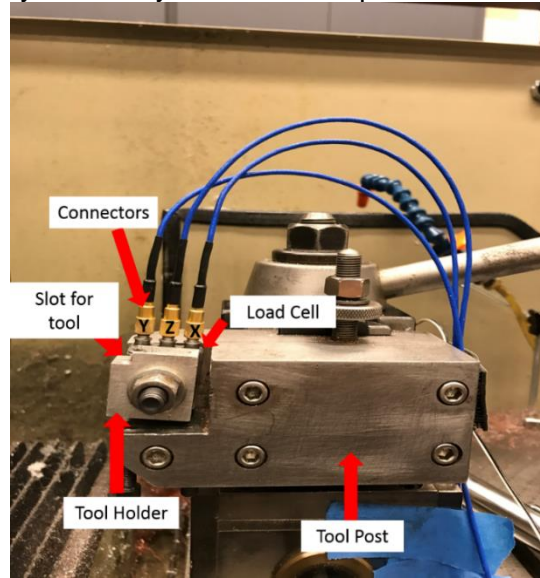


**Figure 2:** Load cell and Tool Holder Set up

To create the impulse to the spring mass system, 4 lb Test fishing line is attached to the tool shank. Figure 3 shows the fishing line attached to the tool holder.



**Figure 3.** Creating the impulse - same view as Figure 2 but zoomed out

The fishing line is loaded slowly by hand until it suddenly snapped. The person pulls up on the spool creating a slowly increasing vertical force until it reaches the breaking strength of the line

and the force is immediately removed. This creates an impulse to the spring/mass system and it vibrates in response.

The piezoelectric load cell generates a voltage proportional to the force applied as the spring/mass system responds to the impulse. Cyclic motion of the mass provides the natural frequency of the oscillation. From there, the amplifier sends the inputs from the load cell to a digital oscilloscope.

## 5.2.2 Analytical Approach

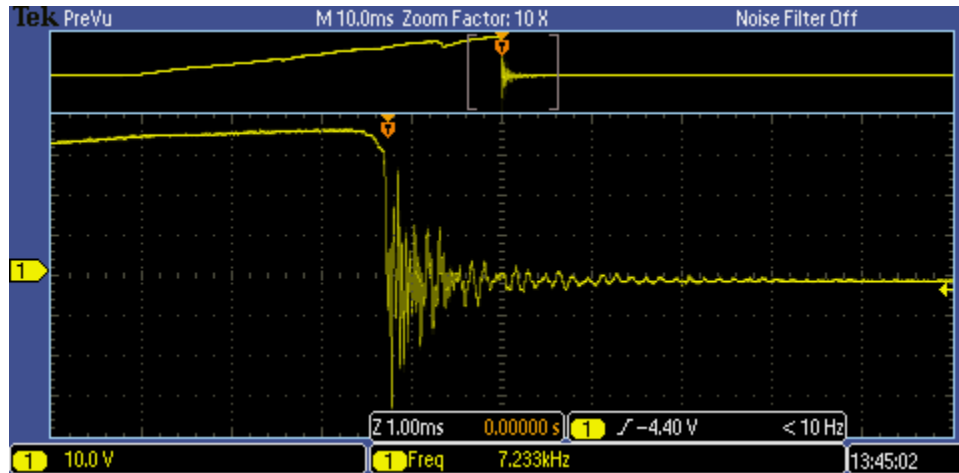


**Figure 4.** Oscillation of load cell after impulse

An oscilloscope can be used to quickly view and measure the oscillation frequencies. The load cell's force measurement is transmitted to the amplifier and then to the oscilloscope. Figure 4 shows an oscilloscope image of an impulse and the corresponding oscillation. The force is being increased from the left and at the marked peak, the fishing line breaks and the force is removed instantaneously. This starts a vibration of the load cell and indicates its natural frequency when it is expanded horizontally and vertically in the lower graph of Figure 4.

The vertical component of the graph in Figure 4 are the forces generated in the piezoelectric load cell when its load is instantaneously removed. The vertical voltage readings are the forces read by the load cell and the horizontal component is time. Initially the force from the fish line is high, but then suddenly drops and the oscillation occurs. This sudden drop indicates an impulse.

To obtain this visual, the following steps are required to set up the oscilloscope:

1. Power on the oscilloscope and amplifier. Be sure to connect the appropriate axis connector to the oscilloscope depending on the orientation of the load cell.
2. Once powered on and connected to amplifier, use the "Autoset" button to quickly get a visual of the signal. The signal is represented by the light-colored line in the center of Figure 4.

3. Apply a force on the load cell by tapping or pushing on it and make sure the signal responds by moving up or down.
4. Next, increase the horizontal scale to at least 4.00 ms and less than 200 ms. This is the range of time by which a snapshot can record enough data to analyze the oscilloscope while also allowing the use of the trigger feature.
5. Set the horizontal axis within the range of 5 V to 20 V. Move the signal up or down on the screen until it is centered.
6. Lightly pull the fishing line upward (or in the direction that the line will be jerked) so that it applies a force on the load cell and note whether the signal moves up or down. Note whether the voltage increases or decreases.
7. If the signal increased, set the trigger slightly below the center line. If it decreased, set the trigger slightly above the center line.
8. Press single and increase the force on the fishing line until it snaps. An image like Figure 4 should appear.

The signal will cease to run continuously, and a snapshot of the oscillation should appear on the screen. To measure the frequency of the oscillation, press the measure button on the oscilloscope and select the frequency feature or save the data as an csv file. This report uses the measure feature of the oscilloscope. It is important when analyzing the data, to focus on the part of the oscillation that is most likely to represent the resonant frequency. Figures 5, 6 and 7 are an example of how much is needed to be cut from the oscillation.

### 5.2.3 Experimental Results

The experiment was repeated three times to find the repeatability of the natural frequency measurement. From the Background section of the report, remember that Drescher’s theoretical calculation of the resonant frequency of just the load cell was 8000 kHz. That calculation corresponded to a vibrating mass of 400g.

**Table 3.** Oscilloscope scaling and results

Test	Horizontal Time Scale (ms)	Vertical Voltage Scale (V)	Measured Frequency (kHz)
1	4	5	9.892
2	10	10	11.92
3	10	10	11.16

Table 3 shows the horizontal and vertical settings and the measured frequency of each Test. The horizontal and vertical scales are set before the signal is triggered. The scales are adjusted when zoomed in to measure the frequency. The scale settings in Table 3 are most useful for set up,



because they ensure that the entire oscillation is included in the single snapshot. Figure 5, 6 and 7 correspond to Tests 1, 2 and 3 respectively. All of the figures have the same vertical scale but the horizontal scale changes. The horizontal scale for Figures 5, 6 and 7 are 200  $\mu$ s, 100  $\mu$ s and 40  $\mu$ s respectively.

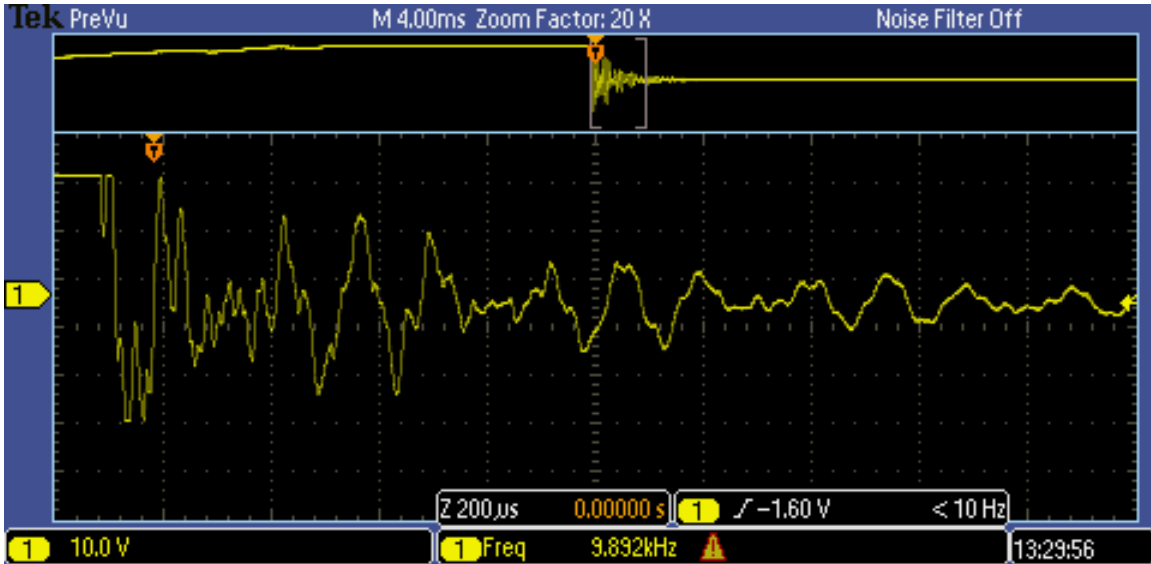


**Figure 5.** Test 1 at 200 ms/div

Figure 5 represents the oscillating deflection of the load cell at 200  $\mu$ sec/division for Test 1. Notice the number next to the label “Freq” at the bottom of the image is the frequency measurement. For this measurement of the oscillation, the frequency is 9.892 kHz. Notice that from the beginning that the oscillation is not uniform. After the sudden drop in the beginning of the image, the amplitude and frequency vary significantly. It appears that there are also a number of high frequency, low amplitude oscillations especially between the first two periods after the impulse.

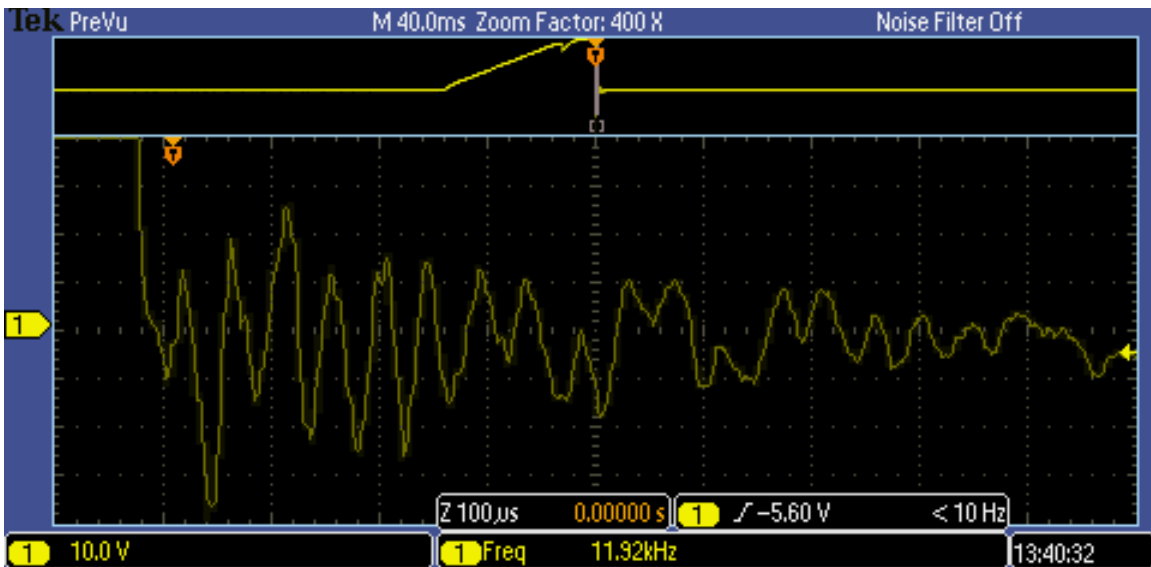


**Figure 6.** Test 2 at 100 ms/div

Figure 6 shows the deflection oscillation for Test 2. Here, the measured frequency was 11.92 kHz. When comparing Figure 6 to Figure 5, the oscillation is clearer, and the frequency is more uniform. Figure 6 is an example of how the expected oscillation should appear.

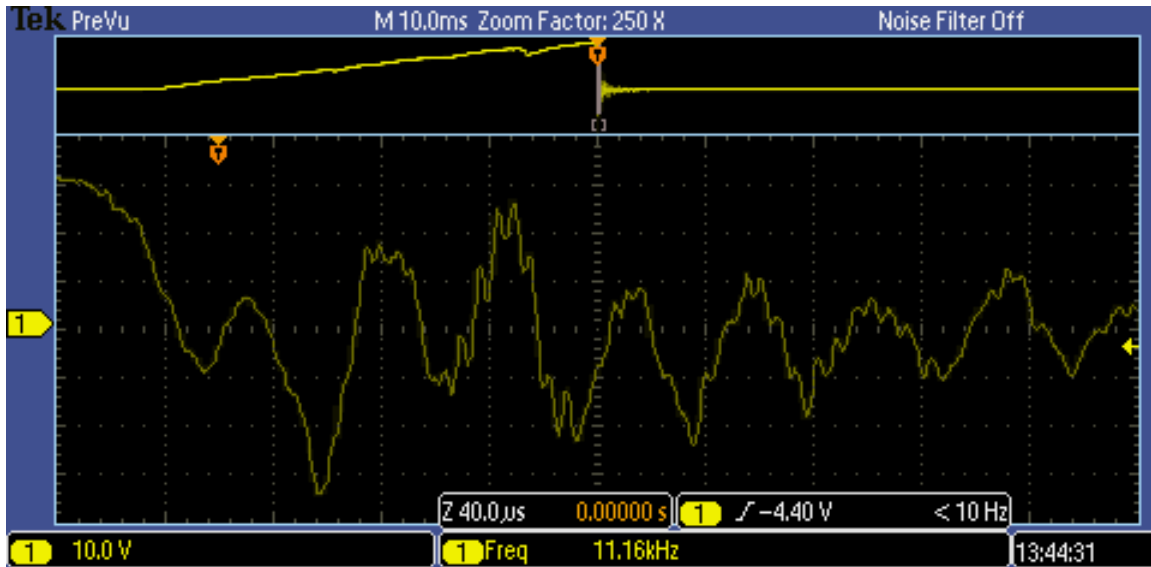


Figure 7. Test 3 at 40 ms/div.

Figure 7 shows a measured frequency of 11.16 kHz. This corresponds to the Test 3 from Table 3. Note that this oscillation is like the oscillation depicted in Figure 5, because it has small spikes of voltage within a period. However, it is also like Figure 6 in that the frequency is uniform.

### 5.3 CONCLUSIONS

According to the oscilloscope measurements, the frequency of the system ranges between 9.8 to 12 kHz. The measurement from Test 1, 9.892 kHz, is the farthest from a theoretical single degree of freedom spring mass motion. The small, high-frequency spikes of voltage appearing between periods and non-uniformity of the frequency throughout the beginning of the oscillation are unexpected for a resonant frequency. The results of Test 1 frequency measurement is probably due to a complication when applying the impulse. For example, the fishing line could have been jerked upward but not snapped. If the line was quickly jerked again and snapped, the first jerk could interfere with the oscillation. Note that the horizontal scale for Test 1 is 200  $\mu$ s. This longer amount of time allows the measurement to include the vibration a longer time away from the impulse in the calculation. This may also interfere with the inaccuracy of the measurement.

Frequency measurements of Test 2 and 3 are closer to the theoretical shape than Test. The frequency measurement for Test 2 and 3 are 11.92 and 11.16 kHz respectively. These are considered more accurate frequency, because the space of time between periods is more uniform

in each. The small spikes of voltage in Test 3, Figure 7 are not a cause for much concern in the frequency measurement, because the amplitude does not affect the frequency measured by the oscilloscope. Note that the values for Test 2 and Test 3 compare similarly to Gebb's measured value of 11.616 kHz using a different method. Therefore, it is reasonable to conclude that the values for Test 2 and 3 are accurate, and creating an impulse by breaking a 4 lb test fishing line is an appropriate method of determining the natural frequency of the piezoelectric load cell.

## REFERENCES

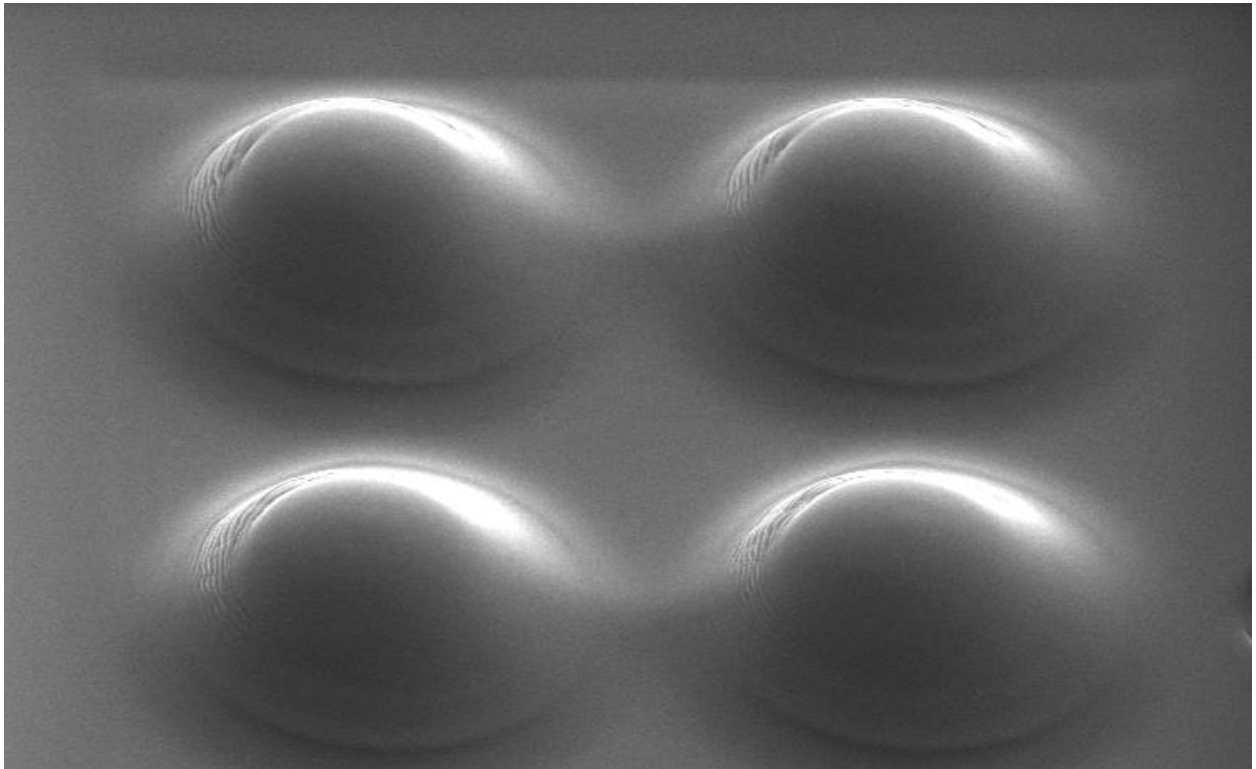
1. Drescher, Joseph Dean. "Tool Force, Tool Edge, and Surface Finish Relationships in Diamond Turning." *North Carolina State University*, 1991.
2. Gebb, David Martin, "Performance Characterization of a Single Abrasive Grit with Force Measurements and Visualization Techniques." *North Carolina State University*, 2014.

## 6 MICROSCALE LENS ARRAY: FOCUSED ION BEAM MILLING OF MICROSCALE FEATURES

**Anthony Wong**  
Research Associate

*This research investigates the fabrication of microscale features in glassy carbon that will be used as a die to stamp features into a mold for injection molding of plastic lenses. The concept is to FIB mill a die with multiple features (4-9) and then stamp those features at a high repetition rate (>100/second) to create a mold for a large lens array. The features are nominally spherical with radii on the order of 20  $\mu\text{m}$  that would, with the parameters given above, create a mold with  $3 \times 10^6$  lenses in an hour.*

*The material removal rate of the FIB has been quantified and it was estimated that a single lens feature could be milled in a matter of minutes. A simulation tool was developed to assist in planning the FIB milling process that is similar to CAM for conventional milling. Finally, the inputs for the simulation, such as beam shape, were quantified.*



## 6.1 INTRODUCTION

As modern electronics have continued to shrink in size, the need for smaller and smaller optics has increased. For instance, a typical smartphone display will have pixels tens of micrometers in size. Some digital camera sensors now have pixels with single digit micrometer dimensions. Matching microscale optics are needed for each pixel to collimate or focus light in these electronic components. For a display such optics would produce higher output intensity while lowering the power consumption of the panels. In this day and age of portable, high-volume electronic devices, low-cost and light-weight microscale lens arrays need to be developed for applications such as this.

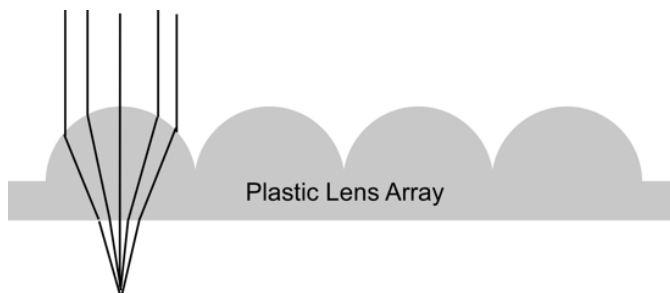


**Figure 1:** An array of plastic lenses to enhance the brightness of a pixel array.

To make an array of over a million lenses as required for these applications, a technique to increase the replication rate must be developed. The multi-step process under development is as follows:

1. Make a male die with 4-10 lens features using a hard material that can be used as an indenter which would look similar to that in 2. This could be made using a Focused Ion Beam or a FIB in conjunction with some other coarse grooving technique (like a flycutter with a shaped cutting tool) that will have a higher material removal rate but with less resolution. It would be finished with the FIB. This task will be the focus of this section.

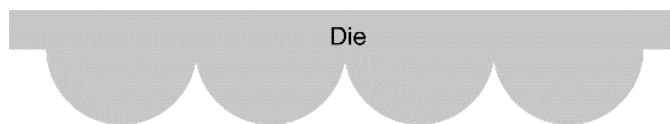
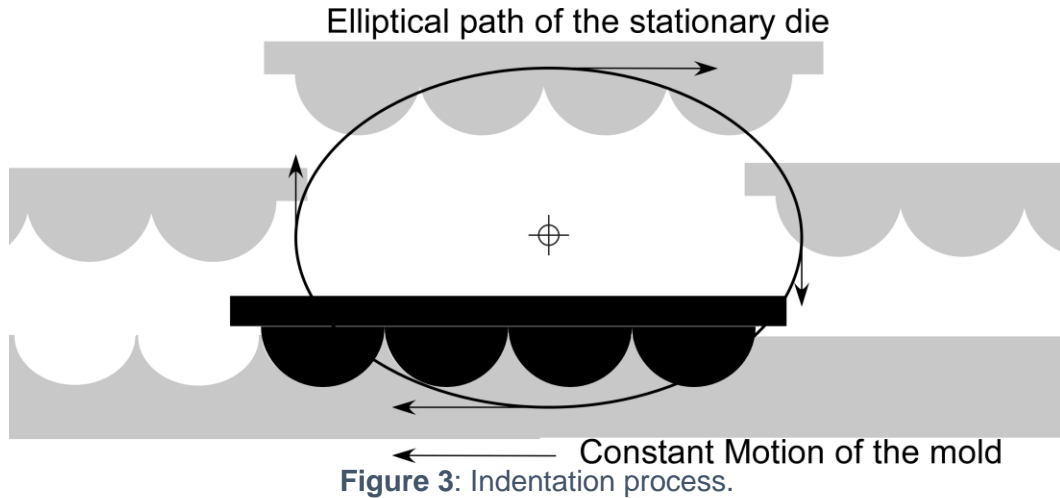


**Figure 2:** Die with lens features

2. Place this die on an actuator that can move in an elliptical path and load against a moving mold shown in Figure 3 to plastically deform the surface and replicate the features. This

replication process will create a mold with millions of copies of the lens feature. The die shape may need to deviate from the lens shape in Figure 1 to control the plastic flow of the displaced material. A description of the indentation process and the material flow is in Section 7 of this Annual Report. The design of the actuator will be another significant part of this project but has not been started at this time.



3. The final step will be to use the mold above in a conventional plastic manufacturing process such as compression or injection molding to create the lens array that will look like Figure 1.

### 6.1.1 Background

A focused ion beam (FIB) is able to precisely accelerate gallium ions at a target with spot sizes as small as tens of nanometers in diameter. When the gallium ions impact the target, molecules from the target will sputter off leaving a new shape. The FIB milling process is controlled by only a handful of parameters. First the beam current determines the shape of the ion intensity distribution. In literature, the beam intensity distribution is often modeled with a Gaussian profile. As the beam current goes up, the width of the distribution increases. The beam current does not change after the cutting process begins as it is related to the optics in the machine, and the focus and astigmatism would change for a new beam current setting. The maximum dwell time, map of dwell times and number of passes are the parameters used to setup the equivalent of a toolpath in conventional milling. The maximum dwell time is the longest amount of time an area would be exposed to the ion beam. The longer the dwell time, the more material will be sputtered. A map of locations and relative dwell times for each (x, y) coordinate tells the machine where to turn the beam on and what percentage of the max dwell time to expose the area. The number of passes is the number of times the "toolpath" will be repeated.

Many researchers have examined the fabrication of concave molds with a focused ion beam. Yoshida et al. [3] made a press mold out of glassy carbon for an array of 20  $\mu\text{m}$  diameter lenses by machining the form with a Nd-YAG, 300 mW laser followed by FIB milling to improve the surface finish and remove debris from the laser machining process. Langridge et al. [4] explored fabricating 1-10  $\mu\text{m}$  diameter parabolic concave features in silicon with the FIB for molding glass. Youn et al. [5] used a FIB to mill glassy carbon molds for microfluidic devices.

In addition to optical mold fabrication, there is a significant body of research on milling arbitrary 3D shapes with the FIB. In particular Vasile, Adams et al. [6-10] describe a method of combining the beam intensity distribution with the sputtering yield to be able to predict the material removal and final shape. Unfortunately, their method is not quite as straight forward as it might initially appear, as the sputtering yield is dependent on the material and angle of incidence. The angle of incidence might increase the sputtering by a factor of 3 or 4 as the angle of incidence changes from normal to 80°, so the angle of incidence dependence must be accurately known.

## 6.2 DETAILS OF THE PROJECT

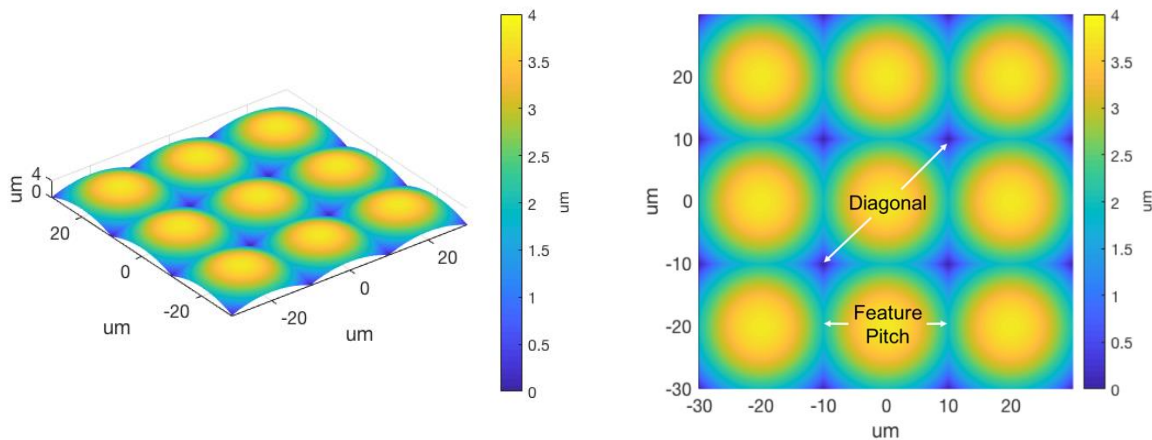


**Figure 4:** Spherical lens array with a 20 $\mu\text{m}$  feature pitch.

The initial shape for the array was decided to be a square grid of spherical lens features with a 20 $\mu\text{m}$  feature pitch as seen in Figure 4. Each feature is a spherical surface with a  $f/1$  shape. For clarity, the  $f$  number is defined here as the geometric focal length divided by the length of the diagonal of the square footprint of the feature. Figure 5 depicts a cross section of one feature across its diagonal. The diagonal is 28.28  $\mu\text{m}$  for a square pitch of 20  $\mu\text{m}$ . For a  $f/1$  shape, the focal length, which in the case of a hemisphere happens to be the radius, will also be 28.28  $\mu\text{m}$ . The height of the feature is 3.8  $\mu\text{m}$ . The maximum angle of incidence of the lens feature is 30° which occurs at the extremes of Figure 5, or the corners of the features in Figure 4.

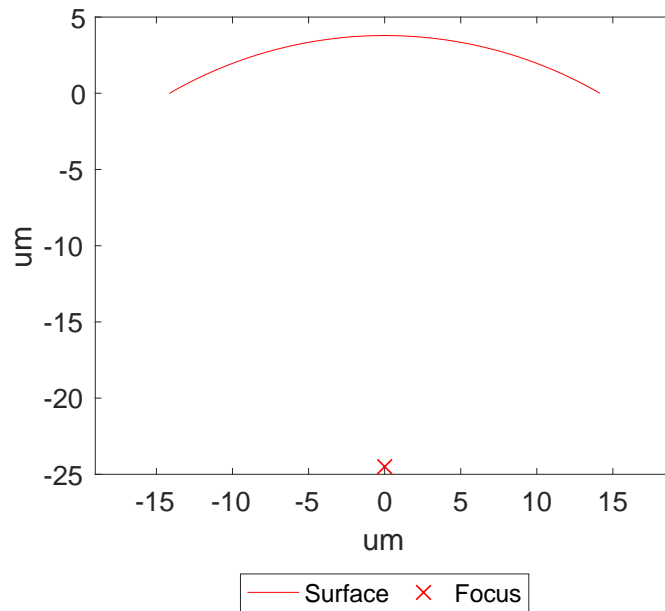


**Figure 5:** Cross section across the diagonal of a feature.

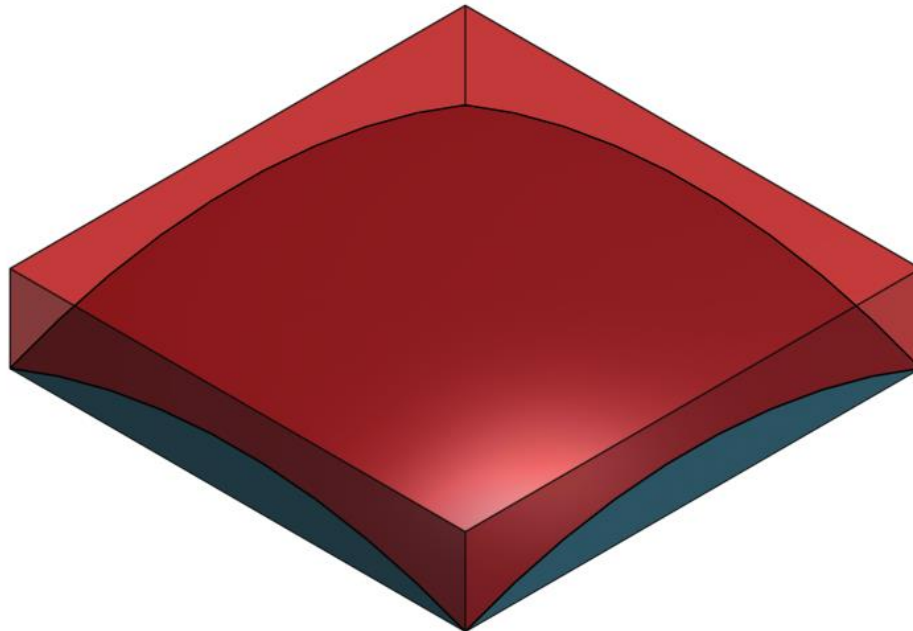


**Figure 6:** Model of a single feature. The bottom piece is the feature of interest. The material to be removed is shown as the translucent top portion.

In Figure 6 a single feature is shown as the bottom portion. Assuming the feature will be cut from a flat, the volume of the material to be removed is shown as the translucent top piece. The volume of the material to be removed for a single feature is  $485 \mu\text{m}^3$ .



It should be noted here that this work is a proof of concept for the manufacturing of an array of microscale optics. Actual optics will differ as the reverse side of the optic and the particular plastic's index of refraction must also be considered. That level of detail is beyond the scope of the project at this point and therefore, this report will focus on only the fabrication of the die and the fidelity of the indentation process. For this portion of the project, the goal is to make a 3 x 3 grid of convex features.

## 6.2.1 FIB Experimental Setup

For the FIB experiments, a FEI Quanta 3D FEG was used at the NC State Analytical Instrumentation Facility (AIF). The Quanta has an electron beam in addition to an ion beam to aid in imaging. A 25 mm X 25 mm X 3 mm SPI Glas 11 grade glassy carbon plate from SPI Supplies (Part Number 4375GCP-AB) was used as the sample material for all experiments. Table 3 shows the properties of this grade of glassy carbon. Glassy carbon was chosen because it is hard and has higher material removal rates than diamond which was used as a die in the previous nanoscale coining work [1-2]. Also Yoshida was able to make similarly sized microscale indentions in glassy carbon with a combination of laser machining and FIB milling [3]. The glassy carbon plate was prepared by applying conductive carbon tape that covered the top surface and wrapped around to the bottom and also adhered the sample to a pin mount. The entire top surface and the conductive tape were coated with Au-Pd to prevent any charging effects in the SEM-FIB. Charging occurs when the SEM sample is an insulator. The insulator builds up charge due to the incident electrons and develops its own electric field which distorts the electron beam causing what appears to be drift in the image. The Au-Pd coating creates a conductive layer connected to the grounded pin mount to prevent any charge from building up. The prepared sample is shown in Figure 7.

**Table 1:** Material properties of SPI Glas 11

<b>Property</b>	<b>Value</b>
Bulk density	1.54 g/cm <sup>3</sup>
Vickers Hardness	340
Compressive strength	580 GPa
Young's Modulus	35 GPa
Coefficient of Thermal Expansion	2.5 x 10 <sup>-6</sup> m/m·K

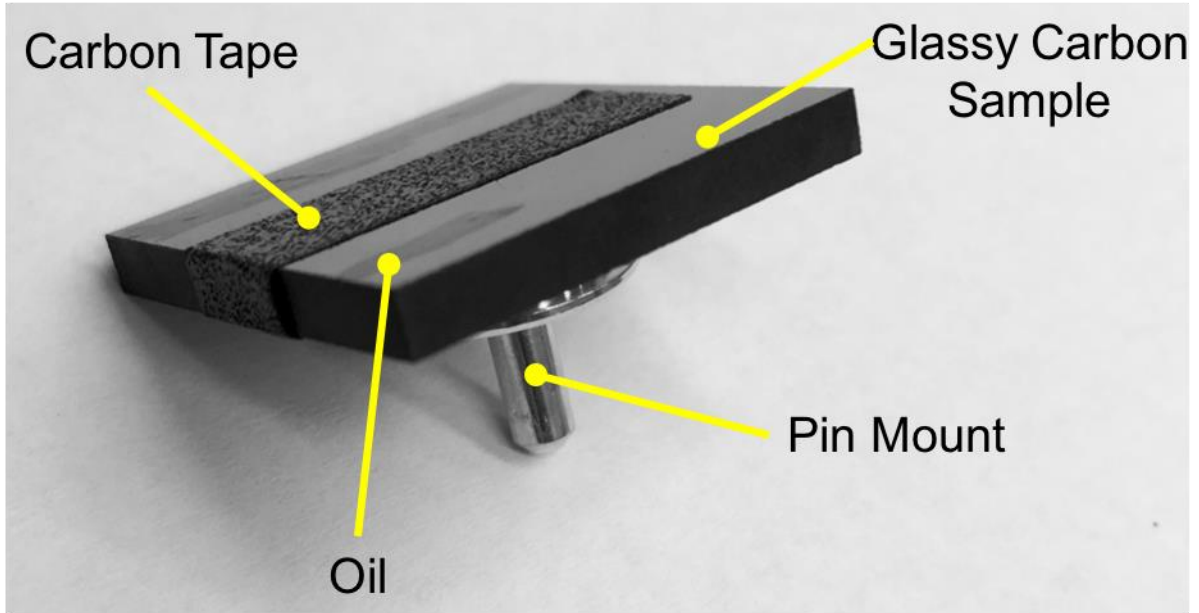


**Figure 7:** Glassy carbon sample prepared for the FIB

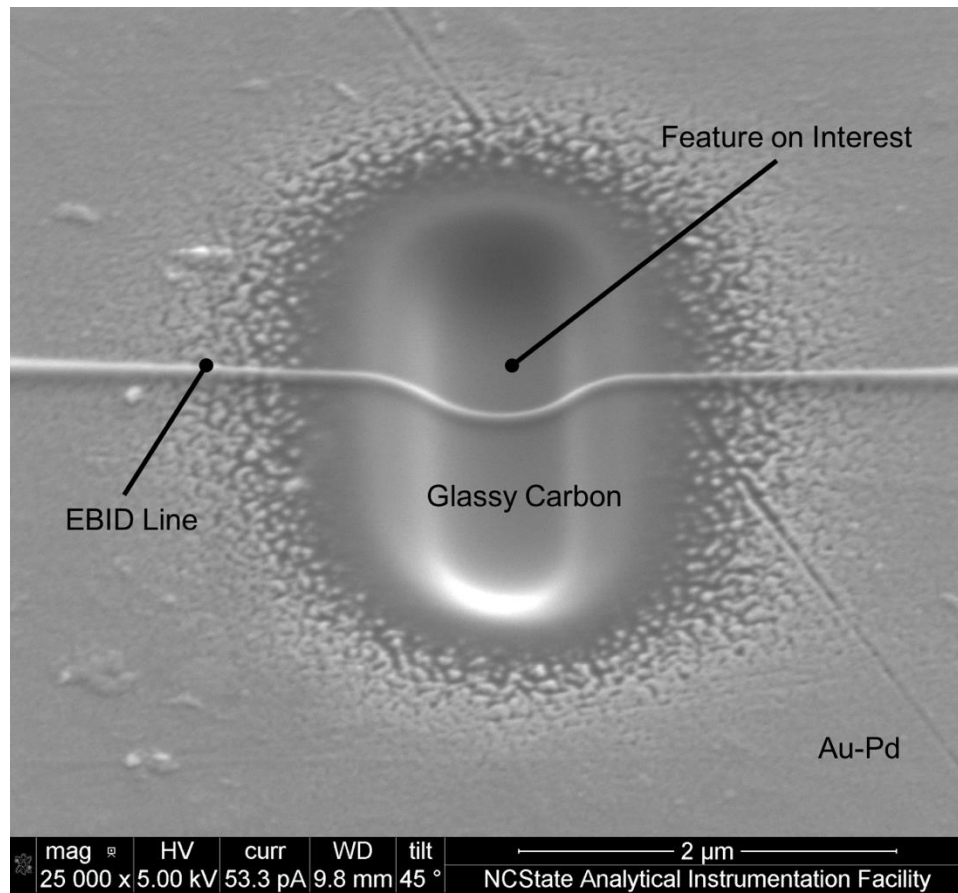


**Figure 8:** Example of EBID line

A Zygo New View 5000 scanning white light interferometer was used to measure the features created by the FIB. The scanning white light interferometer requires reflections from the feature of interest to be able to measure the surface. For some experiments, the surface was too rough, small or angled for light to reflect back to the sensor. For these cases, the surface was measured with the SEM. Before placing the sample into the SEM, a small amount of cutting oil was applied to the surface near the feature of interest but not on it. Figure 7 shows the glassy carbon sample with a line of oil on the surface. Through surface diffusion, a very thin layer of oil would then coat the feature. The hydrocarbon contamination was then polymerized with the electron beam to mark a line on the surface. This line could then be examined and imaged to understand the profile of the shape. This electron beam induced deposition (EBID) is described in more detail in many other places such as Brandon Suit's master's thesis [11]. Figure 8 shows an example of this measurement technique. The lighter material on the sample is the Au-Pd coating.

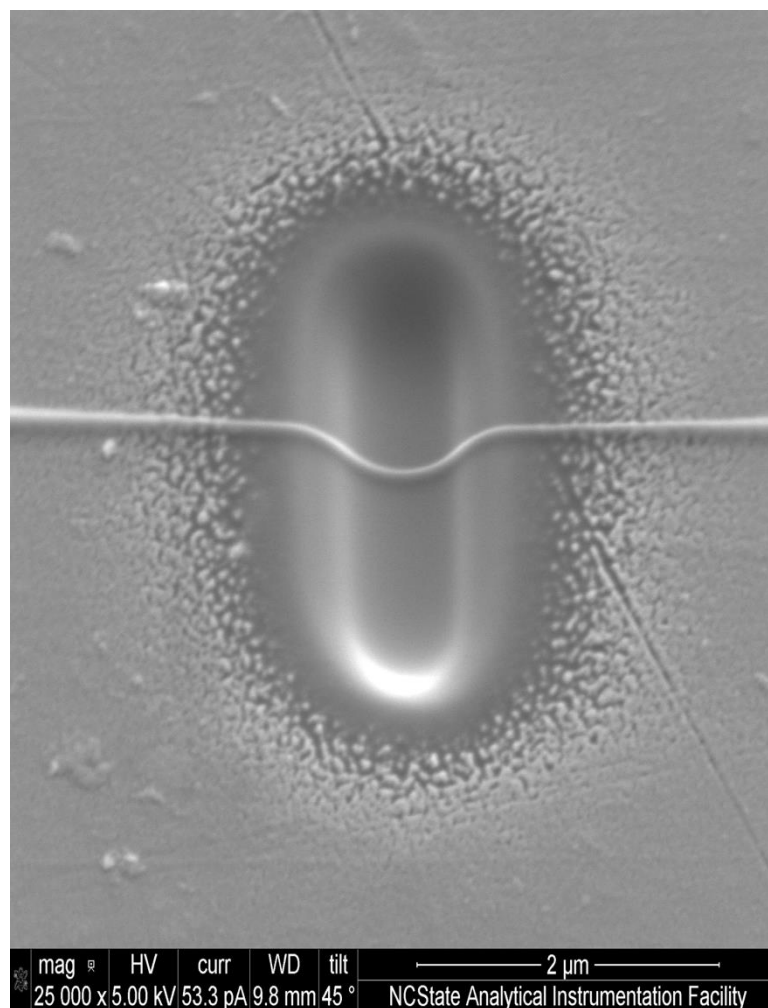


**Figure 9:** EBID image stretched vertically by 141.42% to show the true aspect ratio of a cross-section of the features machined on the FIB.

The vertical depression in the material is the feature of interest, a line created by a 15 nA ion beam. The horizontal line that follows the depression is the deposition created by an electron beam. To make this line, the electron beam was set to 5.0 kV and 53.3 pA. Depending on the amount of hydrocarbon contamination, the beam is set to scan in a line for 1-3 minutes. Then the sample is imaged at a 45° angle. The image is then stretched with image processing software such as Microsoft Paint or IrfanView by  $1/\cos(45)$ , or 1.4142, to simulate rotating the sample an additional 45 degrees and viewing the EBID line normal to the cross section of the feature of interest as seen in Figure 9. Utilizing a Matlab function created at the PEC, the profile of the feature can be measured by marking the EBID line and converting the image pixels to distance based on the scale bar. Figure 10 shows the Matlab function with the image imported and the EBID line marked. The marked points are then exported as (x,y) coordinates which can be plotted and analyzed.

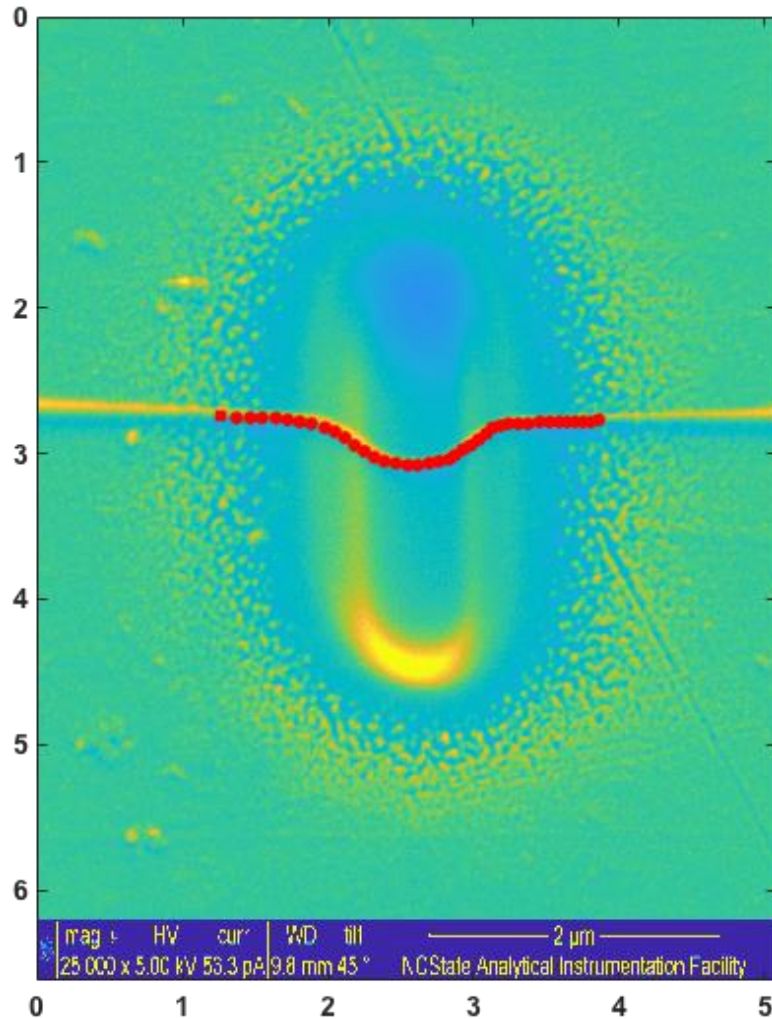


**Figure 10:** Matlab function with the EBID line marked.

## 6.2.2 Material Removal Rate

To determine the material removal rate of the FIB with glassy carbon, a simple experiment was devised. The FIB executed a square milling pattern. Based on Adams' work [10], it was recommended to keep the depth of the feature less than half the width of the feature to minimize redeposition. This means that as the material sputters, it can land back on the material and redeposit, reducing the effective sputtering rate and shape fidelity. This effect can be significant, particularly for deep narrow features where the sputtered material cannot escape. Adams also targeted a dose of  $\sim 5 \times 10^{18}$  ions/cm<sup>2</sup>. Using an assumed material removal rate for the beam current, initial values for the pattern size and dwell time can be estimated. Table 2 shows parameters used for the FIB pattern. The surface was measured with the New View 5000. Then the volume was calculated based on the surface measurement. This volume was divided by the amount of time the pattern required to yield a material removal rate.

**Table 2:** FIB parameters for material removal rate experiments

Parameter	Value
Pattern type	Rectangle
Application	Si
Scan Direction	Bottom to Top
Scan Type	Serpentine
X size	7 $\mu\text{m}$
Y size	7 $\mu\text{m}$
Overlap X	50%
Overlap Y	50%
Magnification	10,000x

Figure 11 shows the cavity created by a 15 nA beam. A maximum dwell time of 100  $\mu\text{s}$  was used. Then the number of passes was adjusted to 3962 to set the total milling time 24 seconds to control the dose. The surface was measured and the volume removed was calculated to be 73  $\mu\text{m}^3$ . This yields a material removal rate of 3  $\mu\text{m}^3/\text{s}$ . The experiment was repeated for a 65 nA current. The total milling time needed to be reduced to 6 seconds to attempt to keep the dose equivalent. The maximum dwell time was reduced to 1  $\mu\text{s}$ , and the number of passes was adjusted to 4615 passes to get the total time down to 6 seconds. The 65 nA beam removed 165  $\mu\text{m}^3$  of material and achieved a material removal rate of 27  $\mu\text{m}^3/\text{s}$ .



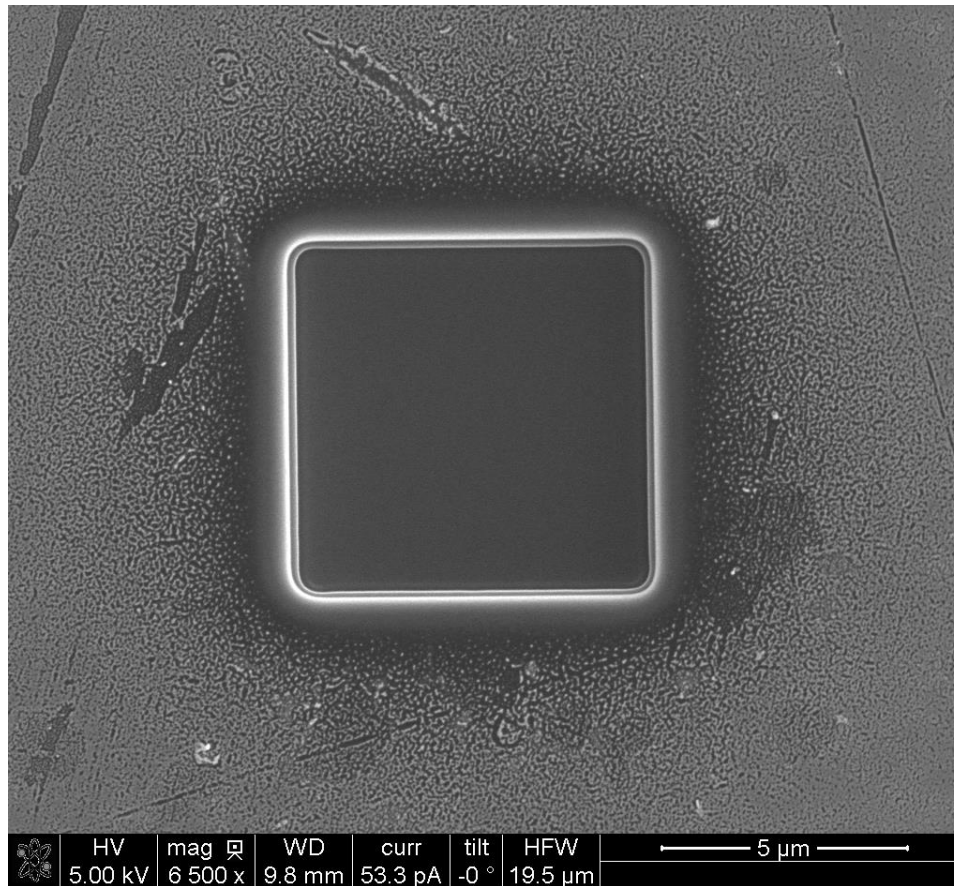


**Figure 11:** 7 μm square milled with a 15 nA ion beam.

The material removal rate allows the time to mill a single feature to be estimated. As mentioned previously, the volume needed to be removed to achieve the desired shape is  $485 \mu\text{m}^3$ . Removal rates of  $3 \mu\text{m}^3/\text{s}$  and  $27 \mu\text{m}^3/\text{s}$  correspond to machining times for a single feature of 162 seconds and 18 seconds respectively. This material removal rate study indicates that the FIB should be able to mill glassy carbon fast enough to make a die with 4 to 10 features in a reasonable amount of time, as in minutes or hours, as opposed to days.

### 6.2.3 Simulation

FIB milling is typically used for preparing samples for a transmission electron microscope or to prototype 2D structures that would otherwise be made with a photolithography process. In these techniques, the FIB will mill down to a discrete number of depths similar to 2.5-axis CNC milling in the conventional manufacturing world. The desired lens shape has a smooth contour and requires variable depth control just like full 3-axis conventional machining. One significant challenge to FIB milling this 3D shape is that no commercial software exists to plan the 3D “toolpath”. In a previous project, the PEC used the FIB to mill diamond dies for coining nanoscale

features. In collaboration with Smart Material Solutions, a local startup that licensed technology [12] developed by the Consortium, the PEC developed a Matlab function to simulate the FIB and how it removes material. This simulation tool is the critical first step to using the FIB to produce a finished surface just as a CAM software package is critical to conventionally milling a 3D shape with a 3-axis CNC machining center.

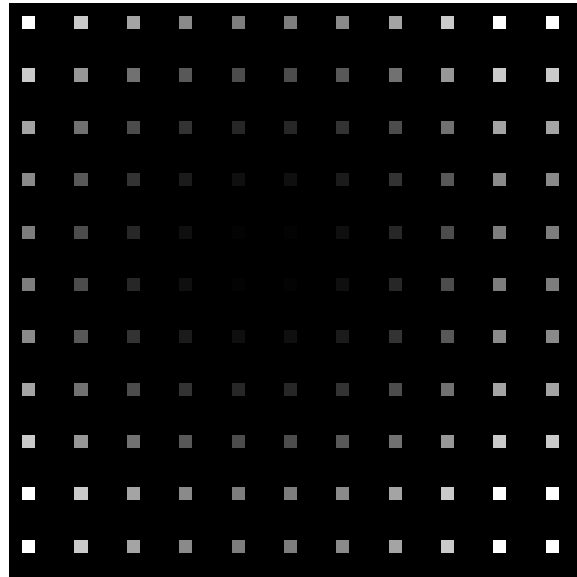


**Figure 12:** Example bitmap pattern for the FIB.

The simulation follows the basic method described by Adams [10]. It begins with a bitmap file. Each pixel represents a location in the FIB's field of view. The color represents the relative dwell time. A black pixel corresponds to no exposure while a white pixel indicates the maximum dwell time. The shades of gray represent the percentage of the maximum dwell that the location will be exposed to. Figure 12 shows an example pattern. In this pattern, the black in the center represents a high spot as black denotes no milling will happen there. The white in the corners are the low spots, so they are brighter which corresponds to longer exposure to the ion beam.

The simulation uses a model for the beam intensity distribution to determine the dose applied to the surface at and around each pixel commanded to turn on the ion beam. Typically, in literature a Gaussian distribution is used for the beam [8]. A removal factor is calculated based on the angle of incidence and the sputtering dependence on the angle of incidence. The beam shape is then convolved with the removal rate to determine the surface. This process is repeated for the number of passes specified to determine the final shape of the surface. Figure 13 shows an example output of the FIB milling simulation with dummy parameters input for the beam shape and sputtering yield. It should be noted that this simulation does not account for redeposition.

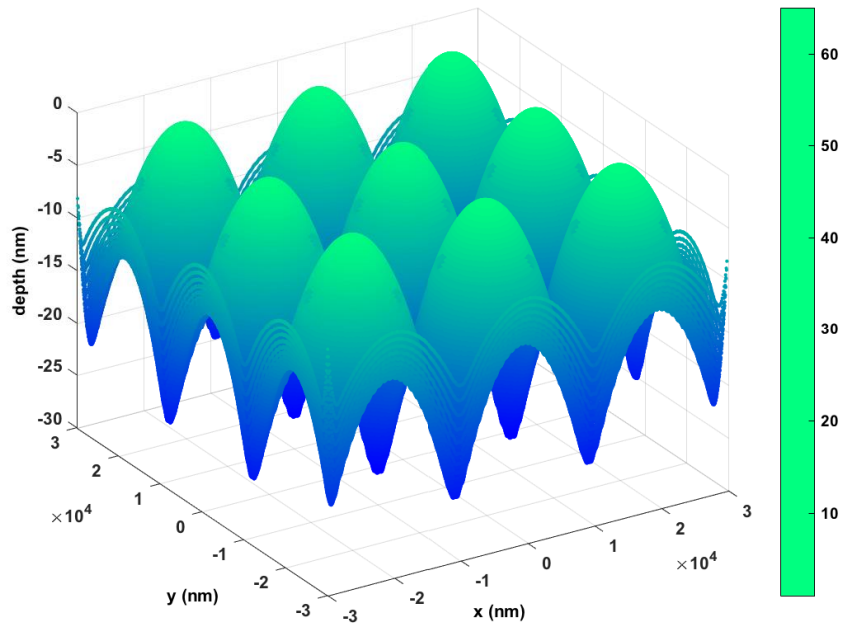


Figure 13: Example output of the FIB milling simulation

### 6.2.4 Beam Shape

The first piece of information to begin the simulation is the beam shape. The beam intensity distribution is difficult to directly measure. However, to begin investigating the beam shape the material removed is used as a surrogate for the beam intensity. The reasoning here is that the material removed will scale linearly with the ion dose for shallow depths.

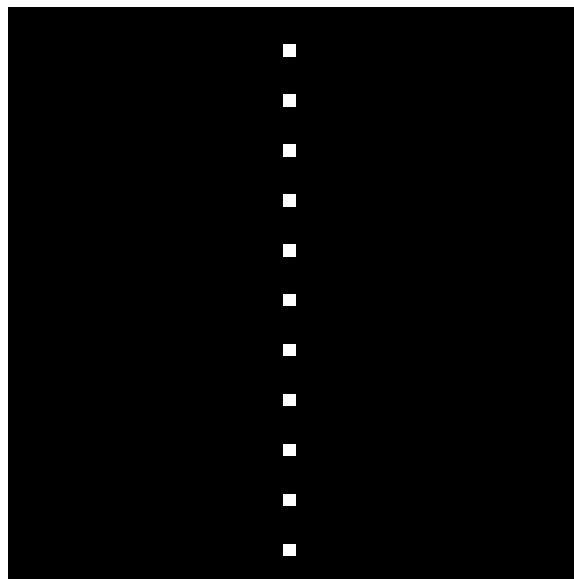
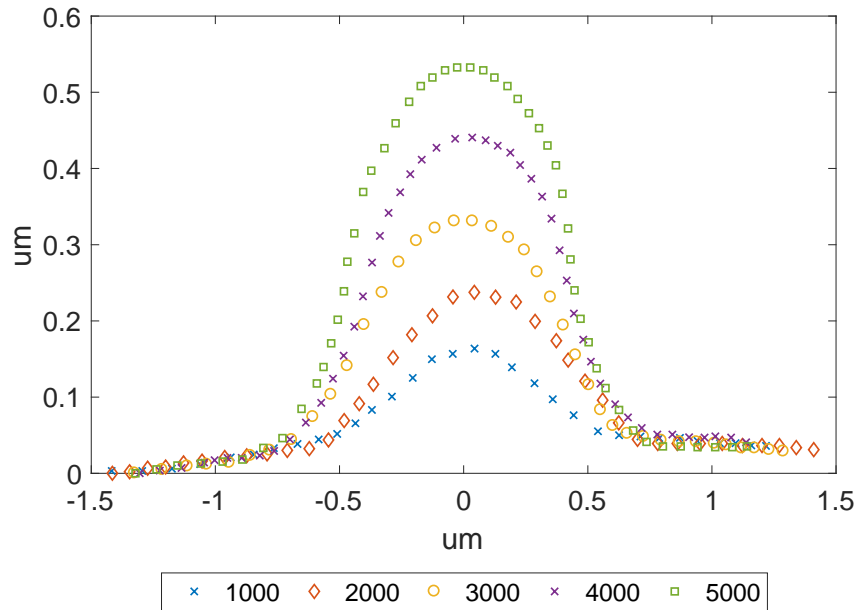


Figure 14: Bitmap for the beam shape experiment



A bitmap was generated with a single line of pixels to mill a thin line the width of the beam. Figure 14 shows the bitmap used to command the FIB. For this bitmap, the pixels are 8 nm. The white pixels are spaced 32 nm apart. The experiment was conducted with a 1 μs maximum dwell time and repeated with 1000, 2000, 3000, 4000 and 5000 passes which increases the depth of the line. The lines were then measured with the EBID. Figure 9 shows a representative line measured with this method. This line was milled with a 15 nA beam current and 3000 passes.

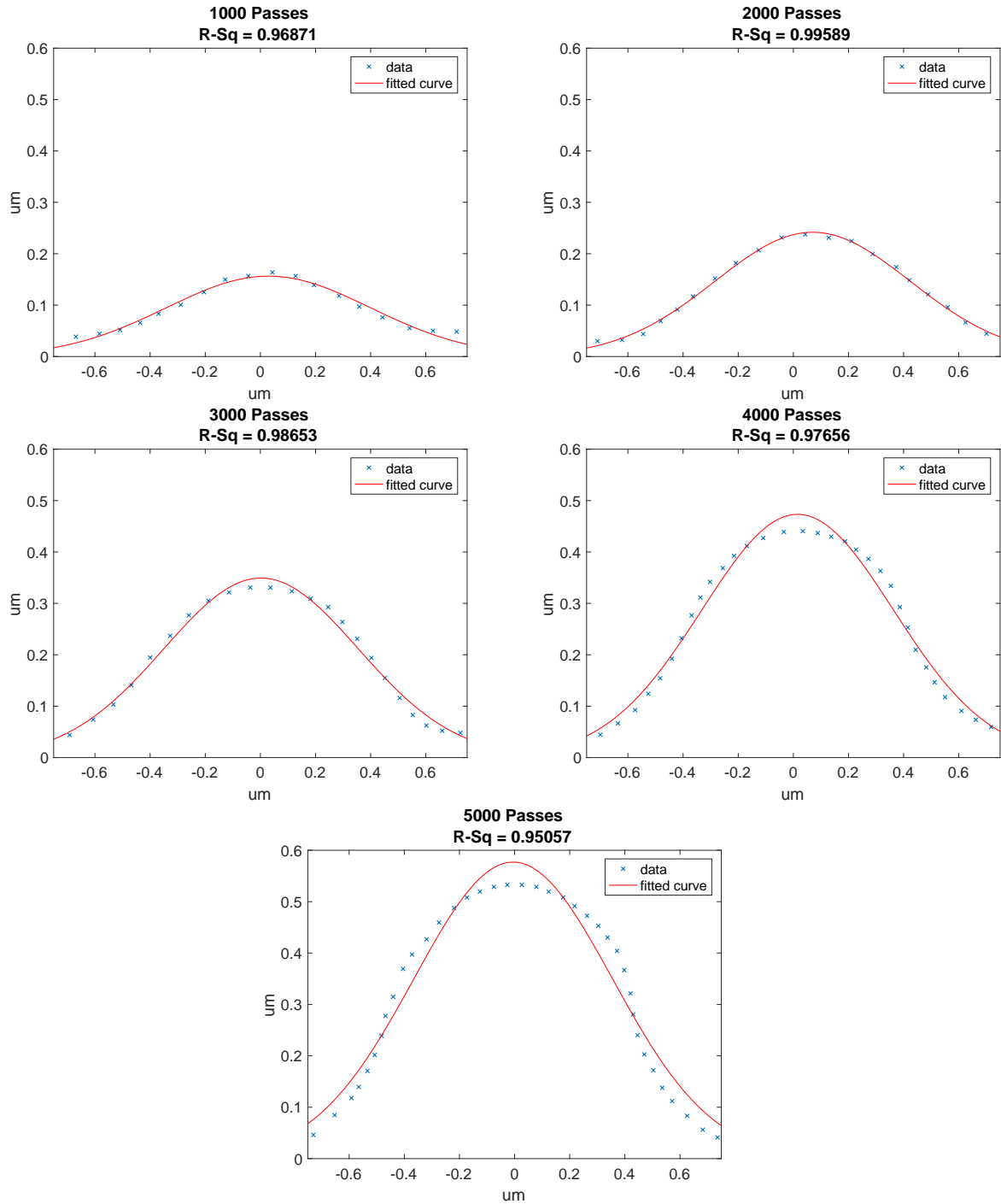


**Figure 15:** Profiles of lines produced by a 15 nA ion beam after n passes.

Figure 15 shows the resulting data for a 15 nA beam current. As can be seen from the figure, increasing the number of passes increases the depth as expected. However, the width stays roughly the same. The data was fitted with a Gaussian equation of the following form:

$$y = a1 \cdot e^{-\left(\frac{x-b1}{c1}\right)^2}$$

In the above equation a1, b1, and c1 are constants, where a1 controls the amplitude, b1 the x shift, and c1 the width of the curve. For the purposes of the beam shape model, the constant c1 is the main parameter of interest. A1 should be proportional to the dwell time, and b1 will be related to how well the data is centered in the measurement coordinate system.



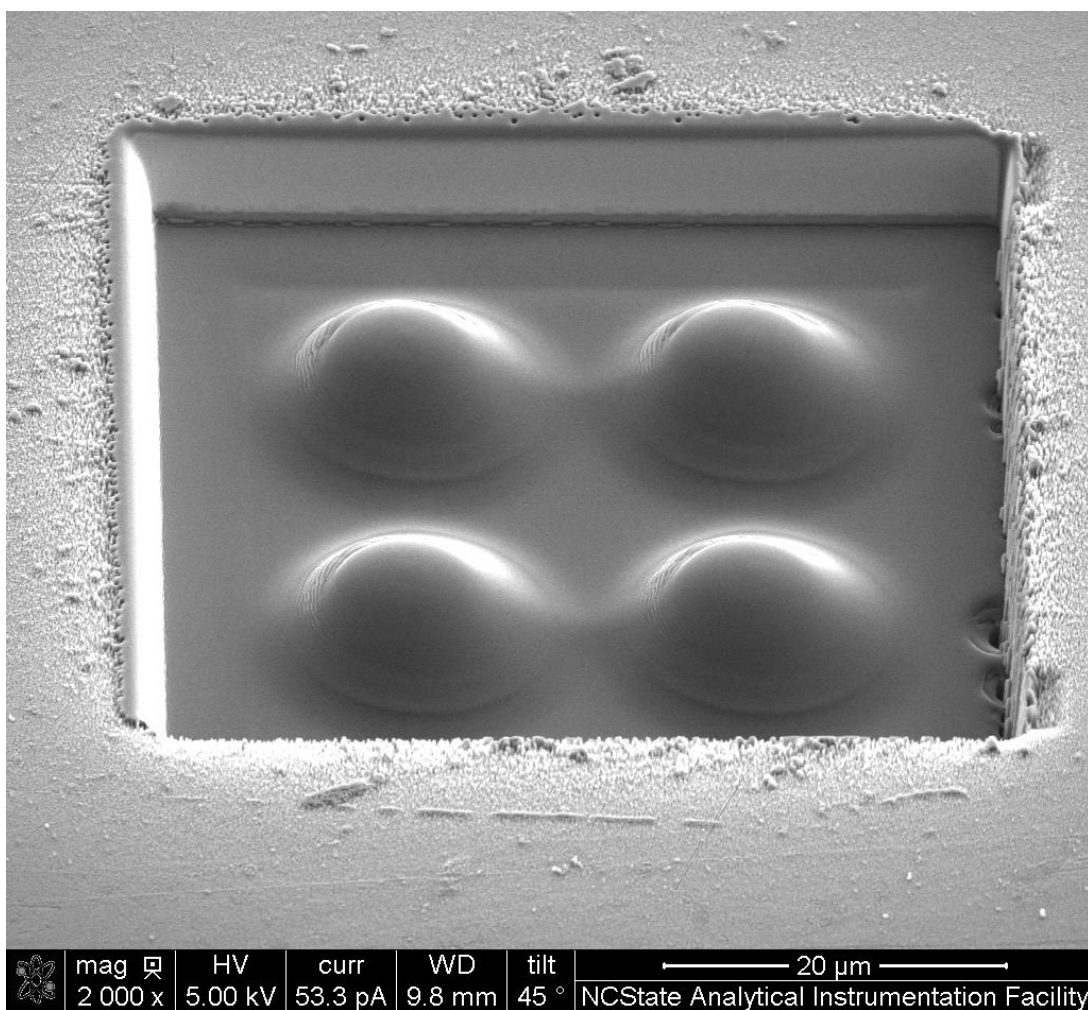
**Figure 16:** Gaussian fitting to 15 nA lines for varying number of passes.

Figure 16 shows the resultant fittings for each experiment along with the R-squared value. The Gaussian distribution fits very well to the data. Table 3 shows the value of  $c_1$  for each experiment. The average of  $c_1$  across the experiment is 0.5048 with a standard deviation of 0.0125. The low standard deviation indicates that the beam shape is stable and not changing with the depth of cut.

This value of c1 can then be included in the FIB milling simulation to begin modeling an actual milling process.

**Table 3: Summary of significant Gaussian fit parameters.**

Number of passes	c1
1000	0.5241
2000	0.5003
3000	0.4984
4000	0.4918
5000	0.5094



**Figure 17.** Four nominally 20  $\mu\text{m}$  radius spheres milled into Glassy Carbon. The material outside of the box will be removed so that the features are above the die base.

Figure 17 shows a glossy carbon sample with four nominally 20  $\mu\text{m}$  radius hemispheres that have been milled into the flat sample. The image shows the features create a die, which when pressed into the mold material will produce an injection mold to create a large array of lenses as shown in Figure 3. The margins of the die in Figure 17 will be removed with the FIB so that the die can press into the mold and create the desired features. This brings up other issues such as the material pushed out of the indented features and how to control that such that the desired molded part is achieved. This is discussed in Section 7.

## 6.3 CONCLUSIONS

In this work, a screening experiment was conducted to see if the FIB could cut a glassy carbon die with 4-10 features in a reasonable amount of time. The experiment indicates that the FIB could cut a single feature in a matter of minutes. From there, the PEC collaborated with Smart Material Solutions to continue to develop a FIB milling simulation tool. This tool was updated to handle microscale features as its original purpose was to model nanoscale features. Finally, experiments on the beam shape were completed and determined the beam width parameter to be input into the simulation tool.

Future work will include determining the sputter yield as a function of angle of incidence. Then the simulation tool will be validated by comparing the simulation output to actual parts. Finally, the simulation tool will need to be inverted to become a planning tool. Instead of predicting the final shape given the bitmap, it needs to output the bitmap given the desired final shape. Section 7 discusses the issues related to pressing this die into a plastically deforming material to produce the mold.

## REFERENCES

1. Zdanowicz, E., *Nanocoining sub-micron features*. Ph.D. thesis, North Carolina State University, Raleigh, NC, (2013).
2. Nowak, W., *Ultrasonic nanocoining of sub-micrometer surface features*. Ph.D. thesis, North Carolina State University, Raleigh, NC, (2014).
3. Yoshida, Y., W. Okazaki and T. Uchida, *Laser and focused ion beam combined machining of micro dies*. Review of Scientific Instruments, 83, (2012).
4. Langridge, M.T., D.C. Cox, R. P. Webb and V. Stolojan, *The fabrication of aspherical microlenses using focused ion-beam techniques*. Micron, 57, p.56, (2014).

5. Youn, S.W., M. Takahashi, H. Goto and R. Maeda, *A study on focused ion beam milling of glassy carbon molds for thermal imprinting of quartz and borosilicate glasses*. Journal of Micromechanics and Microengineering, 16, p. 2576, (2006).
6. Vasile, M., Z. Niu, R. Nassar, W. Zhang, and S. Liu, *Focused ion beam milling: Depth control for three-dimensional microfabrication*. Journal of Vacuum Science and Technology B, 15, p. 2350 (1997).
7. Vasile, M., X. Jushan and R. Nassar, *Depth control of focused ion-beam milling from a numerical model of the sputter process*. Journal of Vacuum Science and Technology B, 17, p. 3085, (1999).
8. Vasile, M., R. Nassar, J. Xie, and H. Guo, *Microfabrication techniques using focused ion beam and emergent applications*. Micron, 30, p. 235, (1999).
9. Adams, D., M. Vasile, T. Mayer, and V. Hodges, *Focused ion beam milling of diamond: Effects of H<sub>2</sub>O on yield, surface morphology and microstructure*. Journal of Vacuum Science and Technology B, 21, p. 2334, (2003).
10. Adams, D., M. Vasile and T. Mayer, *Focused ion beam sculpting curved shape cavities in crystalline and amorphous targets*. Journal of Vacuum Science and Technology B, 24, p. 1766, (2006).
11. Suit, B., *Analysis of accelerated tool wear and built up edge when diamond turning ferrous materials*. M.S. thesis, North Carolina State University, Raleigh, NC, (2016).
12. *Methods and systems for fast imprinting of nanometer scale features in a workpiece* WO 2014052777 A1, April 3, 2014.

## 7. MULTI LENS ARRAY- II: INDENTATION AND CREATION OF THE MOLD

**Gaurav Dave**

Graduate Student

**Sriraghav Sridharan**

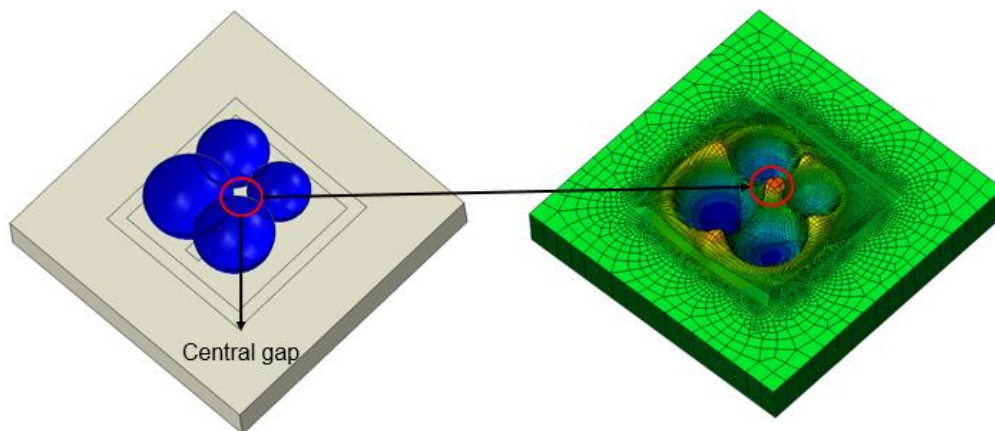
Graduate Student

**Advisor: Dr. Mark Pankow**

Assistant Professor

Mechanical and Aerospace Engineering

*This report is focused on understanding the indentation process for forming micro lens arrays. A finite element model has been developed to understand the plastic flow of this indentation process. It will be used to optimize this process to produce the best possible optical arrays. Preliminary results show promise for understanding how the deformation process works and offer insights on where to minimize the error to the surrounding lenses in a continuous high-speed indentation process.*



## 7.1 INTRODUCTION

This report is a continuation of the previous section on the multi lens array. The objective of this part of the report is to develop and execute a finite element model to understand the manufacturing process involved in fabrication of such a multi lens array. Specifically, the indentation process by which the mold would be manufactured is considered so that the micro lens array can be fabricated quickly, as there over a million lenses. The impact of each indent on the previous indents around it is characterized. The plastic flow from one indent will affect the shape of the other indents around it, which would ruin the profile of the optical lenses. Therefore, the goal is to arrive at an indentation strategy for a mold which is feasible to manufacture in the size scale desired, while minimizing the impact on the optical performance of the micro lens arrays.

## 7.2 DETAILS OF THE PROJECT

The overall model is aimed at understanding the indentation process needed to form the multi lens arrays. Early models are aimed at understanding the process and the impacts of certain decisions, since many of the details of the optical surfaces were still being evaluated.

### 7.2.1 Materials

As a starting point for the analysis, it is important to ascertain the materials to be used for the mold as well as the indenter/die. A relatively “rigid” die is to be used to press down a hemispherical lens shape into the mold. The rigid die could be made of diamond or glassy carbon, both of which are much harder than the metal mold which would be used. The indentation would result in plastic deformation in the mold material, making the desired shape. A soft metal generally used for plastic injection molds can be considered a good starting point for the material in the mold. Therefore, Aluminum 7075-T6 (Al 7075) is used in this study as an arbitrary starting point for which most plastic properties are readily available. It is understood that the mold material could be changed later which would only change the elastic-plastic response in the material model.

The material model used at present is an elastic-plastic model with strain hardening beyond the yield stress point, as shown in Figure 1. The die is modeled as a purely rigid surface which would be unaffected in the analysis. The material properties of Al 7075 are shown in Table 1 and **Figure 1**. Strain hardening captures the material response during plastic deformation. Without a nonlinear plasticity model, a finite element analysis would not be able to simulate large deflections and the permanent deformation.



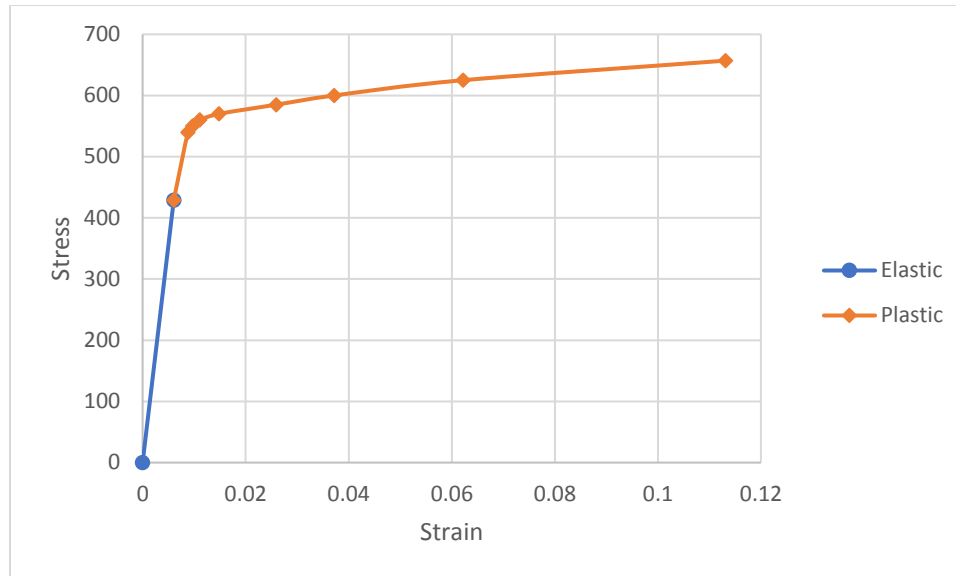


**Figure 1.** Stress strain curve used for Al 7075 [1]

**Table 1.** Density and Elastic constants of Al 7075 [1]

Density (kg/m <sup>3</sup> )	Young's Modulus (GPa)	Poisson's Ratio
2700	71	0.33

## 7.2.2 Indentation Profile

The final shape on the mold would invariably be used to make the optical lens array. Due to the size of the lens and the spacing of the LED pixel there will be overlap between the adjacent sphere's which will produce a square grid pattern. The exact dimensions of the lens are yet to be finalized. The current geometry assumes a worst-case scenario where the diagonal of the square will have a half sphere profile. This will result in a spike at each corner of the square which will be difficult to manufacture. For the sake of the finite element analysis, it is assumed that a center to center distance of 35 $\mu$ m exists between 2 pixels. This distance defines the final diameter of the die to indent onto the mold. As a measure to improve the packing of lenses close to each other, there exists significant overlap between neighboring passes of the indenter. This can be clearly seen in **Figure 2**, where the same indenter is shown in 4 proximal positions. The diameter of the indenter is equal to the diagonal of the square formed by a side of center-to-center distance 35 $\mu$ m, i.e. 49.5 $\mu$ m. The reason for this diameter size is as follows:

The indentations need not have a spherical profile in all directions for the lens, as the edges produce a minimal impact on light output. Therefore, only the diagonal contains the full sphere

while the horizontal and vertical profiles are a portion of a sphere. The profile of the indentation can be better understood using **Figure 3-Figure 5**.

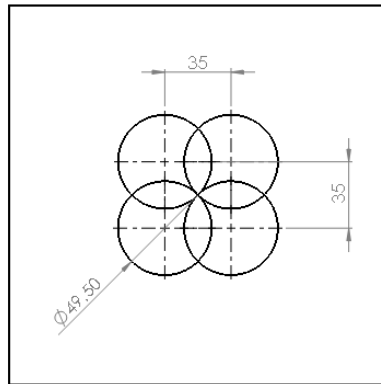
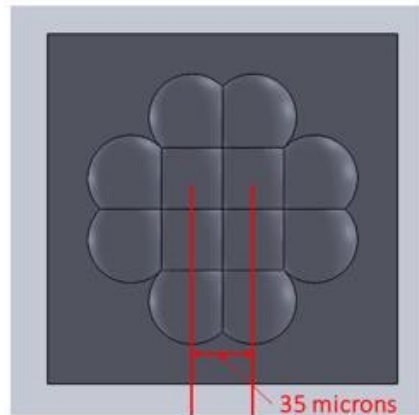


**Figure 2.** Four proximal indenters to show space savings (all dimensions in microns)

**Figure 3** shows a completed 2x2 grid in the center. The overlapping ensures that the spherical shape is truncated on each of the 4 corners. This can be visualized in **Figure 4**, where the highlighted portion shows the shape of 1 lens.



**Top View**

**Figure 3.** Top view of a completed 2x2 grid of lenses in the center region. The impacts around the edge are only to show what the actual center geometry looks like.

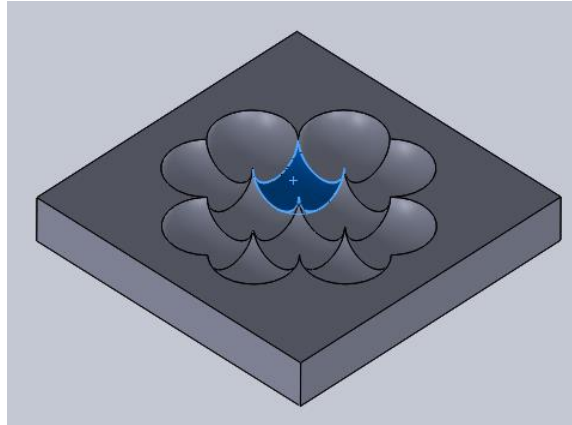


**Figure 4.** Visualization of a single lens shape, with the full spherical profile along the diagonal.

As mentioned before, a section cut in the direction of the diagonal would generate a semi-circular profile, which can be seen in Figure 5.

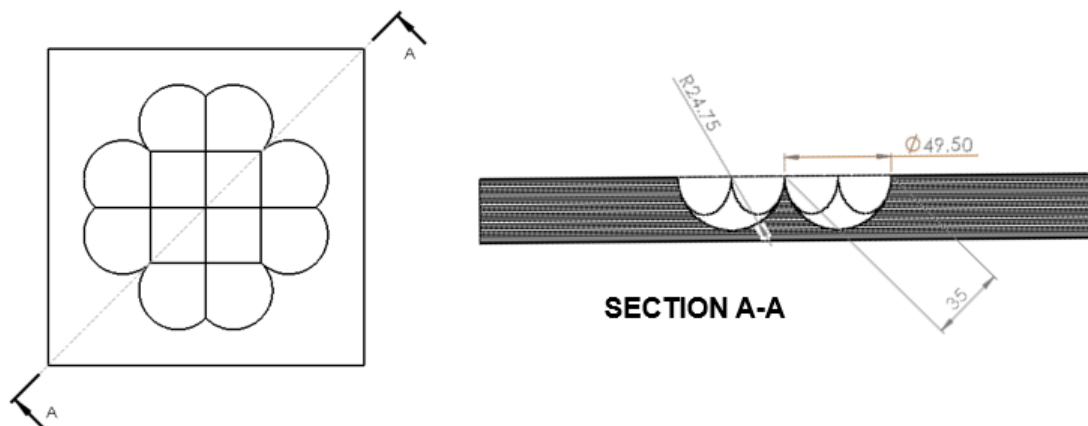


**Figure 5.** Sectioned view of the indentation profile along 45 degrees, showing the full semispherical indentation that would occur.

### 7.2.3 Progressive Indentation

For an indentation of depth  $24.75\mu\text{m}$ , there is a large quantity of material either displaced or deformed with each indentation, when compared to a nano scale indentation. This would invariably lead to material rise on the sides when the die would insert into the mold. As mentioned earlier, the amount of spring back from a material could be a deciding factor in the shape of the lens. Hence, if the indentation process is progressive in nature, i.e., if multiple die heads are used to increase the depth of the indentation, the material rise on the sides as well as the spring back in the mold could be better mitigated. From the standpoint of a finite element analysis, this is good idea as the tendency of distortion in elements leading to erroneous results is higher with higher deformations. Keeping this in mind, this study has modified the rigid die to

have 4 different diameters, essentially making it a 4 piece die. A drawing of this die that was used in this study is shown in Figure 6. The labels A, B, C, and D, as marked in red in Figure 6, represent each step in the indentation, as well as the depth of each step in the indentation process. The choice of the diameter of each shape is arbitrarily chosen at present, and will be optimized in future work. The current profile is used as a baseline to understand the material flow, indentation depth required, and impact on final shape.

**Table 2** shows the current configuration of indenters on the die.

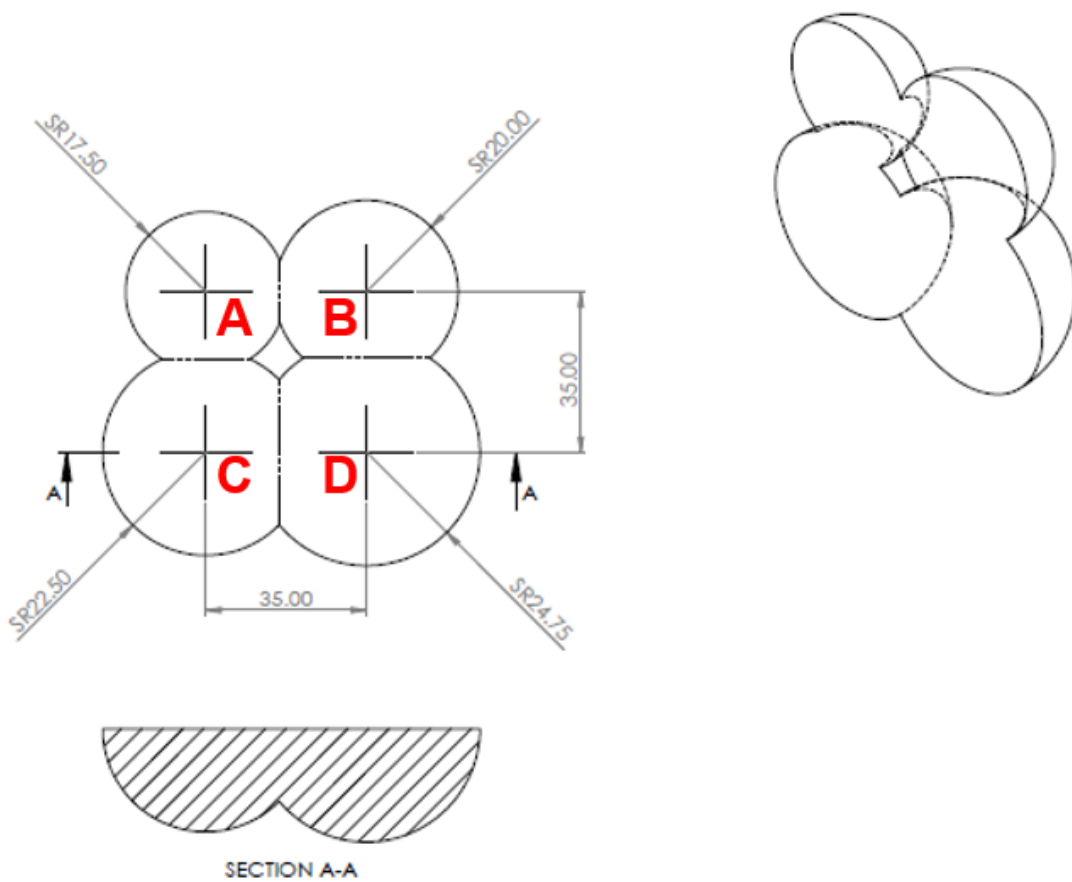


**Figure 6.** Drawing of a 4 piece die for progressive indentation. Each successive indentation A – D produces a larger profile. This progressive nature lowers the plastic flow on the surrounding indents.

**Table 2.** Progressive indenter dimensions

Indenter	Radius in microns
A	17.5
B	20
C	22.5
D	24.75

The plastic flow of the material on the sides of the indenter will be used to our advantage since, one can indent to a smaller depth to get the same final profile. This lowers the actual actuation distance along with the amount of plasticity that needs to occur in the material. This is another parameter which could be tweaked once the material properties are finalized.

In order to create a 2x2 grid in the center as shown in **Figure 3** with a 4 piece indenter discussed above, an indentation strategy needs to be developed which would culminate in that final shape. In this work, a sheet of material mounted on a large drum on a diamond turning machine rotating slowly (~ 1rpm). The indenter will then be placed normal and impact the surface producing the indents. After each “column” of indents it will move over one “column” to produce the next array of lenses. Due to the position of the “A” and “B” dies, the end of each row would lead to the mold having indents corresponding to only “B”. Once the die moves over, this cycle would be repeated, and the end of the second pass would mean only indents of the required depth (24.75µm) remain.

This process could be simplified on to a flat plate (2x2 grid) being indented by a 4 piece indenter in a similar procedure, as shown in **Figure 7** and **Figure 8**. In steps 1-3, the 4 piece indenter moves vertically down. At the end of 3, the grid is partially complete with a “B” shaped depth. Now, the indenter moves 1 pixel pitch to the left, and the process repeats. At the end of 6, there exits two indents of size “B”, and two complete indents of size “D”. Again, the 4 piece indenter moves 1 pixel pitch to the left, and the process repeats till all 4 indents of concern are of size “D”. Thus, it would take a sequence of 9 steps to create the 2x2 grid.

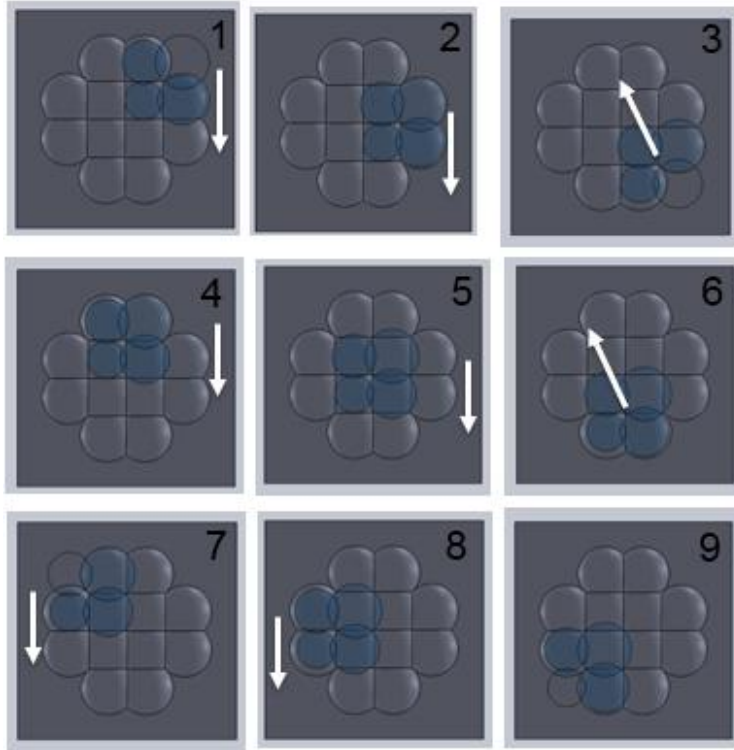


**Figure 7.** Indentation sequence to create a 2x2 grid

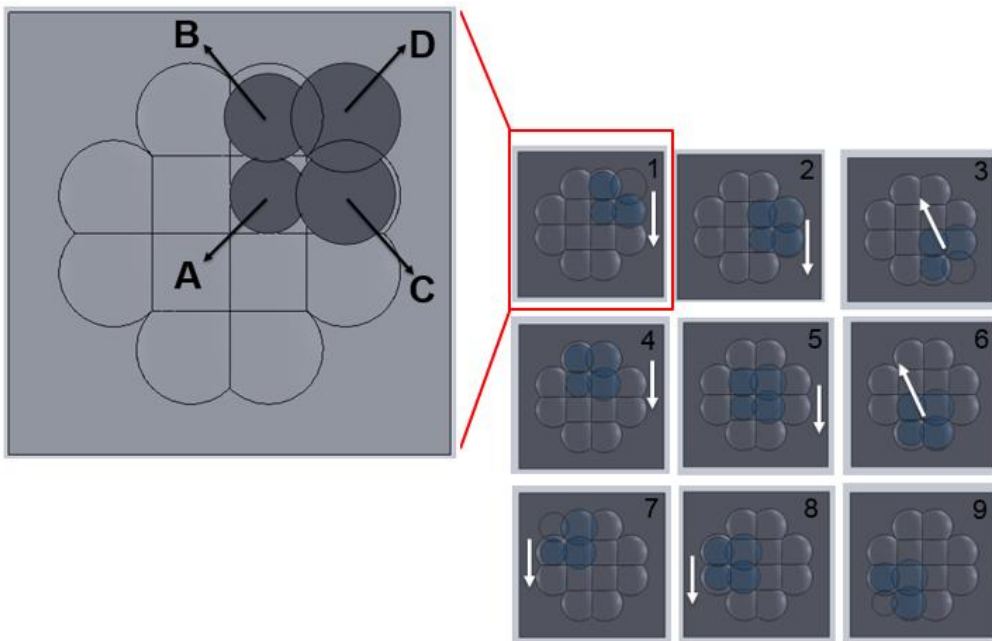


**Figure 8.** Indenter markings

## Finite Element Modeling

The finite element model was developed using the Abaqus™ commercial software. In order to be in the same time range as the actual proposed setup, an explicit analysis is suited to this study, as it would run for the actual time of the process. For this study, each loading operation of the die indenting into the mold was carried out for 1.25e-5 seconds. This means that the overall operating frequency of the process in this simulation is 40 kHz. It should be noted that the analysis results would remain fairly independent of the analysis time as long as the material model considered is rate independent. The loading rate dependency of the mold material is yet to be tackled in this study. A mass scaling factor of 1000 is also applied to each step of this model to improve its computational efficiency, and the inertial effects are kept in check (<5%) of the total energy to ensure the accuracy of the results.

In order to prevent excessive distortion in the elements due to the indentation operation, an adaptive mesh scheme (called Arbitrary Lagrangian-Eulerian, or ALE, in Abaqus™) has been implemented. This scheme would try to maintain the shape of the original mesh and the model would be adjusted after each subsequent iteration. The geometry of the finite element model was evolved, as the indenter diameter and shape was modified. But, each indenter was modeled as a rigid sphere or a hemisphere, which was independent and didn't have to be meshed in a FE model. The specimen was modeled as a deformable body with large deformation and Al 7075 material properties. Interaction between the indenter and the specimen were modeled as default contacts. A preliminary FE model highlighting some of these analysis properties is shown in **Figure 9**.

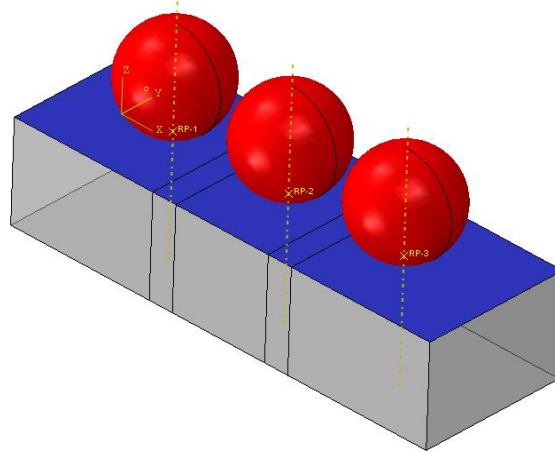


**Figure 9.** Preliminary FE model with highlighted contact surfaces, which will be used to understand how one indent influences the next.

A preliminary model with an indenter radius of 10 $\mu$ m was initially set up to understand some of the material flow properties, which are discussed in the next section.

## Material Spring back

Due to plasticity of Al 7075, there is some spring back expected in the material after the indenter is removed. It is important to characterize this so that we can make a die which produce the final optical shape that includes the spring back. To ascertain this, a preliminary analysis was carried out, as shown in **Figure 10**. This sequence is considered to show both the material rise in the mold, as well as the spring back in the material post-indentation. The arrows indicate the movement direction of the indenter. Although the desired indentation depth is  $10\mu\text{m}$ , the material rise on the sides meant that the indenters were only pushed to  $7.6\mu\text{m}$ . The actual indentation depth would vary after the material model is finalized.

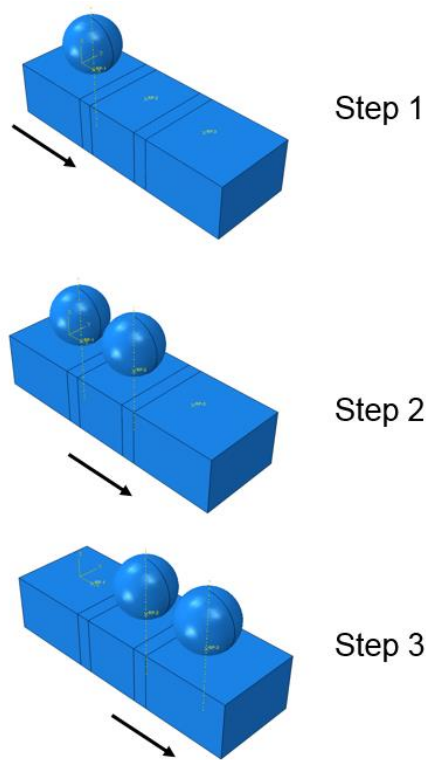


**Figure 10.** Indentation sequence for a preliminary analysis, capturing the overlap that occurs in each step.

**Figure 11** shows the section along the length of the specimen after the 1<sup>st</sup> step, which gives a good indication of the material rise. The maximum deviation from the desired profile is at the bottom of the mold, equal to  $0.441\mu\text{m}$  (4.4% for a  $10\mu\text{m}$  indent). Similar results after the 2<sup>nd</sup> step are shown in **Figure 12**, with maximum deviation being  $0.442\mu\text{m}$  at the bottom of the mold. After the 3<sup>rd</sup> step, the final indentation profile is shown in **Figure 13**, with the maximum deviation being  $0.476\mu\text{m}$ .



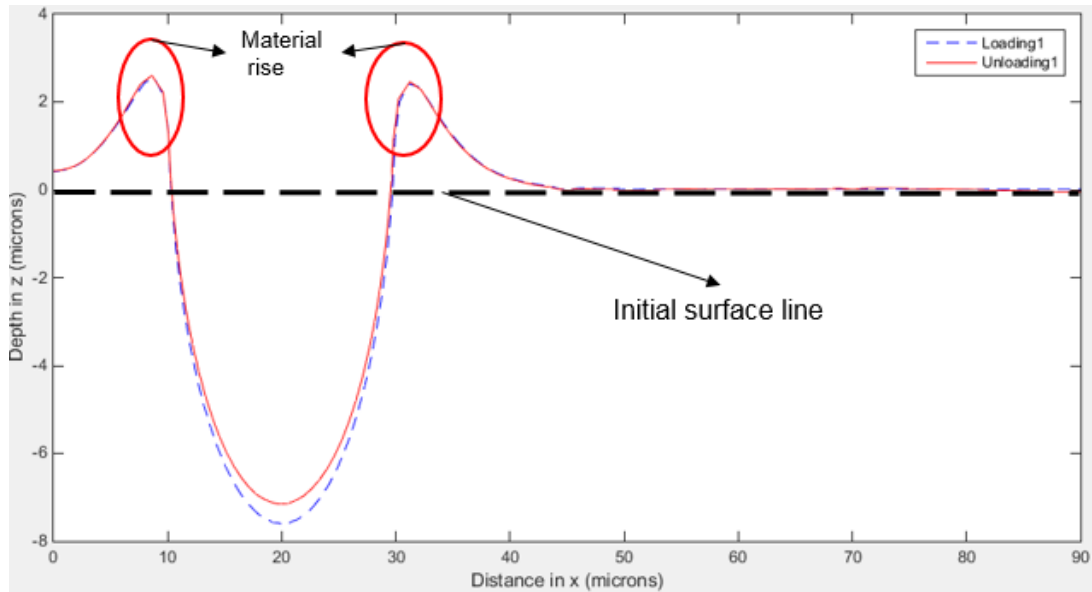


**Figure 11.** Simulation of material rise after step 1, characterizing the spring back that occurs.

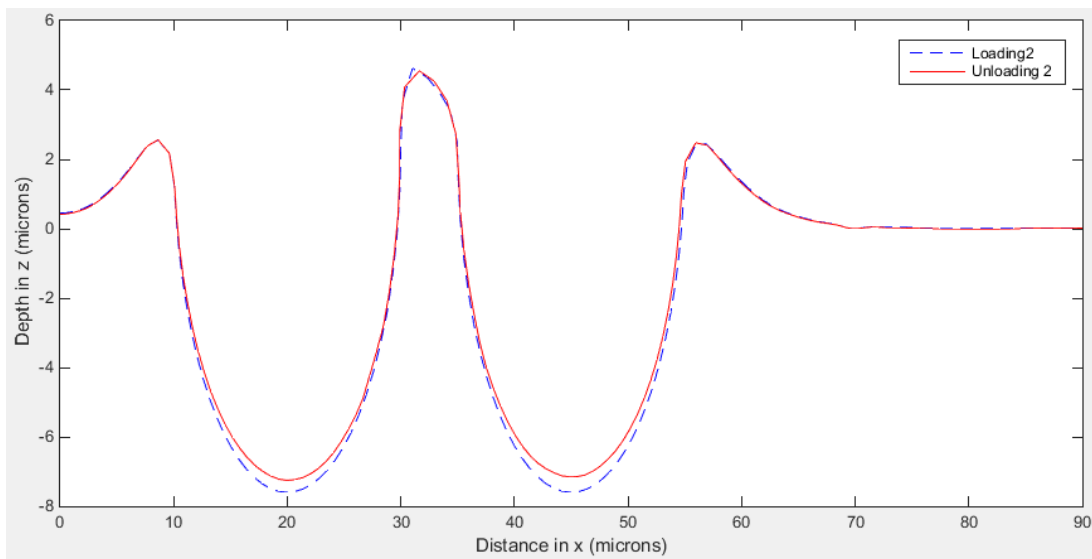


**Figure 12.** Simulation of the material rise after step 2, characterizing the spring back that occurs.

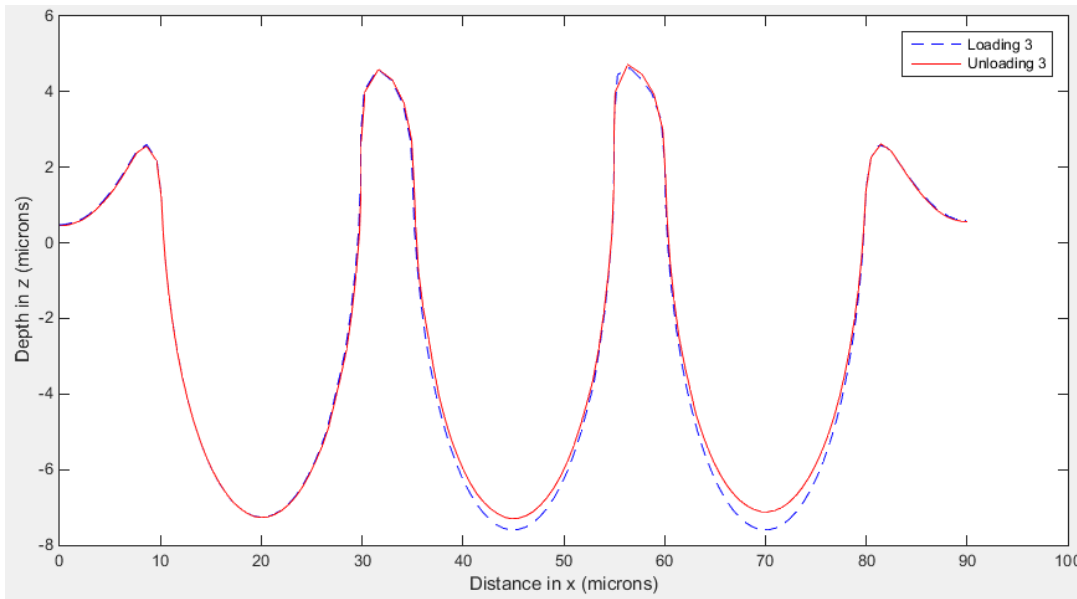


**Figure 13.** Simulation of the material rise after step 3, characterizing the spring back that occurs.

**Table 3.** Characterization of material spring back, after indentation

Step	Maximum spring back ( $\mu\text{m}$ )	Secondary spring back ( $\mu\text{m}$ )
1	0.441	NA
2	0.442	0.347
3	0.476	0.297

As can be seen from these results, the material spring back is smaller for an overlapping step. For instance, the spring back in the 1<sup>st</sup> indentation during the 2<sup>nd</sup> step is slightly smaller than that in the 2<sup>nd</sup> indentation. However, the difference is not great with respect to the scale of the desired profile. **Table 3** summarizes the material spring back for a 10 $\mu\text{m}$  indent. The deviation from the profile due to material spring back is no more than 5%, and is maximum near the tip of the lens.

### Reason for overlap

As can be seen in **Figure 10**, the indentation sequence shows an overlap, i.e., the die is used to indent in the consecutive step even after the indent is already created in a previous step. This is used in all FE models to prevent the change in profile after indentation. The need for this overlap could be easily shown using the following test sequence, as shown in Figure 14 (top view of the assembly). The sequence on the left of the figure does not involve any overlap, whereas the

sequence on the right does. The spherical indenters of radius  $10\mu\text{m}$  are pushed in by  $7.6\mu\text{m}$ . Right now, only 1 row of overlap is kept in this study. With a more complex loading cycle, instead 2 rows of overlap would be needed, which could be tackled based on the FEA results. The results of this test between no overlap and overlap can be visualized by creating a section view of the profile post indentation along the specimen length, as shown in Figure 15 and **Figure 16**, respectively. As can be seen from Figure 15, the second cycle leads to a significant change in the profile of the hemisphere, in more than 1 direction. This is mitigated if the central row of indenters are repeated for each cycle, as no such profile change is visible in **Figure 16**.

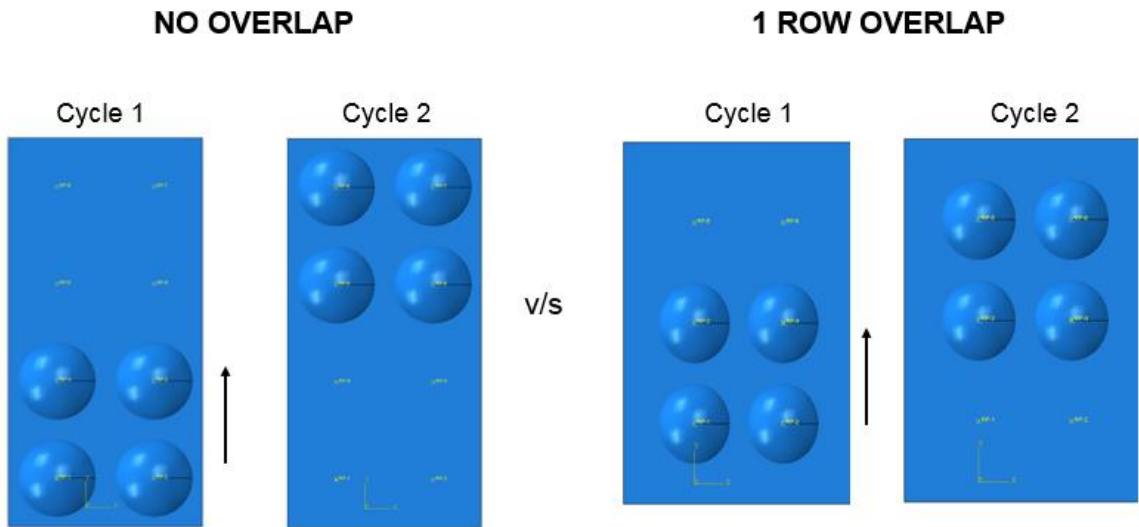


**Figure 14.** Variation of indentation sequence to show the need for overlap: Top view

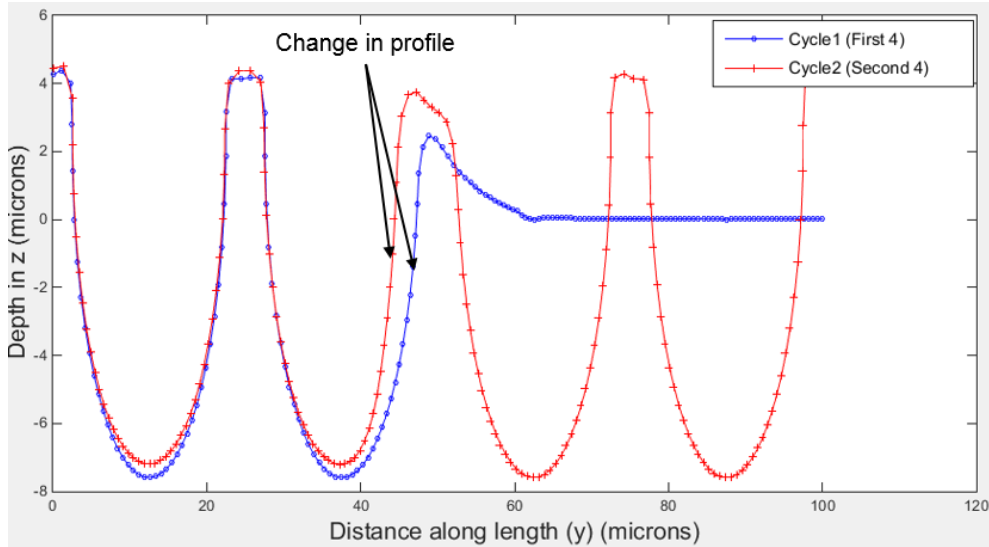


Figure 15 Indentation profile without overlap

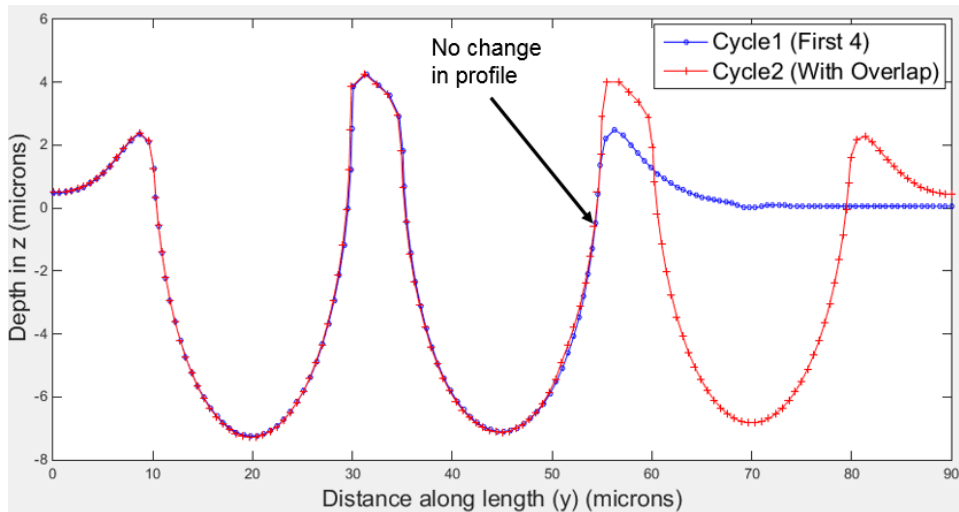


Figure 16. Indentation profile with overlap

Hence, from this test, it can be concluded that at least a single row of overlap would be needed to maintain the desired shape of the desired profile during the creation of the mold.

### Strain Rate Independent Material Selection

One of the issues associated with the selection of the substrate material for the mold is that the indentation process is expected to happen at 1 kHz, which means that the effect or rate stiffening could impact the indentation process. From the preliminary tests performed in this study, the maximum strain reached is around 250%. This would roughly translate to a strain rate of the order of  $10^3$ - $10^4$ /s. Material selection is underway for material which would remain rate insensitive until well above these strain rate values. Otherwise, it would be wise to incorporate those strain rate

hardening effects of Al 7075 in the future. In addition NCSU's BLAST lab has the capability to characterize these rate dependent material properties for both tension and compression.

### Progressive indentation: Finite Element Modeling

The smallest repeating cell of material which has to be indented by the 4 piece indenter, as well as the rigid 4 piece indenter, are built for a FE model, and shown in **Figure 17**. However, such an analysis is difficult to converge as any loading applied would distort the edges of the cell, greatly distorting the geometry. Hence, as a better starting point, **Figure 18** shows a FE model built in this study which would essentially create 1 indentation of the final size.

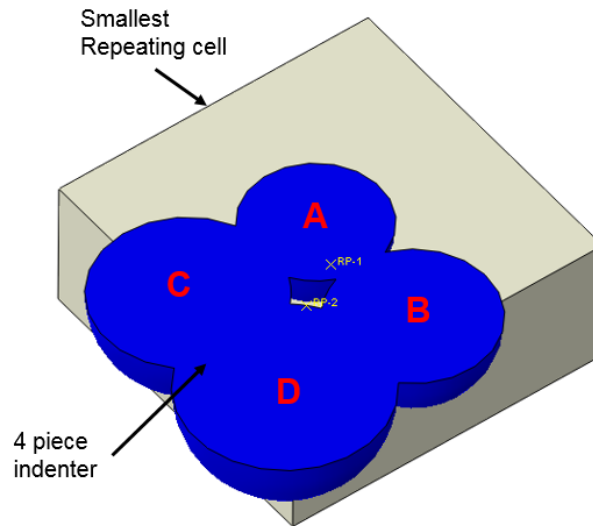


**Figure 17.** Ideal FE model capturing the smallest repeated geometry.

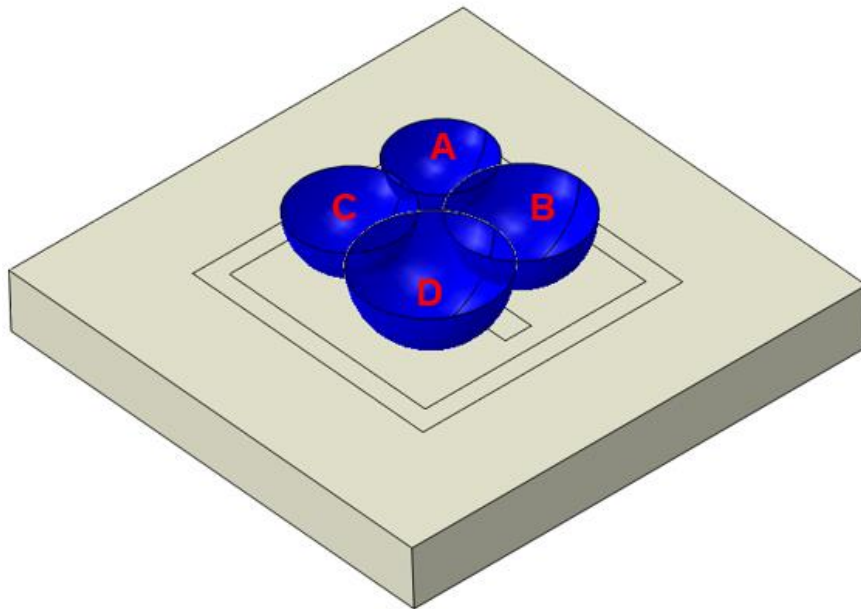


**Figure 18.** FE model used in this study, capturing a larger area to mitigate element distortion at the edges.

The indenters here are modeled as rigid hemispheres. The size of the specimen is such that 4 indentations can be successfully made along the length and the breadth. Although a large specimen would increase the solving time, it helps in applying far field fixed boundary conditions which don't affect the indentation at the center.

Again, this would lead to a multi step progressive indentation process where each step would create a new indent, or increase the size of an existing indent. This procedure for the present analysis is shown in **Figure 19**, with arrows indicating the movement of the 4 piece indenter. For simplicity in the analysis, it is easier to model multiple instances of each indenter instead of translating a 4 piece indenter. This is the reason why only relevant indenters are visible during a particular step.

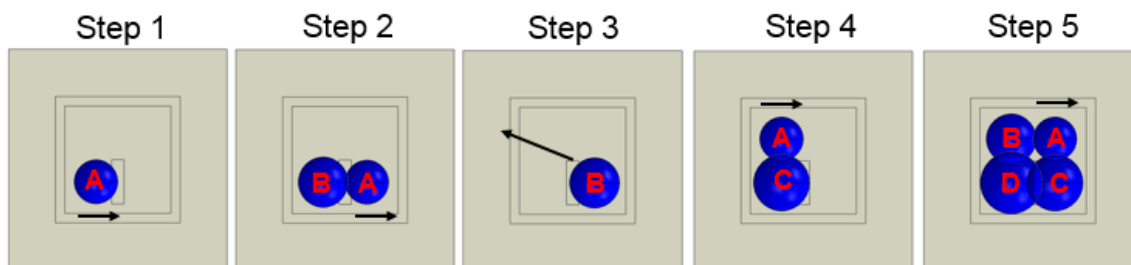


**Figure 19.** Steps in the analysis for progressive indentation

As can be seen from **Figure 20**, the final step involves all 4 indenters in the mold. At present, the analysis was unable to solve beyond a point in the final step. The primary reason for this is the material rise in the center, which is due to the gap between the different indenters. For this analysis, the maximum material rise in the center before the analysis crashed was  $16.86\mu\text{m}$ . Keeping in mind that the overall maximum depth of indentation desired here is  $24.75\mu\text{m}$ , this kind of a sharp and small peak of material rise is the reason for analysis failure, and a problem in finite element solutions. Some sort of refinement of the adaptive mesh, combined with a smaller depth of indentation would be the next step to solve this problem. It should be noted that this modeling is for the worst-case scenario as the lens depth is probably not going to be as large as  $24.75\mu\text{m}$  for that radius. Hence, the analysis should be easier to solve in the future. For reference, the results of the analysis with respect to the depth after each step can be visualized in **Figure 21**.

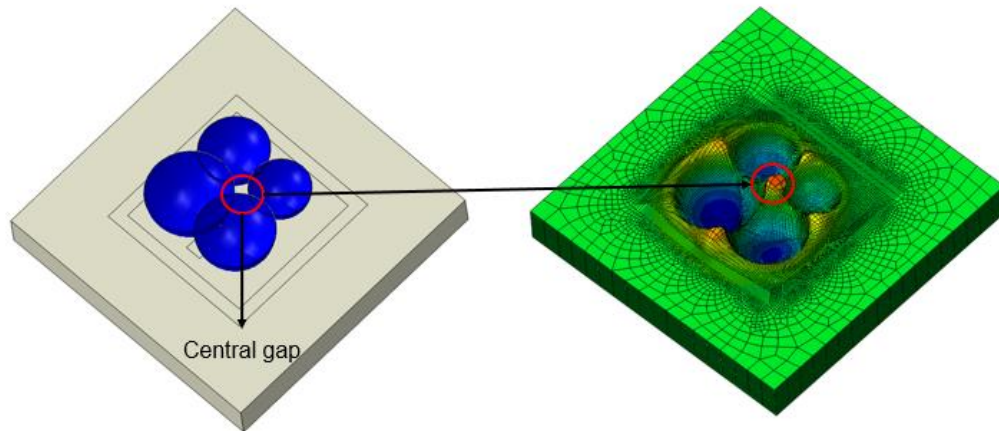


**Figure 20.** Material rise leading to analysis failure

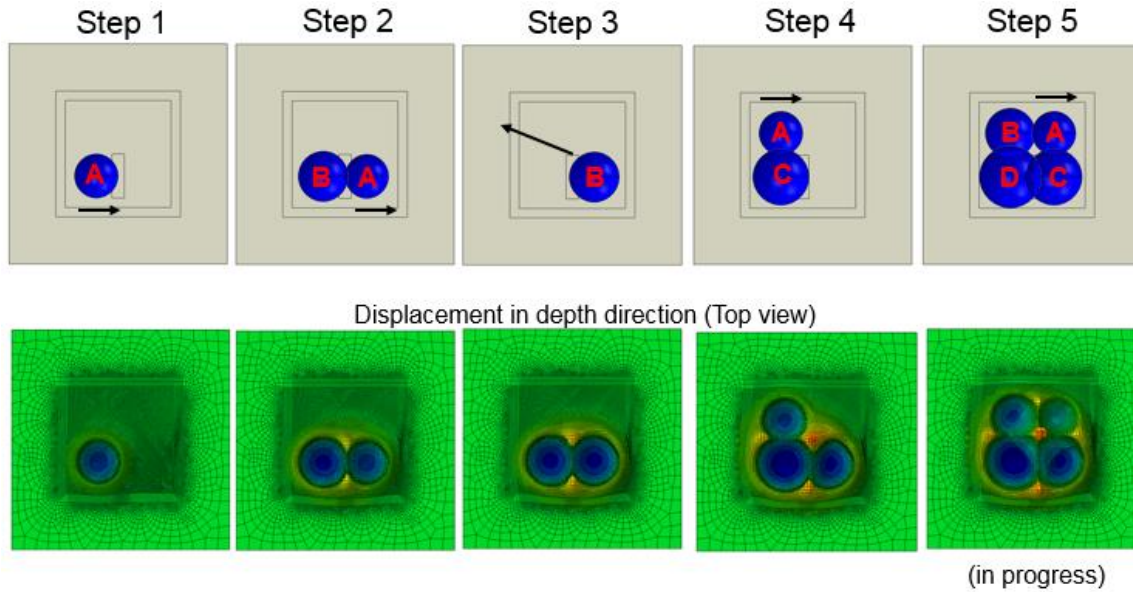


**Figure 21.** Visualization of indent creation

## 7.3 Future Work

### 7.3.1 Experimental Work

We are in the process of performing experiments involving indentation to measure the force time history and understand the plastic flow that occurs in the part. A spherical indenter will be mounted onto the load frame and then a piece of 7075 AL will be indented. A precision stage will be used to move the part between indentations, therefore we can classify the impact of the plastic flow of the shape of each successive impact. Indented samples will be scanned in a Nano CT scanner to obtain the 3D shape of the indentation down to a  $50 \mu m$  resolution.

### 7.3.2 Verification and Validation

This work will involve performing a detailed verification and validation of the experimental work with the computational model. The output from the computational model will be verified against what we are seeing in the experiments. Parameters including the force vs time curves, force vs. deflection. Along with the displacement profiles from the indents will be used in a verification and validation framework to provide a detailed understanding of the capabilities, critical parameters, and limitations of the computational framework. This is an important step because it provides a level of confidence in the model that will allow us to perform optimization of the different indentation parameters and verify the amount of spring back so that we can accurately determine the shape of the indenter to create the best possible optical path.



### 7.3.3 Modification of the grid pattern

Our previous work has shown that overlap is required to ensure that a profile shape is not distorted during successive indentations. This would mean that eventually, the 2x2 grid would need to be modified to a 3x3 grid, as shown in **Figure 22**. Hence, as the 3x3 grid moves from right to left, the repeating cells in the center would help in preserving the end profile.

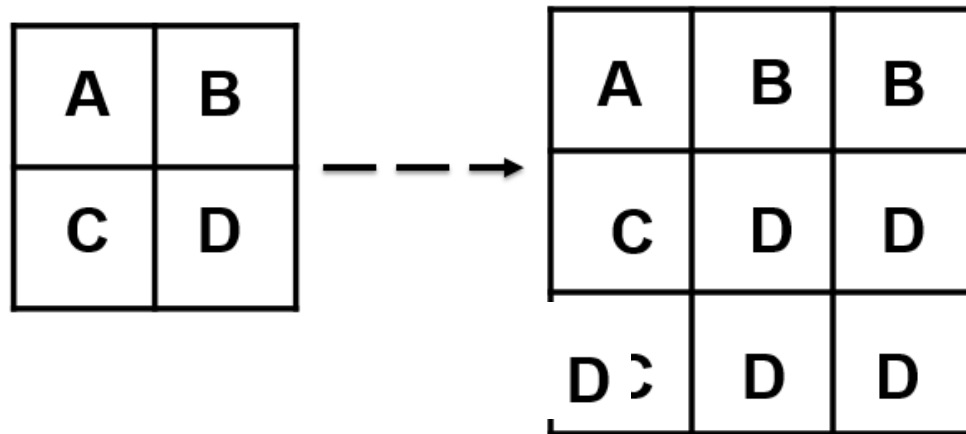


**Figure 22.** 2x2 grid (left) versus a 3x3 grid (right)

## 7.4 CONCLUSIONS

In this work, we have built a framework that will enable us to quickly and rapidly explore the indentation process. The current work has highlighted the need to perform successive indents to minimize the impact of spring back, along with the need for overlap to minimize the impact on the already formed indents, preserving their shape. The current model has the ability to be scaled to different sizes and shapes allowing for determining the effect on different parameters of the indentation process.

We are currently in the process of performing a verification and validation procedure with experimental work to understand and gain confidence in the capabilities of the model. After which we will perform an optimization to produce the best possible indent procedure to maximize our lens arrays.

## REFERENCES

1. T.N. Chakherlou, Y. Alvandi-Tabrizi, A. Kiani, On the fatigue behavior of cold expanded fastener holes subjected to bolt tightening, *International Journal of Fatigue*, Volume 33, Issue 6, 2011, Pages 800-810

# 8 HIGH SPATIAL RESOLUTION INFRARED MASS SPECTROMETRY IMAGING

**Mark T. Bokhart, Milad Nazari, and Måns Ekelöf**

Graduate Students, Chemistry

**Kenneth P. Garrard**

Senior Research Associate, PEC

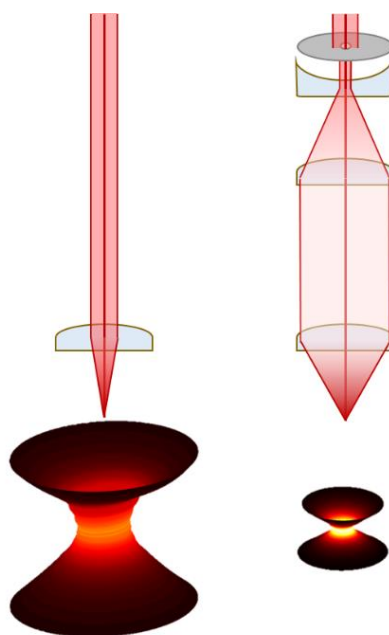
**Jeffrey Manni**

JGM Associates, Burlington MA

**David C. Muddiman**

Professor, Chemistry

*High spatial resolution in mass spectrometry imaging (MSI) is crucial to understanding the biology dictated by molecular distributions in complex tissue systems. Here, we present MSI using infrared matrix-assisted laser desorption electrospray ionization (IR-MALDESI) at 50  $\mu\text{m}$  resolution. An adjustable iris, beam expander, and aspherical focusing lens were used to reduce tissue ablation diameters for MSI at high resolution. The laser beam caustic was modeled using laser ablation paper to calculate relevant laser beam characteristics. The minimum laser spot diameter on the tissue was determined using tissue staining and microscopy. Finally, the newly constructed optical system was used to image hen ovarian tissue with and without oversampling, detailing tissue features at 50  $\mu\text{m}$  resolution.*



## 8.1 INTRODUCTION

Mass spectrometry imaging (MSI) combines the molecular specificity of mass spectrometry with the spatially resolved analysis of an imaging technique [1]. This can be performed in a label-free manner over a range of  $m/z$  values, allowing thousands of analytes to be analyzed simultaneously. The resulting data may be visualized using a variety of software [2] to depict the localization and abundance of each molecule. MSI has been routinely applied to the study of plants [3], proteins [4], lipids [5], and drug distributions [6]. A common goal of nearly all applications is to achieve high spatial resolution without a loss in analyte detectability.

Laser-based MSI methods are the most commonly used methods to date, and an article reviewing the broad field of high resolution laser-based MSI across different technologies was recently published [7]. The spatial resolution of all laser-based MSI methods is inherently tied to the laser spot size. Infrared (IR) laser desorption methods for reducing spot size follow the same general principles as those in the UV regime [8]; however, IR lasers, which are the focus of this manuscript, are not as commonly used in the MSI field. It is also inherently more difficult to achieve a small spot size with at a wavelength of 2940 nm.

For a Gaussian profile laser, the diffraction limited spot size is given by Equation (1).

$$\frac{4 \lambda M^2 f}{\pi D} \quad (1)$$

Where  $M^2$  is the beam propagation quality factor,  $\lambda$  is the wavelength,  $f$  is the lens focal length, and  $D$  is the Gaussian input beam diameter at the lens. To decrease the spot size of the focused laser, it is possible to use a shorter focal length lens ( $f$ ), increase the beam diameter ( $D$ ), or improve the laser beam quality ( $M^2$ ). Spherical aberration can cause significant enlargement of the minimum spot size if not corrected [9]. The spot size determined by spherical aberration is given by Equation (2).

$$\frac{k D^3}{f^2} \quad (2)$$

Where  $D$  and  $f$  are as described above and  $k$  is a material constant. While these can be easily changed in custom sources, adjustments to commercial MSI instruments are more difficult [10]. A short focal length lens presents a unique challenge in MSI because the ablated material must be proximal to and accessible for sampling by the mass spectrometer, often preventing the use of very short focal length lenses. To circumvent this issue, researchers may use transmission geometry IR laser ablation, where the laser is focused on the opposite side of the sample being

analyzed [11]. Alternatively, Römpf and coworkers used an optic with a central drilled hole to allow the ablated material to pass through [12]. The laser beam propagation factor  $M^2$  is a defining parameter detailing the beam quality, with a perfect Gaussian beam having an  $M^2$  of 1. To reduce the detrimental effect of lasers with  $M^2 > 1$ , a spatial filter may be used to remove the non-Gaussian and low laser energy edge [13]. As seen from Equation (1), using the maximum diameter of the lens is beneficial to achieving a diffraction-limited spot size. However, a larger diameter increases the contribution of spherical aberration (Equation (2)) if a plano-convex or meniscus lens is used. Incorporating beam expanding lenses reduces beam divergence and the focal spot size of the IR laser. Alternatively, Hieta and coworkers have used the inherent beam divergence of their laser with a very long path length to completely fill the focusing lens and remove the beam edge [13].

Several methods have been used to achieve spatial resolutions lower than the IR laser spot size. Oversampling involves moving the sample by less than the laser ablation diameter with complete ablation at each position, effectively sampling only a small portion of the total laser spot size [14, 15]. This method results in irregular shapes of tissue ablated from a Gaussian profile laser beam. The coupling of IR laser ablation and a spatially resolved detector has been reported [16, 17] to achieve MSI resolution below the diffraction limit of the IR laser.

Infrared matrix-assisted laser desorption electrospray ionization (IR-MALDESI) is a technique combining infrared laser ablation and electrospray ionization [18, 19]. IR-MALDESI MSI has been used to analyze a variety of biospecimens [20]. The laser ablation diameter on tissue has been previously reported as approximately 150  $\mu\text{m}$  using a single focusing element [19, 21]. This method has been used and optimized for tissue imaging experiments of lipids, metabolites and small molecule drugs [21].

This work details the utility of a multi-element optical system for IR-MALDESI MSI to simultaneously reduce spot size and improve spatial resolution. The multi-element optical system incorporates an adjustable iris, 3.75x beam expander, and aspheric focusing lens to improve the spatial resolution of IR-MALDESI MSI to 50  $\mu\text{m}$ .

## **8.2 EXPERIMENTAL**

### **8.2.1 Materials**

LC/MS grade methanol, ethanol, water, and formic acid were purchased from Fisher Scientific (Pittsburgh, PA, USA). Laser burn paper was purchased from ZAP-IT (ZFC-23, ZAP-IT, Concord, NH, USA). Pre-cleaned microscope slides were purchased from VWR (Radnor, PA, USA).

## 8.2.2 Tissues

Mouse liver tissues were obtained from the College of Veterinary Medicine at North Carolina State University. Hen ovarian tissue was obtained from a C-Strain white leghorn commercial egg laying hen. Animals were managed in accordance with the Institute for Laboratory Animal Research Guide, and all husbandry practices were approved by North Carolina State University Institutional Animal Care and Use Committee. Tissues were harvested and immediately flash-frozen in a dry ice isopentane bath and stored at -80 °C until the time of the experiment. A Leica CM1950 cryomicrotome (Buffalo Grove, IL, USA) operated at -20°C was used to prepare cryosections for analysis. Optimum cutting temperature (OCT) embedding medium (Fisher Scientific, Waltham, MA, USA) was used to adhere the tissue to a 40 mm specimen disc. The tissues were sectioned into 10-µm thick sections and thaw-mounted onto standard glass microscope slides immediately prior to analysis.

## 8.2.3 IR-MALDESI Source

A custom acrylic enclosure housed the ionization source consisting of an X-Y translation stage, electrospray emitter and a portion of the laser optics. Custom software developed in-house was used to drive the X-Y stage with the sample on a Peltier-cooled plate. The plate was cooled to -9 °C to form a thin ice matrix layer on the animal tissue sections to enhance energy absorption and improve ablation dynamics. The ice matrix layer was maintained by purging the enclosure with dry nitrogen (Arc3 Gases, Raleigh, NC, USA) to a relative humidity of approximately 10% throughout the imaging experiments. Two laser pulses at 20 Hz from a mid-IR laser (IR Opolette, Oportek, Carlsbad, CA, USA) tuned to 2940 nm were focused on the sample surface at each stage position. The ablated material was ejected normal to the target surface where it overlapped with an orthogonal electrospray plume.

Stable electrospray was maintained using a solvent composition of 1:1 methanol:water with 0.2% formic acid, a 2.0 µl/min flow rate, 4.0 kV potential, and a 75 µm i.d. silica taper tip emitter (New Objective, Woburn, MA, USA). Geometric parameters of the IR-MALDESI source remained constant through all experiments presented herein. The emitter tip was placed 5 mm above the sample, the laser ablation spot was 1 mm from the emitter tip and 5 mm from the customized extended MS inlet [21, 22]. The IR-MALDESI source was coupled to a Q Exactive™ Plus mass spectrometer (ThermoScientific, Bremen, Germany). Data were collected in positive ion mode with a scan range of 250-1000  $m/z$  and resolving power was set to 140,000 (FWHM at 200  $m/z$ ). Automatic gain control (AGC) was turned off and the injection time was fixed based on the number of laser pulses. The total injection time (IT) is calculated as  $t = 25 + 50(n - 1)$  ms, where  $n$  is the number of laser pulses (e.g., IT = 25 ms for 1 laser pulse, 75 ms for 2 laser pulses, etc.).

The MS .RAW data files were converted to the mzML format using MSConvert [23], and the mzML files were subsequently converted to the imzML format using the imzMLconverter software [24, 25]. The imzML files were then loaded into MSiReader for visualization and analysis of MSI data [26]. Averaged mass spectra and S/N were obtained from Xcalibur version 2.2.

## 8.2.4 Safety

IR laser safety glasses (pn 100-38-200, Laser Safety Industries, Minneapolis, MN, USA) were worn while the laser was on. Curved laser safety shields (TPS8, Thorlabs, Newton, NJ, USA) were installed on the optical breadboard around the mirrors used to steer the beam. All lenses were enclosed in a 1" diameter lens tube. A laser curtain (Laz-R-Shroud, Rockwell Laser Industries, Cincinnati, OH, USA) was erected around the IR-MALDESI laboratory space to isolate the IR laser from the rest of the laboratory.

## 8.2.5 IR Laser and Optics

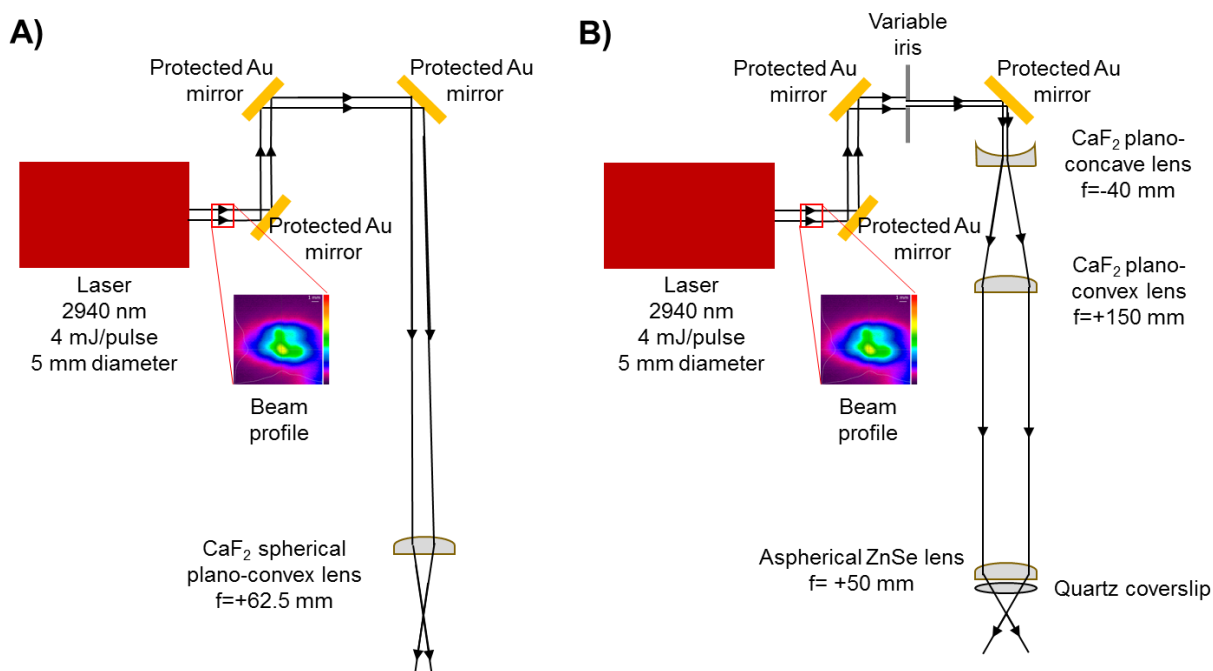


**Figure 1.** Schematic of IR-MALDESI using, **A)** a single spherical focusing lens and **B)** a multi-element beam expander with an iris and an aspheric focusing lens.

An IR Opolette tunable (2700-3100 nm) laser system was purchased from Oportek Inc. (Carlsbad, CA, USA). Protected gold mirrors (PF10-03-M01, Thorlabs, Newton, NJ, USA) were mounted on kinematic mounts (KM100, Thorlabs, Newton, NJ, USA) and were used to align the laser beam.

The laser head and two aligning mirrors were mounted on an optical breadboard above the mass spectrometer. A third mirror directed the beam path through the focusing lenses and in front of the mass spectrometer inlet. Two laser focusing designs were tested sequentially to compare the laser focusing ability of each. The first design consisted of a single, uncoated CaF<sub>2</sub> planoconvex lens (focal length (f) = +62.5 mm, Edmund Optics, Irvine, CA, USA) (**Figure 1A**) and was previously used for IR-MALDESI MSI analyses [19]. The second design incorporated an adjustable iris (SM1D12C, Thorlabs, Newton, NJ, USA), a beam expander, and an aspherical focusing lens. The Galilean beam expander was constructed using a 1" CaF<sub>2</sub> concave lens (f = -40 mm, antireflective (AR)-coated 3-5 μm) (Thorlabs, Newton, NJ, USA) and a 1" CaF<sub>2</sub> convex lens (f = +150 mm, AR-coated 3-5 μm) (Thorlabs, Newton, NJ, USA). The expanded beam was then focused on the target using a 1" ZnSe aspheric lens (f = 50.0 mm, AR-coated 3-5 μm) (Thorlabs, Newton, NJ, USA) (**Figure 1B**). A 25.4 mm diameter quartz coverslip (Alfa Aesar, Haverhill, MA, USA) was placed between the final lens and the target to protect the ZnSe lens. Laser energy was measured using a Nova II laser power meter with a 3A-P laser thermal power sensor (Ophir Optronics, Jerusalem, Israel) for both optical systems.

## 8.2.6 Laser Beam Caustic Measurement

A zap-it film card (ZFC-23, Zap-IT, Concord, NH, USA) was mounted on a microscope slide. After the lens system was focused onto the sample plane, the stage height was adjusted to defined positions located above, at, and below the focal point. A single laser ablation event was recorded on the laser film card at these defined z height positions for both optical systems. Images of each laser ablation spot were obtained using a 10x objective on an LMD7000 microscope (Leica, Buffalo Grove, IL, USA). The burn paper ablation images were then loaded into MATLAB 2016b (Mathworks, Natick, MA, USA) where ellipses were manually fit to the ablation spots. The average fluence at each z position was calculated by taking the average energy divided by the area of each ellipse, which is reported as J/cm<sup>2</sup>.

## 8.2.7 Modeling Laser Beam Focus

Equation 3 is a theoretical model for Gaussian laser beam propagation.

$$W(z) = W_0 \sqrt{1 + \left( \frac{M^2 \lambda}{\pi W_0^2} \right)^2 (z - z_0)^2} \quad (3)$$

Where  $W(z)$  is the beam radius at position  $z$  along the beam optical axis,  $W_0$  is the beam waist radius,  $M^2$  is the beam quality factor, and  $z_0$  is the position of the beam minimum radius with respect to a reference position [27]. Parameters defining the laser beam were calculated by fitting



the theoretical model in Equation (3) in both the XZ and YZ planes to the measured values. The fit was performed in Excel using generalized nonlinear regression. The residuals were calculated for each data point and plotted as a function of z height. The half angle divergence was calculated using a linear regression on the last three points in the curve.

### **8.2.8 Laser Ablation Diameter on Tissue**

Mouse liver tissue was cryosectioned and mounted onto microscope slides. The number of laser pulses was varied from 1-5 and the diameter of the beam shaping iris was set to 2, 4, or 12 mm. For each combination tested, 20 positions on tissue were ablated. After laser ablation, the slides were removed from the stage, excess water was removed, and the tissues were stained with 100  $\mu$ L of histogene staining solution (Applied Biosystems, Foster City, CA, USA) pipetted directly on top of the tissue and allowed to sit for approximately 2 minutes. The slide was then washed with 70% ethanol for 30 seconds followed by 100% ethanol for 30 seconds. Excess ethanol was removed and approximately 50  $\mu$ L of Permount mounting medium (Fisher Scientific, Waltham, MA, USA) was pipetted onto the tissue and a coverslip was mounted on the slide. Digital images of the stained tissues with ablation spots were taken using an LMD7000 (Leica Microsystems, Buffalo Grove, IL, USA) with a 5x objective. The JPEG images were loaded into MATLAB 2016b (Mathworks, Natick, MA, USA) and circles were fitted to the ablation spots using the *imfindcircles* function in the Image Processing Toolbox.

### **8.2.9 MSI with High Spatial Resolution**

Hen ovary tissue was analyzed using the beam expander optic design to perform high spatial resolution IR-MALDESI MSI. A region on the edge of a hen ovarian tissue section was analyzed using a 2 mm iris diameter and two laser pulses, corresponding to the smallest ablation diameter reliably achievable with this optical system. Five regions of interest (ROIs) 41 x 11 voxels in size were analyzed using decreasing step size of the stage in an oversampling mode with 100, 75, 50, 40, and 30  $\mu$ m step sizes. After IR-MALDESI MSI, the tissue was stained using the tissue staining protocol described above.

Additionally, a hen ovary section was analyzed with three paired conditions: 2 mm iris diameter with 50  $\mu$ m raster step size, 4 mm iris diameter with 75  $\mu$ m raster step size, and 12 mm iris diameter with 100  $\mu$ m raster step size, resulting in minimal undersampling of the tissue. A custom birefringent optical attenuator was used to maintain a constant 1.2 J/cm<sup>2</sup> fluence for each iris setting.

## 8.3 RESULTS AND DISCUSSION

### 8.3.1 Multi-lens Optical System

The optical systems presented in **Figure 1** were easily installed and aligned using a 1" tube lens system (Thorlabs, Newton, NJ, USA) to secure all lens components. The inclusion of two mirrors on kinematic mounts on the optical breadboard allowed precise adjustment of the laser path, which was needed to keep the laser beam centered throughout the multi-lens system. The total path length for both optical systems was approximately 1 meter. The output beam profile of the OPO laser was measured using a Pyrocam III HR (Ophir-Spiricon, North Logan, UT, USA) beam profiling camera as seen in **Figure 2**. The beam profile of the laser output was not a perfect Gaussian, which effects the minimum spot size achievable due to the dependence on  $M^2$ . To this end, a variable iris was incorporated into the multi-lens system to block the low-energy fringe of the laser output and thereby improve the minimum focal point. A 3.75x magnification Galilean beam expander was constructed from plano-concave ( $f = -40$  mm) and plano-convex ( $f = +150$  mm) lenses placed such that their focal points were coincident. The expanded beam (approx. 20 mm diameter) was incident on a 1" ZnSe aspherical lens ( $f = +50$  mm), whose shape corrects spherical aberration. A quartz coverslip was placed immediately after the last focusing lens to protect the lens from ablated sample debris.

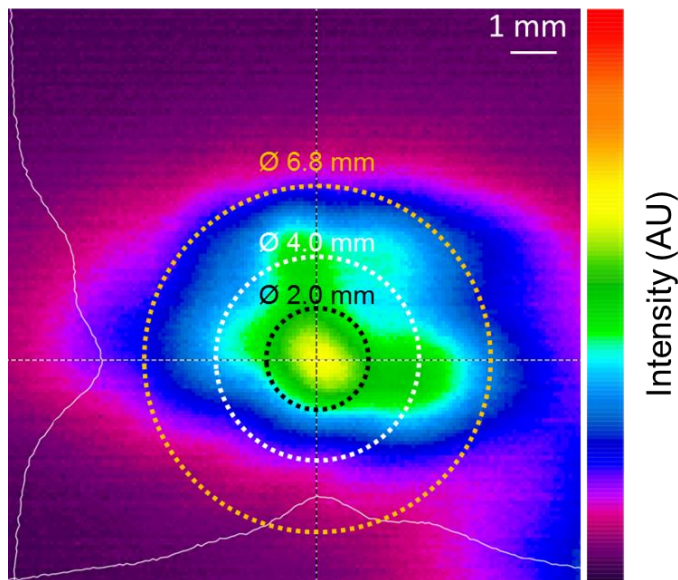


**Figure 2.** Beam profile of the Opolette OPO IR laser at 2940 nm measured using a Pyrocam IIIHR profiling camera. Circles represent the energy profile transmitted at each iris setting; 2 mm (black), 4 mm (white), and 12 mm (gold). A 12 mm iris setting is effectively 6.8 mm diameter due to beam clipping of the 1" optics of the 3.75x beam expander and absorption of laser energy in the lens tube wall.

### 8.3.2 Visualization of Laser Beam Caustic

The laser beam caustic was visualized by placing laser burn paper at various heights relative to the focal point. Although this limited the visualization to regions where there was sufficient fluence to ablate the laser burn paper, it was found to be acceptable to obtain a profile of the laser focus. It is likely that the ablation spots on the burn paper do not exactly reflect the laser beam width where the intensity drops below  $1/e^2$ , the common definition of laser beam width; however, the method is sufficient for comparison between two optical designs, as presented here. **Figure 3** shows the burn paper results for the two optical systems at various z heights.

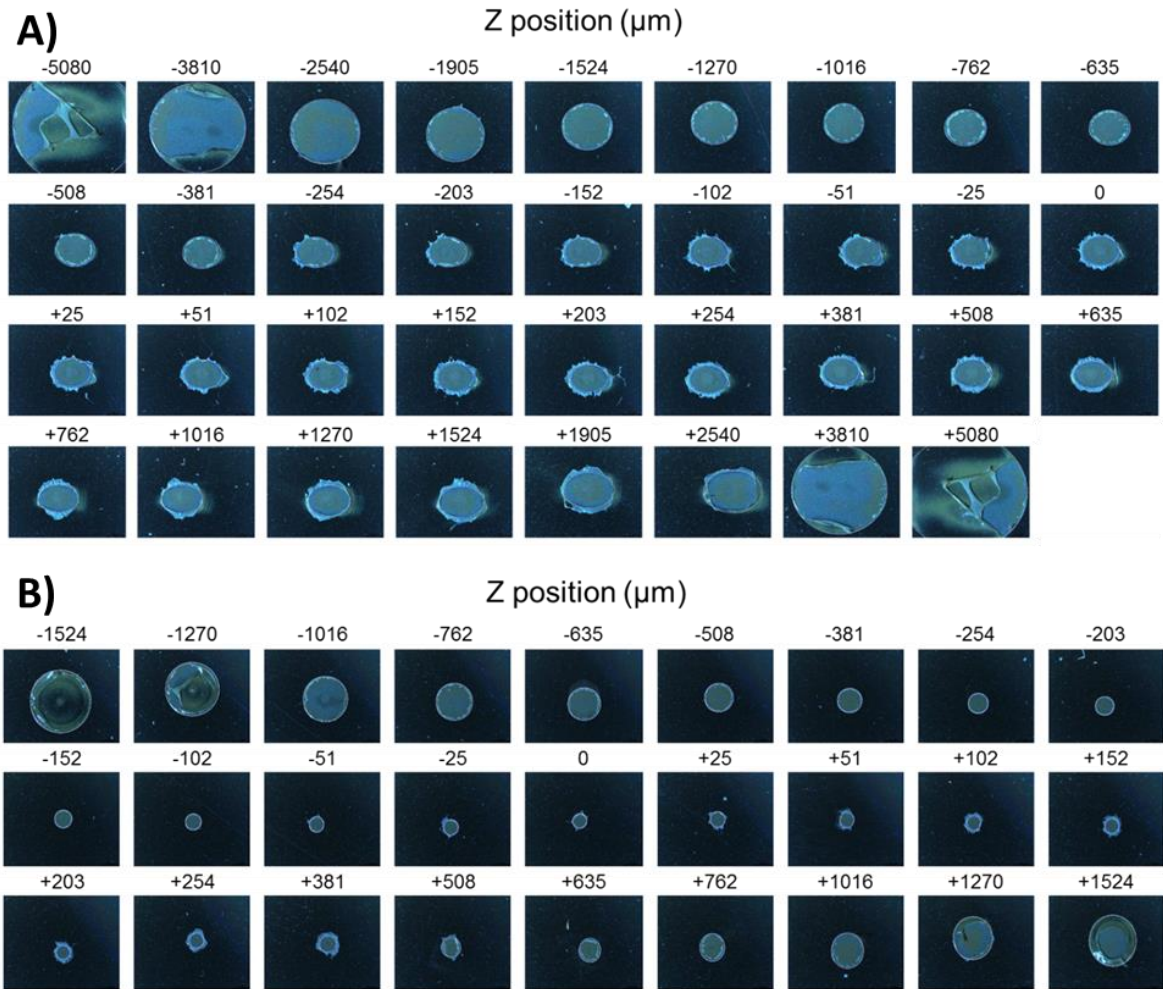


**Figure 3.** A burn spot was recorded on laser burn paper at the specified z positions for **A)** the single focusing lens and **B)** the multi-element optical system. A 10x objective was used to make an optical image of each burn spot, and then fit with an ellipse in MATLAB.

The laser ablation spots for the single spherical focusing lens recorded over a 10.16 mm height are shown in **Figure 3A**. For the multi-element system a much smaller z range of 3.048 mm was used. These spots are shown in **Figure 3B**. MATLAB was used to manually fit ellipses to the laser ablation spots and major and minor axes were recorded along with the corresponding z height. These ellipses were then plotted to give the 3 projections, XY, XZ, and YZ, seen in **Figure 4**. The laser caustics for both systems is also visualized as a 3D surface by interpolation between z heights and the surfaces are color coded according to the average fluence. The two XY projections show the observed laser ablation spots. The 3D surface is representative of the true laser focus as it is not composed of discrete sampling points, rather a continuum of ablation spots based on interpolation of the data collected. To aid in comparing the two beam caustics, the axes and color maps are presented on the same scale. This emphasizes the reduction in the ablation diameter along with reduction in the depth of focus.

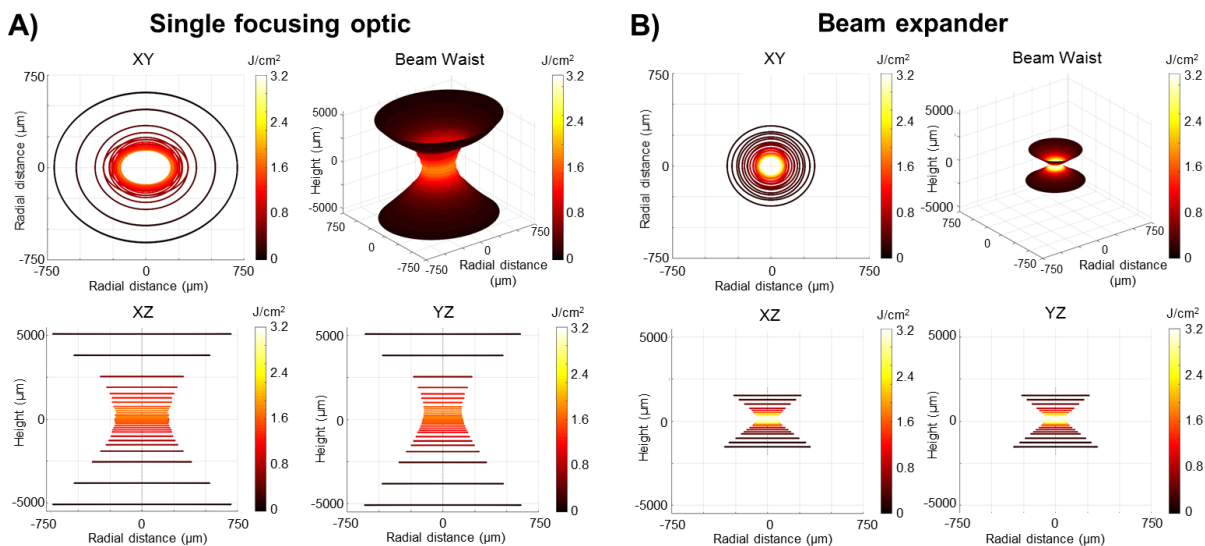


**Figure 4.** Visualization of laser beam caustic for **A)** the single focusing optic and **B)** the multi-element beam expander. The data is represented as projections of ellipses on 3 axes showing the laser focus profile in the XY, XZ, and YZ planes. The color of each ellipse is representative of the average laser fluence at each Z position. These ellipses were interpolated and represented as a 3D surface for each optical design.

The beam expander design gave much more circular ablation spots than the single lens design, a desirable quality for a laser used for MSI. A circular laser ablation allows MS images to be acquired with the same spatial resolution in both the X and Y dimensions, even in the undersampling mode. The reduced ablation area of the beam expander design resulted in a much higher fluence, as indicated by the heatmap. Laser fluence has a direct impact on IR-MALDESI MSI data quality. First, the laser system must have sufficiently high fluence to ablate or desorb

the sample and matrix. Second, at energies above the ablation threshold, the fluence will have an impact on the ablation dynamics and overlap with the electrospray [22]. Third, the ablation fluence determines the number of laser pulses required to completely ablate through the sample [21], which is a requirement for quantitative IR-MALDESI analyses [28]. By the above points, the higher fluence of the multi-element design indicated it would successfully ablate tissue material, possibly with fewer pulses, than the single optic design. Optimizing the laser fluence to a wide variety of sample types for imaging or direct analysis could be accomplished by attenuation, using a polarization based attenuation and an iris to balance the total energy and desired spot size.

### 8.3.3 Modeling Laser Beam Propagation

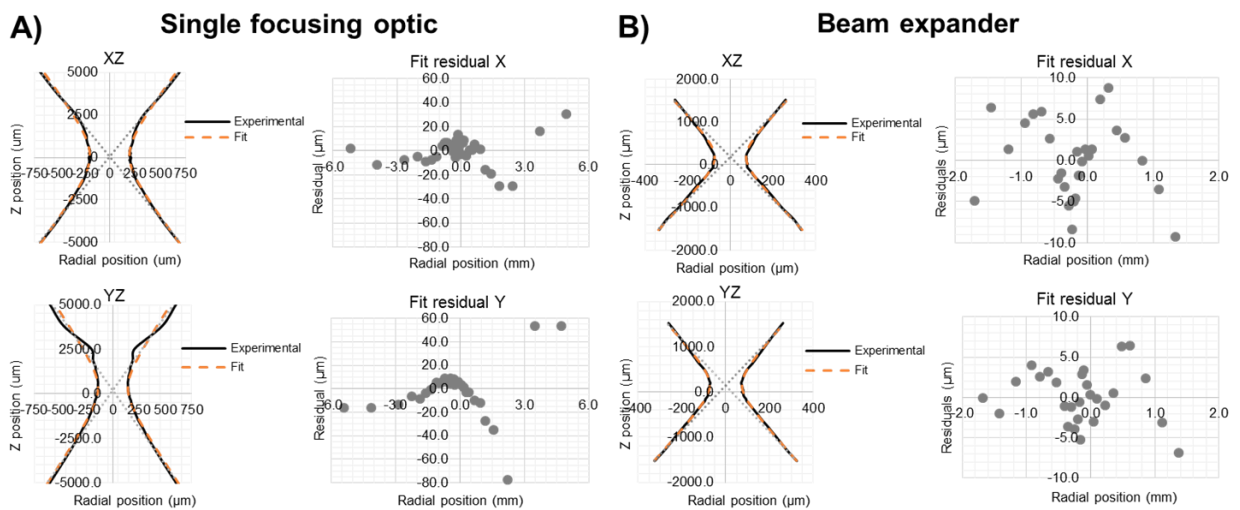
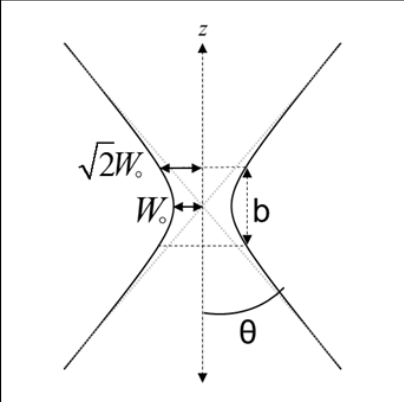


**Figure 5.** Beam propagation modeling for **A)** the single lens optical system and **B)** the multi-element beam expander. Residuals of each fit are presented to the right. Linear regression was used to estimate the far field beam divergence. Note that the X and Y scales in (A) are  $\sim 2x$  larger than (B) and the Z scale is  $2.5x$  larger. The residual scales are  $6x$  larger for (A).

Equation (3) describing laser beam propagation was fit using a generalized reduced gradient nonlinear regression to the beam profile data in the XZ and YZ projections that is shown in **Figure 4**. **Figure 5** displays the laser profile for both projections and both optical systems along with the theoretical model using the best fit parameters. The residuals are also plotted for each fit to estimate the goodness of fit of the model to the data. For the single optic (**Figure 5A**) the residuals indicate that the data deviated from the theoretical fit moderately when the laser spot size was far from the focal point, whereas this was not the case when the beam expander was used (**Figure 5B**). One explanation for this discrepancy may be that the single optic was placed further away from the focal point to fully cover the laser beam caustic. As the laser ablation spots at the furthest

points (XZ/YZ distance) approached the ablation threshold of the laser burn paper and were larger than the image size of the 5x objective, it could lead to an inaccurate estimation of the laser diameter at these points. Linear regression on the last three points of each projection was used to estimate the far field divergence of the laser beam. The model could then be used to estimate the half angle divergence for both optical designs.

**Table 1.** Modeled Beam Characteristics.



Parameter	Single lens		Beam expander	
	X	Y	X	Y
$M^2$ , beam quality	27.0	16.9	15.4	14.7
$W_0$ , beam waist ( $\mu\text{m}$ )	197.0	140.3	74.7	73.1
$b$ , depth of focus (mm)	3.07	2.49	0.78	0.75
$\theta$ , Half angle divergence	7.9°	6.8°	11.3°	11.1°

**Table 1** summarizes the important parameters for modeling laser ablation in IR-MALDESI MSI using the single focusing element or the multi-lens beam expander.  $M^2$  is the beam propagation factor and is a commonly used quality metric. A diffraction limited, perfectly Gaussian beam would have an  $M^2 = 1$ . The multi-lens beam expander shows an improvement in  $M^2$  for both X and Y dimensions. The beam waist,  $W_0$ , is a representation of the minimum spot size. The multi-element system improved spot size by a factor 2.6 and 1.9 for the X and Y dimensions. Reduction in both dimensions is particularly important for microprobe MSI, where the sample is moved in the XY plane. The Rayleigh length of focus,  $\sqrt{2} W_0$ , is the distance along the propagation direction where the cross-sectional area doubles. The depth of focus, or confocal parameter ( $b$ ), is twice the Rayleigh length centered about the minimum. The single focusing lens has an average depth of focus of 2.78 mm, which makes the technique robust to minor changes in sample height on the Peltier stage. The beam expander design has a significantly smaller depth of focus (0.78 mm). While this may require more careful focusing of the optic for the smallest ablation diameters in MSI use, it is sufficiently greater than the sample thickness (10  $\mu\text{m}$ ). Related to the depth of focus is the half angle divergence. This value describes the angle of light being focused and is a direct result of the size of the incoming diameter and the distance to the focusing lens. Like the minimum beam waist, the half angle divergence is influenced by the beam propagation factor,  $M^2$ . The calculated half angle divergence for the beam expander lens system is 3-4° larger than the single focusing lens and is most likely the result of a large input diameter at the final focusing lens.



### 8.3.4 Ablation Diameter on Mouse Liver Tissue

To assess the efficacy of the multi-element optical system for MSI applications, it is necessary to move to tissue, which is a more challenging substrate to ablate and introduces the use of an ice matrix. A combination of iris diameters and number of laser pulses ( $n = 1-5$ ) was used to define the tissue ablation diameter of the beam expander optical design. The 2.0 and 4.0 mm iris only let the most intense laser energy through the optical system, while the 12 mm iris (max) would let nearly all of the laser beam into the system. With the 3.75x beam expander in use, only the center 6.8 mm of the laser output beam would travel through the 1" lens tube system housing the optics without being absorbed by the tubing wall. All combinations of iris and number of pulses were able to completely ablate through the 10  $\mu\text{m}$  thick mouse liver tissue to give a clear circular ablation spot, except for the 2.0 mm iris and 1 laser pulse (**Figure 6A**). The laser ablation areas were calculated by fitting circles to the ablation spots on tissue using the *imfindcircles* algorithm in MATLAB. The reproducibility of ablation spots is represented by the 95% confidence interval in the mean ablation diameter shown in **Figure 6B**, indicating that the ablation diameters are highly reproducible. Most of the tissue was ablated in the first 2 laser pulses, as shown in the marginal increase of ablation diameter in pulses 3-5. In a balance of minimum spot size with complete ablation and shortest ion injection time, the 2 laser pulse setting was selected for evaluation of the multi-element optical system on IR-MALDESI MSI.

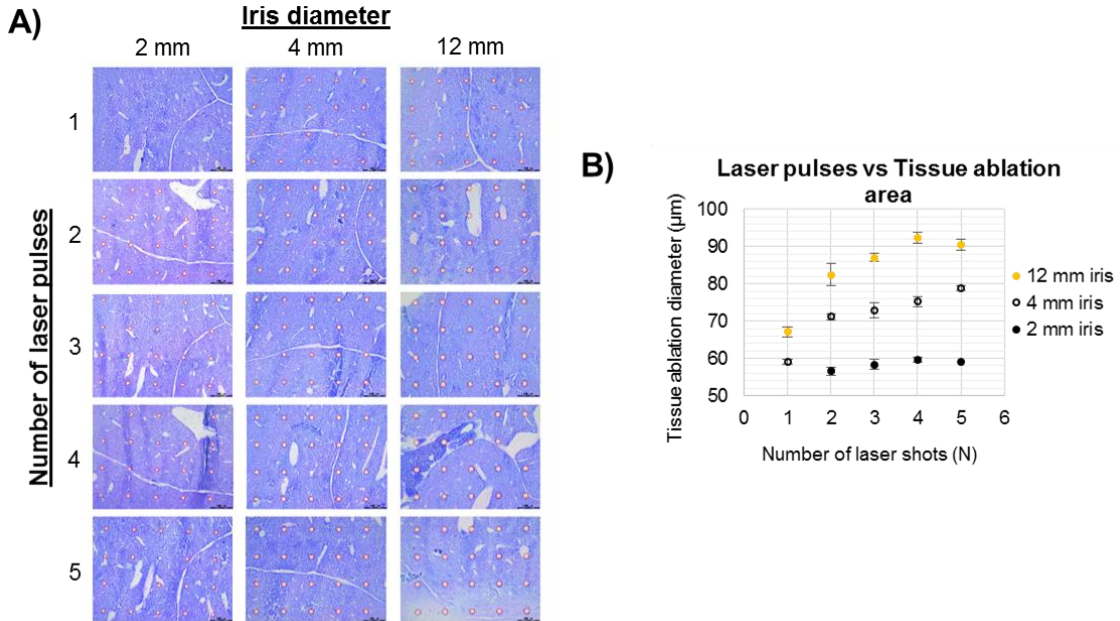


**Figure 6.** Measurement of ablation diameters on mouse liver tissue using ice as a matrix while varying iris diameter and number of pulses. **A)** Stained tissue images after ablation by an IR laser with ablation spots fitted with circles **B)** Average tissue ablation diameters for the iris diameters and number of pulses.

### 8.3.5 High Spatial Resolution IR-MALDESI MSI

The lowest ablation diameter setting, 2.0 mm iris and 2 laser pulses, was chosen to investigate the smallest raster step size that could be used while still generating useful MSI data. Using this configuration, data were collected from the edge of a structurally complex hen ovary tissue at 100, 75, 50, 40, and 30  $\mu\text{m}$  step sizes. The step sizes less than 50  $\mu\text{m}$  represent analysis in an oversampling mode, where the area of tissue being ablated is smaller than the laser ablation diameter. However, as seen in **Figure 7**, the ion abundance of cholesterol ( $m/z$  369.3516  $\pm$  2.5 ppm) at the 40 and 30  $\mu\text{m}$  step sizes neared the limit of detection of the IR-MALDESI source coupled to a Q Exactive™ Plus mass spectrometer, and the detection frequency was not optimal. The MS peak of cholesterol for each raster step size is displayed on the right of **Figure 7**. The ion abundance and signal-to-noise ratio (S/N) is significantly reduced for 40 and 30  $\mu\text{m}$  step sizes compared to the 100, 75, and 50  $\mu\text{m}$  step size. Cholesterol was chosen as it was the most abundant ion detected by IR-MALDESI and, therefore, would require the least volume of ablated tissue to be detected. Methods to improve ion abundance including re-optimization of the IR-MALDESI source geometry to improve ablation and electrospray plume overlap [21], the use of a higher repetition rate laser to reduce ion loss in the MS C-trap, and ionization agent optimization [28, 30, 31] will be the focus of future work.

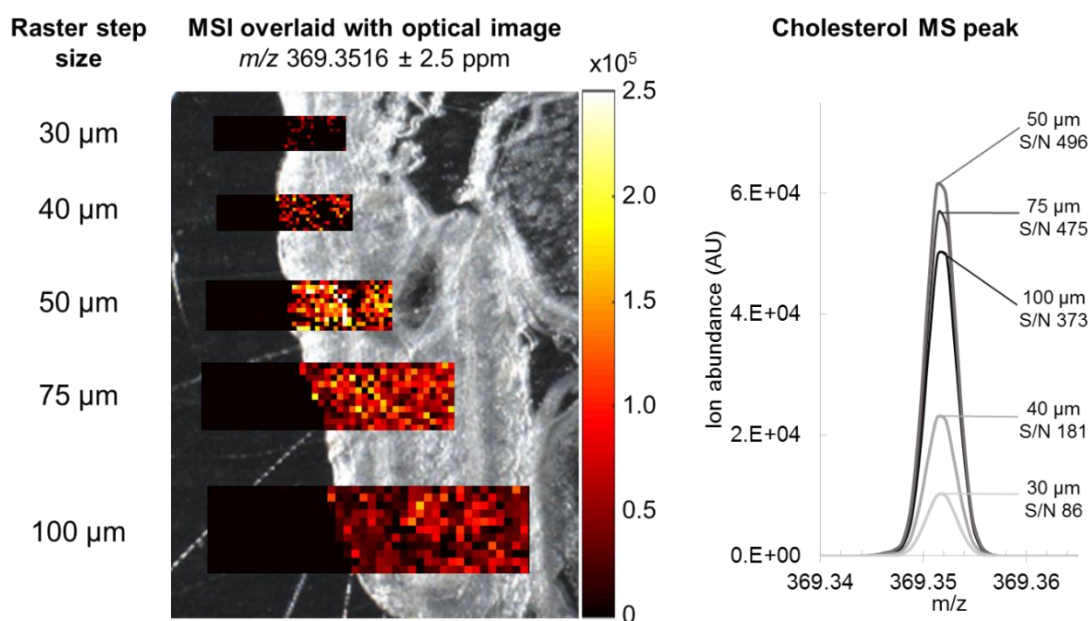


**Figure 7.** MSI of a lipid (cholesterol  $[\text{M}-\text{H}_2\text{O}+\text{H}]^+$ ,  $m/z$  369.3516  $\pm$  2.5 ppm) overlaid on the optical image of the tissue. Regions of interest were analyzed with a range of raster step sizes to demonstrate MSI at high spatial resolution. The average cholesterol  $[\text{M}-\text{H}_2\text{O}+\text{H}]^+$  peak for each raster step size is displayed with corresponding S/N values.



The desired ablation diameter was achieved through adjustment of the iris and the rotation of a polarization-based optical attenuator placed in the beam path. A hen ovary tissue was analyzed at 50, 75, and 100  $\mu\text{m}$  spatial resolution using 2.0 mm, 4.0 mm and 12.0 mm iris diameters, respectively. Because more energy enters the optical system with larger iris diameters, a custom polarization-based attenuator was placed in the beam path to maintain a constant fluence ( $1.2 \text{ J}/\text{cm}^2$ ) between the spatial resolutions of the experiment. **Figure 8A** shows the ion distribution map of cholesterol for 3 sections of the same hen ovary tissue section analyzed at different spatial resolutions. A serial tissue section was stained, and an optical image was included in **Figure 8B** to visually compare tissue morphology to the MS image. The distribution of cholesterol showed concentric rings of high abundance in the developing follicles on the left. A full scan mass spectrum is displayed in **Figure 8C** showing numerous endogenous lipids and metabolites in the hen ovary tissue analyzed at 50  $\mu\text{m}$  resolution. Tissue specific peaks were generated by averaging an on-tissue region and subtraction of an off-tissue region to minimize peak contribution by ambient contaminants. **Figure 9** demonstrates that mass measurement accuracy (MMA) was better than  $\pm 2.5 \text{ ppm}$  for all pixels in the imaging experiment.

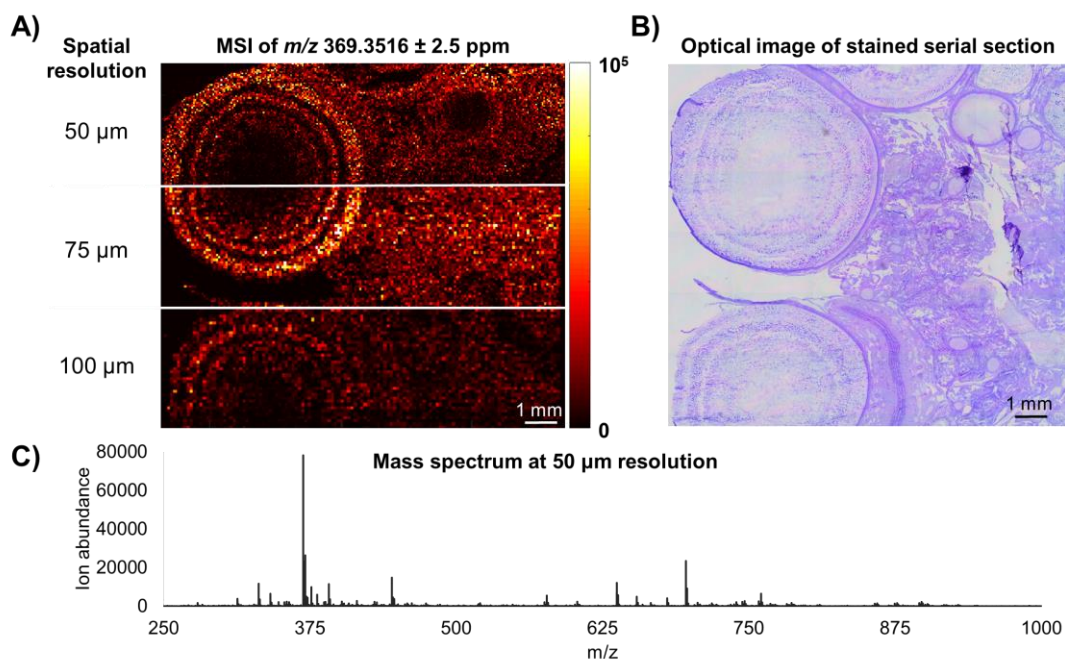


**Figure 8.** **A)** IR-MALDESI MSI of cholesterol  $[\text{M}-\text{H}_2\text{O}+\text{H}]^+$ ,  $m/z$   $369.3516 \pm 2.5 \text{ ppm}$  in hen ovary tissue at 50, 75, and 100  $\mu\text{m}$  spatial resolution. **B)** An optical image of a stained serial section showing the complex morphology of the ovary tissue. **C)** An averaged mass spectrum for the 50  $\mu\text{m}$  spatial resolution experiment.

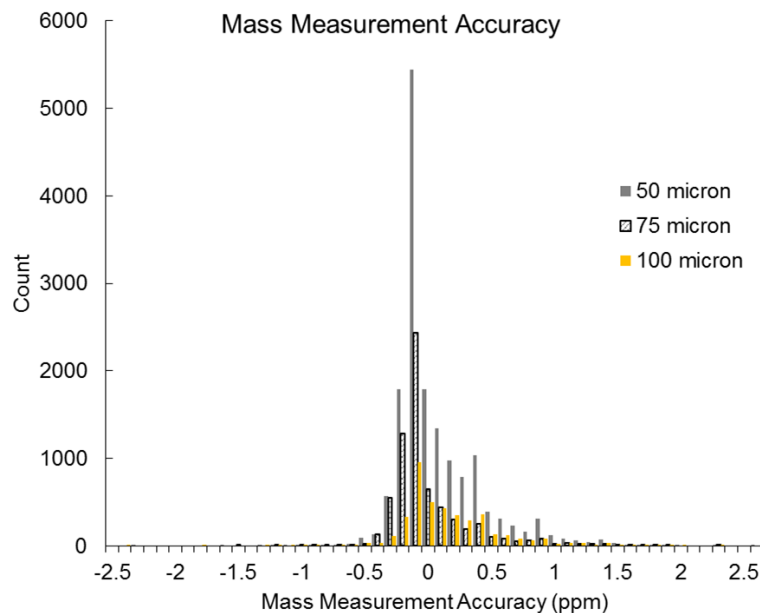


**Figure 9.** Mass measurement accuracy (MMA) of cholesterol MSI presented in **Figure 8**. RAW files were loaded into RawMeat (Vast Scientific) and exported using MZ monitor. MMA was calculated for every cholesterol peak and a histogram was created using 0.1 ppm bin size.

## 8.4 CONCLUSION

A multi-element optical design composed of an adjustable iris, beam expander, and aspherical focusing lens was implemented for high resolution IR-MALDESI MSI. The design was compared to the previously used single lens design, and demonstrated improved beam quality factor ( $M^2$ ) and a smaller minimum waist,  $W_0$ , two of the most important laser ablation parameters in the context of MSI. A hen ovarian tissue was analyzed using the multi-element system, yielding high quality MS images with 50 micron spatial resolution.

### 8.4.1 Acknowledgments

The authors gratefully acknowledge financial support from the National Institutes of Health (R01GM087964), the W.M. Keck Foundation, and North Carolina State University.

## REFERENCES

1. Amstalden van Hove, E.R., Smith, D.F., Heeren, R.M.: A concise review of mass spectrometry imaging. *Journal of chromatography. A.* 1217, 3946-3954 (2010).
2. Ràfols, P., Vilalta, D., Brezmes, J., Cañellas, N., del Castillo, E., Yanes, O., Ramírez, N., Correig, X.: Signal preprocessing, multivariate analysis and software tools for MA(LDI)-TOF mass spectrometry imaging for biological applications. *Mass spectrometry reviews.* (2016).
3. Boughton, B.A., Thinagaran, D., Sarabia, D., Bacic, A., Roessner, U.: Mass spectrometry imaging for plant biology: a review. *Phytochemistry Reviews.* 15, 445-488 (2016).
4. Gessel, M.M., Norris, J.L., Caprioli, R.M.: MALDI imaging mass spectrometry: Spatial molecular analysis to enable a new age of discovery. *Journal of proteomics.* 107C, 71-82 (2014).
5. Gode, D., Volmer, D.A.: Lipid imaging by mass spectrometry - a review. *The Analyst.* 138, 1289-1315 (2013).
6. Nilsson, A., Goodwin, R.J., Shariatgorji, M., Vallianatou, T., Webborn, P.J., Andrén, P.E.: Mass spectrometry imaging in drug development. *Analytical chemistry.* 87, 1437-1455 (2015).
7. Murray, K.K., Seneviratne, C.A., Ghorai, S.: High resolution laser mass spectrometry bioimaging. *Methods.* 104, 118-126 (2016).
8. Riedl, M.J. *Optical design fundamentals for infrared systems.* SPIE press, (2001).
9. Alkelly, A.A.: Spot size and radial intensity distribution of focused Gaussian beams in spherical and non-spherical aberration lenses. *Optics communications.* 277, 397-405 (2007).
10. Zavalin, A., Yang, J., Caprioli, R.: Laser Beam Filtration for High Spatial Resolution MALDI Imaging Mass Spectrometry. *Journal of the American Society for Mass Spectrometry.* 24, 1153-1156 (2013).
11. Jacobson, R.S., Thurston, R.L., Shrestha, B., Vertes, A.: In Situ Analysis of Small Populations of Adherent Mammalian Cells Using Laser Ablation Electrospray Ionization

Mass Spectrometry in Transmission Geometry. *Analytical chemistry*. 87, 12130-12136 (2015).

12. Römpf, A., Schäfer, K.C., Guenther, S., Wang, Z., Köstler, M., Leisner, A., Paschke, C., Schramm, T., Spengler, B.: High-resolution atmospheric pressure infrared laser desorption/ionization mass spectrometry imaging of biological tissue. *Analytical and bioanalytical chemistry*. 405, 6959-6968 (2013).
13. Hieta, J.-P., Vaikkinen, A., Auno, S., Rääkönen, H., Haapala, M., Scotti, G., Kopra, J., Piepponen, P., Kauppila, T.J.: A Simple Method for Improving the Spatial Resolution in Infrared Laser Ablation Mass Spectrometry Imaging. *Journal of the American Society for Mass Spectrometry*. (2017). doi:10.1007/s13361-016-1578-7
14. Jurchen, J.C., Rubakhin, S.S., Sweedler, J.V.: MALDI-MS imaging of features smaller than the size of the laser beam. *Journal of the American Society for Mass Spectrometry*. 16, 1654-1659 (2005).
15. Nazari, M., Muddiman, D.: Cellular-level mass spectrometry imaging using infrared matrix-assisted laser desorption electrospray ionization (IR-MALDESI) by oversampling. *Analytical and bioanalytical chemistry*. 407, 2265-2271 (2015).
16. Luxembourg, S.L., McDonnell, L.A., Mize, T.H., Heeren, R.M.A.: Infrared Mass Spectrometric Imaging below the Diffraction Limit. *Journal of proteome research*. 4, 671-673 (2005).
17. Soltwisch, J., Göritz, G., Jungmann, J.H., Kiss, A., Smith, D.F., Ellis, S.R., Heeren, R.M.A.: MALDI Mass Spectrometry Imaging in Microscope Mode with Infrared Lasers: Bypassing the Diffraction Limits. *Analytical chemistry*. 86, 321-325 (2014).
18. Sampson, J.S., Hawkrige, A.M., Muddiman, D.C.: Generation and detection of multiply-charged peptides and proteins by matrix-assisted laser desorption electrospray ionization (MALDESI) Fourier transform ion cyclotron resonance mass spectrometry. *Journal of the American Society for Mass Spectrometry*. 17, 1712-1716 (2006).
19. Robichaud, G., Barry, J.A., Garrard, K.P., Muddiman, D.C.: Infrared matrix-assisted laser desorption electrospray ionization (IR-MALDESI) imaging source coupled to a FT-ICR mass spectrometer. *Journal of the American Society for Mass Spectrometry*. 24, 92-100 (2013).

20. Bokhart, M.T., Muddiman, D.C.: Infrared matrix-assisted laser desorption electrospray ionization mass spectrometry imaging analysis of biospecimens. *The Analyst*. 141, 5236-5245 (2016).
21. Robichaud, G., Barry, J.A., Muddiman, D.C.: IR-MALDESI mass spectrometry imaging of biological tissue sections using ice as a matrix. *Journal of the American Society for Mass Spectrometry*. 25, 319-328 (2014).
22. Rosen, E., Bokhart, M., Ghashghaei, H.T., Muddiman, D.: Influence of Desorption Conditions on Analyte Sensitivity and Internal Energy in Discrete Tissue or Whole Body Imaging by IR-MALDESI. *Journal of the American Society for Mass Spectrometry*. 26, 899-910 (2015).
23. Kessner, D., Chambers, M., Burke, R., Agus, D., Mallick, P.: ProteoWizard: open source software for rapid proteomics tools development. *Bioinformatics*. 24, 2534-2536 (2008).
24. Schramm, T., Hester, A., Klinkert, I., Both, J.P., Heeren, R.M., Brunelle, A., Laprevote, O., Desbenoit, N., Robbe, M.F., Stoeckli, M., Spengler, B., Rompp, A.: imzML--a common data format for the flexible exchange and processing of mass spectrometry imaging data. *Journal of proteomics*. 75, 5106-5110 (2012).
25. Race, A.M., Styles, I.B., Bunch, J.: Inclusive sharing of mass spectrometry imaging data requires a converter for all. *Journal of proteomics*. 75, 5111-5112 (2012).
26. Robichaud, G., Garrard, K.P., Barry, J.A., Muddiman, D.C.: MSiReader: an open-source interface to view and analyze high resolving power MS imaging files on Matlab platform. *Journal of the American Society for Mass Spectrometry*. 24, 718-721 (2013).
27. Keicher, D.M.: Laser beam characterization results for a high-power cw Nd: YAG laser. *Photonics West'95*. 162-171 (1995).
28. Bokhart, M., Rosen, E., Thompson, C., Sykes, C., Kashuba, A.M., Muddiman, D.: Quantitative mass spectrometry imaging of emtricitabine in cervical tissue model using infrared matrix-assisted laser desorption electrospray ionization. *Analytical and bioanalytical chemistry*. 407, 2073-2084 (2015).
29. Rosen, E.P., Bokhart, M.T., Nazari, M., Muddiman, D.C.: Influence of C-Trap Ion Accumulation Time on the Detectability of Analytes in IR-MALDESI MSI. *Analytical chemistry*. 87, 10483-10490 (2015).

30. Meier, F., Garrard, K.P., Muddiman, D.C.: Silver dopants for targeted and untargeted direct analysis of unsaturated lipids via infrared matrix-assisted laser desorption electrospray ionization (IR-MALDESI). *Rapid Communications in Mass Spectrometry*. 28, 2461-2470 (2014).
31. Nazari, M., Muddiman, D.C.: Polarity switching mass spectrometry imaging of healthy and cancerous hen ovarian tissue sections by infrared matrix-assisted laser desorption electrospray ionization (IR-MALDESI). *The Analyst*. 141, 595-605 (2016).

# 9 MASS SPECTROMETRY IMAGING SOFTWARE

**Kenneth P. Garrard**

Senior Research Scholar, PEC

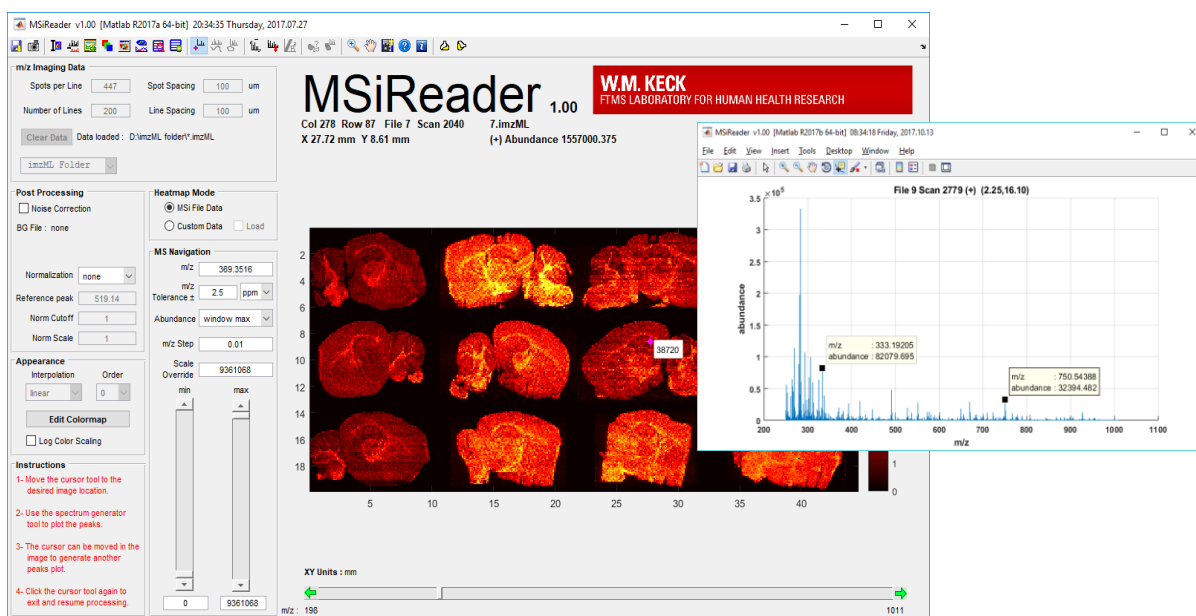
**Mark T. Bokhart and Milad Nazari**

Graduate Students, Chemistry

**David C. Muddiman**

Professor, Chemistry

*A major update to the mass spectrometry imaging (MSI) software MSiReader is presented, offering a multitude of newly added features critical to MSI analyses. MSiReader is a free, open-source, and vendor-neutral software written in MATLAB and is capable of analyzing most common MSI data formats. A standalone version of the software which does not require a MATLAB license is also distributed. Newly incorporated data analysis features expand the utility of MSiReader beyond simple visualization of molecular distributions. A quantification tool allows researchers to calculate absolute concentrations exclusively through MSiReader software, significantly reducing analysis time. An image overlay feature for visualizing complementary imaging modalities, an ionization polarity filter, and a quality assurance feature to calculate and display mass measurement accuracy (MMA) have also been added. Most importantly, as new features have been added performance has not degraded, in fact it has been dramatically improved. These new tools and performance improvements enable the MSI community to evaluate their data in greater depth and in less time.*



## 9.1 INTRODUCTION

Mass spectrometry imaging (MSI) is a rapidly growing research area where mass spectrometric analysis is performed in a spatially resolved manner. MSI data is most commonly represented as heat maps based on ion abundance mapped on the Cartesian coordinates of the analyzed sample. This allows for the generation of images for each spectrally resolved mass-to-charge ratio value (denoted by  $m/z$ ) across the analyzed region. A color scale bar is used to represent the ion abundance. A wide variety of ionization sources and mass analyzers have been used to create MSI datasets. Most commercial software available for analysis of MSI data are vendor-specific and proprietary. However, in recent years there has been increased support for data sharing through a universal data format imzML [1] and the introduction of open-source or free data analysis software such as MSiReader [2], Cardinal [3], BioMAP [4], msiQuant [5], SpectralAnalysis [6], and METASPACE [7]. Each software has unique advantages and disadvantages. Recently, a new version of msiQuant [8] was introduced with the ability to analyze imzML data with software tools to handle MSI quantification data and multimodal imaging capabilities. Cardinal and SpectralAnalysis are software packages that allow advanced statistical analysis of MSI data sets in an untargeted fashion [3, 6]. The recent developments of software packages available for analyzing and processing MSI data were outlined in a recent review article [9].

MSiReader was introduced in 2013 as an open-source, vendor neutral MSI data analysis software written in MATLAB® [2]. At the time of publication, it was the only software capable of analyzing high resolving power mass spectrometry imaging data without data compression. The maximum file size was and still is only limited by the amount of RAM available. MSiReader was initially designed to process and analyze imaging data generated in our laboratory using the infrared matrix-assisted laser desorption electrospray ionization (IR-MALDESI) imaging source [10, 11]; however, since then, it has become an essential tool for research in our laboratory as well as others. At the time of the submission of this manuscript, the original manuscript has been cited over 110 times for diverse applications in proteomics [12], plant and animal metabolomics [13-15], and forensics [16]. Community feedback has led to the incorporation of numerous improvements in the user interface that enhance workflow, as well as tools for spectral export, image export, data binning, colocalization, normalization methods, polarity switching and filtering, as well as quantification.

The evolution of MSI in the past several years has required the constant development and improvement of software packages to facilitate the analysis of a wide variety of MSI data. MSiReader has evolved to include tools that allow complex and customized data analysis workflows to be incorporated into the software, allowing unprecedented analysis of MSI data. In this manuscript, the authors present v1.0 MSiReader, with an improved user interface, more



robust error checking, faster data loading and processing, and newly incorporated features for the analysis of MSI datasets.

## 9.2 EXPERIMENTAL

All experiments mentioned in this manuscript were performed in accordance with local ethical guidelines. Human cervical tissues were obtained from the University of North Carolina Tissue Procurement Facility through UNC IRB #09-0921, and written informed consent was obtained from all patients. Two-day-old whole neonatal mouse pups were obtained from NCSU Department of Molecular Biomedical Sciences. Hen ovarian tissues were acquired from commercial egg laying hens in the NCSU Department of Poultry Science. All husbandry practices were approved by North Carolina State University Institutional Animal Care and Use Committee (IACUC).

All imaging experiments were performed in our laboratory using infrared matrix-assisted laser desorption electrospray ionization (IR-MALDESI) sourced coupled to high resolving power mass spectrometers. The details of IR-MALDESI source design and steps involved in imaging experiments are described elsewhere in detail [10, 17, 18]. In short, the tissues were sectioned into 10-25  $\mu\text{m}$  thick sections using a Leica CM1950 cryostat (Buffalo Grove, IL, USA) and then thaw-mounted onto clean microscope slides. For quantitative MSI analyses, a calibration series of stable isotope labeled version of the analyte was pipetted directly on top of the tissue section prior to IR-MALDESI analysis. The tissue sections were then transferred to the enclosure housing the IR-MALDESI imaging source and placed on a Peltier-cooled stage. The relative humidity inside the enclosure was reduced to  $\sim 10\%$  by purging the enclosure with dry nitrogen gas, and the stage temperature was reduced to  $-10\text{ }^\circ\text{C}$ . After roughly 10 minutes, the enclosure was opened to allow the deposition of a thin layer of ice matrix on the tissue by sublimation of water present in the atmosphere. Once a thin layer of ice was formed over the tissue, the enclosure was closed and the relative humidity was again reduced to  $\sim 10\%$ .

Two mid-infrared laser pulses at a wavelength of 2940 nm were used to desorb material from the tissue sections. The neutral material desorbed from the tissue partition into the charged droplets of the electrospray and are ionized in an ESI-like fashion. Quantitative MSI and whole-body MSI were performed using a Q Exactive mass spectrometer (Thermo Scientific, Bremen, Germany) as described by Bokhart *et al.* [19] and Rosen *et al.* [20], respectively. Polarity switching IR-MALDESI MSI was performed using a Q Exactive Plus mass spectrometer (Thermo Scientific, Bremen, Germany) as outlined by Nazari and Muddiman [21]. Since IR-MALDESI is a pulsed ionization source, the automatic gain control (AGC) is disabled and ions are stored in the C-trap for a pre-determined amount of time denoted by the maximum injection time (IT). Mass ranges, electrospray solvent composition, and the injection times varied for each experiment since these are optimized based on the goals of each experiment.

The .RAW files generated by the Thermo instruments were first converted to mzML format using the msConvert tool from ProteoWizard [22], and then converted to imzML using the imzML converter [23]. The imzML files were subsequently loaded into MSiReader v1.0 for visualization and analysis.

## 9.3 RESULTS AND DISCUSSION

### 9.3.1 Overview of MSiReader Features

MSiReader was developed because of the need to process high resolving power MSI data sets without compromising the integrity of the data with software-imposed limitations on dynamic range or resolution. Initial efforts were directed at providing an efficient workflow for untargeted analysis using new instrumentation. The first version could simply load an mzXML data set and display a heatmap image of ion abundance for any  $m/z$  value and window size chosen by the user. It also provided a tool to plot the spectrum for a single pixel and another to find putative peaks based on a parabolic fitting and thresholding algorithm. Since then, many additional capabilities have been implemented and performance has been greatly improved. Some examples of new capabilities of the software include: saving and reloading an entire session as a MATLAB binary (.MAT) file; peak picking based on differences between reference and interrogated regions of interest; four channel colocalization plots;  $m/z$  abundance rank plots; several normalization options; numerous ways to export, save and reuse data; exporting binned abundance data into a continuous  $m/z$  range in preparation for multivariate analysis; batch generation of images for each  $m/z$  value in a list; extensive customization options via a preferences file; and an application programming interface (API) that eases the task of prototyping new ideas and implementing custom scripts.

The application programming interface provides up to eight special icons on MSiReader's toolbar that can be associated with user-written MATLAB functions. When one of these icons is clicked, the user's code is passed a data structure (called MSi) containing the loaded data cube along with all current parameter settings and handles to all GUI objects. The user's code has access to the library of over 300 functions distributed with MSiReader as well as any installed MATLAB toolbox functions. Several simple examples (e.g., the abundance ratio between two  $m/z$  values across an image) and documentation of the function library and MSi data structure are included in the v1.0 MSiReader release.

The focus of this paper is on the performance improvements made since the initial release and five new and useful tools for: loading multiple data sets at once, absolute quantification, polarity switching, image overlay, and mass measurement accuracy (MMA) quality assurance (QA) plots.

### 9.3.2 Loading and Processing Imaging Data Sets

In addition to the preferred imzML format, MSiReader can load data stored as mzXML, IMG (Analyze 7.5), and Bruker ASCII files. All features of MSiReader are supported for each of the formats and internally the spectra are stored as sparse, processed data. That is, the spectra for each pixel are stored as an independent sequence of  $m/z$ , abundance pairs using double precision floating-point values following the IEEE 754 standard. As each scan is loaded, it can be filtered by any combination of  $m/z$  range, abundance threshold, spatial location or polarity. This can have a significant improvement on performance, especially by removing large numbers of low abundance values from the data cube of a high resolving power instrument. It also allows the user to restrict the spatial and  $m/z$  range of data loaded from very large files. Additionally, a smart abundance filter can be selected whereby any consecutive sequence with more than two abundance values below the threshold is replaced by threshold (or zero) values at each end instead of being removed. This improves the appearance of filtered spectral plots by forcing the lines between data spectral data points to return to the baseline abundance instead of connecting the two data points above the threshold with a straight line.

**Table 1** shows the dramatic improvement in data set loading time for the supported formats that have been made since MSiReader release 0.03 in July of 2013. Even though load time is dominated by the speed of the file storage medium and the amount of RAM available, significant improvements have been made. All tests were done on the same computer, a Dell Precision Tower 5810 (Xeon ES-1607 v3, 3.1 GHz Processor, 64 GB RAM, 256 GB SSD and 4 TB HD) in a newly started MATLAB 2017a session. All code was stored on the SSD and the data sets were on the hard drive. The measured time required for various operations in MSiReader are obtained using the built-in MATLAB *tic* and *toc* functions and displayed in the MATLAB command window.

**Table 1.** MSiReader dataset loading time improvement.

Data Set Format	File Size (GB)	Number of Scans	Memory (GB)	Release 0.03 (sec)	Release 1.0 (sec)	% Decrease
imzML (1)	5.87	7,426	3.97	140	67	52
imzML (2)	3.93	10,608	2.55	140	80	43
imzML (3)	36.40	32,060	25.17	936	706	25
mzXML	1.87	5,551	0.931	109	77	29
ASCII	0.227	4,048	0.064	316	8	97
IMG	0.530	7,275	3.55	73	30	59
IMG	3.23	69,680	27.84	333	80	76

The performance of other tasks in MSiReader has also been improved even though new features and much new code have been added. **Table 2** compares several common operations: updating the heatmap display after changing the *m/z* value, the normalization option, or the window tolerance; exporting raw spectra for the scans in a region of interest (ROI); peak picking based on differences between a reference and an interrogated ROI; and batch export of heatmap images for a list of *m/z* values into a folder (png file format). The heatmap update and batch export tasks were done using the imzML(2) file from **Table 1** and the pixel export and peak picking tasks were done using the imzML(3) file. The 42 scan ROI was the same for both export operations and that ROI was also the interrogated region for the peak picking operation. As shown in the table, significant improvements have been made for these tasks, greatly enhancing the user experience.

**Table 2.** MSiReader operation time improvement.

Operation	Release 0.03 (sec)	Release 1.0 (sec)	% Decrease
Heatmap Update <i>10,608 scans; 3.93 GB data set</i>	13	1	92
Spectrum Export to Excel <i>42 scan ROI; 50 MB output file</i>	365	21	94
Spectrum Export to Text <i>42 scan ROI; 51 MB output file</i>	83	7	92
Peak Picking <i>ROIs: 42 scan reference vs 42 scan interrogated</i>	91	14	85
Batch Image Export <i>10608 scans; 3.93 GB data set; 57 m/z values</i>	681	59	91

### 9.3.3 Loading Multiple Data Sets

A commonly requested feature that is now available in MSiReader is the ability to load and process more than one data set simultaneously. Previously, the only way to accomplish this was to merge all the files into one file, which could be a tedious and time-consuming process, especially for files with different spatial dimensions. Now MSiReader can load all the imzML or mzXML files in a folder on-the-fly and distribute the images into a tiled mosaic defined by the user. The files need not have the same dimensions and smaller files are padded with empty scans such that all images in a row have the same number of scan rows and all images in a column have the same number of scan columns. Each image is centered in its tile and surrounded by at least one empty row and column. After selecting to load a folder, the user is prompted to define the number of tile rows and columns (**Figure 1**). The files are then loaded in alphanumeric order by name or

they may be given a sequence number suffix. The source of each pixel (file and scan number) is retained throughout all subsequent processing. All ROI, peak picking, analysis, export and visualization tools are supported across the image mosaic. For example, the interrogated and reference ROIs for peak picking may be in different image tiles and thus from different data sets.

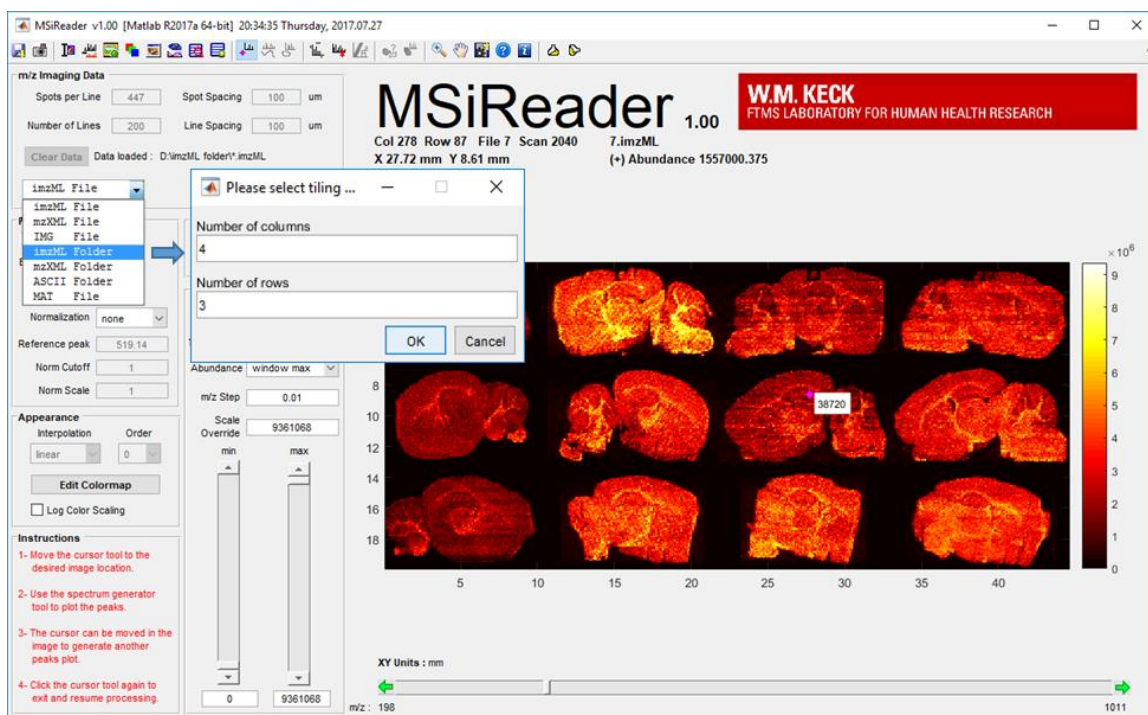


**Figure 1.** Loading multiple imaging data sets. The images presented are for cholesterol  $[M+H^+-H_2O]^+$  in 12 sagittal mouse brain tissue sections.

### 9.3.4 Absolute Quantification for Mass Spectrometry Imaging

Quantification in mass spectrometry imaging is a challenging experiment requiring consideration to many factors that may influence ion abundance during the experiment. This requires the incorporation of a calibration curve and may also require a normalization compound. Visualization and analysis software must support common and advanced data analysis methods. Most MSI software packages allow normalization (ratio) of images to a specific compound or total ion current (TIC), thereby accounting for per-pixel ionization efficiencies. This normalization step has proven itself essential for quantitative mass spectrometry imaging [19].

Incorporation of a spatial calibration curve is essential to any quantitative MSI experiment to relate ion abundance to an absolute amount of a compound. Integration of standards with tissues has been performed in various ways [24] but all require the selection of an ROI for each calibration point in addition to the tissue area to be quantified. The newly introduced MSiQuantification tool

(Figure 2) in MSiReader allows the user to select up to 10 calibration ROIs and define the concentration of each. Once the tissue ROI and at least 3 calibration points have been selected, the user can generate a linear least squares regression for the calibration curve and calculate the concentration of analyte across the selected tissue ROI. After the calibration curve has been defined, the tissue image may be represented as absolute concentration based on the calibration curve. To preserve data analyses and allow additional analyses, the quantification process parameters and ROIs can be saved into a binary file and reloaded later to repeat the analysis using the same exact parameters.

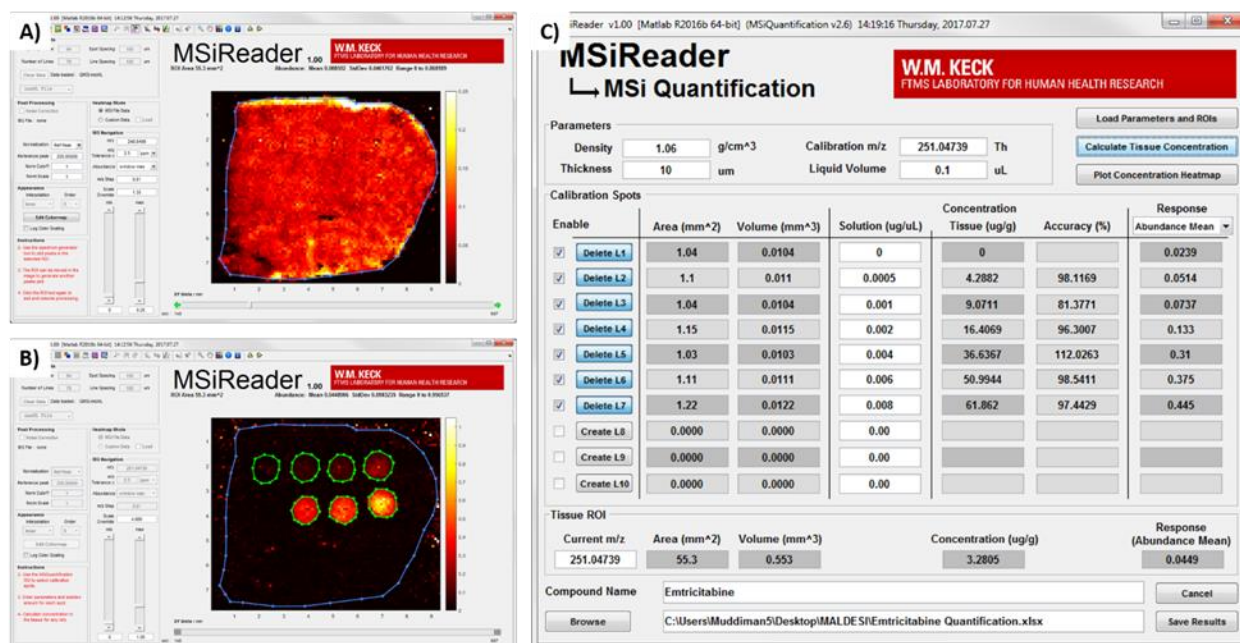


**Figure 2.** MSiQuantification tool for absolute quantification MSI experiments. The tool allows ROIs to be drawn for **A)** an area of the tissue to be quantified and **B)** up to 10 calibration spots. Once the ROIs have been drawn, the concentration of each calibration spot can be input in the MSiQuantification pop-up window **C)**. The ion images presented are for entricitabine  $[M+Na]^+$  in a human cervical tissue section. The calibration curve spots of stable isotope labeled entricitabine  $[M+Na]^+$  were spotted directly on top of the tissue section prior to IR-MALDESI MSI.

### 9.3.5 Polarity Switching Mass Spectrometry Imaging

Lipids and metabolites are some of the most commonly analyzed biomolecules using MSI. Alterations in lipidome and metabolome have been linked to several diseases spanning from hypertension, diabetes, Alzheimer’s diseases, and cancer [25, 26]; therefore, assessing the distribution and abundance of lipids and metabolites in biological tissue specimens is of



paramount importance to provide insight into the onset and progression of disease, as well as the discovery of potential biomarkers. Due to their remarkable structural diversity, lipids and metabolites exhibit preferential ionization efficiencies. Generally, metabolites that are detected in high ion abundance as positive ions are poorly detected (or not detected at all) as negative ions, and vice versa. Therefore, to comprehensively characterize the metabolome, analysis of tissue specimens in both polarities is required. One could perform two MSI experiments, one in each polarity, to obtain extensive metabolome coverage; however, this approach would be costly in terms of time, sample, and materials used. Alternatively, polarity switching MSI can be used to obtain the same biochemical information, while shortening the analysis time and reducing sample consumption by almost half. Indeed, polarity switching MSI has become a valuable analysis mode in recent years [21, 27-30]. The recent surge in reports of polarity switching MSI calls for new software options for analyzing these datasets.

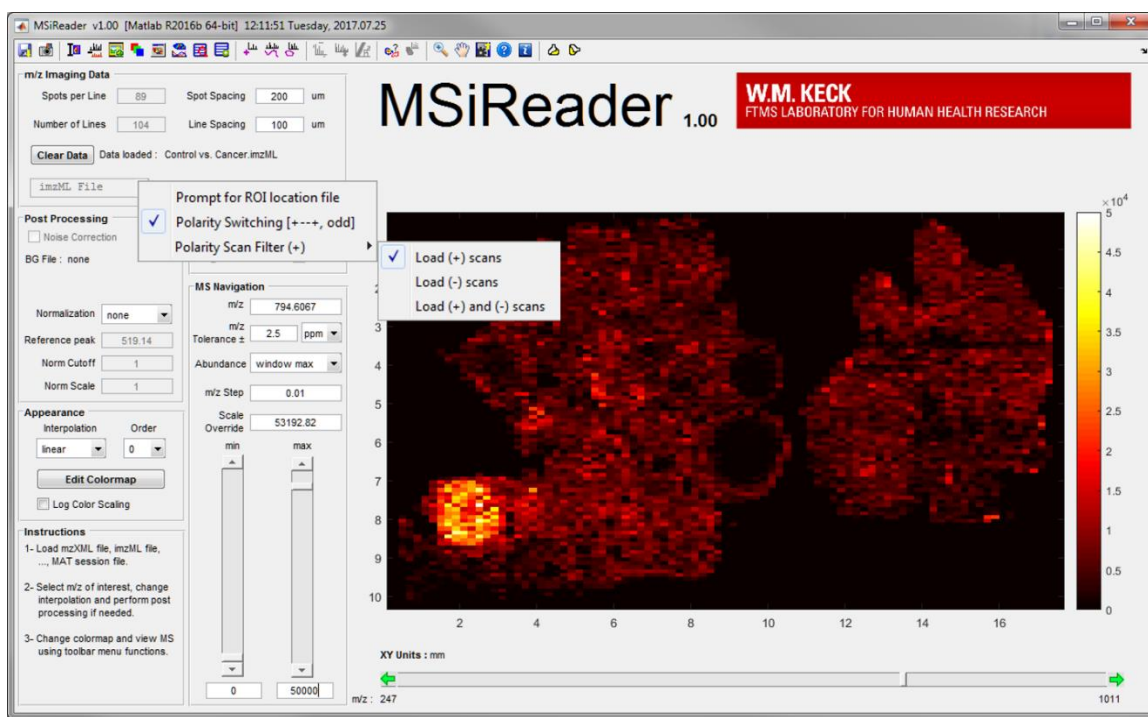


**Figure 3.** Polarity switching and polarity filtering are implemented for the mzXML and imzML file formats as the data is loaded. In this case, healthy (left) and cancerous (right) hen ovarian tissue sections were analyzed using a polarity pattern of [+---, odd] and only the (+) polarity scans are retained.

One of the new features introduced in MSiReader is the ability to parse data using the polarity in which the spectra were acquired. There are different approaches to acquiring polarity switching spectra such as alternating polarities from pixel to pixel [21, 30], from one line to the next [29], or even using a “spiral” step [28] to acquire spectra in positive and negative modes. MSiReader can

analyze these patterns while parsing the data and loading the desired polarity. Furthermore, it can be used to filter out “equilibration spectra” that might have been collected in between polarity switching events during data acquisition. MSiReader implements four polarity switching patterns: [++++], [-++-], [+ -] and [-+]. For the 4-tuple patterns, either the odd (1,3) or the even (2,4) scans are equilibrium scans used to allow the electrospray to stabilize when the polarity is changed from one pixel to the next with no advancement of the sample raster stage. An example of a polarity switching MSI method and equilibration spectra was recently demonstrated by our group [21] and a representative image showing the loading process in MSiReader is shown in **Figure 3**. Additional patterns for data analysis can be readily incorporated into the software using the existing algorithm for reading the file header and scan polarities. In addition, an optional filter parameter allows the user to select the positive image, the negative image, or both images for subsequent processing. If both polarities are retained, polarity is selected when the MSiPeakfinder or MSiSpectrum tools are launched. The filter and polarity selection can also be selected without the switching feature for a file with an arbitrary distribution of polarities – for example, a tiled composite imzML image of multiple tissue samples.

### 9.3.6 Image Overlay Tool

Mass spectrometry imaging allows the spatial distribution of ions to be depicted in a two-dimensional array. The overlap of two complimentary imaging techniques allows researchers to gain deeper insight into the significance of spatial localizations. In combining MSI images with other imaging modalities, the molecular distributions gain meaning in their context to the tissue morphology.

The MSiImage tool has been implemented in MSiReader to import, scale, and align an image (e.g. optical, fluorescence) on an MSiReader heatmap. This includes an adjustable transparency of the image along with resizing, cropping, and rotation. Any file format supported by MATLAB can be imported allowing connection between two analysis methods to be compared. Alignment of classical biology techniques such as staining by haemotoxylin and eosin (H&E) or immunohistochemistry with a MSI data set allows for histology-directed molecular analysis of tissues [31]. An example of an image overlay with the MSI data is demonstrated in **Figure 4**, where the spatial distribution of  $m/z$  367.3363, putatively assigned to desmosterol  $[M+H^+-H_2O]^+$ , is displayed on a semi-transparent optical image of the whole-body section. In addition, the MSiImage function can be used in combination with the colocalization tool in MSiReader to show the distribution of three distinct ions overlaid with another semi-transparent image.





**Figure 4.** MSiImage tool for overlaying an optical image with the ion image of putatively assigned desmosterol ( $m/z$  367.3363,  $[M+H^+-H_2O]^+$ ) obtained in a whole-body IR-MALDESI analysis 2-day old neonatal mouse.

### 9.3.7 Mass Measurement Accuracy

The importance of maintaining high mass measurement accuracy (MMA) throughout MS-based experiments is well-known. Especially for instruments with high resolving power, very small shifts in  $m/z$  can occur due to variation in the detector electronics, magnetic fields, power supplies, etc. over the time that it takes to image a complete sample, which ranges from a few minutes to many hours. This point is more vital in MSI analyses since there are no chromatographic separations and deviations in MMA could lead to generation of incorrect ion images or identification of incorrect analytes in untargeted studies. MMA is a metric describing the difference between the

measured mass-to-charge ratio of an ion and the real, exact mass-to-charge ratio of that ion. It is expressed as a value in parts-per-million (ppm) as shown in Equation 1.

$$MMA = \frac{mz_{measured} - mz_{actual}}{mz_{actual}} \times 10^6 \quad (1)$$

In our laboratory, the MMA for an analyte observed in MSI analyses were calculated by exporting the centroid  $m/z$  value for the peak at each scan over the user-defined ROI (often the tissue section) to an Excel sheet using MSiReader and then calculating the MMA for each scan. Another option could be to use a separate program to export the centroid  $m/z$  from the raw file. These processes are laborious and time consuming, and do not provide information about changes in the MMA as a function of spatial location or time.

To circumvent these issues and speed up the analysis process, we have introduced new quality assurance features in MSiReader that allow users to generate heatmaps of MMA for the scans within the user-identified ROI or all scans in the file. This feature uses the  $m/z$  value input by the user as the “true” value and picks the most abundant peak in the  $m/z$  window as the “experimental” value to calculate the MMA at each scan. The MMA for each scan is then plotted in a heatmap, where possible deviations at specific locations within the ROI can be easily observed. **Figure 5** demonstrates how this function can be useful for assessing the quality of the data. The MMA of glutathione ( $m/z$  306.0766, [M-H<sup>+</sup>]) across a healthy ovarian tissue section was plotted to ensure there were no deviations in the course of MSI analysis. In addition, a histogram of the MMAs, as a function of number of scans or the abundance at each scan, can also be exported to a separate figure (along with the MMA heatmap or separately). This tool can serve as a facile method to check the MMA of the analyte(s) of interest throughout the imaging experiment. If needed, the MMA values, along with the scan number from which they were calculated, can be exported into an Excel sheet for further investigation. The MMA heatmap feature allows for generation of correct ion images and putative identification of unknown metabolites based on their accurate mass in untargeted analyses. In addition, this feature is useful in targeted and quantitative MSI experiments to ensure there are no outliers that could potentially undermine the results.

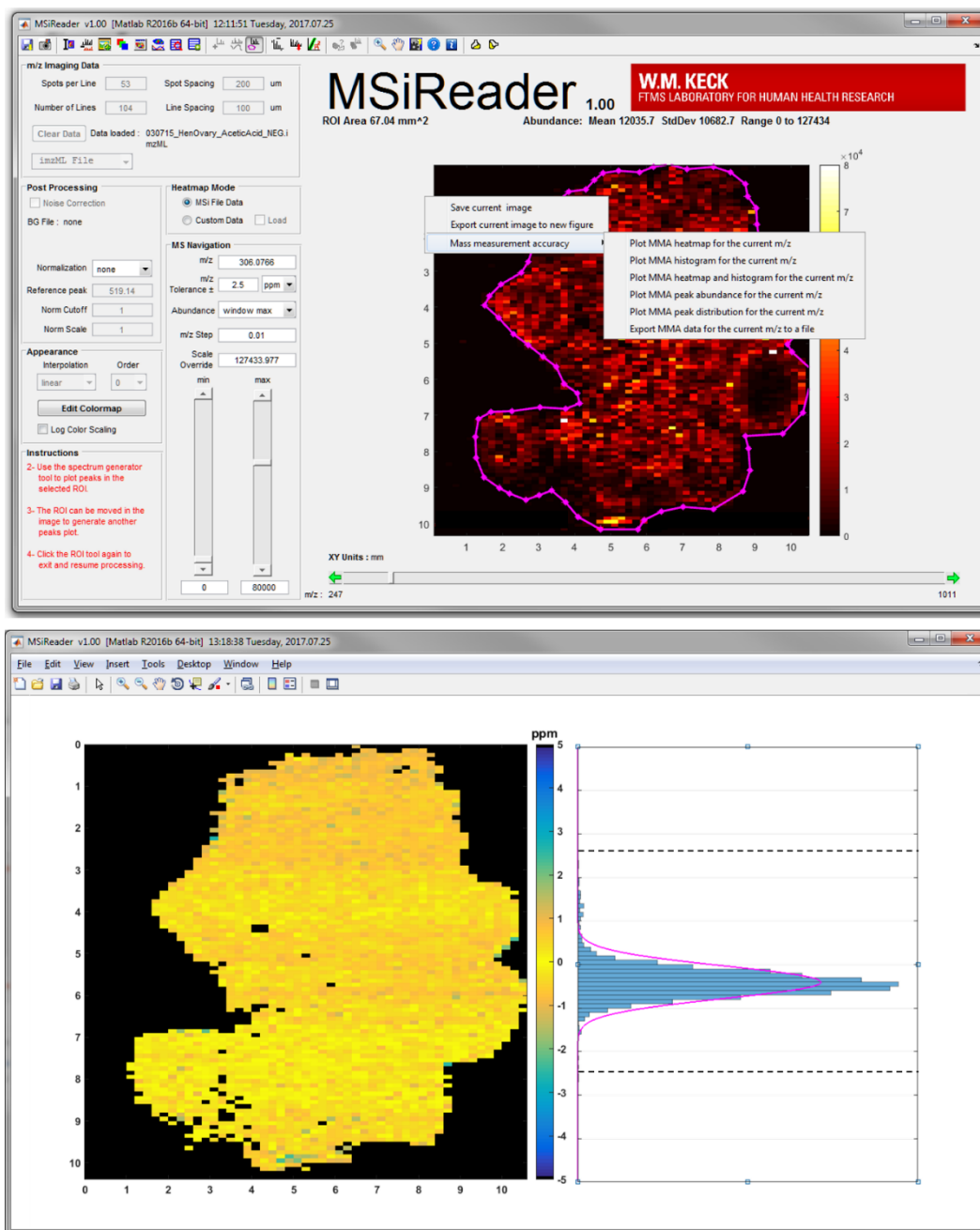


**Figure 5. Top)** Screenshot of MSiReader interface showing the ion image of glutathione ( $m/z$  306.0766,  $[M-H]^+$ ) in a healthy hen ovary tissue section analyzed with negative mode IR-MALDESI. The mass measurement accuracy function can be accessed by right-clicking on the image axes. **Bottom)** Heatmap of MMA in ppm of glutathione over the tissue region (denoted by magenta line on the ion image). Calculated MMA values for all interrogated voxels are presented in histogram form with an overlaid Gaussian fit, demonstrating normality of the MMA distribution. The dashed lines on the histogram demonstrate the  $\pm 2.5$  ppm tolerance used to generate the ion image.

## 9.4 CONCLUSIONS

Since its introduction to the MSI community in 2013, MSiReader has been downloaded and used by over 1000 researchers worldwide and has been cited in more than 110 publications. Over the past four years, new algorithms have been implemented into the software, new features have been added to enhance the analysis workflows, and significant performance improvements have been made based on the feedback from the MSI community. Some of the major features added to v1.0 such as the MSiQuantification tool, ability to analyze polarity switching files, image overlay, and MMA heatmaps were discussed in this manuscript. These features have enabled our group, and others in the MSI community, to carry out important research projects. For instance, the MSiQuantification has simplified the data analysis steps required to obtain absolute quantification of analytes in tissue sections, while the MMA feature provides a necessary, and often overlooked, quality assurance step to ensure instrument stability and high data quality over the course of an imaging experiment. The influence of the user community and our own research objectives continue to provide an opportunity for further development of this useful and free software tool.

### 9.4.1 Acknowledgements

The authors thank Drs. Guillaume Robichaud, Jeremy Barry, and Eli Rosen for their discussions regarding MSiReader development. Additionally, feedback from MSiReader users across the world is greatly appreciated. The authors gratefully acknowledge financial assistance received from the National Institutes of Health (R01GM087964), the W. M. Keck foundation, and North Carolina State University.

## REFERENCES

1. Schramm, T., Hester, A., Klinkert, I., Both, J.P., Heeren, R.M., Brunelle, A., Laprevote, O., Desbenoit, N., Robbe, M.F., Stoeckli, M., Spengler, B., Rompp, A.: imzML--a common data format for the flexible exchange and processing of mass spectrometry imaging data. *Journal of proteomics*. 75, 5106-5110 (2012).
2. Robichaud, G., Garrard, K.P., Barry, J.A., Muddiman, D.C.: MSiReader: an open-source interface to view and analyze high resolving power MS imaging files on Matlab platform. *Journal of the American Society for Mass Spectrometry*. 24, 718-721 (2013).
3. Bemis, K.D., Harry, A., Eberlin, L.S., Ferreira, C., van de Ven, S.M., Mallick, P., Stolowitz, M., Vitek, O.: Cardinal: an R package for statistical analysis of mass spectrometry-based imaging experiments. *Bioinformatics*. (2015).

4. Stoeckli, M., Staab, D., Staufenbiel, M., Wiederhold, K.-H., Signor, L.: Molecular imaging of amyloid  $\beta$  peptides in mouse brain sections using mass spectrometry. *Analytical Biochemistry*. 311, 33-39 (2002).
5. Kallback, P., Shariatgorji, M., Nilsson, A., Andren, P.E.: Novel mass spectrometry imaging software assisting labeled normalization and quantitation of drugs and neuropeptides directly in tissue sections. *Journal of proteomics*. 75, 4941-4951 (2012).
6. Race, A.M., Palmer, A.D., Dexter, A., Steven, R.T., Styles, I.B., Bunch, J.: SpectralAnalysis: Software for the Masses. *Analytical chemistry*. 88, 9451-9458 (2016).
7. Palmer, A., Phapale, P., Chernyavsky, I., Lavigne, R., Fay, D., Tarasov, A., Kovalev, V., Fuchser, J., Nikolenko, S., Pineau, C., Becker, M., Alexandrov, T.: FDR-controlled metabolite annotation for high-resolution imaging mass spectrometry. *Nat Meth.* 14, 57-60 (2017).
8. Källback, P., Nilsson, A., Shariatgorji, M., Andrén, P.E.: mslQuant – Quantitation Software for Mass Spectrometry Imaging Enabling Fast Access, Visualization, and Analysis of Large Data Sets. *Analytical chemistry*. 88, 4346-4353 (2016).
9. Ràfols, P., Vilalta, D., Brezmes, J., Cañellas, N., del Castillo, E., Yanes, O., Ramírez, N., Correig, X.: Signal preprocessing, multivariate analysis and software tools for MA(LDI)-TOF mass spectrometry imaging for biological applications. *Mass spectrometry reviews*. (2016).
10. Robichaud, G., Barry, J.A., Garrard, K.P., Muddiman, D.C.: Infrared matrix-assisted laser desorption electrospray ionization (IR-MALDESI) imaging source coupled to a FT-ICR mass spectrometer. *Journal of the American Society for Mass Spectrometry*. 24, 92-100 (2013).
11. Bokhart, M.T., Muddiman, D.C.: Infrared matrix-assisted laser desorption electrospray ionization mass spectrometry imaging analysis of biospecimens. *The Analyst*. 141, 5236-5245 (2016).
12. Gemperline, E., Keller, C., Jayaraman, D., Maeda, J., Sussman, M.R., Ané, J.-M., Li, L.: Examination of Endogenous Peptides in *Medicago truncatula* Using Mass Spectrometry Imaging. *Journal of proteome research*. 15, 4403-4411 (2016).
13. Bhandari, D.R., Wang, Q., Friedt, W., Spengler, B., Gottwald, S., Römpf, A.: High resolution mass spectrometry imaging of plant tissues: towards a plant metabolite atlas. *The Analyst*. 140, 7696-7709 (2015).

14. Gemperline, E., Jayaraman, D., Maeda, J., Ané, J.-M., Li, L.: Multifaceted Investigation of Metabolites during Nitrogen Fixation in Medicago via High Resolution MALDI-MS Imaging and ESI-MS. *Journal of the American Society for Mass Spectrometry*. 26, 149-158 (2015).
15. Liebeke, M., Strittmatter, N., Fearn, S., Morgan, A.J., Kille, P., Fuchser, J., Wallis, D., Palchykov, V., Robertson, J., Lahive, E.: Unique metabolites protect earthworms against plant polyphenols. *Nature communications*. 6, (2015).
16. Forbes, T.P., Sisco, E.: Chemical imaging of artificial fingerprints by desorption electro-flow focusing ionization mass spectrometry. *The Analyst*. 139, 2982-2985 (2014).
17. Robichaud, G., Barry, J.A., Muddiman, D.C.: IR-MALDESI mass spectrometry imaging of biological tissue sections using ice as a matrix. *Journal of the American Society for Mass Spectrometry*. 25, 319-328 (2014).
18. Nazari, M., Bokhart, M.T., Muddiman, D.C.: Whole-body Mass Spectrometry Imaging by Infrared Matrix-assisted Laser Desorption Electrospray Ionization (IR-MALDESI). e53942 (2016).
19. Bokhart, M., Rosen, E., Thompson, C., Sykes, C., Kashuba, A.M., Muddiman, D.: Quantitative mass spectrometry imaging of emtricitabine in cervical tissue model using infrared matrix-assisted laser desorption electrospray ionization. *Analytical and bioanalytical chemistry*. 407, 2073-2084 (2015).
20. Rosen, E., Bokhart, M., Ghashghaei, H.T., Muddiman, D.: Influence of Desorption Conditions on Analyte Sensitivity and Internal Energy in Discrete Tissue or Whole Body Imaging by IR-MALDESI. *Journal of the American Society for Mass Spectrometry*. 26, 899-910 (2015).
21. Nazari, M., Muddiman, D.C.: Polarity switching mass spectrometry imaging of healthy and cancerous hen ovarian tissue sections by infrared matrix-assisted laser desorption electrospray ionization (IR-MALDESI). *The Analyst*. 141, 595-605 (2016).
22. Kessner, D., Chambers, M., Burke, R., Agus, D., Mallick, P.: ProteoWizard: open source software for rapid proteomics tools development. *Bioinformatics*. 24, 2534-2536 (2008).
23. Race, A.M., Styles, I.B., Bunch, J.: Inclusive sharing of mass spectrometry imaging data requires a converter for all. *Journal of proteomics*. 75, 5111-5112 (2012).

24. Porta, T., Lesur, A., Varesio, E., Hopfgartner, G.: Quantification in MALDI-MS imaging: what can we learn from MALDI-selected reaction monitoring and what can we expect for imaging? *Analytical and bioanalytical chemistry*. 407, 2177-2187 (2015).
25. Gowda, G.N., Zhang, S., Gu, H., Asiago, V., Shanaiah, N., Raftery, D.: Metabolomics-based methods for early disease diagnostics. *Expert review of molecular diagnostics*. 8, 617-633 (2008).
26. Johnson, C.H., Ivanisevic, J., Siuzdak, G.: Metabolomics: beyond biomarkers and towards mechanisms. *Nature reviews Molecular cell biology*. 17, 451-459 (2016).
27. Thomas, A.I., Charbonneau, J.L., Fournaise, E., Chaurand, P.: Sublimation of new matrix candidates for high spatial resolution imaging mass spectrometry of lipids: enhanced information in both positive and negative polarities after 1, 5-diaminonaphthalene deposition. *Analytical chemistry*. 84, 2048-2054 (2012)
28. Korte, A.R., Lee, Y.J.: Multiplex mass spectrometric imaging with polarity switching for concurrent acquisition of positive and negative ion images. *Journal of the American Society for Mass Spectrometry*. 24, 949-955 (2013).
29. Janfelt, C., Wellner, N., Hansen, H.S., Hansen, S.H.: Displaced dual-mode imaging with desorption electrospray ionization for simultaneous mass spectrometry imaging in both polarities and with several scan modes. *Journal of mass spectrometry : JMS*. 48, 361-366 (2013).
30. Ellis, S.R., Cappell, J., Potočnik, N.O., Balluff, B., Hamaide, J., Van der Linden, A., Heeren, R.M.: More from less: high-throughput dual polarity lipid imaging of biological tissues. *The Analyst*. 141, 3832-3841 (2016).
31. Chaurand, P., Schwartz, S.A., Billheimer, D., Xu, B.J., Crecelius, A., Caprioli, R.M.: Integrating Histology and Imaging Mass Spectrometry. *Analytical chemistry*. 76, 1145-1155 (2004).





# 10 CHARACTERIZATION OF SINGLE ABRASIVE GRIT WITH FORCE AND VISUALIZATION TECHNIQUES

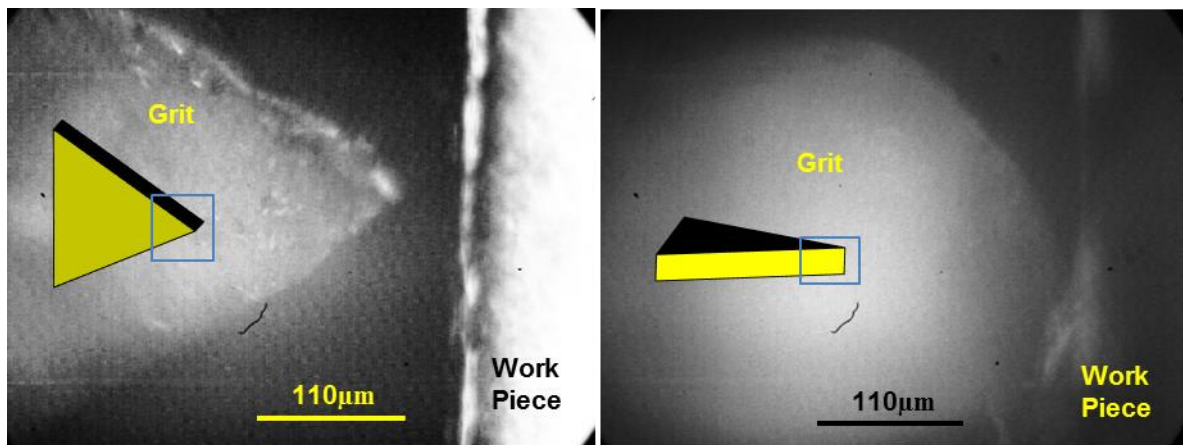
**David Gebb**

Graduate Student

**Thomas A Dow**, Professor

Mechanical and Aerospace Engineering

*The goal of this project was to study the tool wear, geometry and forces based on operating parameters in a grinding process experienced by a single abrasive grits. Individual abrasive grits on a coated abrasive are generally within a given size range but can have a range of cutting geometries. Grit geometries can also change as grits wear and fracture. Experiments were performed to determine an effective experimental procedure for testing and visualizing a single triangular shaped alumina grinding grit remove material. Two different geometries of the individual grits were tested in the two different orientations shown below.*



*Cutting forces were measured using a three axis load cell and simultaneous high speed video was recorded at 6006 frames per second. The experimental depth of cut varied from 5 – 60  $\mu\text{m}$  and the surface cutting speed from 1 – 8 meters per second. High Speed videos were used to measure chip shear angles by measuring chip speeds. Shear angle measurements were limited to a maximum of 1 m/s cutting speed by the video quality at high speed. Material build up at the cutting interface was sometimes observed when tool forces rose to the point of grit fracture. Abrasive grit geometry was measured through workpiece surface profiling techniques and optical microscopy. Machining experiments were completed on 304 stainless steel, 4330V steel, 1215 steel and 52100 steel.*

## **10.1 BACKGROUND**

### **10.1.1 Machining Processes**

Tool wear characterization is important to many industrial applications as it aids in the improvement and understanding of the quality and efficiency of the tool. Understanding the tool wear characterization allows better implementation of cutting and grinding conditions that improve the life of a tool which correlates to the cost of shaping a workpiece or the reliability of a product.

Grinding and machining operations have been researched and many publications date back to the 1940's and 1950's. Research was conducted before this but according to Merchant [1] this was an important era in the development in the current understanding of machining processes. In 1993 Merchant [1] stated "Thus there is now growing emphasis on research to increase the limits of the quality-determining capabilities of various machining processes." Even today there is still a demand to determine competencies for machining processes. Classical models developed during this time period are still used as a basis due to their simplicity. Contributions from Ernst, Merchant, and Piispanen [2] developed the idea that machining was a product of a concentrated shear plane resulting in a chip and ultimately leading to the orthogonal cutting model described by Merchant [3] in 1945. The models have progressed to represent cutting as a result of shear angle and even simulating cutting based on material properties. An extensive review of cutting models is given by Shaw [2]. However, each model has its limits. Shaw [2] attributes the limits of any model to the over-simplification of the intricate material removal process. Other models have been more recently employed by Drescher [4] and Arcona [5] in predicting forces in precision machining. There is not a model that works for all forces, tools, and cutting geometries.

### **10.1.2 Abrasive Grinding**

Grinding is a generic term that describes machining with abrasive particles. An abrasive particle is synonymous to abrasive grits or abrasive grains, and shortened further to just a grain or grit. Grinding processes can be further defined by the method that abrasives are held together. The two main categories of grinding abrasives are bonded and coated abrasives [6,7]. Bonded abrasives include products like grinding wheels and are composed of grits held together by a bonding matrix. Bonded abrasives make up the majority of abrasive products. Coated abrasives are made up of a row of abrasive grits that are attached to a substrate backing material with resin. The substrate material can be a cloth, paper, or polymer material and include products such as an abrasive disk, sandpaper, or abrasive belt.

The physics of grinding may be compared to machining but can also be vastly different due to the irregularity of the abrasive particles used to cut material and produce chips. While orthogonal cutting the tools generally have a well-defined cutting region that is then worn down by machining, grinding is made of up of many grits acting cooperatively in the cutting process. Individual grits have various shapes and sizes that may remove material with different cutting morphologies which has been found to be dependent on the tool and workpiece contact conditions [8-12]. The geometry variation between grits on a single abrasive product can create inconsistency in how material is removed and impact the quality of surface finish between a grinding product at identical machining conditions [13,14]. In grinding the majority of the grits either rub or do not contact the workpiece, while only a few grits are actively removing material [12,15]. Furthermore, Shaw [6] explains that grinding is influenced by the large cutting edge radius of the tool and often times, large negative rake angle, creating a small region of plastic deformation in the workpiece and chip. Komanduri [16] also compared grinding of a single grit to cutting with a large negative rake angle tool.

The variability within individual grits has brought up a consideration of how to study abrasive grits. Shaw [6] distinguishes two approaches to study grinding as deterministic or stochastic; testing individual grits [15] or testing the overall performance of a grinding belt/wheel. The deterministic approach will be taken within the context of this work even though single grit performance may be hard to compare at a wide range of grinding conditions with non-uniform geometry between grits. Experiments are conducted while considering that each grit/workpiece contact is different on an abrasive belt due to different grit width, depth, length and position [6,17,18].

### **10.1.3 Grinding Wear**

The mechanisms in which an individual grit contacts a workpiece can be much different than single point turning. Main mechanisms of individual grit/workpiece contact are rubbing, plowing, and cutting [18,19]. No material is removed through rubbing and plowing but still impacts forces and grit wear. Rubbing is due to frictional forces of the contacting grit and plowing displaces material without fully removing it from the workpiece. Cutting is what actually removes material from the workpiece, but still may be accompanied by rubbing and plowing. Cutting is also the most efficient method of material removal, or energy used per material volume removed.

Mechanisms of wear in grinding are typically attritious wear, fracturing, and grain pull out [6,17,18,20,21]. Grain pull out was not a mechanism of wear that was be studied because it occurs at the bonding agent of a grinding belt or wheel, not at an individual grit. Attritious wear is a flattening of the flank face or dulling of the grit cutting radius. Effects of attritious wear may lead to an increase in forces and fracture. Attritious wear can also have a large impact if the cutting tool and workpiece have a chemical affinity. In the case of alumina on steels, flank wear is low

since the two materials are fairly inert, [20]. Grain fracture can either be a small scale, retaining grit shape, or a large scale splitting the grit into multiple fragments. The individual microstructure has a large impact on which type of fracture is most common [18].

### 10.1.4 Grinding Performance

Wear is typically measured in a large scale perspective via a grinding ratio, or the volume of material removed from the workpiece,  $V_{Removed}$ , to volume of wear on the abrasive product,  $V_{Wear}$ . A grinding ratio represents the overall performance of a coated abrasive or grinding wheel where the quantitative values of material are significant enough for measurements and comparisons. The grinding ratio is given in Equation 1.

$$G = \frac{V_{Removed}}{V_{Wear}} \quad 1$$

The grinding ratio can also be measured by the change in weight of the workpiece and abrasive product. The weight of the wear is then related to the equivalent volume of the material. In some applications of grinding, the weight may be more convenient to measure than the volume. However, the grinding ratio was not applied to the single abrasive experiments in this thesis. The methods employed to measure removed workpiece material or wear of a single abrasive grit was not sufficient for practical volume measurements.

### 10.1.5 Coated Abrasive

As previously mentioned the two major subsets of grinding is bonded and coated abrasives. Bonded abrasives have been the most common form of grinding but coated abrasives have grown to be more common due to recent advances in the consistency of material removal of a coated abrasive product over its life. Bonded abrasives are generally used for general grinding, sharpening, and cutting applications while coated abrasives are used in surface-treatment applications from smoothing and finishing to stock material removal.

Coated abrasives are generally manufactured by orienting grits on the backing belt by an electrostatic charge [6]. The charge arranges the grits with the longest, most slender, dimension vertical while the rest of the geometry is oriented without certainty. This process provides good placement with many sharp grit edges facing outwards. A first coat of resin is used to hold the grits in place after the electrostatic field is removed and a second coat of resin is used to further secure them [20]. The outer layer of resin completely covers the coated abrasive. In a larger perspective, the positioning of the grits on the coated abrasive are loosely controlled so that spacing between grits is variable.

Recent advancement of coated abrasive products includes micro-replication techniques that replaced randomly oriented and geometrically shaped grains with a replicated geometrical structure. Such products promised to remove material more consistently and efficiently and improve a longer life and better surface finish. One of the first products was named Trizact by 3M and consisted of three-dimensional pyramids that were uniformly distributed across the product surface [14]. The pyramid structures were made of multiple layers of smaller abrasive material that wore down and cut with new abrasive material. Another design was introduced in 2009 that had shaped abrasive grains that also promised an improvement of material removal, belt life, and surface finish. The millimeter sized structures are flat triangular prisms shown in Figure 1 on the left, while conventional grinding grits that are irregular and blocky in shape are shown on the right of Figure 1. Shaped abrasive are proposed to act more like individual cutting tools that remove material instead of a blocky grain that “plows” through material [22]. The shaped abrasive grits are made out of an alumina material which is often used in high tensile materials such as steel alloys.

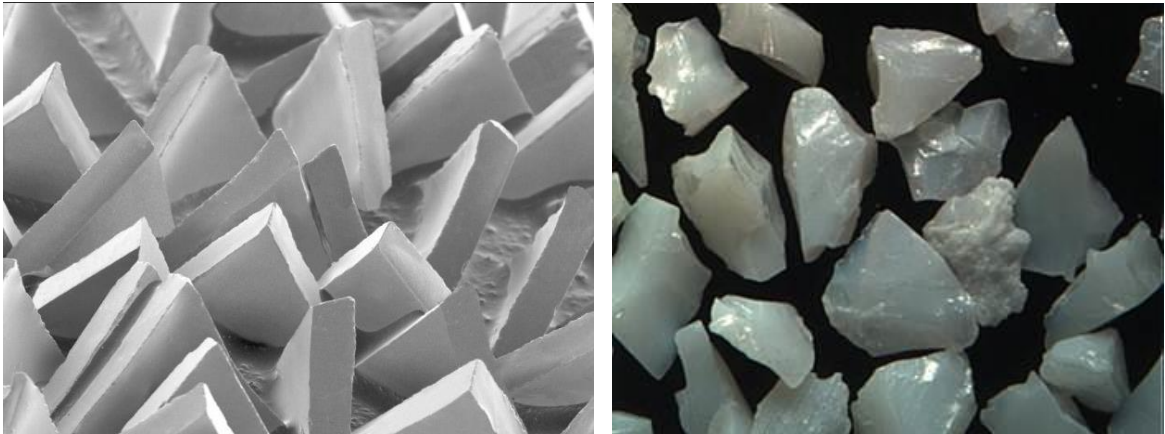


**Figure 1.** SEM image of shaped alumina grits [22] (left), crushed alumina grits (right).

## 10.2 ALUMINUM OXIDE GRIT MATERIAL

Aluminum oxide has the general material composition  $\text{Al}_2\text{O}_3$  and is also referred to as alumina, corundum and emery. Alumina is a generic term and may refer to a pure alumina substance or may have other material compositions added for various physical properties. Alumina is known for its physical properties of high hardness and strength. It can have non-uniform properties due to material impurities and tends to fail by fracture, but impurities and material microstructure can impact the fracture force or location.

A useful characteristic of certain  $\text{Al}_2\text{O}_3$  grits is that cutting can be more efficient than other ceramics because it fractures frequently. This allows a single grit to have a majority of its total life cutting with a sharp edge which is much more efficient. Alumina grits are often used for ferrous

metals like steel for this characteristic which reduces the effect of abrasive wear [6,18]. The alumina grits used in the experimentation described in this thesis were made of an unknown composition.

## 10.3 EXPERIMENTAL APPARATUS

### 10.3.1 Alumina Grit Geometry

Even though grinding consists of removing material with many cutting surfaces from a plethora of grits, an individual grit removes a small amount of material at localized geometry and depth of cut. The coated abrasive of interest in is shown in Figure 2. It consists of a large number of triangular  $\text{Al}_2\text{O}_3$  grits that are glued to a fiber belt. As shown in Figure 2, the result of grit mounting is mostly upright triangular abrasives that are randomly orientated with respect to direction of travel of the abrasive belt.



**Figure 2.** Alumina grits on coated abrasive. SEM image (left) [22], abrasive belt (right).

The approximate dimensions of the grits are given in Figure 3; however individual grits may have slightly different dimensions and geometrical fluctuations. The benefit of using the shaped abrasive grits is that each grit has similar surfaces on a large scale for repeatable mounting, visualization with the high speed video system, and testing in distinct orientation differences. The relatively flat faces of the grit were used as regions to focus the high speed optical system for insight on the cutting process.



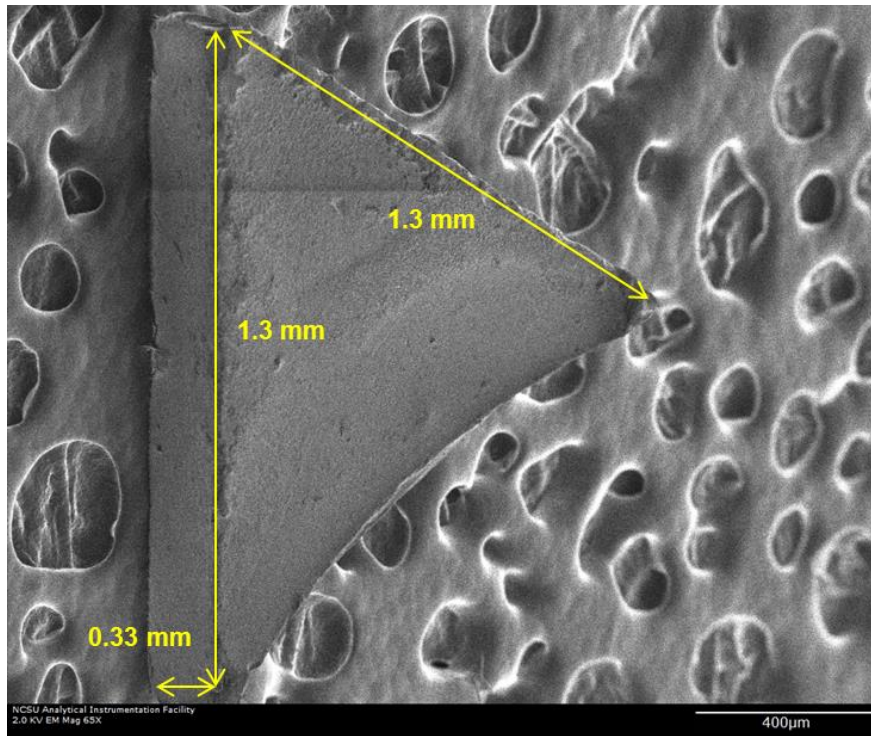


**Figure 3.** Nominal grit dimensions on a carbon tape background in a SEM.

However, even though the grit shape itself is generically similar, there are still individual differences between grits on the scale of the chip formation. Figure 3 shows the variability of a single grit on the micrometer scale.

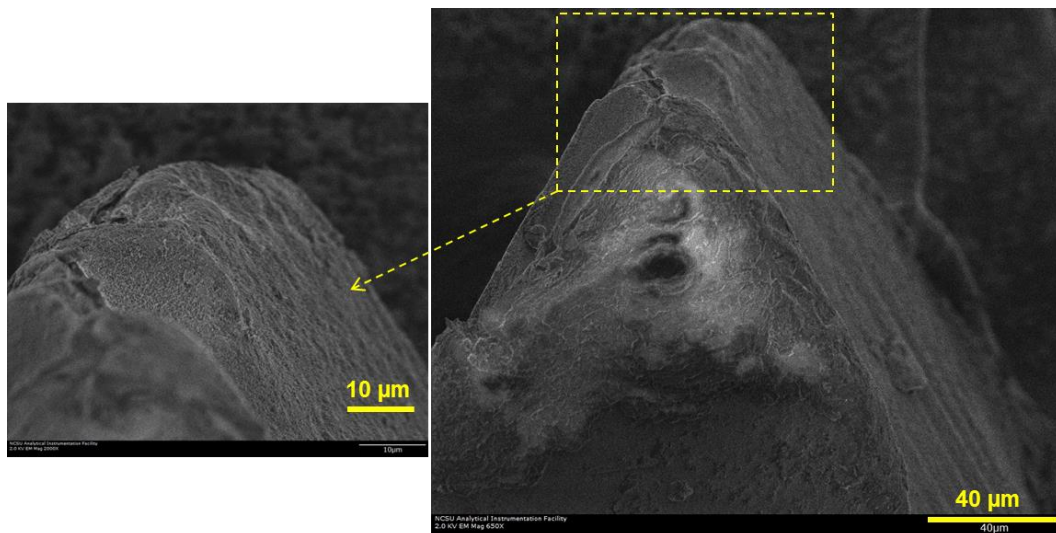


**Figure 4.** Grit geometry and variability at the scale of cutting.

A typical depth of cut may be in the range of 10  $\mu\text{m}$ . Looking at the figure there is variability at the nose with different ridges and high spots on the grit. A case study was done to measure the cutting radius of a specific grit to give the order of magnitude of the grit geometry. The measurement followed the procedure that Lane [23,24] and Shi [25,26] used for measuring diamond tools, called an EBID (Electron Beam Induced Deposition) measurement. The recorded edge radius was 20  $\mu\text{m}$ . This was only used as a general scale relation since individual grits would be different.

### 10.3.2 Precision Lathe

The single grit grinding process was studied using a high precision, two axis lathe shown in Figure 5. The lathe is a Taylor Hobson ASG 2500 diamond turning machine (DTM) with two orthogonal slides. The X-axis carries the tool and the Z-axis carries the spindle. The DTM axes are moved by specifying a coordinate position and movement feed rate. The machine is equipped with feedback control for accurate movement. The DTM axes are equipped with laser interferometer system that allows a movement resolution of 2.47 nm. The axes are driven by DC servo motors that are converted to a linear motion through 0.2 inch pitch lead screws. The workpiece was attached to the spindle that rotates around the z-axis on an air bearing at speeds ranging from 100 to 1600 RPM.

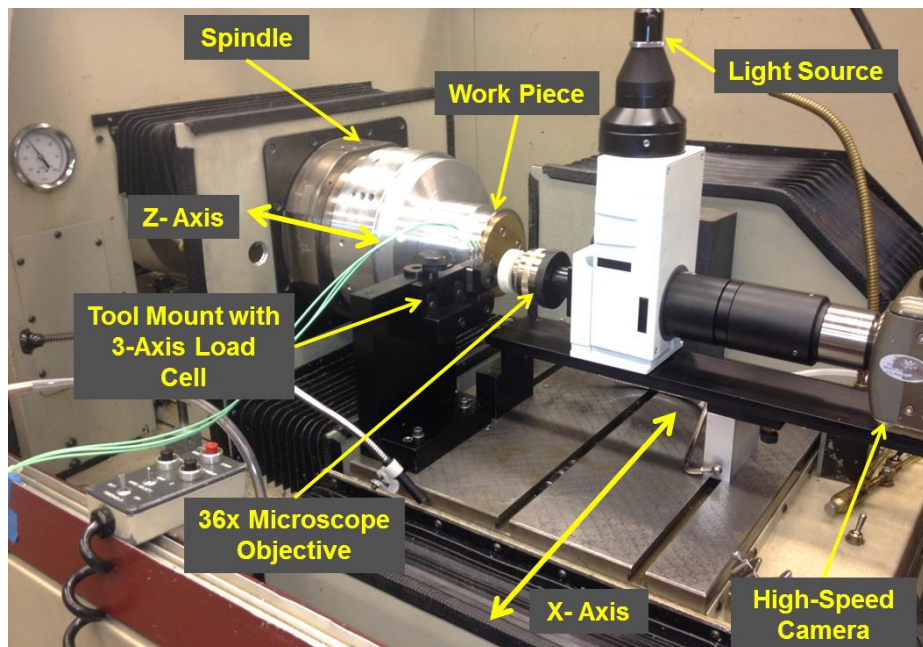


Figure 5. Experimental setup.

Workpieces were thin disks with diameters between 3.5 to 5 inches and thicknesses between 1/32" to 1/4". The workpiece was attached to the DTM spindle. Excess run out of the workpiece was removed before experiments by facing off the workpiece diameter with a carbide tool. A



segmented workpiece could replace the cylindrical workpiece for discontinuous cutting experiments.

A tool mount was bolted on the x-axis of the DTM and could be adjusted for various tool heights. Using the tool holder, the cutting edge of the tool was aligned with the center of the workpiece. The grit was held on a tool shank that could be removed from the tool mount for tool wear analysis. The tool mount also held the three-axis load cell used to record cutting forces. A high speed camera with a 36x microscope objective captured the cutting process simultaneously as forces were recorded. A high intensity light source illuminated the grit and chip field of view of the camera for the short exposure times needed for a high frame rate.

### 10.3.3 Load Cell and dSpace System

The load cell was a Kistler model 9251A three axis piezoelectric load cell; two axes are in shear and one in compression. The load cell measured cutting, thrust, and side forces that were tangential, normal and axial to the workpiece as shown in Figure 6.

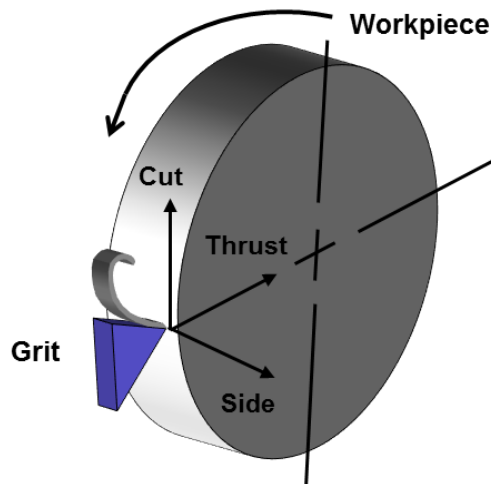


**Figure 6.** Grit and workpiece setup with cut, thrust and side force components.

The cutting and thrust forces were measured with the shear axes and the side force with the compressive axis. The sensitivity of the compression axis is 4 pC/N and the shear axes were 8 pC/N while the stiffness of the compression axis was 2600 N/ $\mu$ m and the shear axes were 1000 N/ $\mu$ m. The natural frequency of the two shear axes, corresponding to the cutting and thrust forces, was measured to be 11.6 kHz. The load cell and amplifier could measure forces up to 45-50 N.

The load cell was calibrated by fitting a linear regression to measurements of 200, 500, and 1000 gram weights. The resulting slope of the linear regression for each load cell axis is the calibration

factor. (See Section 5 of this Annual Report). A dSpace data acquisition system was set to record the data at a sample time of 5 kHz. The data collected was the cutting, thrust, and side forces, as well as spindle position, spindle velocity, and either the x or z DTM axis position. A choice between measuring the x or z axis position was due to a limitation of serial ports on the dSpace system. The dSpace system was also used to trigger the high speed camera for simultaneous visual data collection when the force measurements were triggered. The trigger was a voltage signal sent to the camera once the thrust force signal reached a magnitude of 0.12 V or about 0.5 N. The data that was recorded by the dSpace system was also recorded once the thrust force reached the aforementioned trigger magnitude.

### 10.3.4 High Speed Video System and Optics

The high speed camera in Figure 7 was aligned with the grit and workpiece to provide high speed imaging of the cutting process. The camera and grit were both positioned on the DTM x-axis so they moved together while the workpiece moved independently on the z axis. The camera was mounted on a stand that could be adjusted for fine focus of the camera. The focus was adjusted by a flexure mechanism shown in Figure 7. A screw on the flexure is advanced by 25  $\mu\text{m}/\text{rev}$  which causes a slight bending of the flexure, moving the entire camera a few micrometers towards the workpiece. A 36x Newport reflective microscope objective and a 1.2x camera attachment was used to magnify the cutting interface. The combined optical system had a magnification of 43.2x which corresponded to a 440  $\mu\text{m}$  by 330  $\mu\text{m}$  viewing window of the cutting process and depth of view of 30  $\mu\text{m}$ .

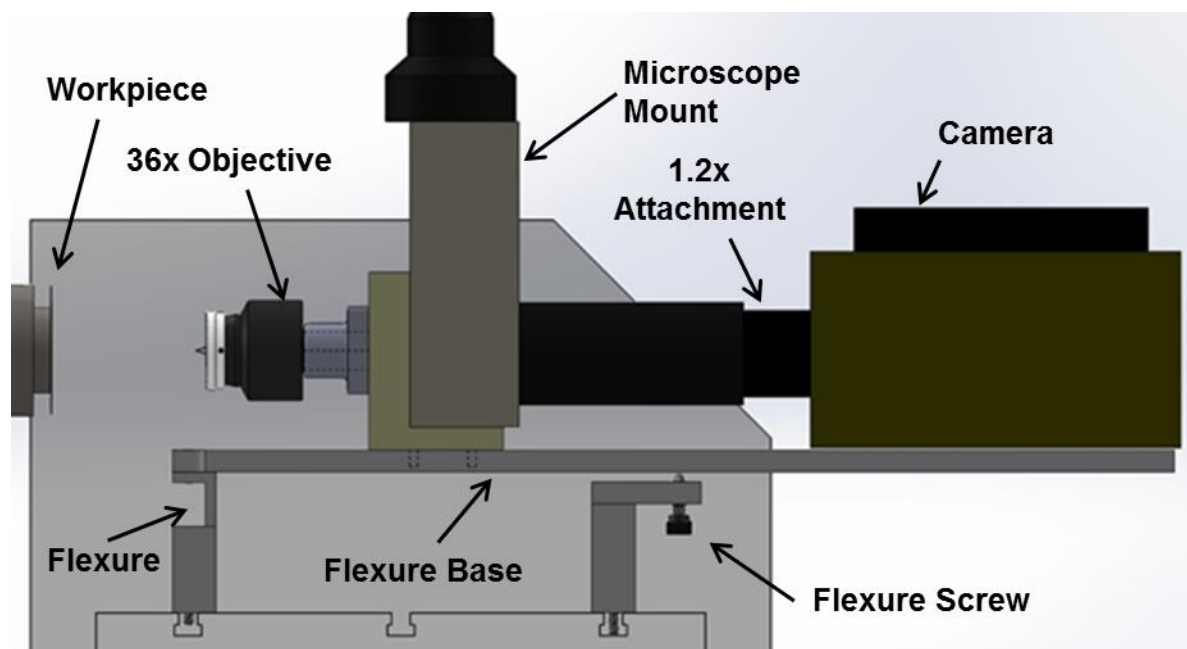


Figure 7. Camera setup and flexure focus mechanism.

The high speed camera is a Phantom Cam v7.3 with a detector array of 800 x 600 pixels that can run at speeds up to 6006 FPS (frames per second). The video camera contained 16 GB (gigabytes) of memory, which corresponds to about 3.4 seconds of continuous video footage at 6006 fps or 6.8 seconds at 3000 fps. The camera was capable of a circular recording buffer, meaning it could record video a set time before and after the trigger time. Information on how the high speed imaging system was used to capture cutting is given in Section 10.8.2. The shutter speed could be as short as 1  $\mu$ s. However, as the shutter speed was reduced, more light was required to produce the same image intensity on the detector. The shutter speed was typically set at 10  $\mu$ s to 20  $\mu$ s for experiments to provide acceptable images.

The shutter speed had a large impact on motion blur for moving objects in the field of view; a shorter speed could capture faster objects. Clarity of material visualization suffered at long exposure times and resulted in blurred still frame images. The exposure time was balanced to capture both objects in motion and stationary ones. A Prior Lumen 200 light source was directed to the field of view through the top of the microscope mount. The light is redirected in the microscope mount to follow the same optical path as the video camera. The light source was a 200 W white light halogen source.

## 10.4 PRELIMINARY IDEAS FOR GRIT MOUNTING AND WEAR

The first method of testing the grit was by cutting with a long edge of the triangular grit with a workpiece thinner than the grit (<1 mm). This is different than how the grit would be oriented on the coated abrasive in Figure 8. This method was designed so the resulting tool wear would leave an unworn fiducial region that could be compared to the worn region. Figure 8 describes the grit orientation and expected wear pattern. This concept has been used extensively for diamond tools [4,5,23,25]. However, grit wear was much different than the anticipated pattern described earlier.

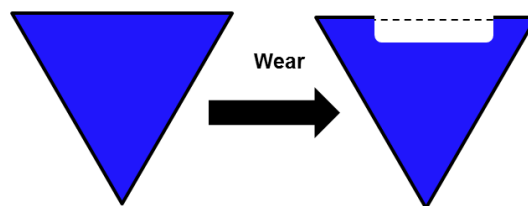


**Figure 8.** First mounting techniques and estimated wear pattern.

More significant difficulties in early experiments involved problems of grit mounting with epoxy alone. The epoxy was a 3M two part structural epoxy, called DP-460 off white. The DP 460 was cured at 60°C for two hours for maximum bond strength. Two methods of using epoxy to secure the grit are shown in Figure 9. Epoxy was placed around and under the grit on a flat mount and

also in a small notched hole that fit the tip of the grit. Both methods utilized epoxy as the main source of securing the grit.



**Figure 9.** Epoxy mounting on a flat surface (left) and in a notched hole (right).

When the epoxy did not fail, the grits were found to fracture in large sections that did not leave regions of the tool untouched by wear as anticipated in 8. An example of how much of the grit was removed during the fracture is given in Figure 10.

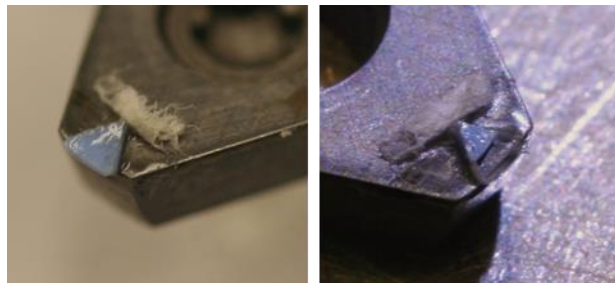


**Figure 10.** Grit before fracture (left), grit after fracture (right).

In both methods to secure the grit from Figure 11, once cutting and thrust forces were above 20 N either the epoxy was likely to fail or fracture occurred. The forces reached that magnitude because the grit was in contact with the workpiece across about a 0.8 mm width, which created a large chip area. The epoxy failed in tension while the shear stress direction of the epoxy could resist larger forces.

The tensile stress was a direction that applied a moment and lifted the grit from the surface of the holders and the shear stress was in a direction that moved the grit around the mounting surface. For adhesives in general, tensile stress may also be referred to as peel or cleavage stress for oblique forces with respect to the adhesive layer. Most epoxies have a high shear strength and low tensile strength. The cutting forces employed on the grit were not pure tension or shear but a combination. It was determined that epoxy alone did not have the necessary strength to hold the grit and a different design with mechanical support was needed to constrain the grit.

## 10.5 GRIT GEOMETRY FOR FORCE AND WEAR EXPERIMENTS

### 10.5.1 Grit Geometry

As mentioned in the grinding background, the shaped grits are mounted on coated abrasive product with the tip of a triangular surface upright, but the precise placement and orientation is uncontrolled. To represent the alignment for possible mounting, the grit was tested at two extreme grit orientations and one intermediate orientation. The testing orientation also provided an experimental basis for an optimal grit placement. The two extreme grit orientations, shown in Figure 11, could create either a zero rake angle or a negative rake angle with respect to the workpiece. Although grit irregularities may not provide a perfect  $0^\circ$  or  $-30^\circ$  rake angle, the general rake angle was referenced to distinguish the orientation.

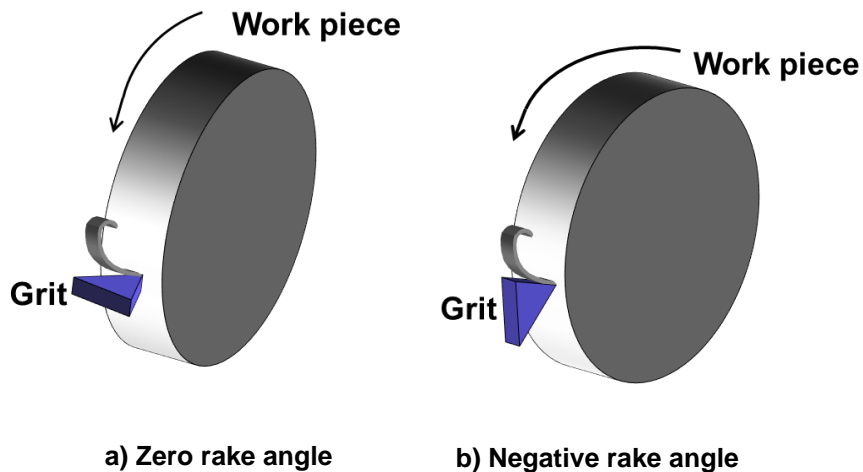


Figure 11. Extreme grit orientations

### 10.5.2 Tool Holder Design

Developing a method to support an individual grit (only 1.3 mm along each side) was an important part of the project. A repeatable mounting technique was needed for grit placement for grits that varied in size. For simplicity the grit holder was equipped with two perpendicular faces to ensure the grit was laid flat and flush against the faces as shown in Figure 12. The perpendicular faces ensured grit orientation with respect to the large triangular face and edge of the grit.

Originally only a clamping system was used when developing the holder design. However, a firm clamp was found to induce extra stress on the grit that could result in fracture after attachment. Also a clamp alone also would not provide sufficient torsional support for a grit with an irregular surface. The final tool holder used both epoxy and a clamp to hold the grit in place shown in

Figure 12. The clamp held the grit in compression, resisting possible tensile forces where the epoxy was weak. The epoxy was used to resist twisting and slip in the clamp and would act as shear stress on the epoxy.

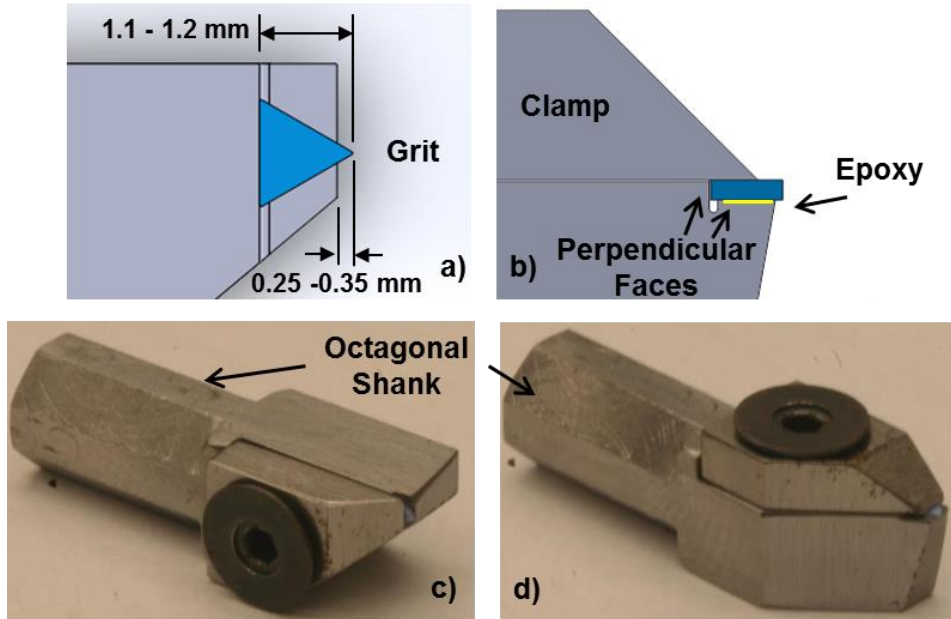


**Figure 12.** Tool Holder: a) Top view and, b) Side view of grit placement with respect to the perpendicular holder surfaces and epoxy placement. c) Grit holder in the negative rake orientation and, d) the zero rake orientation.

The resulting mount left an exposed tip of the grit that hung over the edge of the holder for use in cutting experimentation. The grit extended past the tool holder 0.25 mm to 0.35 mm based on grit size and manual placement as shown in Figure 12. The grit was considered unusable when it didn't overhang the edge of the mount. The holder shank also had an octagonal shape to orient the grit at the different grit orientations on a coated abrasive. The extreme orientations could be achieved as well as a position in between the extremes at 45°. The grit orientations changed the tool rake angle as will be discussed in the following sections.

### 10.5.3 Negative Rake Angle Orientation

The negative rake angle orientation had a nominal rake angle of -30° and was oriented with respect to the workpiece shown in Figure 13. It is important to note that the rake angle could be larger than -30° due to localized geometry such as an extremely blunt grit. The center of the grit was vertically aligned with the center of the spindle and workpiece.

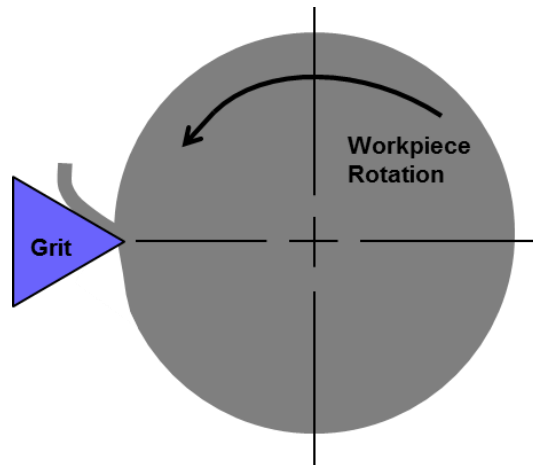


**Figure 13.** Negative rake angle orientation.

The negative rake angle geometry was nominally a 300  $\mu\text{m}$  wide tool which could vary depending on the specific grit shape. Figure 14a shows a relatively flat grit which would cut along most of the width, depending on the depth of cut. Conversely Figure 14b shows irregular geometry with a high spot which results in a narrow contact area that changes as the depth of cut increases. Large irregularities in the grit width for this orientation made the contact area variable for different grit experiments.

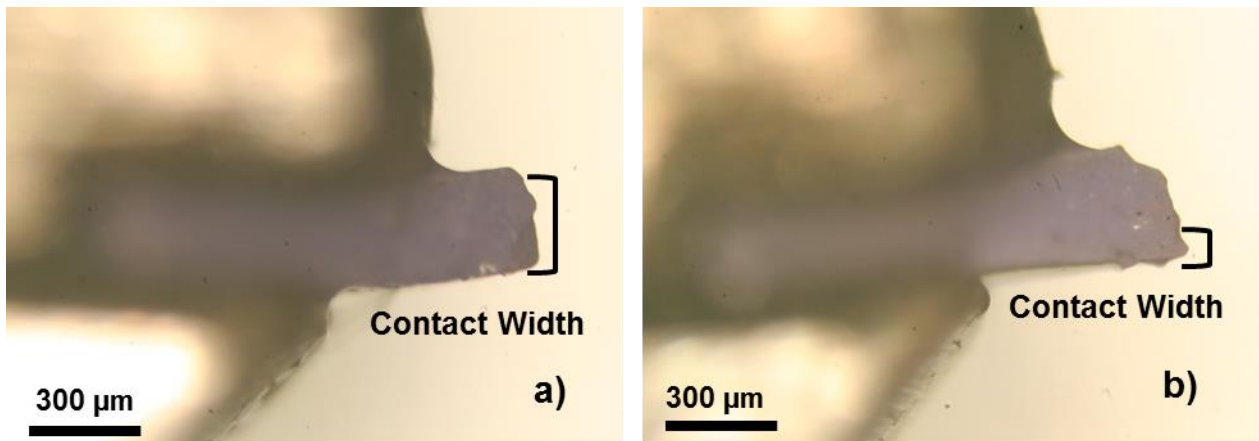


**Figure 14.** Microscope image of grit contact width for negative rake orientation.

### 10.5.4 Zero Rake Angle Orientation

The zero rake orientation had the triangular surface of the grit as the rake face. The overall rake angle, excluding any localized geometry differences, created a zero degree rake angle, shown in Figure 15. As with the negative rake orientation, a large cutting edge radius would change the localized rake angle. Another factor that could influence the localized rake angle is if the grit had any characteristics resembling a chamfered or curved edge. However, care was taken in



experiments to select grits without such characteristics. The grit cutting edge was aligned to the vertical center of the spindle.

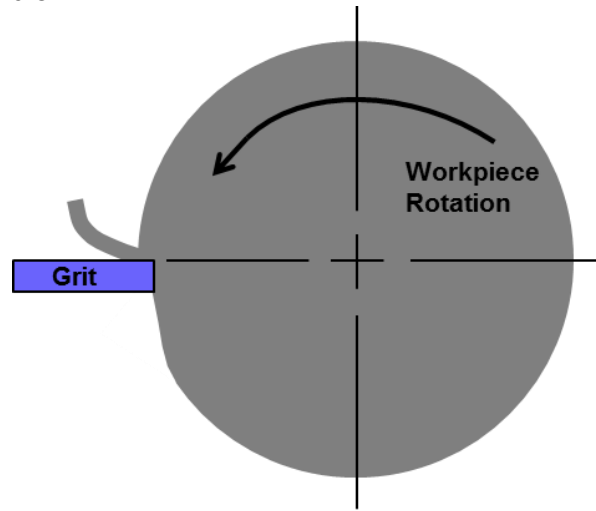


**Figure 15.** Zero rake angle orientation.

The tool width in contact with the workpiece had variability between grits, but it was much more repeatable than the negative rake orientation. The average grit had a triangular tip with about a 60° angle before any wear occurred. The variability of the rake face geometry of two different grits is illustrated in Figure 16.

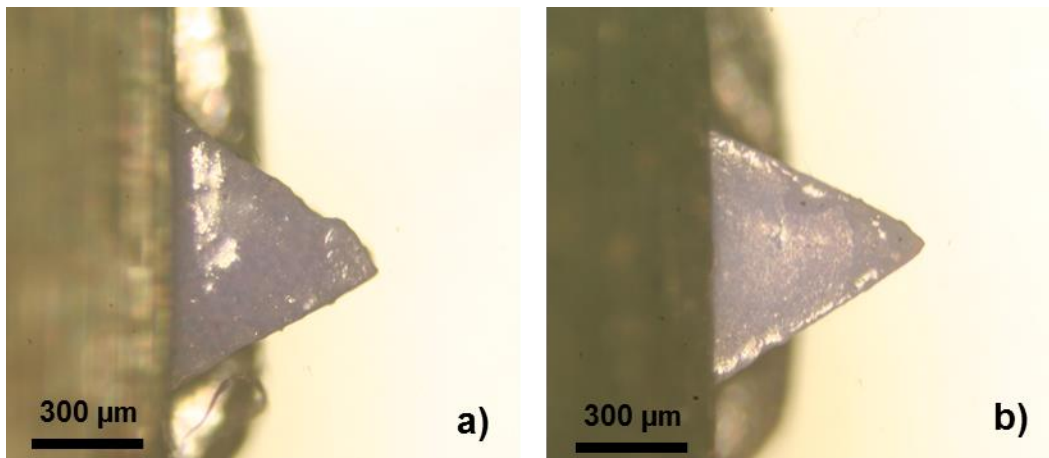


**Figure 16.** Microscope image of two grit rake faces for the zero rake orientation.

The contact width of the zero rake grits was dependent on the depth of cut. As the depth of cut increased so did the contact width as the triangular edges were moved further into the workpiece. The grits shown in Figure 16 were the same grits from Figure 14 but in the perspective of the triangular face which is the rake face for the zero rake orientation. The zero rake orientation could be slightly rotated to assist in high speed imaging of the grit.



## 10.5.5 Halfway Rake Angle

The halfway rake angle is oriented with the tool holder halfway between the zero and negative rake orientation. The cutting geometry is different from the two previous orientations and the rake faces are now oblique with respect to the cutting direction.

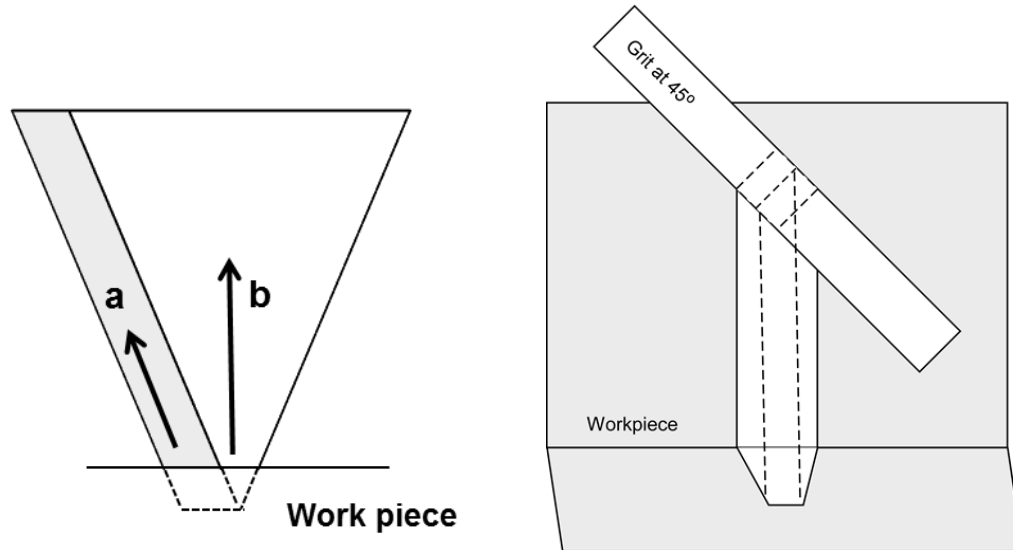


**Figure 17.** Halfway rake orientation oblique faces: orthogonal to cutting direction (left), top perspective (right).

To illustrate the two effective oblique rake angles, Figure 17 shows two perspectives of the grit. The arrows represent the material flow along the faces of the grit. The arrow labeled “a” shows the material flow on the rectangular face while the arrow labeled “b” shows the material flow along triangular face. The arrow labeled “a” is on the negative rake angle orientation rake face and “b” is on the zero angle rake angle orientation rake face. The left section shows the rake faces from the perspective of the cutting direction while the right gives a top down perspective. The characteristics of the halfway rake are a combination of the zero and negative rake orientations.

## 10.6 GRIT CUTTING ASSESMENT WITH FORCES AND IMAGING

### 10.6.1 Background and Forces

Cutting forces can communicate important information about the cutting process. In diamond turning applications where very sharp cutting edges are used, the cutting and thrust forces can be monitored to determine when the workpiece surface finished degrades. The cutting and thrust forces can be related to a model for certain parameters to determine tool edge geometry, as described by Drescher [4] and Arcona [5,28]. This is important with precision machining when the

surface finish of a part is a critical parameter. However, after initial experiments it was found that the cutting forces for the alumina grit could not be used to characterize wear with diverse grit geometry.

Up to this point, it has been assumed that the grit would cut and wear similarly to orthogonal machining conditions and tools. It was expected that the resulting cutting would produce a steady state force with small variation between experiments due to grit geometry. However results showed that unlike orthogonal machining, there was not a precise steady state force or wear rate.

### 10.6.2 Feed Direction

The two main cutting methods that were used for cutting experiments were a plunge and a traverse cut. Figure 18 illustrates the two methods. In the plunge cut, the tool was fed in the radial direction of the workpiece while the workpiece rotated, but not moving in any other direction. The experiment was characterized by a constant depth of cut and a tool width that increased as the tool plunged further into the workpiece. The increase in tool width was due to non-uniform geometries and high spots. The traverse feed described when the tool was fed along the outer surface of the workpiece or traversed along the workpiece axis. The experiment was characterized by a controlled width and depth of cut. The width of the cut was determined by the traverse feed and only used a small region of the grit to actively removed material. Each technique was used for different objectives and is described in each respective section of experiments. As the experimental procedure progressed, the two cutting methods were eventually combined.

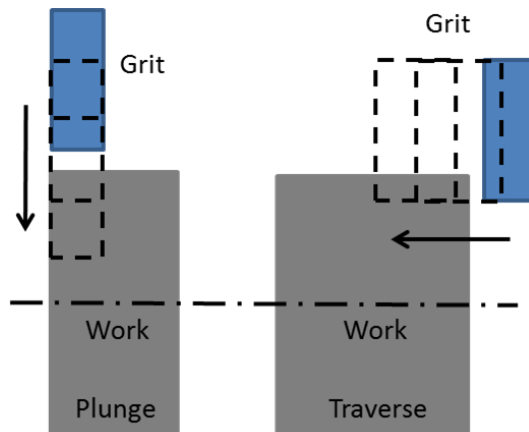


Figure 18. Feed directions.

### 10.6.3 General Experimental Procedure

The workpieces were prepared prior to experiments by machining with a carbide tool for a consistent surface finish. The feed rate was related a theoretical surface roughness of  $0.1 \mu\text{m PV}$

(peak to valley). However, it was discovered that the carbide tool and feed rate produced a PV of 1-3  $\mu\text{m}$  for steel workpieces. The geometry of a new carbide tool had a 400 $\mu\text{m}$  nose radius. The cutting speed for each experiment was determined by the spindle speed and workpiece diameter. The workpiece diameter was measured for each experiment and the spindle speed set to the surface speeds described in the experimental results.

## 10.7 TRAVERSE EXPERIMENTS AND CHARACTERISTICS

The first set of experiments used a traverse feed to move the tool across the workpiece. The traverse feed determined how quickly the grit passed over the surface in the axial direction. For this method the grit had no radial feed but was positioned at a set depth of cut, unless the tool wore. The workpiece moved along its cylindrical axis and rotated as shown in Figure 19. The depth of cut was changed for separate experiments to systematically test the grits. The traverse feed determined the contact width of the grit. If the traverse feed was low enough to produce overlapping cuts, the contact width of the grit that removed material was determined by the feed distance per revolution of the workpiece. If the remaining geometry of the grit that was larger than the feed, it could potentially contact the surface that was just cut. However, if the grit was an irregular shape, the contact area could be at any point along the grit. Overlapping tool paths were used before groove geometry was measured. In most cases, the traverse feed experiment provided a more consistent and controlled workpiece removal rate in than the plunge experiment.

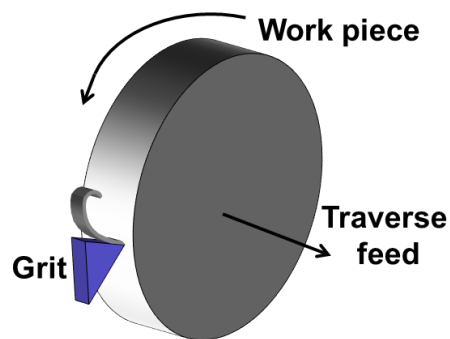


Figure 19. Traverse feed experimental representation.

### 10.7.1 Traverse Cut Grit Experiments

The original traverse cut experiment was conducted with a single grit that was used for consecutive experiments. The grit was replaced once the worn or fractured did not extend past the tool holder or was less than 50-100  $\mu\text{m}$  of overhang. A depth of cut was set before the experiment began, but the depth of cut could vary if the grit wore, broke or accumulated material pick up at the interface. Grit fracture events and material pickup did occur. After each experiment

was performed, the workpiece was faced off with a carbide tool to create a flat surface. Pictures of the grit profile were taken after major fracture events to correlate wear and forces but also to determine common fracture characteristics.

The experiments described next were performed with a surface speed of 1 m/s and a traverse cutting feed of 2.38 mm/min. This traverse feed resulted in overlapping tool paths by 12  $\mu\text{m}/\text{rev}$ . This only used about 4 % of the 330  $\mu\text{m}$  nominal grit width to remove material for the negative rake orientation. For certain grit geometries, the region of the grit width that was not removing material could rub the workpiece and influence forces. This included grits with flat edges or a large radius edge. Each traverse experiment could potentially reach cutting distance up to 20 m but could be shortened by fracture or wear.

### **10.7.2 Traverse Cut Case Study at the Zero Rake Orientation**

The zero rake orientation was used in a traverse experiment on 304 SS material. Experiments were performed with a surface speed of 1 m/s and a traverse cutting feed of 2.38 mm/min. A traverse feed of that magnitude resulted in overlapping tool paths that corresponded to about 12  $\mu\text{m}/\text{rev}$ . There were several cases in which a grit sustained no distinguishable fractures, even after several experimental cutting lengths of 20 m.

Each individual cutting test produced mostly constant forces, averaging at 1.9 N and 1.8 N for cutting and thrust. All experiments were conducted on a single grit at a set 5  $\mu\text{m}$  depth of cut. The averages of all experimental forces and standard deviations are given in Figure 20. The data in Figure 20 demonstrates the average cutting and thrust forces over the course of eighteen consecutive cuts before the grit fractured beyond use and the first experiment started with an unused grit. Fractures that stopped individual cutting tests early occurred at experiments represented by data points at 180m, 211m and 330m. The same grit was used after the fractures occurred. The experiments had similar cutting and thrust forces. The standard deviation, especially for the thrust force, increased drastically at 232m shortly after a fracture occurred.

Data points from Figure 20 represent an average force during a single experiment or several data points representing distinct forces in an experiment. For instance, experiments that had distinguishable periods of constant force differences, similar to Figure 20, were separated into two force averages. Values at 205 m and 211 m are representative of the individual experiment in Figure 20 where the average forces from 0 - 6 m and 6 - 13 m in Figure 20 were averaged. Material pickup at the cutting interface was hypothesized to be the cause of the rise in forces at 6 m and 13 m in Figure 21. The experiment eventually ended in a grit fracture at a 10 N cutting force and 8 N thrust force.

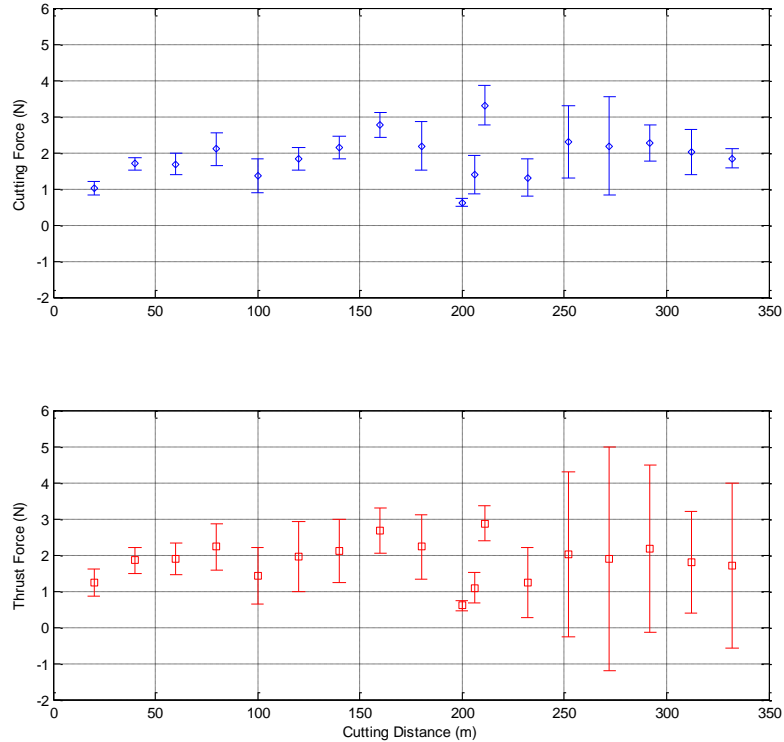


**Figure 20.** Zero rake: consecutive traverse tests at  $5\mu\text{m}$  depth, 1 m/s speed, and  $12\mu\text{m}$  feed using a single grit on 304 SS.

For Figure 21, the forces were averaged for data from 0 to 6 m and 6 to 13 m. Although the forces and standard deviation changed in the experiments, there was nothing to relate the results to, other than assuming the geometry must have arbitrarily changed at fracture. The lack of understanding of cutting geometry involved with the experiments in Figure 20 motivated improved experiments described later.

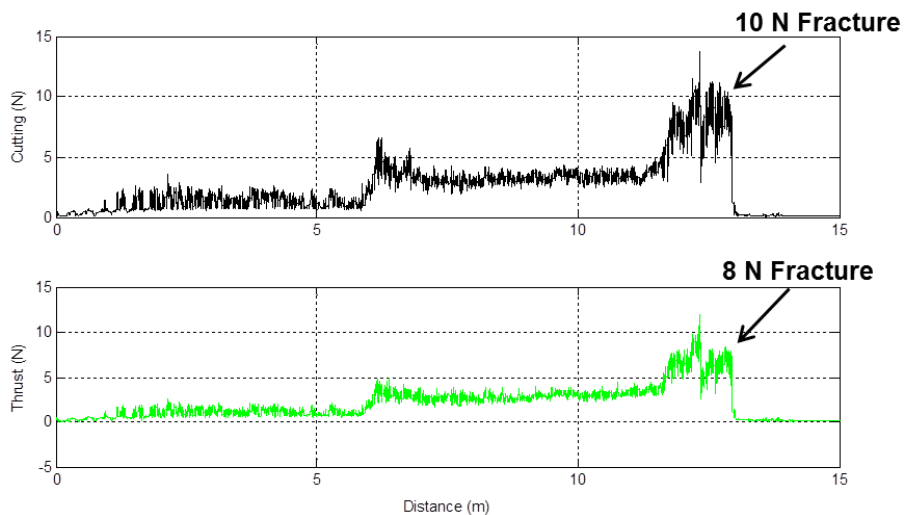


**Figure 21.** Traverse experiment at  $5\mu\text{m}$  depth and 1 m/s for a zero rake grit on 304 SS.

### 10.7.3 Traverse Cut Case Study at the Negative Rake Orientation

The negative rake angle orientation, described in Section 10.5.3, was tested with the same traverse feed parameters described in Section 10.7.1. Experiments were performed with a surface speed of 1 m/s and a traverse cutting feed of 2.38 mm/min. A traverse feed of that magnitude resulted in overlapping tool paths that corresponded to about 12  $\mu\text{m}/\text{rev}$ . The experiments consisted of a series of experiments at both 5  $\mu\text{m}$  and 10  $\mu\text{m}$  depths of cut. The negative rake angle orientation proved to expedite fracture events and had significantly shorter periods of continuous cutting compared to the zero rake orientation. A combination of new grits and grits that had recently fractured were used in the experiments. Experiments for the negative rake orientation had highly variable forces as shown in Figure 22.

The irregularity of forces during experiments on the negative rake grit has been partly attributed to material pickup. The data for each trial ended when the grit stopped contacting the workpiece due to a fracture. The overall average force and standard deviation of each test run is given in Figures 23 and 24 for two grits, one at 5  $\mu\text{m}$  and one at 10  $\mu\text{m}$  depth of cut. The average force was calculated by averaging all the force data of a single experiment pass, effectively taking an average force for all of Figure 22. There were no cases of distinct force differences in an individual experiment like was shown in Figure 21.

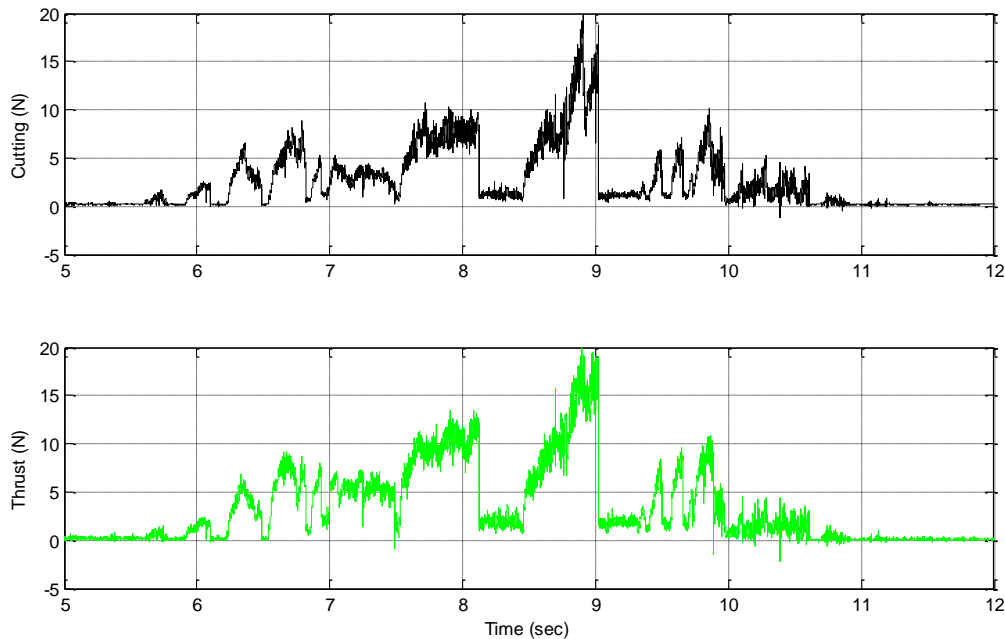


**Figure 22.** Sample negative rake angle traverse experiment at a 12  $\mu\text{m}$  feed and 1 m/s speed on 304 SS.

The standard deviation was often larger than the average force due to the large force fluctuations demonstrated in Figure 22. The standard deviation data given in Figure 24 shows the 5  $\mu\text{m}$  depth experiments, which are the seven experiments shown to the right of the 5  $\mu\text{m}$  mark, and the 10  $\mu\text{m}$  experiments, shown by the five experiments to the right of the 10  $\mu\text{m}$  mark. Consecutive experiments were plotted for each grit (at 5  $\mu\text{m}$  or 10  $\mu\text{m}$  depth of cut). As the grit wore and fractured, the variation of experimental forces increased. The variation was attributed to the effect of fracture and material pickup in combination with the grit geometry changing. Even though the two grits were tested with separate depths of cut, 5 $\mu\text{m}$  and 10 $\mu\text{m}$ , there was no direct correlation between forces and depth of cut. Out of the twelve experiments between the two depths of cut there may have been an average force, but it was indistinguishable with the amount of variation and sample size tested.

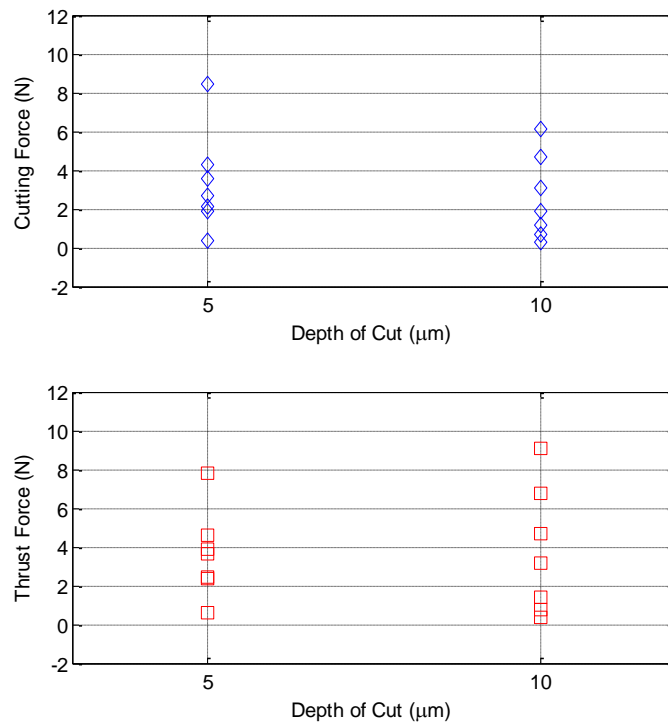


**Figure 23.** Average cutting and thrust forces for negative rake angle traverse experiments at a 12  $\mu\text{m}$  feed and 1 m/s speed on 304SS.

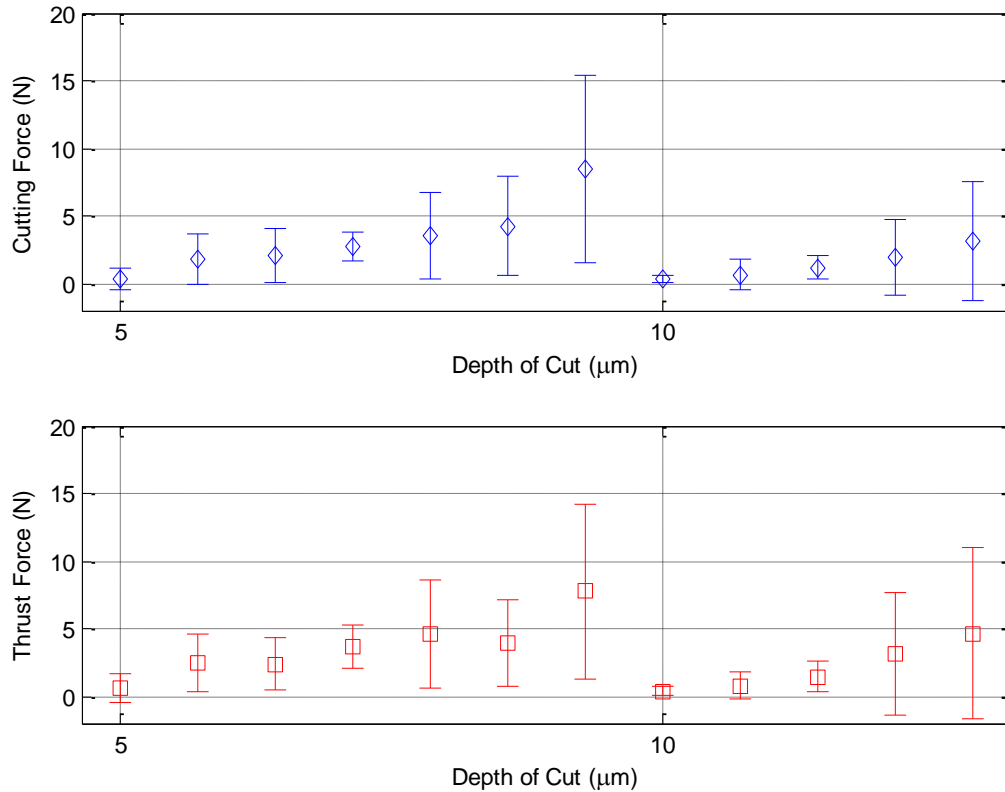


**Figure 24.** Standard deviation for cutting and thrust forces at 5μm and 10 μm depths for negative rake angle traverse at 12 μm feed and 1 m/s speed on 304SS.

For each test run, the maximum force in Figure 25 was much larger than the average force in Figure 26 shows the maximum force from each experiment in the negative rake Traverse Experiments. The maximum force did not follow any type of trend but often resulted in a grit fracture. Figure 25 shows the cutting and thrust forces for thirteen experiments that lead to fracture. The experiments were for 5 μm and 10 μm depth of cut but fracture forces were not related to this parameter. The variation in the maximum forces could have been due to variable strength grits in conjunction with material pick up.



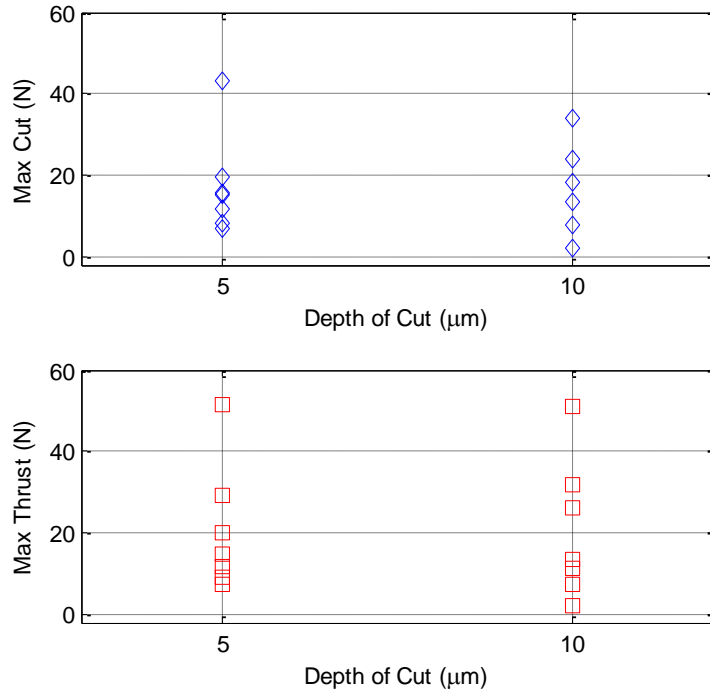


**Figure 25.** Maximum forces for the negative rake traverse experiments at a 12 μm feed and 1 m/s speed on 304SS.

To compare experimental force data with consistency further hypothesis were made regarding the effect of material pickup on forces. In several instances the raw force data showed points in time which the forces appeared to drop to a steady state value. It was hypothesized that the apparent steady state forces were a base force in which there was no material pickup on the tool. If the hypothesis was correct then material pickup on the tool would go through dynamic states of accumulation on the tool followed by a rapid knocking loose of the material. The rapid change to the base force is highlighted in Figure 26, originally shown as Figure 22. The base force was a short steady state region in the force data that lasted nearly a second in some cases. The base forces were distinguished by the repetitive and seemingly steady force signature.

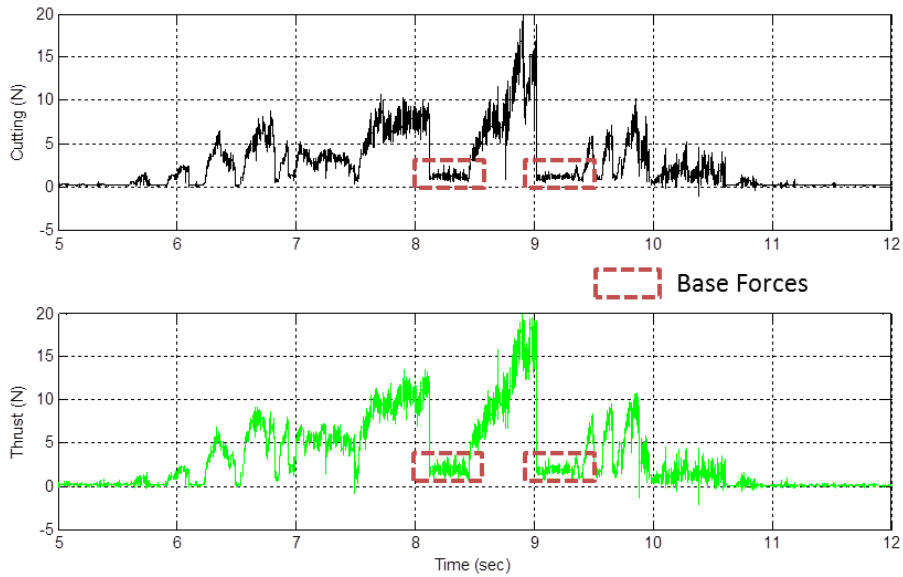


**Figure 26.** 5  $\mu\text{m}$  depth, negative rake angle: experimental data and base forces.

The base force data for the negative rake angle experimental data was extracted from several experiments and plotted in Figure 27. The base forces were present for three of the seven experiments from the 5  $\mu\text{m}$  depth of cut data and four of the five experiments for the 10  $\mu\text{m}$  depth.

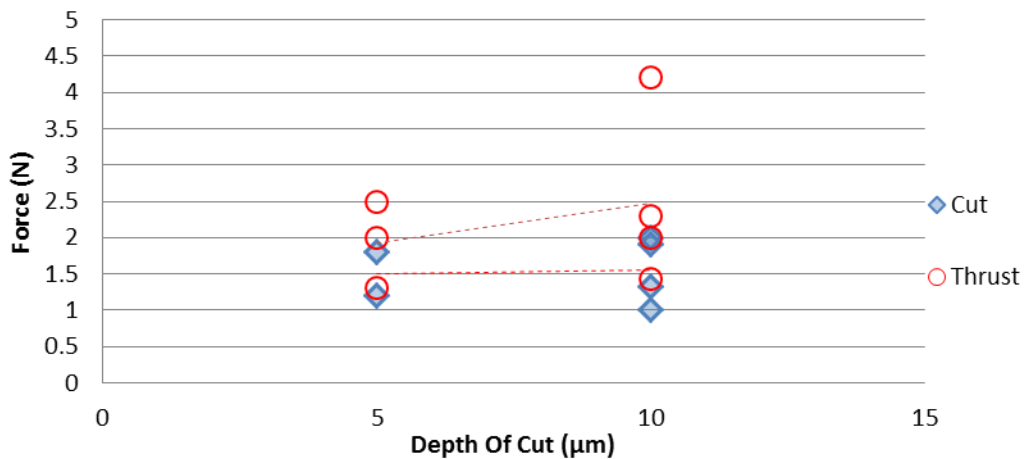


**Figure 27.** Negative rake traverse experiment base forces at 12  $\mu\text{m}$  feed and 1 m/s speed on 304 SS.

Experiment forces were not completely steady state but were characterized by variable forces particularly from fracture or material pickup.

## 10.7.4 Traverse Cut Summary

The traverse experiments with two grit orientations could be directly compared since a single traverse feed rate was used. The negative rake angle base forces were compared to the zero rake experiments at a 5  $\mu\text{m}$  depth of cut. The forces for both experimental cases were within the same general range but the notable difference was that the negative rake orientation had a lower cutting to thrust force ratio. When comparing only the average force of each experimental orientation (not considering base forces for the negative rake) the negative rake angle average forces were much higher at a 4.8 N and 5 N cut and thrust compared to the zero rake at 1.9 N and 1.8 N cut and thrust. However the grit orientations were influenced by different tool geometry. Recall that the cutting geometry for the zero rake orientation had a nominal 20  $\mu\text{m}$  nose radius while the negative rake orientation had a nominal width of 300  $\mu\text{m}$ .

The overall result of the traverse cutting experiments in both the zero and negative rake orientations was that the experimental data could not be easily related between similar experiments. In fact the actual grit geometry that participated in cutting was unknown. The experimental results revealed the need to define the cutting geometry for each orientation. Defining geometry will improve the basis for which forces can be compared. Later experimental procedures that clarified cutting forces by measuring the grit groove geometry were developed.

A further outcome of initial experimentation was general grit characteristics were observed and provided initial steps for further testing. A qualitative difference between the orientations was that the negative rake orientation had frequent force spikes which many times resulted in fracture while the zero rake orientation was much more consistent. Another characteristic taken for further experimentation was to use much larger traverse feed rates or non-overlapping traverses. The larger feed rates had a twofold purpose. The first was so tool grooves could be identified but also to increase the overall removed material. The Traverse experiments had a theoretical removed chip area of less than 150  $\mu\text{m}^2$  in all conditions and having a larger removed chip area would provide more distinguishable forces between experiments of different parameters.

## 10.8 PLUNGE EXPERIMENTS AND CHARACTERISTICS

For the plunge cut shown in Figure 28, the grit moved radially into the workpiece at a set feed rate and workpiece speed. This produced a nominal depth of cut as long as no wear or fracture occurred. The plunge experiment differs from the traverse experiment in that it has no traverse feed so the entire width of the grit contacts the workpiece material.

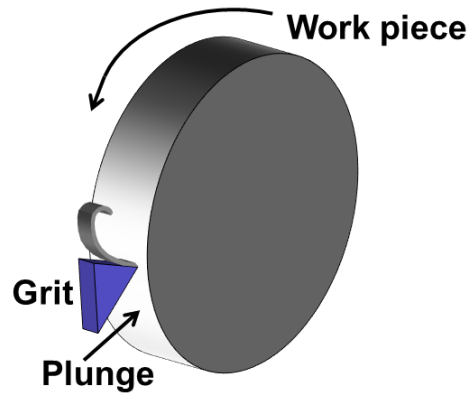


**Figure 28.** Plunge cut experiment representation.

The grit depth of cut was set by advancing the grit a specific distance into the workpiece for each revolution. After the first workpiece revolution the depth of cut was constant as the grit advanced further into the workpiece. In most cases the entire contact width of the grit was used to cut the workpiece in the plunge experiments. However, if the end of the grit was not flat, the contact area would grow over several workpiece revolutions. The grit contact area for the end of a non-uniform grit is shown in Figure 29 as the grit advanced further in the radial direction of the workpiece.

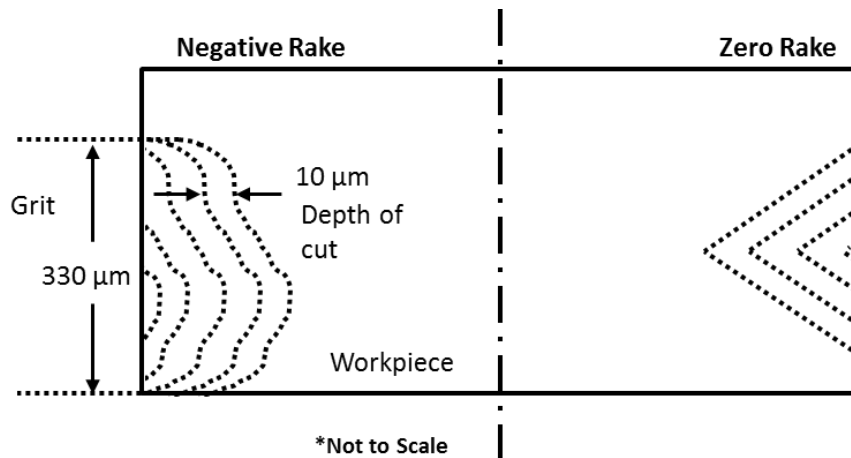


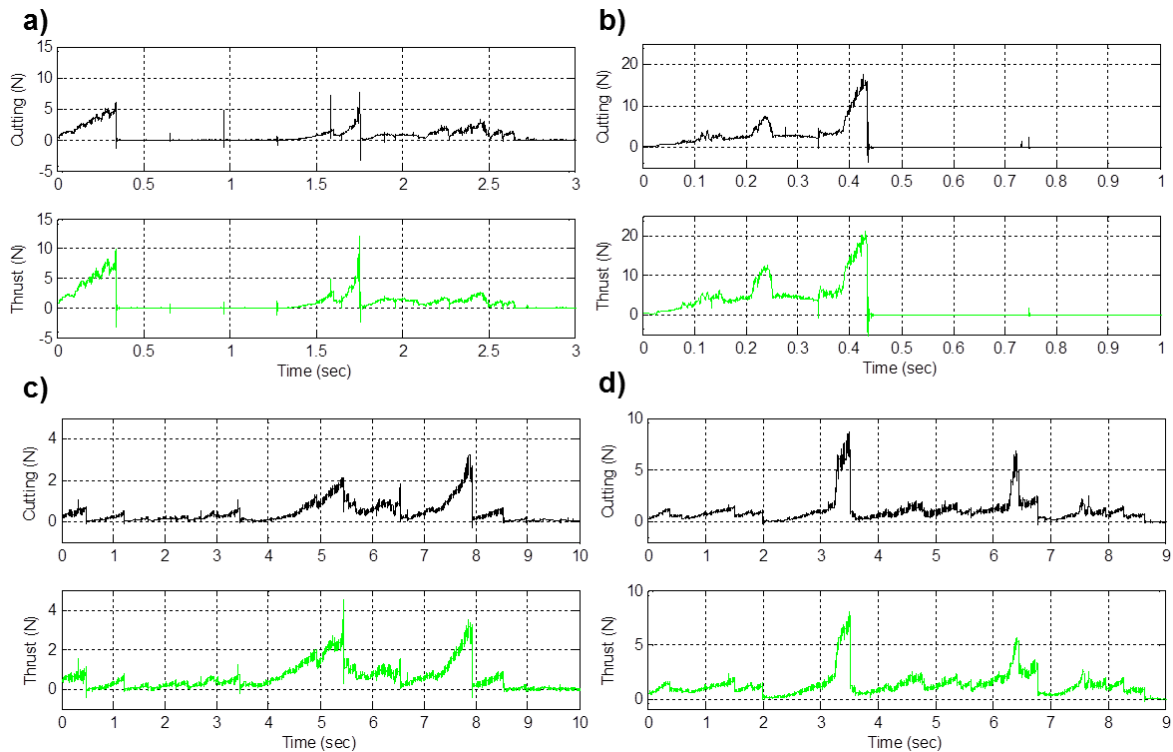
**Figure 29.** Grit contact area for plunge experiment in the extreme orientations.

After the entire width of the grit contacted the workpiece, the forces should be able to reach a point in equilibrium for the negative rake orientation. However, the zero rake orientation forces would not reach a steady state. As the grit would feed into the workpiece a larger area of the triangular face would contact the workpiece and cause higher forces. The zero rake orientation was not used for plunge experiments for this reason.

An important benefit of the plunge cut was that a small fracture did not result in the end of the experiment since the grit continued to feed into the workpiece. A fracture would stop cutting for a short period of time until the grit fed into the workpiece the distance of the fracture and contacted the workpiece material again. However, a large fracture would stop cutting if the fracture reduced the grit size smaller than the overall plunge distance or total depth of the experiment.

### 10.8.1 Plunge Cut Grit Experiments for Negative Rake Orientation

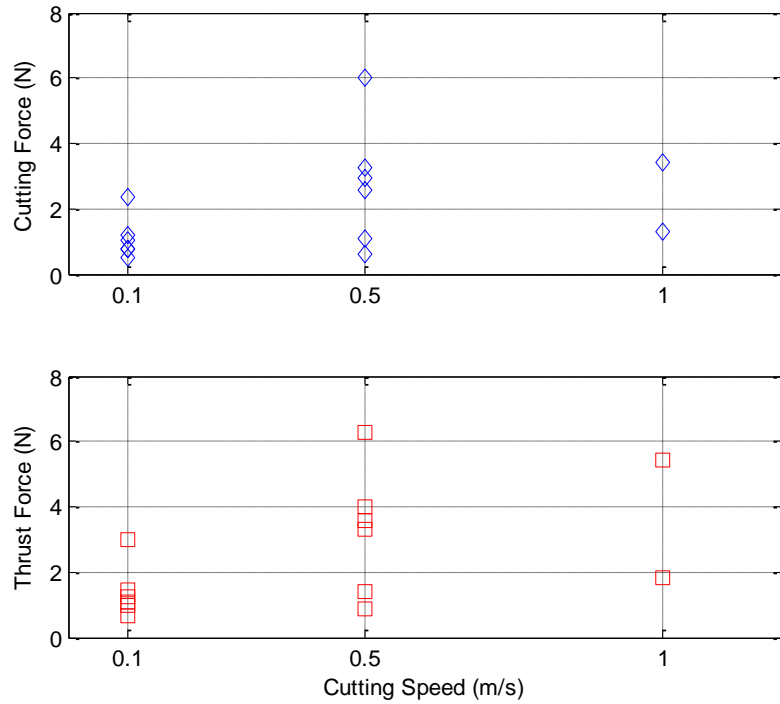
The plunge cut experiments were conducted in the negative rake orientation on 304 SS. The negative rake plunge experiments were characterized by large force increases as cutting progressed into the workpiece. Often the experiments lasted only a few seconds before the forces increased rapidly and the grit fractured. In most cases a different grit was used in each experiment, there were a few exceptions when grits sustaining small fractures were reused for another experiment. The plunge cut experiments were set to feed the grit into the workpiece to create a 10  $\mu\text{m}$  cutting depth. The depth may have varied due to uncontrolled material pickup on the grit, which would give a higher apparent depth of cut.



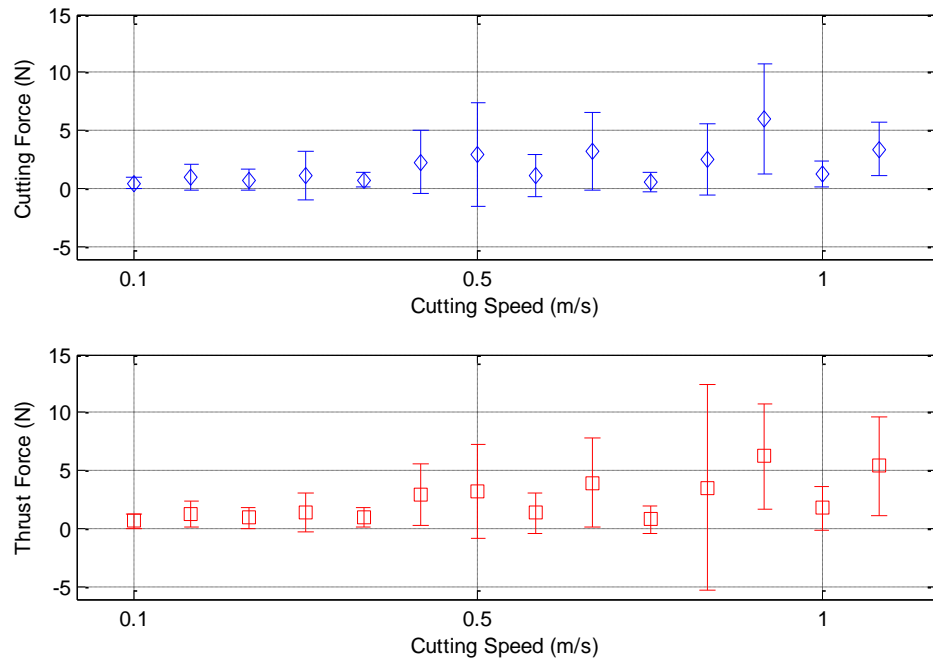
**Figure 30.** Negative rake plunge experimental forces for four experiments at 10  $\mu\text{m}$  depth of cut on 304 SS 0.1 m/s, .5 m/s, 1 m/s.

Figure 30 describes the results of four experimental measurements of the rise and drop in forces for the negative rake experiments. Each experiment shown in Figure 30 represents a different grit. Each showed different force patterns when cutting 304 SS workpiece material with a 10  $\mu\text{m}$  nominal depth of cut at either a 0.1 m/s, 0.5 m/s or 1 m/s cutting speed. In Figure 30a. The force dropped to zero after a fracture occurred in the experiment before 0.5 s. The remaining section of the grit began cutting again at 1.5 sec. Figure 30d showed forces for grits that varied due to material build up and small fractures. Small fractures could have occurred that only removed sections of the grit that were active in removing material which would result in a drop in forces that still has a cutting force after the drop. The difficulty of comparing multiple experiments is further shown in the figure. It was determined that the characteristic force rise in separate experiments did not follow a specific pattern. However, there was a qualitative characteristic rise in forces that was linked to material build up at the cutting interface. This was observed with the high speed imaging system described in the next Section.

The average experimental forces for fourteen experiments at 0.1 m/s, 0.5 m/s, and 1 m/s speeds and at 10  $\mu\text{m}$  depth of cut are given in Figure 31. The average force was calculated by taking the average force during a single experiment as was done with the negative rake traverse experiments. Much like the traverse experiments, there was a large variation in average forces as shown in Figure 32. The standard deviation plot is separated into the first six experiments at 0.1 m/s, six subsequent experiments at 0.5 m/s and the last two experiments at 1 m/s. Various cutting speeds were used in the plunge cut experiments to reduce motion blur and increase video quality using a shutter speed of 20  $\mu\text{s}$ . When speed was varied there was no distinguishable force trend. The average cutting force for all of the experiments was 2 N and the average thrust force was 2.5 N.



**Figure 31.** Average forces for negative rake plunge at 10  $\mu\text{m}$  depth of cut on 304 SS.



**Figure 32.** Average force and standard deviation of negative rake plunge at 10  $\mu\text{m}$  depth of cut on 304 SS.

The force plots of the plunge experiments from Figure 30 were characterized with consecutive fractures where fractures normally occurred at the maximum force. The maximum forces for the experiments are plotted in Figure 33. The large force difference illustrates that the nominal cutting parameters could not be used to explain the forces.

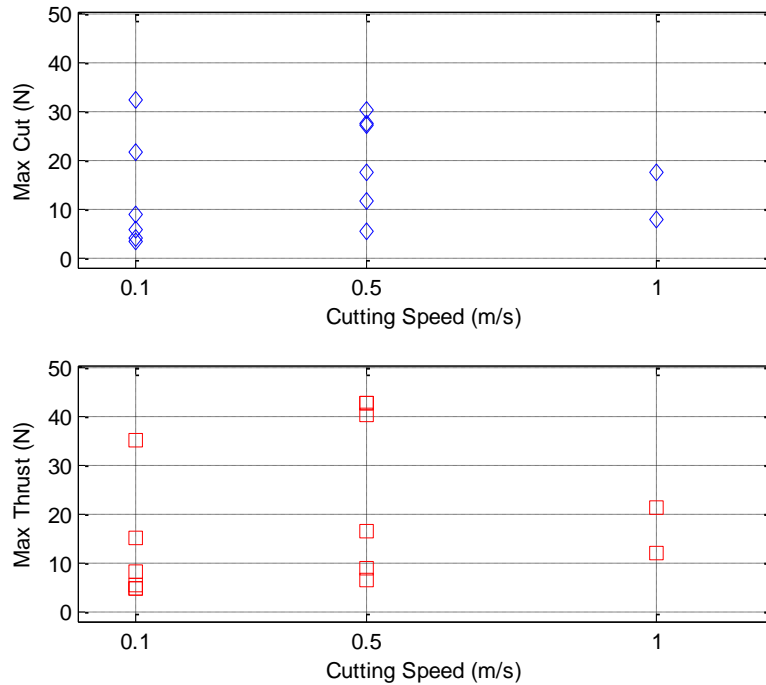


**Figure 33.** Maximum forces for the negative rake plunge experiments at 10  $\mu\text{m}$  depth of cut on 304 SS.

### 10.8.2 High speed camera Imaging

Recording real time video and force data provided key insights to both grit fracture and cutting, especially events that happened in fractions of seconds. The video footage captured during the grit cutting had great value to it; however the resulting still frame images were of lower quality compared to similar stationary optical microscope image. The value of the video was in the rapid accumulation of images at speeds up to 6006 FPS. The video and force measurements were triggered simultaneously when the thrust force signal reached 0.12 V which is equivalent to about 0.5 N. The force and video data were used to correlate effects of material build up, chip formation, and grit fracture. The high speed video camera shutter speed was set to 20  $\mu\text{s}$  for experiments.

The traverse cut experiments produced overall poor video quality compared the plunge cuts. The workpiece in traverse experiments was out of focus in most videos because it moved in the direction corresponding to the camera focal depth. This resulted in a blurred workpiece image and grit/workpiece contact in the majority of recorded videos. Plunge cut experiments were used



to improve the video quality of grit cutting. The plunge cut enhanced cutting visualization because both the grit and workpiece were focused on the camera in the negative rake orientation. The front face of the grit was aligned with the front face of the workpiece by focusing the grit surface on the high speed video camera and then moving the workpiece axis until it was also in focus. This provided the best chance for a clear video of the grit/workpiece interaction. However, motion of the chips would sometimes obstruct the viewpoint of the tool and workpiece. Grit geometry also had a pronounced impact on the video image quality as discussed in the following sections.

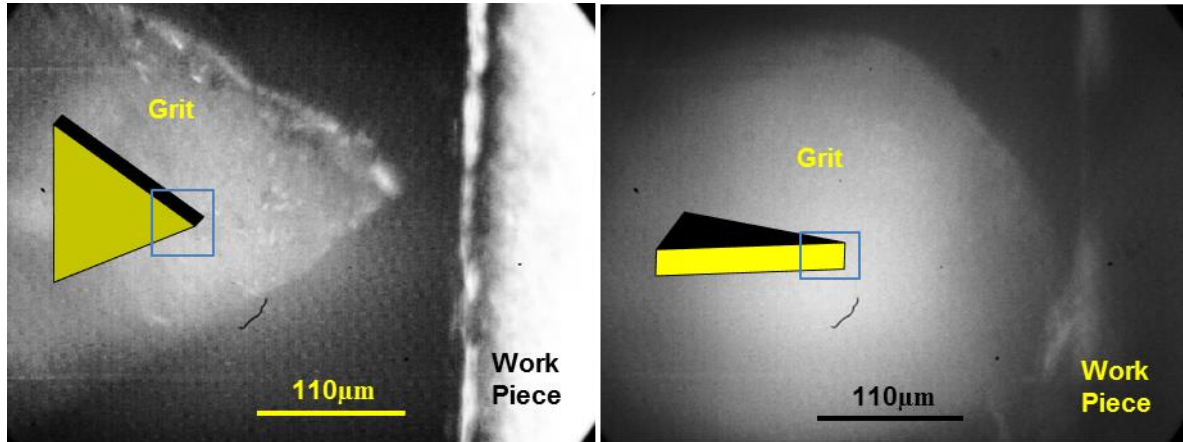


**Figure 34.** 42x Grit video at 20  $\mu$ s shutter speed: negative rake (left), zero rake (right).

### 10.8.3 View of Grit and Focal Depth

The quality of the video image is influenced by the depth of field of the camera. The depth of field is a measurement of how much an object would appear to be in focus. The optical lens' relatively small focal depth,  $\pm 15 \mu\text{m}$ , in comparison to the geometry of the grit created issues with capturing focused images. Grit orientation played a big role in recording focused video, drastically changing the video quality. A still picture taken from the video camera at the extreme grit orientations is shown in Figure 34. A grit representation is provided to clarify the orientation. The viewing window of the camera was  $440 \mu\text{m}$  by  $330 \mu\text{m}$  which showed most of the grit that overhung the holder. In all video images the workpiece is shown on the right moving down, corresponding to a counter clockwise spindle direction. This resulted in the chip formation on the top side of the grit, or top side of the localized geometry.

The negative rake orientation provided a flat, broad face for the focal plane of the video image. Video and images taken during cutting provided a view of events that happened on the front triangular face of the grit. However, the grit width, about  $300 \mu\text{m}$  for the negative rake orientation, was much larger than the focal depth of the optics. This limited the camera focus to the front surface of the grit and only events that were happening near the front surface could be recorded.

Inferences on material build up and chip formation along the entire cutting width of the tool contact was not possible.

The 30° angle of the face of the zero rake orientation resulted in a blurred outline of the grit. The zero rake image was focused on a diagonal edge running through the depth of field, and only a blurred outline of the rounded top edge could be seen. With either orientation the camera was focused on the tip of the grit so part of the contact area of the grit was recorded. Even though the entire grit may not be in focus in the zero rake orientation, the cutting interface and chip formation would be recorded with careful focus on the potential contact region.

Figure 35 shows a negative rake oriented grit that was focused on the front face but does not appear to be in contact with the workpiece. The grit was in contact with the workpiece at some point which was out of the focal plane. The grit geometry has been outlined to assist visualization of the cutting contact region which could not be seen. Although the grit was in focus, the workpiece contact was not, preventing a view of the chip formation. While grits with this type were not ideal candidates for chip video, they may be beneficial for capturing grit fracture if it occurs at the front of the grit.

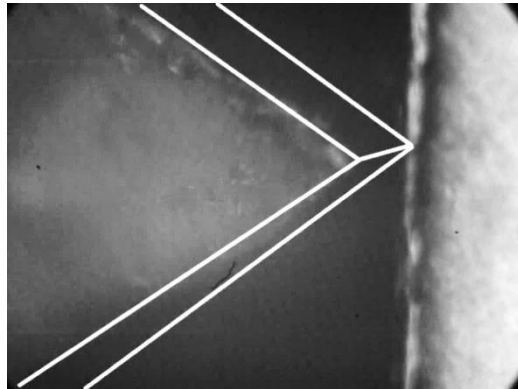


**Figure 35.** Grit variation and focal depth at 20  $\mu$ s shutter speed.

#### **10.8.4 Fracture and Forces**

An obvious correlation between the recorded videos and forces was a fracture event. Initial fracture videos showed material buildup at the cutting interface and then recorded fracture events shortly thereafter. However, fracture did not always occur after visible build up. Figure 36 shows the related video and force data immediately after a fracture. In the still frame provided, the workpiece was shown on the right and was moving from the top of the page to the bottom while the grit was stationary on the left.

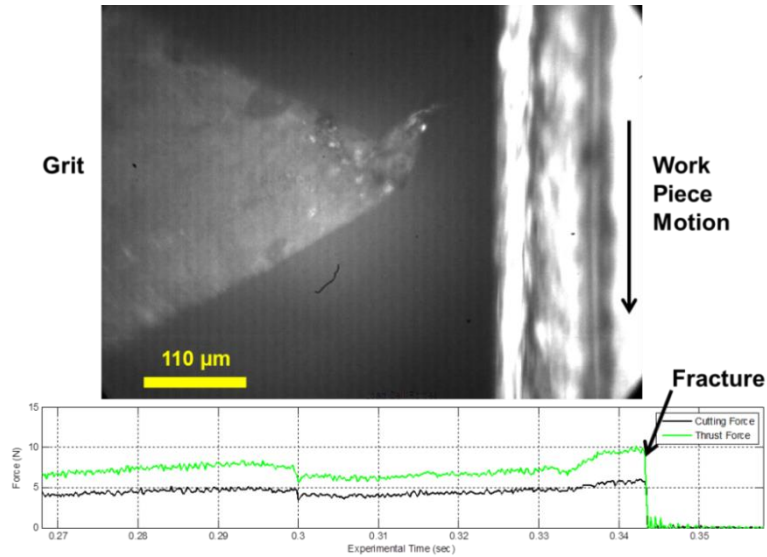


**Figure 36.** Force and video combined.

As the fracture occurred and the grit broke, there was a distinct drop of forces. The videos captured the fractures as they occurred. Still shots are provided here but are no substitute for the recorded video which provided insight and continuity to material movement.

### 10.8.5 Material Build Up and Chip Formation

Qualitative observations of the chip formation and fluctuation were observed during the experiments. The view of the chip was sometimes unclear due to motion blur or the chip flowing out of the view of the camera. When the chips moved into and out of focus it sometimes showed different aspects of the chip. From the side view, serrated edges were observed but such detail was only viable for general observations. The videos sometimes showed continuous chip formation but would also lead to events where material and chips clustered together and obstructed the cutting interface. Figure 37 demonstrates both chip formation and material build up.

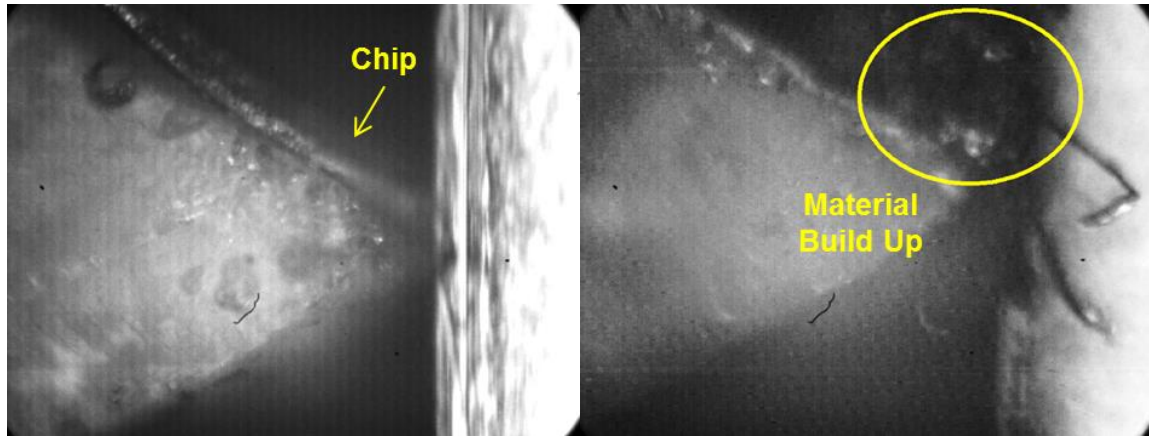
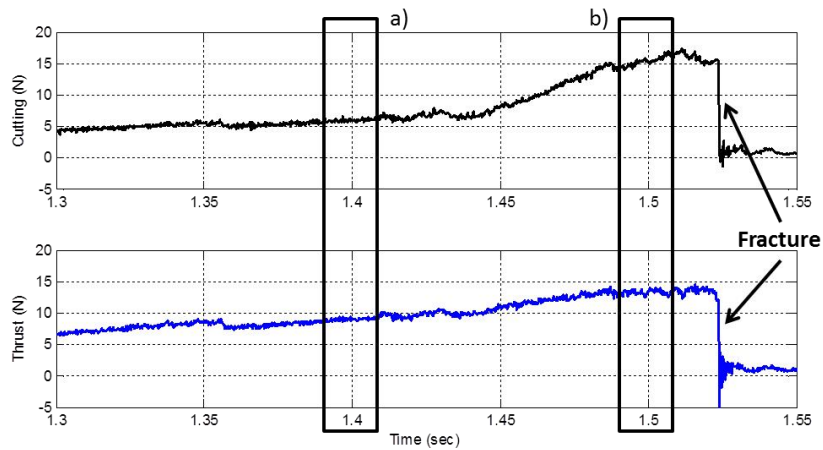
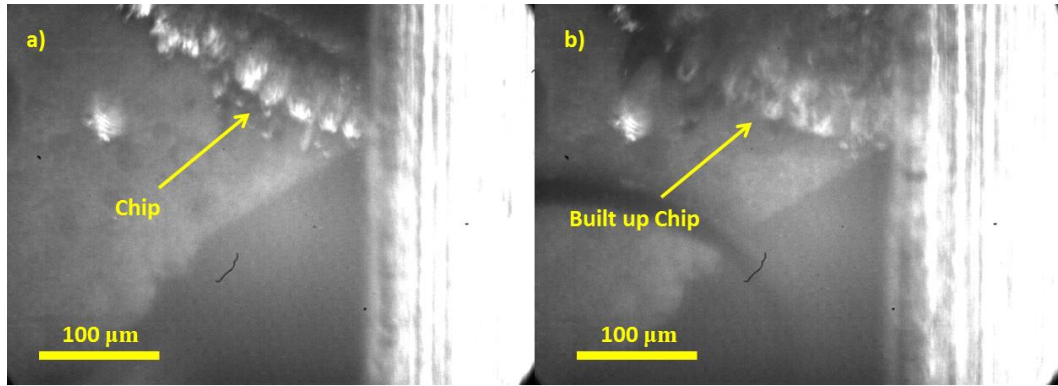


**Figure 37.** Chip formation (left) and material build up (right).

Chip formation varied slightly based on grit orientation. In most cases of the negative rake orientation, shown in Figure 37, the chip had a defined side edge that was in line with the triangular face of the grit. The chip also has a slight rounded top to it which is out of focus of most videos. The zero rake orientation chips were generally a triangular shape with a vertex pointing away from the grit rake face. The vertex of the chip was lined up with the tip of the grit that is removing material. In most videos of the zero rake orientation only the tip of the chip was in focus depending on the focusing location.

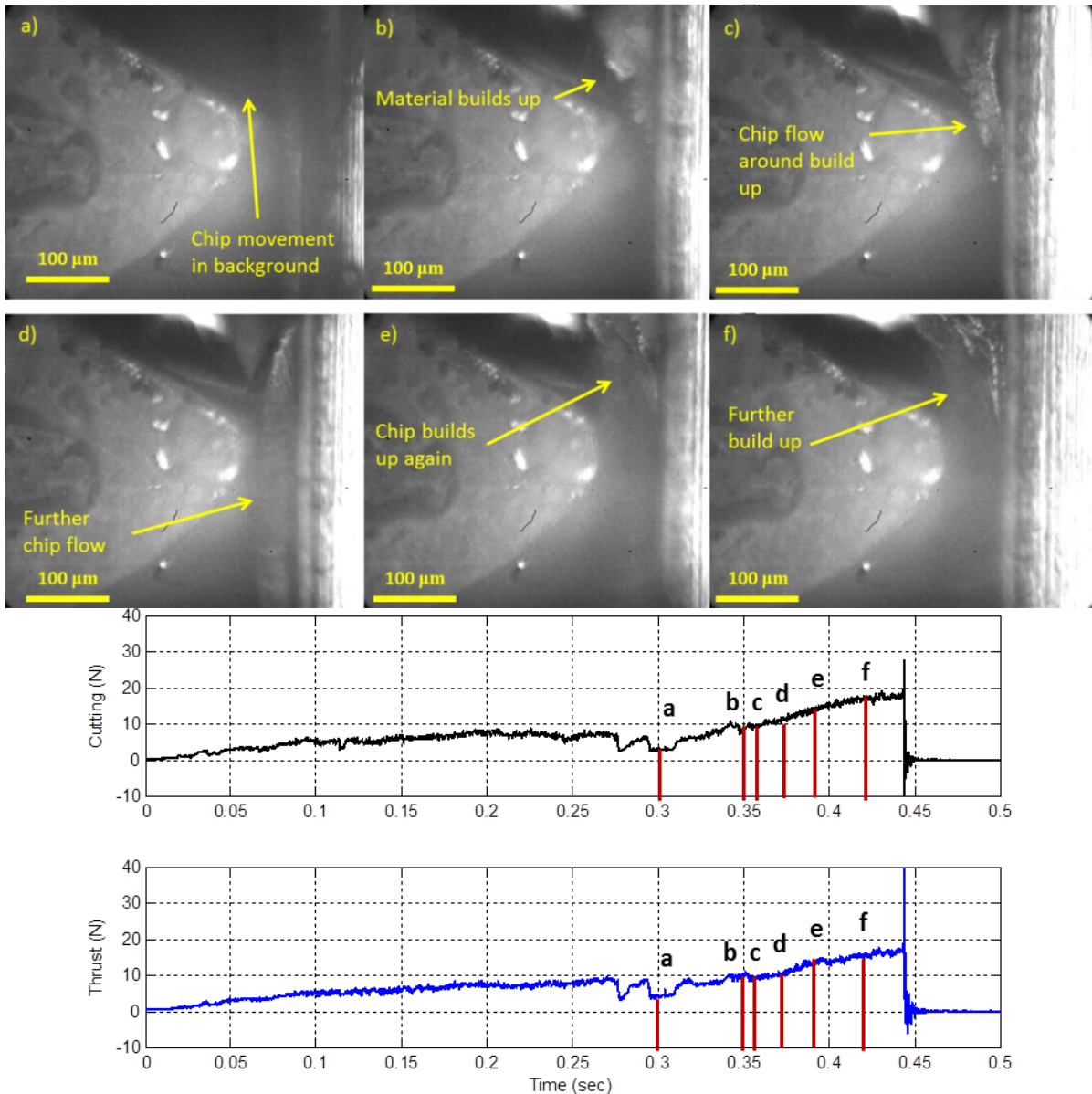
The material build up in Figure 37 sometimes appeared to completely stop all chip flow in the view of the camera. It was not clear if chip formation had completely stopped or if chip formation was out of the view of the camera. The high speed imaging system aided in recognizing some characteristics in the forces. Several key videos showed the chip flow accumulated, ceased, or slowed down; followed by an increase in forces. However all force rises were not validated by a video that showed the chip flow stop or accumulate. The videos that did not show chip flow, but documented a rise in force, were attributed to the event happening out of the view of the high speed camera.

Figure 38 shows a negative rake plunge at 0.5 m/s cut at a 10  $\mu\text{m}$  depth of cut when the chip was freely flowing in Figure 38a but the chip formation started to slow down and broaden before it became relatively stationary in Figure 38b. Shortly thereafter, the chip built up at the cutting interface and a fracture occurred. The built up chip can be recognized in the still frames by noting that there is a dark empty space above the chip in Figure 38a while Figure 38b shows material surrounding the entire cutting interface.



**Figure 38.** Material build up and resulting force increase.

Figure 39 shows images from a 0.5 m/s cut at a 10  $\mu\text{m}$  depth of cut. Figure 39a shows chip progression that was out of focus on the camera and barely seen, but the material eventually built up in Figure 39b. A chip then began to flow from the apparent location of the built up material in Figure 39c and 39d. However, the material once again began to build up in Figures 39e and 39f before a fracture occurred, shown by the large drop in forces.



**Figure 39.** Buildup progression of a negative rake plunge at 10  $\mu\text{m}$  depth and 0.5 m/s speed on 304 SS at time: a) 0.300 s, b) 0.350 s, c) 0.353 s, d) 0.368 s, e) 0.389 s, f) 0.420 s.

Figures 38 and 39 illustrated chip build up cases that resulted in fracture; however this was not always the case as shown in Figure 40. Here the material built up produced a rise in forces and then fell away. It was a 1 m/s cut at 2.5 $\mu\text{m}$  depth. The chip is partially seen in Figure 40a and it accumulated at the cutting interface in Figure 40b. Eventually the clump of material fell away from the cutting interface at Figure 40c and a chip continued to form in Figure 40d. The chip in Figure 40d was partially out of range of the camera so it was blurred and is hard to see in a still frame image. The conditions that lead to chip build up that fell away from the cutting interface



were unknown. However these experiments showed that material build up or chip accumulation at the cutting interface could cause the forces to rise which could lead to fracture.

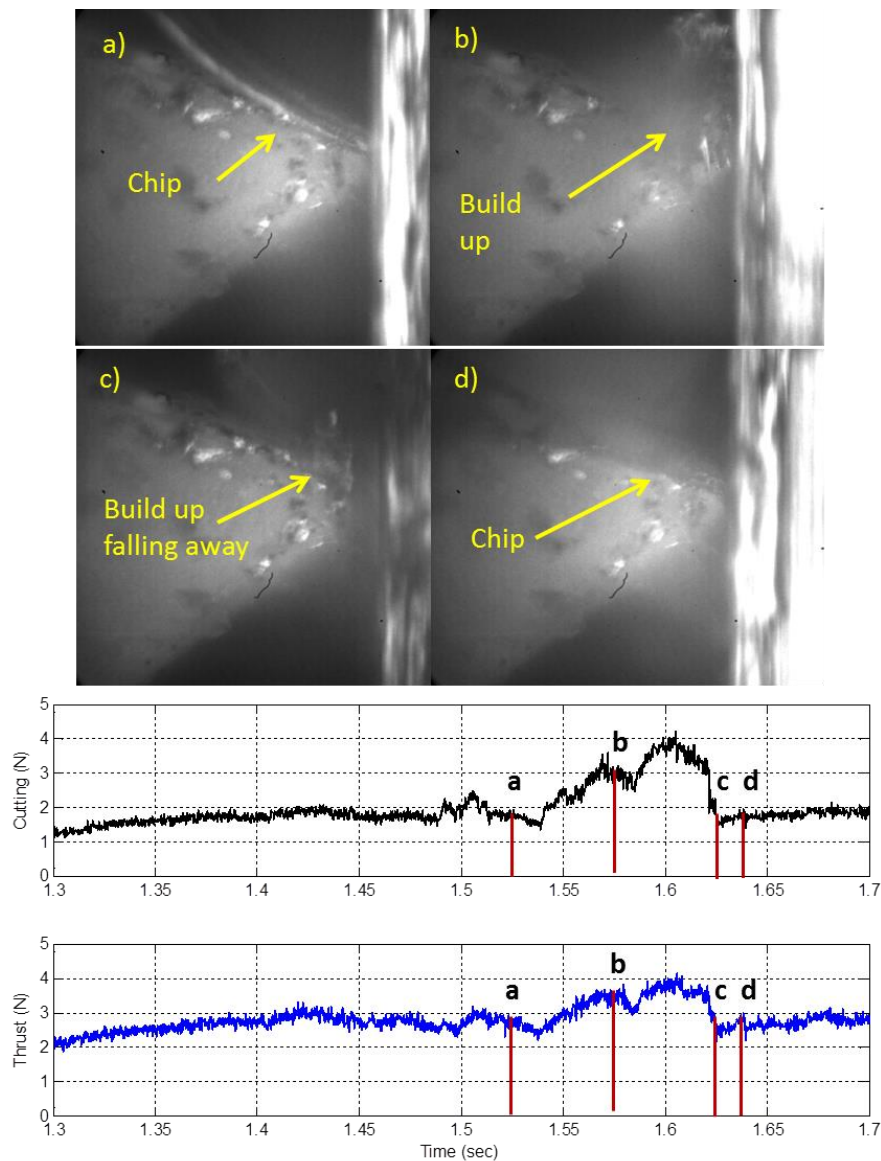


**Figure 40.** Buildup progression of a negative rake plunge at 2.5  $\mu\text{m}$  depth and 1 m/s speed on 304 SS at time: a) 1.524 s, b) 1.575 s, c) 1.625 s, d) 1.637 s.

### 10.8.6 High Speed Video Conclusions

The plunge cuts provided good cutting images and showed many cases of chip build up and fracture. The chip build up at the cutting interface was found to raise forces which could lead to fracture of the grit. The highly variable cutting conditions and possibility of material build up and fracture demonstrated how inconsistent similar experiments appeared. Although the grit geometry

and parameters had some impact on individual results with the experimental setup, the impact was indistinguishable when only using forces and video to characterize cutting. To understand the grit cutting process work was done to better define the actual cutting conditions, such as how much material was removed. This would also assist in obtaining quantifiable results.

## 10.9 CONCLUSIONS

A grit tool holder was developed to hold and test shaped alumina grits in similar orientations that would occur on a coated abrasive product. Methods were explored to quantify and compare single grit performance for grinding applications. Studying individual grains is challenging due to localized geometry differences and differences between individual grits. Macroscopic abrasive grits were used in experiments to have a more controlled shape and contour compared to crushed grits, but even the shaped grits contained localized geometry differences at the location of material removal. The differences in localized geometry produced cutting and thrust forces that had variation in experiments at the same parameters.

Methods were developed to observe individual grits in the process of material removal action. A high speed camera was used to capture video of cutting at 6006 Frames Per Sec (FPS). The video quality was dependent on the planarity of the grits, but was used to effectively distinguish chip formation, material build up, and fracture for individual grains. Grit geometries that deviated from the high speed imaging field of view resulted in a blurred image. A lower magnification lens could be used to have a larger depth of view at the expense of the image magnification. The high speed imaging optics were used in conjunction with experimental forces to visualize material pickup accumulate at the tool/chip interface as the tool forces increased. Several instances of cutting correlated material pickup with a rise in cutting forces that induced fracture. However, material pickup was not always present in videos when the force rose and a fracture occurred. Occurrences that were not captured on video were attributed to the event not being located within the focal depth of the optics.

Grit fracture characteristics and chips were also visualized with the high speed video. It was used to determine shear angles for cutting speeds at 1 m/s and below. However, shear angle measurements could only be taken during periods of high speed video when distinct chip characteristics were present. More shear angle measurements are needed to validate the experimental shear angles because only small segments of videos were considered clear enough for measurements.

In light of geometrical differences affecting grit characteristics, experimental analysis was developed to distinguish and compare grits of slightly different geometry. Workpiece measurement techniques were used to successfully compare experiments where variable grit



geometry would otherwise make comparisons difficult. Surface profiles were used to measure the removed chip area of non-overlapping tool paths so experimental forces could be directly related to each other. The methods to define the contact area were based on the Arcona [5] model. The measured surface profiles and grit contact geometry provided a basis for repeatable experimental results. Distinct relationships between experimental parameters were found, but more experimental samples are needed for conclusive results. Preliminary results showed that the workpiece hardness directly impacts cutting and thrust forces. Forces between 304 SS, 1215 steel, and 52100 steel were compared. 1215 steel had 8% lower cutting forces and 14% lower thrust forces than the 304 SS, while significantly harder 52100 steel was 116% and 285% greater than cutting and thrust forces than the 304 SS material.

The specific shaped grit that was studied had two distinct orientations of possible cutting conditions but could also be mounted anywhere between the two orientations. The two extreme rake angle orientations were represented by either a 0° rake angle with a 20 µm edge radius or a -30° rake angle with a 300 µm wide flat face, which were used as extreme experimental conditions. A third orientation was tested which was halfway between the two previous orientations. The measurement techniques used for grit comparison were utilized to show that the 0° rake angle orientation removed material at the lowest force at a given removed chip area on 304 SS. The -30° rake grit orientation produced 32% higher cutting forces and 86% higher thrust forces than the 0° rake at comparative material removed areas for a 304 SS workpiece. The halfway rake orientation had the largest experimental forces at 87% and 199% greater cutting and thrust forces than the 0° rake orientation. Comparative cutting statistics and relationships were demonstrated and could be used to more effectively design and compare various grit shapes by using the measurement techniques. The measurement and experimental methods can effectively distinguish cutting characteristics and parameters in single grit testing.

The experimental methods and measurement techniques were used effectively to compare single grit performance. It was possible to compare experimental data with respect to specific cutting energy. The specific cutting energy could be used to determine effective experimental conditions to use specific grit geometry, determine effective parameters for different material workpieces or be expanded to compare grit friability.

The experimental data was compared to a force model described by Arcona [5], but was determined to not be an effective tool for grit performance prediction at this time. Nevertheless experimental data was also compared to Third Wave AdvantEdge cutting simulation package [34].

# REFERENCES

- 1 ME Merchant. Some Observations on the Past and Present of Research on Machining and Grinding, Applied Mechanics Reviews. 46 (1993) 72-73.
- 2 MC Shaw. Some Observations Concerning the Mechanics of Cutting and Grinding, Applied Mechanics Reviews. 46 (1993) 74-79.
- 3 ME Merchant. Mechanics of the Metal Cutting Process. I. Orthogonal Cutting and a Type 2 Chip, J.Appl.Phys. 16 (1945) 267-275.
- 4 JD Drescher, Tool Force, Tool Edge, and Surface Finish Relationships in Diamond Turning. PhD Dissertation, North Carolina State University. (1991).
- 5 C Arcona, Tool Force, Chip Formation, and Surface Finish in Diamond Turning, PhD Dissertation, North Carolina State University. (1996).
- 6 MC Shaw, Principles of abrasive processing, Clarendon Press; Oxford University Press, Oxford; New York, 1996.
- 7 JA Schey, Introduction to manufacturing processes, McGraw-Hill, Boston, 2000.
- 8 S Kalpakjian, Manufacturing engineering and technology, 6th ed., Prentice Hall, New York, 2010.
- 9 S Mezghani, M El Mansori. Abrasiveness properties assessment of coated abrasives for precision belt grinding, Surface and Coatings Technology. 203 (2008) 786-789.
- 10 3M, 3M Cubitron II Abrasives. [http://solutions.3m.com.au/wps/portal/3M/en\\_AU/Cubitron-II/Home/](http://solutions.3m.com.au/wps/portal/3M/en_AU/Cubitron-II/Home/), Jul 2013 (2014).
- 11 S Malkin, Grinding technology : theory and application of machining with abrasives, Industrial Press, New York, 2008.
- 12 WB Rowe, Principles of modern grinding technology, William Andrew, Oxford ; Burlington, MA, 2009.
- 13 SW Date, S Malkin. Effects of grit size on abrasion with coated abrasives, Wear. 40 (1976) 223-235.

- 14 AP Mercer, IM Hutchings. The deterioration of bonded abrasive papers during the wear of metals, *Wear*. 132 (1989) 77-97.
- 15 J Shibata, I Inasaki, S Yonetsu. The relation between the wear of grain cutting edges and their metal removal ability in coated abrasive belt grinding, *Wear*. 55 (1979) 331-344.
- 16 T Kayaba, K Hokkirigawa, K Kato. Analysis of the abrasive wear mechanism by successive observations of wear processes in a scanning electron microscope, *Wear*. 110 (1986) 419-430.
- 17 RG Visser, RC Lokken. The effect of the severity of the grinding mode on the wear characteristics of grade 36 Al<sub>2</sub>O<sub>3</sub>- and Al<sub>2</sub>O<sub>3</sub>-ZeO<sub>2</sub>-coated abrasive belts, *Wear*. 65 (1981) 325-350.
- 18 AL Carrano, JB Taylor. Geometric Modeling of Engineered Abrasive Processes, *Journal of Manufacturing Processes*. 7 (2005) 17-27.
- 19 X Chen, W Brian Rowe. Analysis and simulation of the grinding process. Part II: Mechanics of grinding, *Int.J.Mach.Tools Manuf.* 36 (1996) 883-896.
- 20 ZB Hou, R Komanduri. On the mechanics of the grinding process – Part I. Stochastic nature of the grinding process, *Int.J.Mach.Tools Manuf.* 43 (2003) 1579-1593.
- 21 R Komanduri. Some aspects of machining with negative rake tools simulating grinding, *International Journal of Machine Tool Design and Research*. 11 (1971) 223-233.
- 22 MC Shaw, *Metal cutting principles*, Oxford University Press, New York, 2005.
- 23 BM Lane, *Development of Predictive Models for Abrasive and Chemical Wear of Diamond Tools*, PhD Dissertation, North Carolina State University. (2010).
- 24 BM Lane, M Shi, TA Dow, R Scattergood. Diamond tool wear when machining Al6061 and 1215 steel, *Wear*. 268 (2010) 1434-1441.
- 25 M Shi, *Thermo-Chemical Tool Wear in Orthogonal Diamond Cutting Steel and Stainless Steel*, MS Thesis, North Carolina State University. (2010).
- 26 M Shi, B Lane, CB Mooney, TA Dow, RO Scattergood. Diamond tool wear measurement by electron-beam-induced deposition, *Precis Eng.* 34 (2010) 718-721.
- 27 Kistler., *Data Sheet. Type 9251A, 9252A, 9250A4, 9251A4*. Kistler Instrument Corp., Amherst, NY.

- 28 C Arcona, TA Dow. An Empirical Tool Force Model for Precision Machining, Journal of Manufacturing Science and Engineering. 120 (1998) 700-707.
- 29 E Miller, Deflection Prediction and Error Correction of High Speed Miniature Milling Tools, MS Thesis, North Carolina State University. (2000).
- 30 L MatWeb, <http://www.matweb.com/>, MatWeb: Material Property Data. 2014.
- 31 H Ernst, ME Merchant. Chip Formation, Friction, and High Quality Machined Surface, Surface Treatment of Metals (ASM). (1941) 299-378.
- 32 TD Marusich, M Ortiz. Modelling and simulation of high-speed machining, Int J Numer Methods Eng. 38 (1995) 3675-3694.
- 33 H Bil, SE Kılıç, AE Tekkaya. A comparison of orthogonal cutting data from experiments with three different finite element models, Int.J.Mach.Tools Manuf. 44 (2004) 933-944.
- 34 Third Wave Systems, AdvantEdge, v6.2-010 (1997-2014).

# 11 DESIGN OF A MICROFLUIDIC DEVICE TO EXTRACT DYES FROM FIBERS FOR FORENSIC ANALYSIS

**Sean P Gunning**

Graduate Student

**Kenneth P Garrard**

Senior Research Scholar, PEC

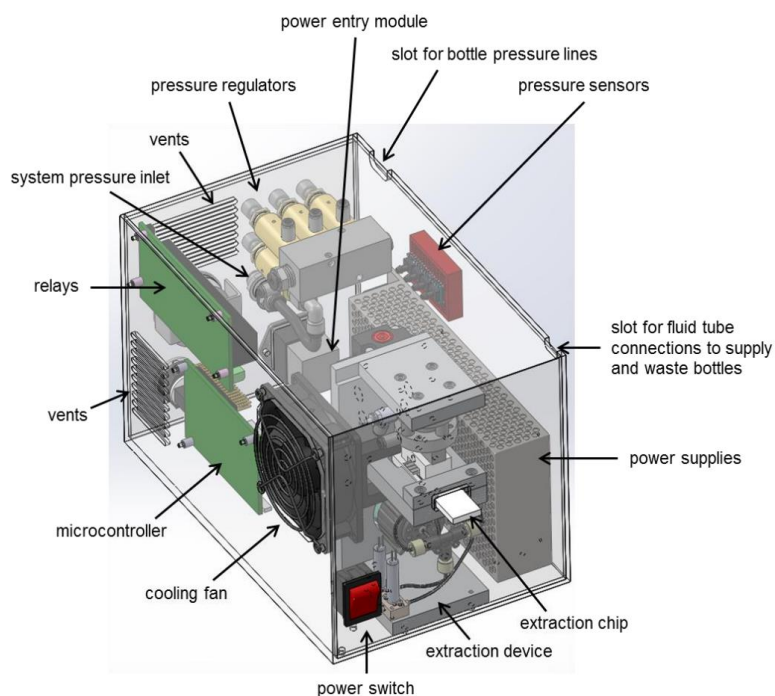
**Stephen Furst**

Smart Material Solutions, Inc.

**Thomas A Dow**

Professor, Mechanical and Aerospace Engineering

*Analysis of fiber evidence from a crime scene is an important aspect of criminal investigation. Fibers are identified and compared by morphology and the molecular makeup of the coloring dyes. Separation of dye from fiber is a tedious process involving aggressive and hazardous solvents that can take a skilled lab technician up to 30 minutes per sample. It is also destructive. The objective of this research was to design and build a microfluidic system to automate the extraction process using a minimal amount of a sample.*



## 11.1 INTRODUCTION

Due to the quantity of textile materials in the environment, there is a high probability of fiber transfer during the commission of a crime. As a result, identification of fiber samples often plays a critical role in criminal investigations. In a typical case, a sample of known origin must be compared to an evidence sample to determine if both could have the same origin. A wide variety of techniques are available to test this hypothesis and each provides a different type of information. Forensic fiber examinations begin with non-destructive visual comparison of characteristics such as color, diameter, cross-sectional shape, birefringence, refractive index and fluorescence. These techniques include light microscope, UV-visible spectrometry and Fourier Transform Infrared spectrometry.

One way to add additional specificity is to identify the dyes used to color the fabric. Such analysis are more sensitive but destroy the evidence sample. Among the quantitative techniques available are high performance liquid chromatography, capillary electrophoresis, pyrolysis-gas chromatography /mass spectrometry and time-of-flight mass spectrometry. The latter technique is becoming increasingly popular for identifying the dye material from a fabric with a high degree of molecular specificity. It can measure the mass of a distribution of different dye molecules extracted from the fiber sample.

However, to use these analytic techniques, dye molecules must be separated from the fiber sample. While useful and pertinent research has been conducted to optimize macroscopic extraction conditions, what is needed is a microfluidic device that can quickly and automatically extract the dye from the fabric. The resulting dye solution could then be loaded into an LC column for separation and subsequent detection by mass spectrometry. Such a system would make it feasible for the forensic examiner to apply the quantitative methods to a larger number of samples while minimizing the risk of human error and sample contamination. Microfluidic systems have been developed for a variety of applications from chemical analysis to DNA amplification. The differences in the dye extraction problem are 1) the requirement to insert a macroscopic solid object into the device and 2) aggressive extraction solvents such as pyridine that limit the compatible materials.

This paper describes the development of a system to automate the dye extraction process. The system uses a microfluidic cavity to separate the dye from tiny fiber strands less than 3 mm in length and 50  $\mu\text{m}$  in diameter and then prepare the dye for MS analysis – all in less than 10 minutes. This automation is less labor-intensive and allows the forensic examiner to analyze multiple samples at once. Additionally, the system could provide a higher sample concentration than can be achieved manually, thus reducing the size of fiber needed to make a positive ID.

## 11.2 EXTRACTION SYSTEM

The process begins with the forensic examiner placing a small fiber sample onto a flexible microfluidic cavity (10 $\mu$ l volume) shown in Figure 1. This is typically done using a microscope and tweezers. The examiner then seals the chamber by placing the glass cover over the cavity and checks that the fiber is clamped in place. This design feature allows the examiner to see the fiber both before and after the process.

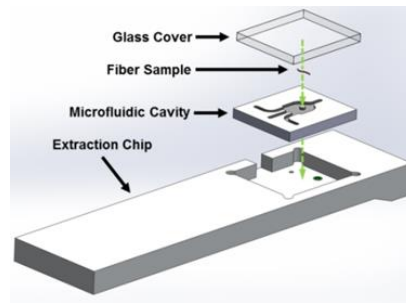


**Figure 1.** The fiber sample is placed on the machined FFKM microfluidic cavity, sealed with a glass cover and inserted into the extraction system.

A significant design challenge was finding a material that would seal the cavity as well as stand up to the pyridine solvent. The solution was to use FFKM – often called elastomeric Teflon – to create the extraction cavity and then seal it with a glass cover. The FFKM cavity was machined with a 1/32" milling tool operating at 30,000 rpm for these prototypes but could be molded in a production version.

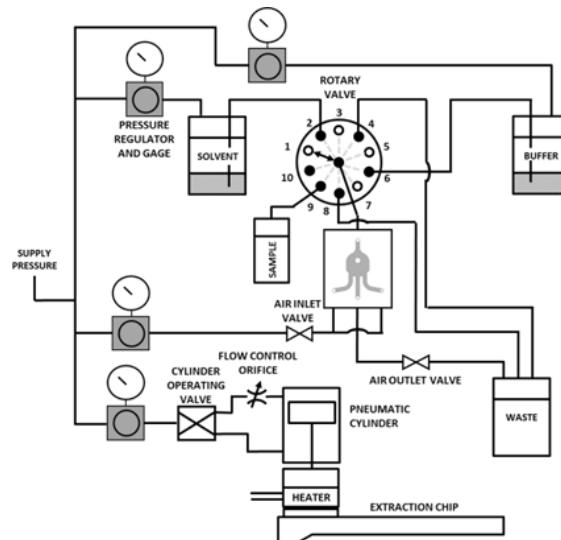


**Figure 2.** Extraction system layout.

## 11.2.1 Dye Extraction

The extraction chip holding the sealed microfluidic cavity is then inserted into the system and fits under the heater at the bottom of Figure 2.

Figures 2 and 3 show the components and steps in the extraction process. When the chip is inserted into the system (3A), it breaks the beam of an optical switch and triggers a pneumatic cylinder to seal the cavity (Figure 3A-3C). The cylinder loads the glass against the flexible cavity to seal the cavity as well as the fluid connections through the bottom of the extraction chip (Figure 3D).

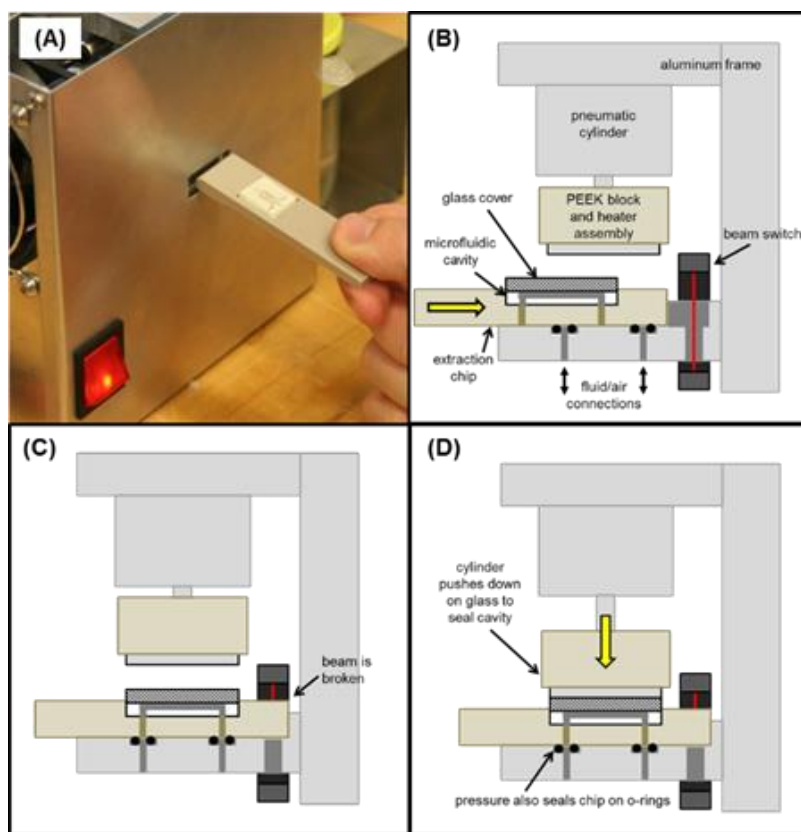


**Figure 3.** The chip is inserted into the system (A-C), breaking the beam of an optical switch. (D) A pneumatic cylinder is triggered, providing sealing pressure to the cavity and fluid connections.

Fluid, air, waste, and extracted dye are routed to and from the microfluidic cavity through shut-off valves and a 10-position rotary valve shown in Figure 2. Pressurized reservoirs supply solvent (a mixture of pyridine and water) into the cavity to immerse the fiber.



A resistive heater in the clamping block heats the solvent through the glass cover to produce solvent temperature of 90°C in less than 50 sec. High temperature reduces the extraction time of the dye.

### 11.2.2 Evaporation

After the dye is extracted, the pyridine is evaporated by flowing air through the cavity. This process was also a challenging aspect of the design. The number and shape of the air passages and the air volume/speed were instrumental in creating controlled evaporation of the solvent without blowing the mixture out of the chamber. For a fluid temperature of 90°C, the evaporation process is completed in 1 minute.

### 11.2.3 Re-dissolution

After the pyridine is evaporated, the dye molecules coat the cavity walls. A buffer solution is introduced into the cavity to re-dissolve the molecules. The temperature of this process needs to be controlled for best results. The buffer solution and reconstituted dye molecules are then pumped through the inlet to a sample container or directly into an HPLC-Mass Spectrometer for analysis. Waste fluid and solvent vapors are pumped to a waste container that is vented by an activated charcoal filter.

## 11.3 RESULTS

Figure 4 shows a red-dyed fiber in the microfluidic cavity before and after extraction with the device.

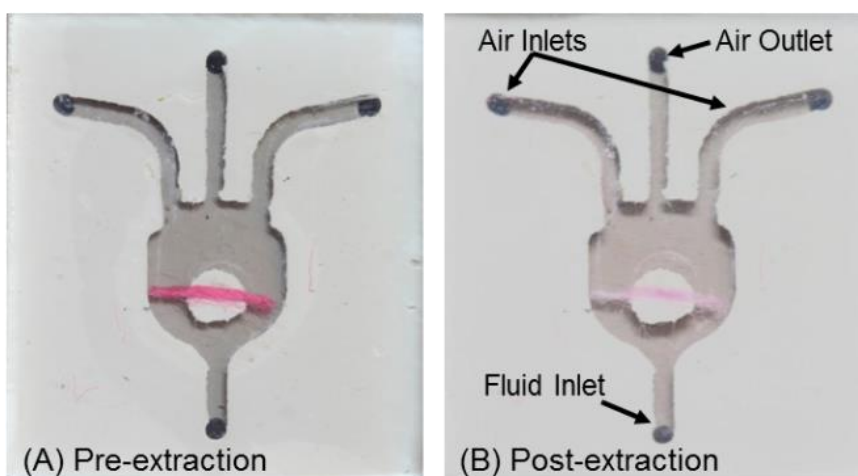


**Figure 4.** Microfluidic cavity and red fiber (A) before and (B) after dye extraction.

The device has been used to successfully extract direct dyes from cotton threads (a bundle of fibers) and acid dyes from nylon threads as small as 3 mm in length. Timing of each extraction step was as follows:

1. Solvent introduction and heating for extraction → 3-5 min.
2. Evaporation of solvent → 2 min.
3. Waste ejection and buffer introduction → <1 min.
4. Re-dissolution of dye and ejection of sample → 1-2 min. (longer for larger sample volume)

### 11.3.1 HPLC and MS Measurements

High Pressure Liquid Chromatography (HPLC) and Mass Spectrometry (MS) were used to analyze the red dye extracted from the fiber sample. The HPLC separates the molecules based on polarity and MS measures the mass/charge ratio. The results for the extracted red dye are shown in Figure 5. The retention and EIC time from the HPLC Fig 5(A) identify a region of interest and the charge ratio ( $m/z$ ) of 631.08 from Fig 5(B) identify the DR 81red dye molecule. This extraction system was successfully employed with HPLC-MS analysis for the detection of the dyes listed in Table 1.

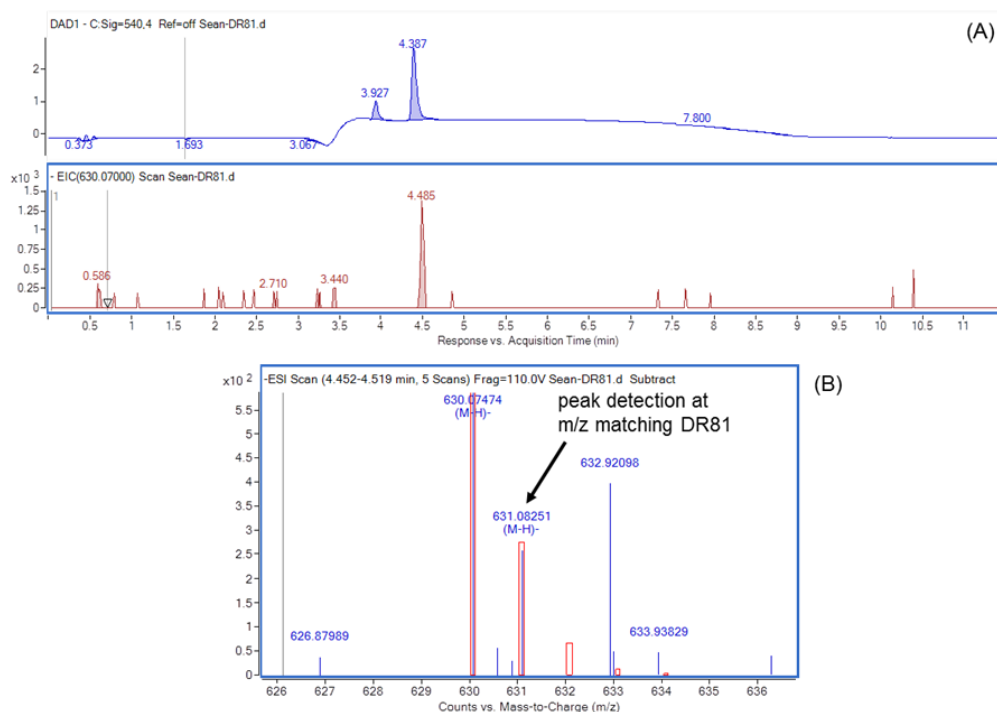


**FIGURE 5.** Results of analysis of Direct Red 81 ( $C_{29}H_{21}N_5O_8S_2$ ) extracted dye sample. (A) The retention time and EIC time from LC analysis and (B) the mass spectrum show the detection of the DR81 dye.

**Table 1.** List of Extracted Dyes

Color Index Name	Fiber Material	<i>m/z</i>
Direct Green 26	Cotton	544.08
Direct Red 81	Cotton	314.53
Direct Yellow 106	Nylon 6,6	298.99
Acid Blue 25	Nylon 6,6	393.05
Acid Yellow 49	Nylon 6,6	424.00
Acid Red 186	Nylon 6,6	514.33
Acid Red 114	Nylon 6,6	785.10
Acid Yellow 151-9	Nylon 6,6	807.07

### 11.3.2 Direct Injection to MS

The direct coupling of the extraction system output to an Agilent Quadropole Time of Flight - MS (QTOF-MS) device significantly improves the limits of detection for the system. The QTOF-MS and the dye extractor are shown in Figure 6. Acid Blue 25 dye was extracted from an individual nylon fiber (< 1 ng) less than 10 mm in length. The sample was sent directly to a mass spectrometer from microfluidic system, where the characteristic *m/z* (393.05) of the ions was detected.

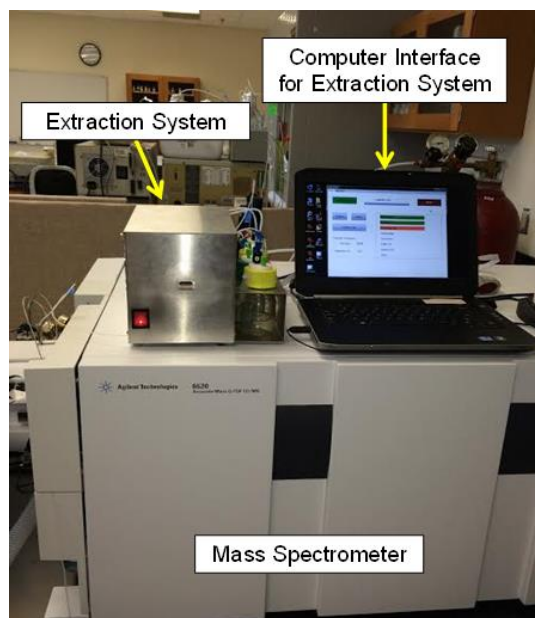


**Figure 6.** Direct coupling of extraction system to mass spectrometer.

In addition to extraction from individual fibers, the system can be used to extract from multiple fibers with different dye colors simultaneously. Acid Blue 25 and Acid Yellow 49 dyes were extracted from individual nylon fibers in a single test where direct injection to the mass spectrometer was used. The mass spectra of the individual dyes is easily distinguished in Figure 7.

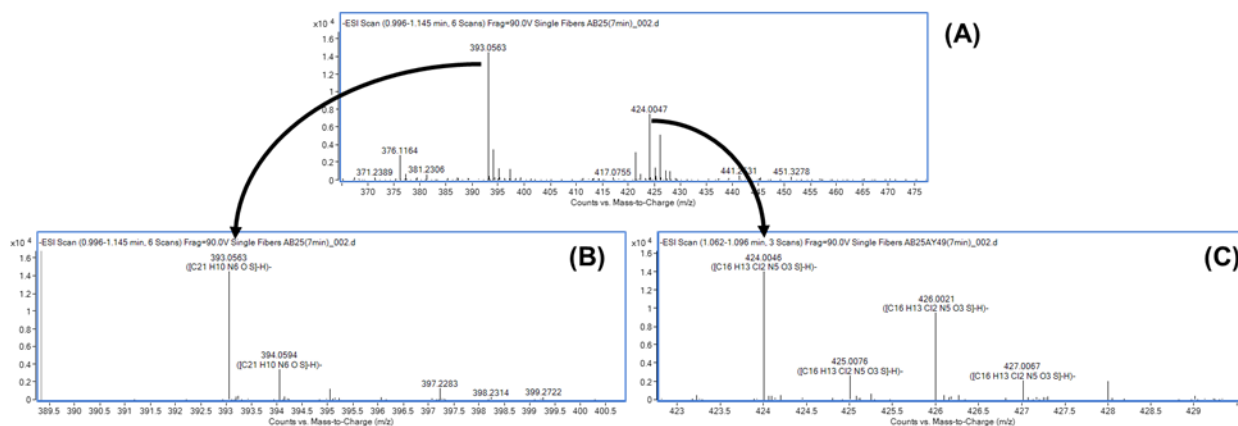


**Figure 7.** (A) Mass spectra of Acid Blue 25 and Acid Yellow 49 dyes from combined extraction (individual fibers 5-10 mm in length). The individual mass spectra of (B) Acid Blue 25 and (C) Acid Yellow 49 are easily distinguishable.

## 11.4 CONCLUSIONS

Automated dye extraction from trace fibers in a microfluidic system has been achieved. The extraction process is accomplished in under 10 minutes with minimal fabric and chemical volume. While the extraction is taking place, the forensic examiner is free to prepare the next sample for extraction in a parallel machine, thus increasing throughput and addressing the back-log of samples currently awaiting analysis within the justice system.

Future work will push detection limits to their maximum by minimizing fluid volume to extract dye from even smaller samples. Furthermore, solid-extractions applications are being developed for drug testing, hair analysis, food quality control, etc. Since the device provides control over operation conditions (temperature and process times), extraction can be optimized for a variety of dye and fiber types, as well as other solid-extraction applications.

# FACULTY

## **THOMAS A. DOW**

Director, Precision Engineering Center

Dean F. Duncan Distinguished University Professor in Mechanical Engineering

Professor, Department of Mechanical and Aerospace Engineering

BS, Mechanical Engineering, Virginia Polytechnic Institute, 1966

MS, Engineering Design, Case Institute of Technology, 1968

PhD, Mechanical Engineering, Northwestern University, 1972

After receiving his PhD degree from Northwestern University in 1972, Dr. Dow joined the Tribology Section of Battelle Columbus Laboratories and worked there for ten years. His research interests were in the areas of friction and wear and included studies on a wide variety of topics from lubrication of cold-rolling mills using oil-in-water emulsions to wet braking effectiveness of bicycle brakes to elastohydrodynamic lubricant film generation in ball and roller bearings. He developed experimental apparatuses, established analytical models, and corroborated those analyses with experimental measurements. Dr. Dow joined the faculty at North Carolina State University in 1982 and was instrumental in developing the academic and research program in precision engineering. His current research interests include precision machining, real-time control, metrology, micro-coining and nano-coining. He was one of the founders of the American Society for Precision Engineering and currently acts as the Executive Director.

## **RONALD O. SCATTERGOOD**

Professor  
Materials Science and Engineering Department

BS, Metallurgical Engineering, Lehigh University, 1961  
MS, Metallurgy, Massachusetts Institute of Technology, 1963  
PhD, Metallurgy, Massachusetts Institute of Technology, 1968

R.O. Scattergood is a Professor in the Department of Materials Science and Engineering. He received BS degrees in Mining Engineering and Metallurgical Engineering from Lehigh University. His MS and PhD degrees were obtained in Metallurgy from M.I.T. In 1968 he became a member of the basic research staff in the Materials Science Division at the Argonne National Laboratory. In 1981, he joined the faculty as a Professor of Materials Engineering at North Carolina State University.

Professor Scattergood's major research interests have been focused on the mechanical behavior of solids. He has worked in the areas of strengthening mechanisms in solids, mechanical testing, fracture and toughening in ceramics, tribology, processing, properties and thermal stability of nanocrystalline materials and precision machining processes. He has published over 250 papers.

## **MARK R. PANKOW**

Director, Ballistic Loading and Structural Testing Laboratory  
Assistant Professor, Department of Mechanical and Aerospace Engineering

BS, Mechanical Engineering, California Polytechnic State University, San Luis Obispo, 2005

MS, Mechanical Engineering, University of Michigan, 2007

PhD, Mechanical Engineering, University of Michigan, 2010

After receiving his PhD degree from the University of Michigan in 2010, Dr. Pankow joined the Army Research Laboratories and worked there for two years. His research interests were in the areas of dynamic failure of composite materials. His work was both experimental and computational in nature. Dr. Pankow joined the faculty at North Carolina State University in 2012. His current research interests include dynamic testing (ballistic, blast, impact), computational modeling of composites, and deployable structures. He is the editor for the American Society for Composites.

## DAVID C. MUDDIMAN

Jacob and Betty Belin Distinguished Professor of Chemistry  
Founder and Director of the W.M. Keck FTMS Laboratory for Human Health Research

B.S., Chemistry, Gannon University, 1990  
Ph.D., Analytical Chemistry, University of Pittsburgh, 1995

Prior to moving his research group to North Carolina State University in 2006, David was a Professor of Biochemistry and Molecular Biology and Founder and Director of the Proteomics Research Center at the Mayo Clinic College of Medicine in Rochester, MN. Prior to this appointment, David was an Associate Professor of Chemistry at Virginia Commonwealth University. It was there that he began his professional career as an assistant professor with an adjunct appointment in the Department of Biochemistry and Molecular Biophysics and as a member of the Massey Cancer Center in 1997. These academic appointments followed a postdoctoral fellowship at Pacific Northwest National Laboratory in the Environmental Molecular Sciences Laboratory under Richard D. Smith from 1995-1997. David was born in Long Beach, CA in 1967 but spent most of his formative years in a small town in Pennsylvania. Dr. Muddiman is Editor of *Analytical and Biological Chemistry* and Associate Editor of the *Encyclopedia of Analytical Chemistry* as well as on the Editorial Advisory Board of *Mass Spectrometry Reviews*, *Molecular and Cellular Proteomics*, *Rapid Communications in Mass Spectrometry*, and the *Journal of Chromatography B*. He also serves on the advisory board of the NIH Funded Complex Carbohydrate Research Center, University of Georgia and the Yale/NIDA Neuroproteomics Center, Yale University. Dr. Muddiman has served as a member of the ASMS Board of Directors and Treasurer of US-HUPO, and he is currently the President of US HUPO. His group has presented over 500 invited lectures and presentations at national and international meetings including 20 plenary/keynote lectures. His group has published over 250 peer-reviewed papers and has received four US patents in addition to two patents pending. He is the recipient of the 2015 ACS Award in Chemical Instrumentation, 2010 Biemann Medal (American Society for Mass Spectrometry), 2009 NCSU Alumni Outstanding Research Award, the 2004 ACS Arthur F. Findeis Award, the 1999 American Society for Mass Spectrometry Research Award, and the 1990-1991 Safford Award for Excellence in Teaching (University of Pittsburgh). Dr. Muddiman's research is at the intersection of innovative mass spectrometry technologies, systems biology, and model organisms for diseases and bioenergy, and is funded by the National Institutes of Health, the National Science Foundation, the Department of Energy, and The United States Department of Agriculture.



## **VICTORIA M MILLER**

Assistant Professor, Department of Materials Science and Engineering

BSE, Materials Science and Engineering, University of Michigan, 2011

PhD, Materials, University of California Santa Barbara, 2016

Assistant Professor Victoria Miller joined the Department of Materials Science and Engineering at North Carolina State University in August 2017. Prior to NCSU, she worked as a research scientist at UES, Inc. onsite at the Materials and Manufacturing Directorate of the Air Force Research Laboratory in Dayton, Ohio. She completed her PhD in the Materials Department at the University of California Santa Barbara in 2016, and her BSE at the University of Michigan in 2011.

## **BRENDAN T. O'CONNOR**

Associate Professor

Department of Mechanical and Aerospace Engineering

BS, Mechanical Engineering, Marquette University, 2000

MS, Mechanical Engineering, University of Massachusetts, 2004

PhD, Mechanical Engineering, University of Michigan, 2009

After receiving his BS from Marquette University, Dr. O'Connor joined Norian/Siani Engineering, an engineering consulting firm in Boston MA. He then returned to the University of Massachusetts and joined the Industrial Assessment Center, conducting energy audits of industrial facilities. During his PhD, Dr. O'Connor turned his research towards solar power, with a focus on organic electronic materials processing. After his graduation, Dr. O'Connor joined the Polymers Division at the National Institute of Science and Technology as an NRC-NIST Postdoctoral Fellow. At NIST, Dr. O'Connor conducted research on processing and mechanical properties of organic electronic films, primarily for flexible transistor applications. He then joined NC State University in 2011. At NC State, Dr. O'Connor's research interests are focused on polymer semiconductor device processing and characterization. His research efforts include developing plastic solar cells with unique optoelectronic characteristics, and developing mechanically robust flexible and stretchable electronic devices.

# STAFF

## KENNETH P. GARRARD

Senior Research Scholar  
Precision Engineering Consortium and  
Molecular Education Technology and Research Innovation Center

BS, Computer Science, North Carolina State University, 1979  
MS, Computer Studies, North Carolina State University, 1983

As a full-time researcher at the Precision Engineering Consortium for over 31 years, Mr. Garrard's interests and duties have included the development of high performance control systems for ultra-precision machines and software for custom, multiprocessor computer systems. He participated in the development of the original PEC fast tool servo as well as three other fast tool servo systems that have been delivered to commercial and government sponsors. One of these systems was built specifically for the machining of off-axis segments of conic surfaces of revolution and another was used for the fabrication of inertial confinement fusion targets. He has performed numerous prototype fabrication projects that required unique machine configurations and controller software. He is also co-inventor of the spherical coordinate measurement machine, *Polaris3D*, and was the developer of algorithms for its control and for the analysis of measurement data.

Since 2012 he has collaborated with the Molecular Education Technology and Research Innovation Center to assist with the implementation of video system directed sample stage motion control, region of interest selection, laser optics and instrument synchronization for IR-MALDESI imaging. This led to the development of the open-source *MSiReader* software package for analysis and visualization of very large Mass Spectrometry Imaging data sets.

Mr. Garrard has a long-standing interest in the analysis of scientific data, computational geometry, signal processing, programming language structures, sorting and searching algorithms, multiprocessor computer architecture and the design and implementation of hard real-time systems. He is a regular contributor to the Mathworks user community web site.

## **Anthony Wong**

Research Associate

BS, Mechanical Engineering, NC State University, 2005

MS, Mechanical Engineering, Massachusetts Institute of Technology, 2012

Mr. Wong joined the Precision Engineering Consortium in 2017 as a member of the technical staff. His current research interests include machine design and metrology. Prior to coming to the PEC, he had 7 years of industry experience including positions at Caterpillar, AKG of America, ShopBot Tools and Keystone Tower Systems.

## GRADUATE STUDENTS

**CHARAN BODLAPATI** obtained his B.S. degree in Mechanical Engineering at Osmania University, Hyderabad, India. During undergrad, he had a variety of experiences, including working as the Design Lead for university motorsports team which participated in FSAE Italy (2015), and as an intern in the department of materials at Ashok Leyland, Hosur. He joined PEC in March 2017 as a research assistant. His current interests include precision machining, polymers and engineering design.

**NOA MCNUTT** obtained his B.S. in Mechanical Engineering at NC State in December 2017. Noa joined the PEC as an undergraduate researcher in January 2017, working on a Los Alamos National Laboratory funded project. He became a grad student at the PEC in January 2018, researching dry machining methods for ductile metals. Noa grew up in Raleigh and his interests outside of the lab include biking, skiing, golf and cars.

## UNDERGRADUATE STUDENT

**ALYSSA EDWARDS** joined PEC in January 2017 as an undergraduate studying Mechanical Engineering at NCSU. During her time at PEC, she has gained experience in fabrication, metrology and design. Her research at PEC includes determining a method to quantify the natural frequency of a piezoelectric load cell used in diamond turning experiments. She will intern with Eaton Corp. during Summer 2018 and plans to receive her B.S. in Mechanical Engineering in May 2019. Alyssa was raised in Bostic, NC. and enjoys hiking as well as playing basketball and volleyball.





# GRADUATES OF THE PRECISION ENGINEERING CONSORTIUM

## 2016

Brandon Suit

## 2014

David Gebb  
Sean Gunning  
David Brehl  
John Nowak

## 2012

Brandon Lane  
Zachary Marston

## 2010

Meirong Shi

## 2009

Qunyi Chen  
Erik Zdanowicz

## 2008

Lucas Lamonds  
Stephen Furst

## 2006

Nadim Wanna  
Robert Woodside

## 2005

Brett Brocato  
Nathan Buescher  
Karalyn Folkert

## 2004

Karl P. Freitag  
Simon Halbur  
Witoon Panusittikorn  
Travis Randall

## 2003

Stuart Clayton  
David Hood  
Patrick Morrissey  
Nobu Negishi  
Tao Wu

## 2002

David Gill  
David Kametz

## 2001

Markus Bauer  
Matthew Cerniway  
Matias Heinrich  
Bryan Love

## 2000

Brad Austin  
Byoung Loh  
Michael Long  
Edward Miller  
Wonbo Shim

## 1999

Konrad Jarausch  
Bradley Jared  
Edward Marino

## 1998

Robert Day  
John Fasick  
Paul Minor  
Keith Sharp

## 1997

Eugenio Decrescenzo  
Hector Gutierrez  
Ayodele Oyewole  
John Richards  
Robert Skolnick



**1996**

Chris Arcona  
Christian Haeuber  
Bradley Jared  
Quan Ma  
Alex Ruxton  
Anthony Santavy  
Brent Stancil  
Anand Tanikella  
Donna Thaus

**1995**

Konrad Jarausch  
Charles Mooney  
Keith Sharp  
John Tyner

**1994**

Jeffrey Abler  
William Allen  
James Cuttino  
Michele Miller  
Ganesh Rao

**1990**

Scott Blackley  
Byron Knight  
John Pellerin  
Mary Beth Smith

**1989**

Joseph Drescher  
Karl Falter  
David Grigg  
Michael Luh  
Hakan Ozisik  
Denise Skroch  
Elizabeth Smith

**1988**

Thomas Bifano  
Peter Blake  
Steven Fawcett  
Michael Loewenthal

**1987**

John Carroll  
Dan Luttrell  
Gary Mitchum  
Larry Mosley

**1986**

Mark Cagle  
James Gleeson  
Jerry Kannel  
Mark Landy

**1985**

Damon Christenbury

# ACADEMIC PROGRAMS

Problems and limitations associated with precision manufacturing can originate in the machine, the process, or the material. In fact, most problems will probably be caused by a combination of these factors. Therefore, improvement of current processes and development of new manufacturing methods will require knowledge of a multi-disciplinary array of subjects. The educational goal of the Precision Engineering Center is to develop an academic program which will educate scientists and engineers in metrology, control, materials, and the manufacturing methods of precision engineering.

The graduate students involved in the Precision Engineering Center have an annual stipend as research assistants. They can take up to 3 classes each semester while spending about 20 hours per week on their research projects. These students also work in the Center full-time during the summer months.

The Precision Engineering Center began in 1982 with an emphasis on the mechanical engineering problems associated with precision engineering. As a result, the original academic program proposed was biased toward courses related to mechanical design and analysis. However, as the research program has developed, the need for complementary research in sensors, materials, and computers has become obvious. A graduate student capable of making valuable contributions in the computer area, for example, will require a significantly different academic program than in mechanical engineering. For this reason, the Center faculty has set a core curriculum and each student in the program is required to take at least 3 of these core courses. The remainder of the courses for the MS or the PhD degree are determined by the university or department requirements and the faculty committee of the student.

The required courses are:

- MAE 545 Metrology in Precision Manufacturing
- PY 516 Physical Optics
- MAT 700 Modern Concepts in Materials Science
- CSC (ECE) 714 Real Time Computer Systems

## **PhD DEGREE PROGRAM**

The PhD program in Precision Engineering has been set up as a multi-disciplinary program, drawing upon courses throughout the University to provide background and expertise for the students. It should contain required courses to insure solid grounding in the fundamentals plus electives to prepare the student in his area of specialization. Because Precision Engineering is concerned with an integrated manufacturing process, students interested in computer control, materials, machine structure, and measurement and actuation systems are involved in the program. Student research projects include the wide variety of topics addressed in this report. Each student's thesis should have an experimental component because Precision Engineering is basically a hands-on technology.

## **MS DEGREE PROGRAM**

The Master of Science degree will have a higher percentage of application courses than the PhD degree. The emphasis will be to develop the foundation for involvement in precision engineering research and development. A total of 30 credits, including 6 credits for the MS thesis, are required. The thesis, while less comprehensive than the PhD dissertation, will be directed at important problems in Precision Engineering. Typically, the MS program will take four semesters plus one summer.

## **UNDERGRADUATE PROGRAM**

The undergraduate degree broadly prepares an engineering student for industrial activities ranging from product design and engineering sales to production implementation. Because a large share of engineers only have the BS degree, these will be the people who must implement the new technology developed in research programs like the Precision Engineering Center. Therefore, a way must be found to acquaint engineers at the BS level with the techniques, problems, and potential of precision manufacturing.

In most undergraduate degree programs only limited time is available for technical electives. However, these electives offer the student the opportunity to expand his knowledge in many different directions. Beginning graduate courses (such as metrology) can be used as undergraduate electives.

Undergraduate projects and summer employment have also been utilized to include undergraduate students into the research program of the Center. During the 1998-1999 academic year, four undergraduate students in Mechanical Engineering were involved various projects at the PEC.

## STUDY PLANS

Study plans for several example students are given below both for the MS and the PhD degree. Because of the breadth of the field and the wide range of thesis topics, few if any study plans will be exactly the same. The plan will depend upon the student's background, his interests, his thesis topic, the department, and the chairman and members of his committee.

## PhD PROGRAM IN MECHANICAL ENGINEERING

### Major Courses:

- MAE 740 Advanced Machine Design I
- MAE 741 Advanced Machine Design II
- MAE 706 Heat Transfer Theory & Applications
- MAE 713 Principles of Structural Vibration
- MAE 760 Computational Fluid Mechanics and Heat Transfer
- MAE 545 Metrology in Precision Manufacturing
- MAE 715 Nonlinear Vibrations
- MAE 716 Random Vibration
- MAE 714 Analytical Methods in Structural Vibration
- MAE 742 Mechanical Design for Automated Assembly
- MAE 895 Doctoral Dissertation Research

### Minor Courses:

- MA 511 Advanced Calculus I
- MA 775 Mathematical Methods in the Physical Sciences I
- CSC 780 Numerical Analysis II
- PY 516 Physical Optics
- ECE 716 System Control Engineering
- MAT 700 Modern Concepts in Materials Science
- ECE 726 Advanced Feedback Control
- ECE 764 Digital Image Processing

## PHD PROGRAM IN MATERIALS ENGINEERING

### Major Courses:

- MAT 710 Elements of Crystallography and Diffraction
- MAT 700 Modern Concepts in Materials Science
- MAT 556 Composite Materials
- MAT 715 Transmission Electron Microscopy
- MAT 795 Defect Analysis/Advanced Materials Experiments
- MAT 753 Advanced Mechanical Properties of Materials
- MAT 712 Scanning Electron Microscopy
- MAT 895 Doctoral Dissertation Research

### Minor Courses:

- PY 414 Electromagnetism I
- ST 502 Experimental Statistics for Engineers I
- MAE 740 Advanced Machine Design I
- MAE 741 Advanced Machine Design II
- MAE 545 Metrology in Precision Manufacturing
- PY 516 Physical Optics
- MA 401 Applied Differential Equations II

## PHD PROGRAM IN ME (FOR STUDENT WITH MS DEGREE)

- ECE 716 System Control Engineering
- ECE 791 Gate Array Design
- MAT 700 Modern Concepts in Materials Science
- PY 516 Physical Optics
- MA 502 Advanced Mathematics for Engineers and Scientists II
- MA 775 Mathematical Methods in the Physical Sciences I
- MA 780 Numerical Analysis II
- MAE 732 Fundamentals of Metal Machining Theory
- MAE 740 Advanced Machine Design I
- MAE 741 Advanced Machine Design II
- MAE 545 Metrology in Precision Manufacturing
- MAE 716 Random Vibration

## **MS PROGRAM FOR ME STUDENT**

- MAE 713 Principles of Structural Vibration
- MAE 740 Advanced Machine Design I
- MAE 545 Metrology in Precision Manufacturing
- MAT 700 Modern Concepts in Materials Science
- PY 516 Physical Optics
- MA 501 Advanced Math for Engineers and Scientists I
- MA 502 Advanced Math for Engineers and Scientists II
- MAE 695 Master's Thesis Research

## **MS PROGRAM FOR COMPUTER SCIENCE STUDENT**

- CSC 501 Operating Systems Principles
- CSC 506 Architecture of Parallel Computers
- CSC 512 Compiler Construction
- ECE 521 Computer Design and Technology
- CSC 715 Concurrent Software Systems
- MAE 545 Metrology for Precision Manufacturing
- MAE 789 Digital Control Systems
- ECE 764 Digital Image Processing

## **MS PROGRAM FOR MATERIALS SCIENCE STUDENT**

- MAT 700 Modern Concepts in Material Science
- MAT 710 Elements of Crystallography and Diffraction
- MAT 715 Transmission Electron Microscopy
- MAT 712 Scanning Electron Microscopy
- MAT 722 Advanced Scanning Electron Microscopy and Surface Analysis
- MAE 545 Metrology for Precision Manufacturing
- PY 516 Physical Optics
- ECE 738 IC Technology and Fabrication
- MAT 695 Master's Thesis Research

## **MS PROGRAM FOR PHYSICS STUDENT**

- PY 516 Physical Optics
- PY 552 Introduction to Structure of Solids I
- PY 753 Introduction to Structure of Solids II
- PY 781 Quantum Mechanics I
- PY 782 Quantum Mechanics II
- PY 783 Advanced Classical Mechanics
- PY 785 Advanced Electricity and Magnetism I
- PY 786 Advanced Electricity and Magnetism II
- MAT 700 Modern Concepts in Material Science
- MAE 545 Metrology for Precision Manufacturing
- PY 695 Master's Thesis Research

## **SHORT COURSES AND TV COURSES**

Six graduate level courses: Scanning Electron Microscopy (MAT 712), Advanced SEM Surface Analysis (MAT 722), Modern Concepts in Material Science (MAT 700), Mechanical Properties of Materials (MAT 705), and Metrology (MAE 545) have been offered as video courses nationwide via National Technological University. In a typical year, approximately 120 students from industry and national laboratories participate in these courses. Future plans call for a MS program in Precision Engineering to be offered via the television network.

## TECHNICAL REPORTS

Volume 1 - 1983	December 1983	136 pages
Volume 2 - 1984	January 1985	168 pages
Volume 3 - 1985	January 1986	294 pages
Volume 4 - 1986	January 1987	255 pages
Volume 5 - 1987	December 1987	336 pages
Volume 6 - 1988	December 1988	362 pages
Volume 7 - 1989	March 1990	357 pages
Volume 8 - 1990	March 1991	385 pages
Volume 9 - 1991	March 1992	382 pages
Volume 10 - 1992	March 1993	289 pages
Volume 11 - 1993	March 1994	316 pages
Volume 12 - 1994	March 1995	268 pages
Volume 13 - 1995	January 1996	251 pages
Volume 14 - 1996	January 1997	232 pages
Volume 15 - 1997	January 1998	298 pages
Volume 16 – 1998	January 1999	258 pages
Volume 17 – 1999	January 2000	232 pages
Volume 18 – 2000	January 2001	274 pages
Volume 19 – 2001	January 2002	201 pages
Volume 20 – 2002	January 2003	328 pages
Volume 21 - 2003	January 2004	208 pages
Volume 22 – 2004	February 2005	207 pages
Volume 23 – 2005	February 2006	264 pages
Volume 24 – 2006	March 2007	274 pages
Volume 25 – 2007	March 2008	192 pages
Volume 26 – 2008	March 2009	209 pages
Volume 27 – 2009	March 2010	192 pages
Volume 28 – 2010	March 2011	139 pages
Volume 29 – 2011	March 2012	210 pages
Volume 30 – 2012	March 2013	164 pages





# FACT SHEET – PRECISION ENGINEERING CONSORTIUM (PEC)

## HISTORY

### **1982-1985 ONR Selected Research Opportunity**

Based on several years of evaluation of the state of the field known as precision engineering in Europe and Japan, the Office of Naval Research decided to ask for proposals in this area. Ralph Burton, the head of MAE at NC State, and Thomas Dow, who had just joined the University from the Battelle Research Labs, headed a proposal team consisting of faculty from NC State and Research Triangle Institute. The proposal involved research in the areas of metrology, fabrication and controls. The proposal from NCSU was funded along with proposals from Purdue, Stanford and Maryland.

### **1985 PEC Affiliate Meeting**

Buoyed by the success of the SRO project and interactions with precision engineering industries across the country, a meeting was held in Raleigh with 31 representatives from 26 potential industrial affiliates of the PEC. At the end of this meeting, the 5 original members - Kodak, Moore, GM, Texas Instruments and Livermore National Labs - signed up to provide \$25K each to help support the Center. Support from these and other Affiliates, along with new projects funded by ONR, NSF and others, has allowed the PEC to educate a new generation of precision engineers and scientists. Our web site is [www.pec.ncsu.edu](http://www.pec.ncsu.edu)

### **1986 ASPE Founded**

The success of the PEC and the need to provide a forum for communication within this broad field led to the formation of the American Society for Precision Engineering in 1986. The impetus was a meeting held one year earlier in Raleigh that was jointly organized by Lawrence Livermore Labs and the PEC. There were about 60 attendees at that meeting and the question was posed - should a new society be created to serve the field? A majority of the attendees indicated “yes” and a not-for-profit corporation was chartered in North Carolina by Tom Dow, Ron Scattergood and John Strenkowski. The first meeting was held in Dallas, TX in the fall of 1986 with Tom’s wife as a voluntary staff member. Currently the ASPE has offices in Raleigh with 3 employees and a worldwide membership of 800. The 2017 Annual Meeting was held in Charlotte, NC and had more than 375 attendees with 42 exhibit companies, 25 tutorials and 40 oral presentations and 93 posters. Tom Dow serves as the Executive Director. Web site: [www.aspe.net](http://www.aspe.net)

### **1986-1991 University Research Initiative**

In 1986, a new DOD initiative was announced and NC State submitted a multi-disciplinary proposal with faculty from mechanical engineering, materials science, physics, computer science and electrical engineering. There were 35 proposals submitted in the manufacturing area and only the NC State concept was funded. This project was funded at \$1M per year for 5 years.

### **1988 First Building on Centennial Campus**

The \$5M URI grant to the PEC was the largest single research grant received by the University up to that time. This grant came at a time when the University acquired a 1000 acre research campus from the state named Centennial Campus. Based on the space need for this program as well as the desire to begin development of the CC, a building for the PEC was started in April of 1987 and the Center was moved to Centennial Campus in February of 1988. This building was inaugurated in April of 1988 with Dr. Saalfeld, Technical Director of ONR, as one of the guest speakers.

### **List of PEC Affiliates**

These companies have contributed \$30K per year as a membership fee and also support specific research projects with additional support. The membership fee partially supports the administrative staff member as well as the two research engineers.

- |                              |                                   |
|------------------------------|-----------------------------------|
| 1. Aerotech, Inc             | 15. Martin Marrietta              |
| 2. Burleigh Instruments      | 16. Materials Analytical Services |
| 3. Corning, Inc              | 17. Moore Special Tool            |
| 4. Cummins Engine Co.        | 18. NIST                          |
| 5. Digital Instruments       | 19. Oak Ridge National Labs       |
| 6. General Motors            | 20. Oculus VR                     |
| 7. Hughes                    | 21. Office of Naval Research      |
| 8. IBM                       | 22. Panasonic                     |
| 9. Kodak                     | 23. Pneumo Precision Inc          |
| 10. Lexmark                  | 24. Rank Taylor Hobson            |
| 11. Livermore National Labs  | 25. StorageTek                    |
| 12. Lockheed Martin          | 26. Teledyne, Inc.                |
| 13. Los Alamos National Labs | 27. Texas Instruments             |
| 14. 3M                       | 28. Vistakon, Inc                 |